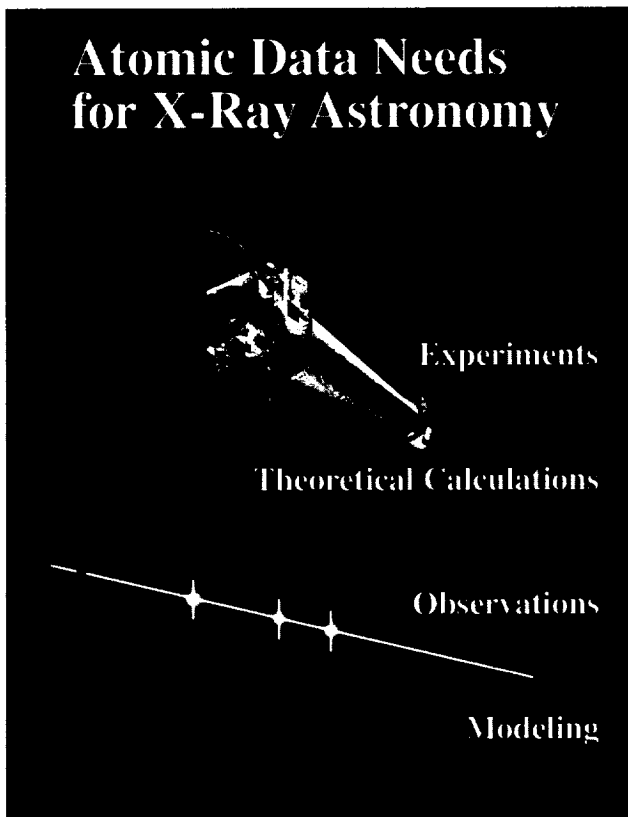




Atomic Data Needs for X-ray Astronomy

Edited by:

Manuel A. Bautista, Timothy R. Kallman, and Anil K. Pradhan



*Proceedings of a workshop held at
NASA Goddard Space Flight Center
Greenbelt, Maryland
December 16-17, 1999*

The NASA STI Program Office ... in Profile

Since its founding, NASA has been dedicated to the advancement of aeronautics and space science. The NASA Scientific and Technical Information (STI) Program Office plays a key part in helping NASA maintain this important role.

The NASA STI Program Office is operated by Langley Research Center, the lead center for NASA's scientific and technical information. The NASA STI Program Office provides access to the NASA STI Database, the largest collection of aeronautical and space science STI in the world. The Program Office is also NASA's institutional mechanism for disseminating the results of its research and development activities. These results are published by NASA in the NASA STI Report Series, which includes the following report types:

- **TECHNICAL PUBLICATION.** Reports of completed research or a major significant phase of research that present the results of NASA programs and include extensive data or theoretical analysis. Includes compilations of significant scientific and technical data and information deemed to be of continuing reference value. NASA's counterpart of peer-reviewed formal professional papers but has less stringent limitations on manuscript length and extent of graphic presentations.
- **TECHNICAL MEMORANDUM.** Scientific and technical findings that are preliminary or of specialized interest, e.g., quick release reports, working papers, and bibliographies that contain minimal annotation. Does not contain extensive analysis.
- **CONTRACTOR REPORT.** Scientific and technical findings by NASA-sponsored contractors and grantees.
- **CONFERENCE PUBLICATION.** Collected papers from scientific and technical conferences, symposia, seminars, or other meetings sponsored or cosponsored by NASA.
- **SPECIAL PUBLICATION.** Scientific, technical, or historical information from NASA programs, projects, and mission, often concerned with subjects having substantial public interest.
- **TECHNICAL TRANSLATION.** English-language translations of foreign scientific and technical material pertinent to NASA's mission.

Specialized services that complement the STI Program Office's diverse offerings include creating custom thesauri, building customized databases, organizing and publishing research results . . . even providing videos.

For more information about the NASA STI Program Office, see the following:

- Access the NASA STI Program Home Page at <http://www.sti.nasa.gov/STI-homepage.html>
- E-mail your question via the Internet to help@sti.nasa.gov
- Fax your question to the NASA Access Help Desk at (301) 621-0134
- Telephone the NASA Access Help Desk at (301) 621-0390
- Write to:
NASA Access Help Desk
NASA Center for Aerospace Information
7121 Standard Drive
Hanover, MD 21076-1320

NASA/CP-2000-209968



Atomic Data Needs for X-ray Astronomy

Edited by:

*Manuel A. Bautista and Timothy R. Kallman
NASA Goddard Space Flight Center, Greenbelt, Maryland*

*Anil K. Pradhan
The Ohio State University, Columbus, Ohio*

National Aeronautics and
Space Administration

Goddard Space Flight Center
Greenbelt, Maryland 20771

October 2000

Available from:

NASA Center for Aerospace Information
7121 Standard Drive
Hanover, MD 21076-1320
Price Code: A17

National Technical Information Service
5285 Port Royal Road
Springfield, VA 22161
Price Code: A10

ORGANIZED BY

Laboratory for High Energy Astrophysics
NASA Goddard Space Flight Center

Scientific Organizing Committee

Manuel Bautista (NASA/GSFC), co-chair
Timothy Kallman (NASA/GSFC), co-chair
Peter Beiersdorfer (LLNL)
Nancy Brickhouse (CfA)
Duane Liedahl (LLNL)
Richard Mushotzky (NASA/GSFC)
Anil Pradhan (Ohio State Univ.)
Nicholas White (NASA/GSFC)

Local Organizing Committee

Manuel Bautista (NASA/GSFC)
Timothy Kallman (NASA/GSFC)

Preface

This publication contains written versions of most of the invited talks presented at the workshop on “Atomic Data Needs for X-ray Astronomy”, which was held at NASA’s Goddard Space Flight Center on December 16-17, 1999.

The idea of hosting such a workshop emerged from an imminent need to update and complete current atomic datasets in anticipation of a new era of high quality X-ray spectra starting with the launching of Chandra and XMM-Newton observatories. At first, our vision of the workshop was of a short and limited attendance event, given the specialization of the topic. But it was soon realized, from the response to the first workshop announcement, that the topic was of much interest to researchers working in X-ray spectra (physicists and astronomers). As a result, the workshop grew to approximately 120 participants from several countries.

The kind of atomic data that interests us are those parameters needed for analysis and modeling of spectra shortward of $\sim 100 \text{ \AA}$ and relevant to ionic species of astronomical interest. The physical mechanisms of interest in the formation of spectra include photoionization, collisional ionization, recombination (radiative and dielectronic), collisional excitation (by electrons and protons), and radiative deexcitation. Unique to X-ray spectroscopy are the ionization and excitation processes from inner-closed shells, in addition to the challenges in interpreting the medium resolution ($\Delta\varepsilon/\varepsilon \sim 0.05 - 0.1$) data obtained by current X-ray astronomy experiments. Line wavelengths are of interest too, particularly owing to the high resolution spectra from the new experiments.

The workshop was divided into five major areas: Observational Spectroscopy, Theoretical Calculations of Atomic Data, Laboratory Measurements of Atomic Parameters, Spectra Modeling, and Atomic Databases.

One comforting finding from the workshop is that the enthusiasm felt by X-ray

astronomers about the new observational missions seems to be shared by theoretical and experimental physicists. Talks were presented about several exciting new projects and experimental and theoretical techniques devoted to X-ray spectroscopy. Simultaneously, several new tools for spectral analysis and modeling have recently been developed, together with improved atomic databases.

These proceedings are expected to be of interest to producers and users of atomic data. Moreover, the contributions presented here have been written in a way that can be used by a general audience of scientists and graduate students in X-ray astronomy, modeling, and in computational and experimental atomic physics.

Table of Contents

I. Observational Spectroscopy

Spectroscopy and X-Ray Astronomy <i>Stephen S. Holt</i>	1
Initial Results from the Chandra High Energy Transmission Grating Spectrometer <i>C.R. Canizares, D.S. Davis, D. Dewey, K.A. Flanagan, J. Houck, D.P. Huenemoerder, H.L. Marshall, M.L. Schattenburg, N.S. Schulz, M. Wise</i>	5
First Results of the Chandra-LETGS <i>P. Predehl, B. Aschenbach, H. Bräuning, W. Burkert, V. Burwitz, G. Hartner, J. Trümper</i>	11
Chandra and the Emission Line Project <i>N. S. Brickhouse and J. J. Drake</i>	19

II. Theoretical Atomic Calculations

Theoretical Calculations of Atomic Data for Spectroscopy <i>M.A. Bautista</i>	25
Distorted Wave Calculations and Applications <i>A.K. Bhatia</i>	41
The RmaX Network: R-matrix Calculations for X-ray Atomic Processes <i>K.A. Berrington</i>	65
The Iron Project <i>A.K. Pradhan</i>	69
Photoionization and Recombination <i>S.N. Nahar</i>	77
K-Shell Photoionization of Fe <i>B.M. McLaughlin, D. Donnelly, K.L. Bell, M.P. Scott, and F.P. Keenan</i>	85
The R-matrix with Pseudostates Method <i>T.W. Gorczyca, N.R. Badnell, D.C. Griffin, D.M. Mitnik, and M.S. Pindzola</i>	97

III. Experimental Atomic Data

Laboratory Data for X-Ray Astronomy <i>P. Beiersdorfer, G.V. Brown, H. Chen, M.F. Gu, S.M. Kahn, J.K. Lepson, D.W. Savin, S.B. Utter</i>	103
---	-----

Time-Resolved Atomic Spectroscopy with Fast-Ion Beams, Heavy-Ion Storage Rings and Ion Traps <i>E. Träbert</i>	117
Tokamak Spectroscopy for X-ray Astronomy <i>K.B. Fournier, M. Finkenthal, D. Pacella, M. J. May, V. Soukhanovskii, M. Mattioli, M. Leighab and J. E. Rice</i>	127
X-Ray Photoionized Plasmas in the Laboratory <i>R.F. Heeter, J.A. Emig, M.E. Foord, R.S. Thoe, P.T. Springer, J. Bailey, M. Cuneo, and C. Deeney</i>	135
Modeling X-Ray Photoionized Plasmas: Ion Storage Ring Measurements of Low Temperature Dielectronic Recombination Rate Coefficients for L-Shell Iron <i>D.W. Savin, N.R. Badnell, T. Bartsch, C. Brandau, M.H. Chen, M. Grieser, G. Gwinner, A. Hoffknecht, S. M. Kahn, J. Linkemann, A.Müller, R. Reponow, A.A. Saghiri, S. Schippers, M. Schmitt, D. Schwalm, A. Wolf, and P.A. Závodszky</i>	143
IV. Modeling Astronomical Spectra	
The Completeness Criterion in Atomic Modeling <i>Duane A. Liedahl</i>	151
Coronal Plasmas Modeling and the MEKAL Code <i>J.S. Kaastra and R. Mewe</i>	161
V. Atomic Databases	
Atomic Databases <i>C. Mendoza</i>	167

Spectroscopy and X-Ray Astronomy

Stephen S. Holt

Goddard Space Flight Center, Code 600, Greenbelt MD 20771 USA

Abstract. The new x-ray astronomical observatories have sufficient spectroscopic capability to allow the determination of plasma conditions in the form of velocities, temperatures, densities, and turbulence parameters at levels that were previously unattainable. The utilization of these diagnostics are possible only if the atomic and plasma physics are well-enough understood to match the observational sensitivity.

1. Introduction

X-rays provide an undistorted view of the sky. Even if all the mass in the universe was in baryons, and its average density was high enough to eventually halt its expansion (both of which assumptions are inconsistent with recent observations), the universe would still be transparent to X-rays, on average.

The first non-solar X-rays were detected almost 40 years ago (Giacconi et al. 1962), in a rocket flight with Geiger counter detectors that were sensitive to few-keV X-rays but had no spectroscopic capability within its energy acceptance window. Nevertheless, that first detection of X-rays, from both a strong source in the constellation Scorpius (Sco X-1) and a seemingly diffuse component over the whole sky, could be considered to be a spectroscopic measurement of sorts. The very detection of few-keV X-rays virtually demands effective source temperatures of the order of at least tens of millions of degrees. In fact, the argument that such X-rays therefore required a “blue” star (i.e., “hot” stellar counterpart, in relative astronomical terms) was the rationale for the correct identification of Sco X-1 with the blue stellar object in the error box provided by a rotation modulation collimator observation from a subsequent rocket flight (Clark, et al. 1965).

Up until the present time, it is fair to say that the concentration of community effort in X-ray astronomy has been associated with imaging, rather than spectroscopy. This has primarily been associated with the identification of X-ray sources with optical and radio counterparts, and the subsequent determination of class properties. The earliest “imaging” was accomplished by the mechanical restriction of detector fields-of-view, but the subsequent development of true X-ray telescopes with both magnification and fine angular resolution have allowed the true imaging of extended sources and the reduction of observational backgrounds.

Nevertheless, most of the significant breakthroughs in our understanding of the fundamental nature of X-ray sources have come from analyses of aspects of the observations that are other than imaging. Some of the most fundamental have come from timing analyses. For example, the determination of the basic nature of the brightest (in apparent magnitude) X-ray sources was the result of the analysis of temporal variability alone, in much the same way as was the identification of radio pulsars powered by the slowing-down of rotating neutron stars (Gold 1968). X-ray pulsars were found in the early results from the first X-ray astronomical satellite *Uhuru*, but there were two very troubling aspects to the measurements. First, the pulse periods seemed much too long to match the X-ray luminosities (since the radio pulsar explanations required the power to go like the inverse fourth power of the period) and, even more troubling, the putative neutron stars in X-ray sources were speeding up instead of slowing down!

The resolution of this puzzle again came from two complementary temporal measurements on very different timescales: days and seconds (Schreier et al. 1972). The discovery of periodicity in the disappearance of the signal from some X-ray sources on timescales of days suggested to some observers that the signal dropouts might be eclipses in binary systems observed from close to their equatorial planes. This suggestion was clinched when *Uhuru* was able to measure Doppler variations consistent with exactly

the day-scale eclipse=orbital periods in their second-scale pulse periods. The total disappearance of the signal was a clear indication that the X-ray source region was much smaller than the ordinary stellar component of the binary system, and the secular speed-up of the pulsations was consistent with the transfer of angular momentum with mass accretion to the neutron star.

New spectroscopic observations are playing an increasingly important role our understanding of the X-ray sky, and our group at the Goddard Space Flight Center has led the community in the development of spectroscopic instrumentation. The new generation of X-ray observatories is providing data of high enough quality that sophisticated modeling is required to use them to full advantage.

2. Some Definitions and Rules of Thumb

X-ray astronomers generally use energy E instead of wavelength λ , and the preferred unit of energy is eV.

The term “energy resolution” δE means the full-width-half-maximum of the detector response at a given energy E . It is also measured in eV.

The dimensionless term “resolving power” R is the ratio of the photon energy E to the energy resolution δE at that energy.

If the temperatures are high enough for the atoms of a specific atomic number to be totally ionized, the only lines that will be observed are those associated with recombination from hydrogenic atoms. Transitions to the ground state from the first excited state (Ly α) produce lines with energies $10.2Z^2$ eV, so that the Ly α lines in the span of elements from oxygen to iron cover the energy range 0.65 keV to 6.9 keV, corresponding to most of the bandpass of current X-ray astronomical facilities. In very hot cosmic plasmas, therefore, where even- Z elements are much more abundant than odd- Z elements, an energy resolution of about 370 eV ($\delta E=10.2[(10)^2-(8)^2]$) (corresponding to a resolving power of only about 2 near oxygen Ly α) would be sufficient to unambiguously separate all the elemental species of interest. At energies near Ly α for Fe, the required δE would be 800 eV, corresponding to an R of about 9.

At somewhat lower temperatures, lines from helium-like ionization states dominate the emission spectrum over a relatively wide temperature range. Here the resonance line (corresponding to the $1s2p - 1s^2$ transition) for a given element is separated from the Ly α line from the same element by about $10Z$ eV. Here the δE required to resolve hydrogenic from helium-like oxygen would be about 70 eV ($R=10$), while 250 eV ($R=30$) would suffice for iron.

For cold gas, where the atoms are neutral (or low states of ionization), the energy separation between the helium-like resonance line and the K-line produced in the transition to the ground state after an inner-shell electron is removed from a close-to-neutral atom is, similarly, about $10Z$ eV.

In the spirit of defining a hierarchy of levels of spectroscopic sophistication, the lowest level might be that associated with merely recognizing temperature-equivalent conditions of at least ten million degrees by identifying the mere presence of X-rays above 1 keV. The next level might be the values discussed above that are required to separate elemental species, and the next again might be those required to separate ionization states in atoms into the three categories: cold, hot (helium-like) and very hot (hydrogenic).

Continuing the hierarchy, the next level might be that required to investigate the components of the K-emission from helium-like atoms, and from the satellite lines from slightly lower ionization species. There have been a variety of combinations of the relative strengths of the helium-like resonance, forbidden and intercombination lines that can provide plasma diagnostics (e.g., Bahcall and Sarazin 1978). Here the line separation is approximately Z eV, providing a requirement for δE of <10 eV ($R>700$) for oxygen and about 25 eV ($R>300$) for iron.

3. Gas Counter Spectroscopy

The proportional counters used for the earliest X-ray astronomical measurements had resolving powers of no more than 3 at iron, or about a factor of 3 too poor to provide the requirement defined in the previous section to barely be capable of detecting emission from isolated hydrogenic lines. The brightest X-ray sources detected in the first generation of X-ray astronomy, with fluxes of about 10^{-9} erg/(cm²-s) for the ten brightest, could provide hundreds of detected photons to mechanically-collimated propor-

tional counters in few-minute sounding rocket observations. First-generation "spectroscopy" generally characterized these sources as being consistent with either power laws or bremsstrahlung continua (or both) over a dynamic range similar to the resolving power of these detectors. This was actually a pretty good match, since spectral lines contribute much less to the luminosity than does the continuum at X-ray temperatures, and each of the few independent energy bins accumulated enough counts for about 10% statistical precision, which was not much worse than the detector calibration.

The advent of satellite observations provided the opportunity for deeper observations. This meant not only that the detectors had to be better-calibrated, but that better resolving power could be usefully applied. Several groups worked hard to provide proportional counters with the limiting resolving power of gas amplification systems of about 6 at 6 keV (for good proportional counters, δE is proportional to \sqrt{E}). This increased resolving power did not quite meet the definition of the last section that was based upon the separation of even- Z elements, but since iron is much more abundant than other heavy elements it allowed for the unambiguous detection of emission lines in sources with prominent (large equivalent continuum width) Fe-K features like Cas A (Serlemitsos et al. 1973). Careful detector calibration was essential since, in general, both line features and continuum gradients had to be "detected" via the residuals from the inconsistency of data with model spectra rather than from the prominent appearance of line features in the raw data.

4. Some Brief Remarks About Dispersive vs Non-dispersive Spectroscopy

The *Einstein Observatory* provided breakthroughs in spectroscopy as well as imaging. Dispersive gratings and crystal spectrometers, which had been used to measure the X-ray spectra of huge solar flare fluxes available in rocket flights, could not easily be made with large enough effective geometric areas or reflection efficiencies to be useful for non-solar X-rays in early satellites. Coupling the dispersive gratings/crystals with the telescope provided large area with small focal plane detectors. The gratings were limited by the fact that the spectra were dispersed on the images of (typically) extended sources, and the crystals were limited by the fact that only a small bite of the whole spectrum could be dispersed (and registered) at any time. Both instruments provided some investigations with dispersed X-ray spectra at a resolving power of about 100, far exceeding what was possible at that time with non-dispersive detectors.

The new *Chandra* and *XMM* observatories have grating spectrometers, which utilize their imaging detectors to obtain resolving powers approaching 1000 at energies less than 1 keV (but <100 at the Fe-K lines). The first results from the *Chandra* gratings presented in this volume are spectacular, and demonstrate the need for careful calculations of the line spectra expected from higher ionization states.

As spectacular as these results are, non-dispersive spectrometers can offer several distinct advantages over dispersive techniques. They can have quantum efficiency approaching unity. They can simultaneously multiplex this efficiency over the entire energy bandpass of the telescope. They can utilize their imaging and spectroscopic capabilities simultaneously without interference. And, while dispersive techniques must have R proportional to wavelength (and therefore inversely proportional to energy), non-dispersive systems can have R increasing with energy faster than \sqrt{E} and can actually provide higher R at higher E .

5. Non-dispersive Spectroscopy

The *Einstein Observatory* also included a new non-dispersive spectrometer that provided somewhat more general capability at a new level of sensitivity. The *Einstein* "solid state spectrometer" was a cryogenically cooled (to about 120 K) non-imaging silicon detector with $R=20$ at the K-lines of Si and S (this would have been $R=40$ at the K-lines of Fe, but Fe-K energies were above the high-energy cutoff of the telescope).

The Japanese-led *ASCA* mission (the name is both a homonym for a fabulous mythic Japanese bird *Asuka* and the acronym for *Advanced Satellite for Cosmology and Astrophysics*; it was called *Astro-D* prior to its launch) carried the first CCD array, which provided true imaging capability with spectroscopic

resolving power corresponding to that of the *Einstein* solid state spectrometer. *ASCA* had telescopes with sensitivity out to 10 keV, so that the Fe-K lines could be investigated.

All three of the new generation of X-ray observatories: *Chandra*, *Astro-E* and *XMM* each have imaging arrays of CCDs, with effective areas (at 1.5 keV) of about 500, 1600, and 2500 cm², respectively.

The totally new spectroscopic capability of *Astro-E* is the "quantum microcalorimeter." Operating at a temperature of less than 100 mK, the detector "noise" associated with the exchange of phonons between the X-ray absorber and the cold sink can be of the order of 1 eV. This instrument was originally chosen to be part of the complement for *Chandra* (Holt 1987). Practical imaging arrays of 32 detectors have been made for *Astro-E* with the total system "noise" being such that the energy resolution of each of the pixels is <10 eV, so that R at Fe-K is >500.

Such high resolving power makes the microcalorimeter competitive with dispersive techniques, but with the distinct advantages of high efficiency, simultaneous response over the whole available energy range, and no dispersion of the photons in the focal plane that can be confused with source extent. This is especially important in the case of line emission from spatially extended (i.e., larger than about 30 arc-seconds) objects that are rich in line emission, such as supernova remnants and clusters of galaxies.

At the time of this writing, the *Chandra* and *XMM* observatories are operational, while there has just been a tragic launch failure of *Astro-E*. This prevents the eagerly anticipated application of microcalorimeter technology, but it is planned to be the key focal plane instrument for future missions with even better resolution (<2 eV) with the utilization of TES (transition edge sensors) instead of FET (field effect transistor) readouts.

6. Summary

It is hoped that the next generation X-ray observatory *Constellation-X* will be launched before the end of the decade. Its next generation non-dispersive imaging spectrometer, baselined to be a focal plane array of microcalorimeters with TES readouts, will have a resolving power in excess of 3000 for Fe-K lines. *Constellation-X* will be optimized for spectroscopic investigations, but will naturally have large aperture in order to take advantage of its spectroscopic capability. The better the resolution, the larger the necessary aperture in order to assure that the statistical precision of the data is consistent with the calibration accuracy in each resolution element for typical observations. *Constellation-X* is expected to have an effective area in excess of 15000 cm² at 1.5 keV. With this aperture, the angular resolution is not expected to match that of *Chandra*, and is baselined at about 1/4 arc-minute. Remembering that X-ray telescopes have grazing-incidence geometries, an aperture this large would require a focal length of order 100 m if accomplished with a single telescope. The word "constellation" in the name derives from the fact that the baseline design includes multiple launches of extendible telescopes in order to achieve the total aperture.

Just as the increased resolving power demands increased aperture, it also demands increased understanding of the spectra associated with all ionization states of elements heavier than carbon.

References

- Bahcall, J. N. & Sarazin, C. L. 1978, *ApJ*, 219, 781
 Clark, G., Garmire, G., Oda, M., Wada, M., Giacconi, R., Gursky, H., & Waters, J. R. 1965, *Nature* 207, 584
 Giacconi, R., Gursky, H., Paolini, F., & Rossi, B., 1962, *Phys. Rev. Lett.* 9, 439
 Gold, T. 1968, *Nature* 218, 731
 Holt, S. S. 1987, *Astrophysical Letters and Communications* 26, 61
 Schreier, E., Levinson, R., Gursky, H., Kellogg, E., Tananbaum, H., & Giacconi, R. 1972, *ApJ*, 172, L79
 Serlemitsos, P. J., Boldt, E. A., Holt, S. S., Ramaty, R., & Briskin, A. F. 1973 *ApJ*, 184, L1

Initial Results from the Chandra High Energy Transmission Grating Spectrometer

C.R. Canizares, D.S. Davis, D. Dewey, K.A. Flanagan, J. Houck, D.P. Huenemoerder,
H.L. Marshall, M.L. Schattenburg, N.S. Schulz, M. Wise

MIT Center for Space Research

Abstract. The High Energy Transmission Grating Spectrometer (HETGS) on the Chandra X-ray Observatory provides spectral resolving powers of 200-1000 over the range 0.4-8.0 keV (1.5-30 Å) with effective area of 2-200 cm². Initial observations during the activation and calibration phases of the mission show that the HETGS is performing as predicted prior to Chandra launch. The talk presented very preliminary results that illustrate the power of the HETGS for performing detailed studies of a wide range of celestial sources, including plasma diagnostics. This written version gives a brief summary of that talk with examples of preliminary spectra of Capella, the Crab pulsar, SS433 and the SNR E0102-72.

1. The Chandra HETGS

The High Energy Transmission Grating (HETG) on the Chandra X-ray Observatory consists of an array of periodic gold microstructures that can be interposed in the converging X-ray beam just behind the High Resolution Mirror Assembly (see Canizares et al. 2000a). When in place, the HETG disperses the X-rays according to their wavelength, creating a spectrum that is recorded at the focal plane by the linear array of CCDs designated ACIS-S (HETGS refers to the full system). There are two different grating types optimized for medium and high energies, designated MEG and HEG. These have periods of 4000 Å and 2000 Å respectively. The grating elements are gold, and are of appropriate thickness to “blaze” the grating in its energy range, enhancing the diffraction efficiency in the first orders (this results from destructive interference in zeroth order between the radiation that passes through the gaps and the grating bars). The MEG covers the outer two Chandra mirror segments, which provide most of the effective area at mid and lower energies, and the HEG the inner two, which give all the high energy area. The gratings were fabricated in the MIT Center for Space Research Space Nanostructures Laboratory using an extension of techniques used for VLSI circuit fabrication.

The HETGS provides spectral resolving power of 200-1000 for point sources (about 0.02 Å for MEG, and 0.01 Å for HEG) and effective areas of 2-200 cm² over the band 0.4-8 keV. The HETG positive and negative orders of the dispersed spectrum appear in the focal plane on either side of the undispersed zeroth order source image. The grating patterns of the HEG and MEG are offset in angle from each other by 10 deg. so their spectra make a shallow “X”-pattern at the focal plane. Multiple overlapping orders are removed by using the moderate energy resolution of the ACIS detector. The HETGS complements the LETGS, which is optimized for lower energy X-rays. For a full description of Chandra see the “Proposer’s Observatory Guide” and references therein (available at <http://chandra.harvard.edu>).

Preliminary analysis of in-flight calibration data indicate that the HETGS is performing as predicted prior to the Chandra launch, with effective areas within ~ 10% of the expected values except from 6-12Å where there are systematic uncertainties of up to 20% still to be reduced by calibration. We note that the increased charge transfer inefficiency in the ACIS CCDs caused by unforeseen radiation damage early in the mission has no significant impact on the performance of the HETGS.

The data presented here were processed and analyzed with a combination of standard CXC and custom software. Each detected photon is assigned a dispersion angle, θ , relative to the undiffracted zero-order image. The angle is related to the order, m , and wavelength, λ , through the grating mean period, P , by the simple grating equation, $m\lambda = P \sin \theta$. The order is determined using the approximate

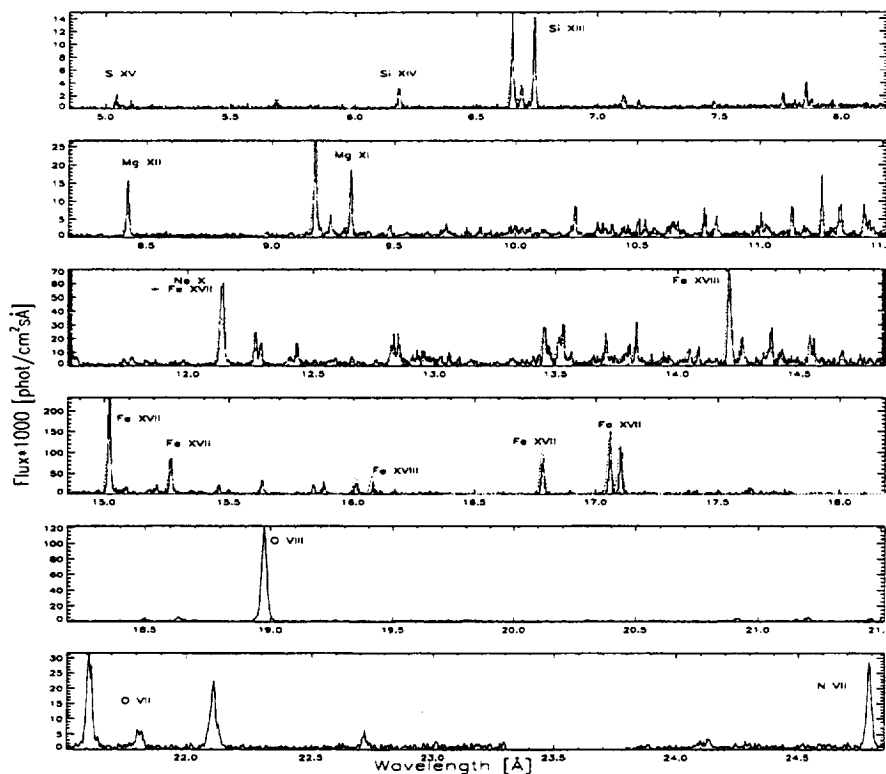


Figure 1. The HEG (dark line) and MEG (light line) spectrum of Capella (top four panels) and MEG only (bottom two panels). Data for $\pm 1^{\text{st}}$ orders are summed for a total of 89 ks

energy measured by the ACIS-S CCD's. The counts are divided by the effective area to provide a photon flux per bin. Some small remaining calibration errors in wavelength and effective area have not yet been removed.

2. Capella

Capella (α Aurigae) is an RS CVn binary system with an active corona well studied in the ultraviolet and with previous X-ray telescopes (see Brickhouse et al. 2000, and references therein). A first analysis of the HETGS observation of Capella is presented in Canizares et al. (2000b). Complementary results from the LETGS are in Brinkman et al. (2000).

We combined data from three HETGS observations totaling 89 ksec. The dispersed spectrum is shown in Figure 1.

The spectrum shows a forest of lines and line blends, including the strong transitions from H-like and He-like ions of N, O, Mg, Ne, Si, S, and the L lines of several ionization states of Fe, from Fe XVII through Fe XIX. The HEG and MEG complement each other in resolution and in area. The HEG can be used to resolve lines blended in the MEG, while the MEG generally has more effective area in the central portion of the Chandra band (for example, scrutinize the 6.7Å and 12.3Å region in Figure 1).

Even a cursory examination of the spectrum gives some new information about Capella's corona. The spectrum contains lines with a wide range of ionization levels, from N VII λ 24.8 through Ne X λ 13.4 to S XV λ 5.0. The temperatures of maximum emissivity for these three lines are $\log T=6.3$, 6.8 and 7.2, respectively, suggesting emission from plasma with a significant range of temperature. It is clear that plasma must be present over nearly a decade in temperature. This is consistent with ultraviolet spectra

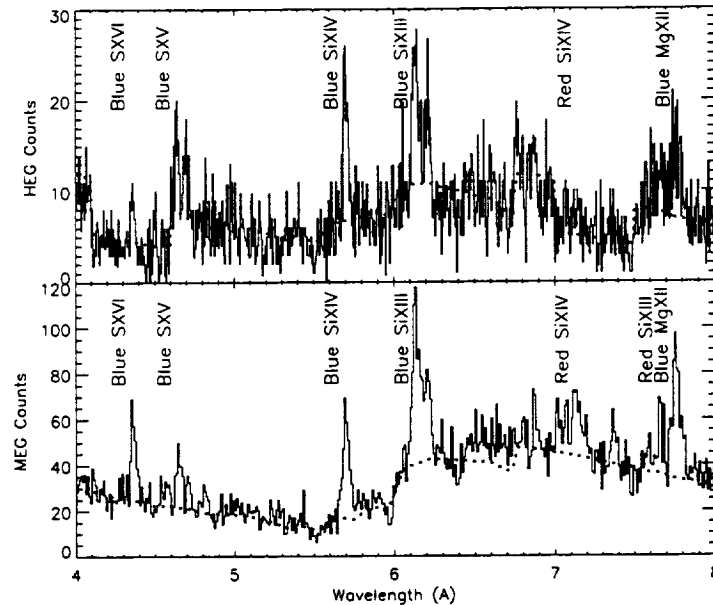


Figure 2. A portion of the HEG (top) and MEG (bottom) spectra of SS 433 observed with the Chandra HETGS, showing the blue-shifted H- and He-like lines of S (S XVI and S XV), the corresponding lines of Si (Si XIV and Si XIII) as well as the red-shifted counterparts to the Si lines. Note that the lines are broadened and that the He-like triplets of S and Si are resolved.

from EUVE (Brickhouse et al. 2000). But prior to Chandra the X-ray data were equally well explained with only two temperature components (Swank et al. 1981; Schmitt et al. 1990).

An approximate upper envelope to the true VEM distribution is given by the family of curves formed by plotting the ratio of line strength to corresponding emissivity for a collection of lines (see for example, Griffiths and Jordan 1998; Vedder and Canizares 1983). For a given element, the abundance affects only the overall normalization of the envelope of all lines from that element. We find reasonable agreement with the emission measure distribution deduced from EUVE emission lines by Brickhouse et al. (2000). The Fe XXV $\lambda 1.85$ line is not detected, which sets an upper limit on any high temperature emission during this observation.

Clearly, a much more detailed analysis is required, leading to a good determination of the emission measure distribution. The He-like lines discussed by Pradhan and others at this meeting are well resolved for nearly all the alpha-group elements, and can be used as temperature and density diagnostics (Pradhan 1982; Doschek 1990). And we can look for or set limits on the optical depth to resonant scattering, which constrains the column density (Saba et al. 1999). These diagnostics will help us understand the structure of Capella's corona, such as the characteristic dimensions of the coronal loops.

3. SS433

SS433 is another interesting target for the HETGS. This is a Galactic binary with a compact object (either neutron star or black hole) and relativistic jets (Margon 1984). Strong red and blue shifted lines are well studied in the optical and have been seen at moderate spectral resolution by ASCA (Kotani 1996). The lines move back and forth with a 163d period, the result of precession of the emitting jet.

The HETG MEG spectrum is shown in Figure 2. There are prominent red and blue shifted lines from Mg, Si and S, corresponding to $v/c = 0.26$, which is the expected value for the jet precession phase at the time of the observation. The observed red and blue shifts are offset due to the transverse Doppler effect, and the relative enhancement of the blue shifted compared to the redshifted lines is expected

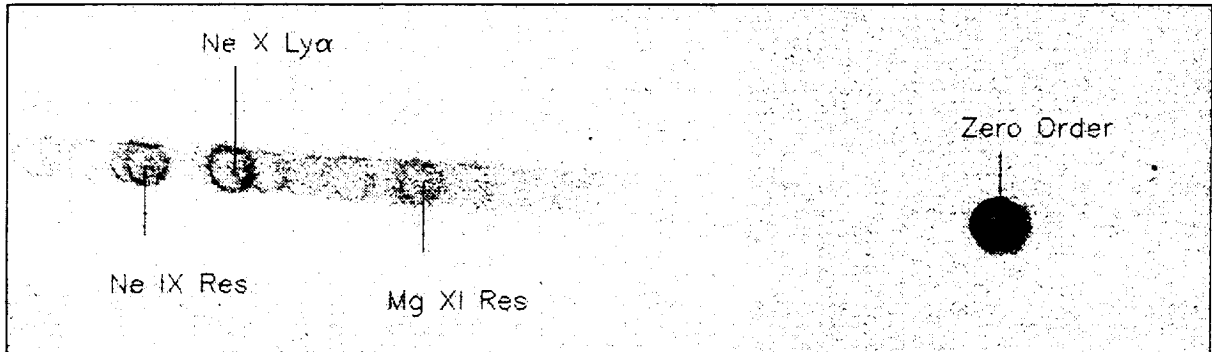


Figure 3. A portion of the MEG spectrum of E0102-72

from Doppler boosting. The lines are clearly resolved, with line widths corresponding to $\sim 1000 \text{ km s}^{-1}$, which is similar to the values seen in the optical spectrum, but was previously unresolved in X-rays.

We are planning to obtain additional observations at other precession phases during the next observing period. The hope will be to use spectra such as this one to deduce the structure of the jets and maybe learn something about the acceleration processes.

4. The Crab Pulsar

Not all spectra we have obtained so far contain the rich emission lines seen in stellar coronae like Capella or in SS433. For example, the spectrum extracted for the Crab pulsar is comparatively featureless. To within the current uncertainties of the calibration, it appears to be a perfect power law absorbed by interstellar material. There is evidence for structure in the interstellar absorption, as expected and as was first observed with much less sensitivity and spectral resolution by the FPCS on *Einstein* (Schattenburg 1986) around the oxygen absorption edge. Observations like these should be good probes of the abundance and possibly even the physical state (gaseous vs. bound in grains) of the absorbing material.

5. The Supernova Remnant E0102-72

Although the HETGS (and LETGS) work best on point sources, it is also extremely useful for studying moderately extended sources, particularly objects like supernova remnants (SNRs), which like the stellar corona are optically thin plasmas dominated by strong emission lines.

An early target is E0102-72 in the Small Magellanic Cloud, which is one of a handful of oxygen rich remnants thought to be the product of a type II SN in a massive star (Dopita 1981; Hyashi 1994). A portion of the dispersed spectrum is shown in Figure 3. One sees an image of the remnant in zeroth order, and then multiple images reproduced in the “light” of individual strong X-ray lines, in analogy to a spectroheliogram of the sun.

Several things have emerged from our very preliminary analysis. First, we see very strong O, Ne, and Mg, but little or no Fe. There are slight differences in the images for different ions of the same element, much less for different elements. This shows that ionization conditions vary over the remnant, as had been suspected from inconsistencies in the non-equilibrium models deduced for different species with ASCA (Hyashi 1994). A preliminary analysis also shows Doppler shifts of individual bright clumps in the ejecta on either side of the ring, indicating a complex velocity structure with amplitudes of $1000 - 2000 \text{ km s}^{-1}$.

Acknowledgments. This work was supported by NASA through contract NAS8-38249 and through the Chandra X-ray Center contract SV1-61010 from the Smithsonian Astrophysical Observatory. We thank the entire Chandra team, especially all our colleagues who helped develop the HETG.

References

- Brickhouse, N.S., Dupree, A.K., Edgar, R.J., Liedahl, D.A. Drake, S.A., White, N.E., Singh, K.P. 2000, *ApJ*, 387.
- Brinkman, A.C., et al. 2000, *ApJ* (submitted)
- Canizares, C.R. et al. 2000a, in preparation
- Canizares, C.R. et al. 2000b, *ApJ* (submitted)
- Dopita, M.A., Tuohy, I.R., Mathewson, D.S. 1981 *ApJ* 248, L105
- Doschek, G.A. 1990, *ApJS*, 73, 117
- Griffiths, N.W., Jordan, C. 1998 *ApJ*, 497, 883
- Hyashi, I. et al. 1994, *PASJ*, 46, L121
- Kotani, T., Kawai, N., Matsuoka, M., Brinkman, W. 1996, *PASJ*, 48, 619
- Margon, B. 1984, *ARA&A* 22, 507
- Pradhan, A. K. 1982, *ApJ*, 263, 497
- Saba, J.L.R., Schmelz, J.T., Bhatia, A.K., and Strong, K.T., 1999 *ApJ*, 510, 1064.
- Schmitt, et al. 1990, *ApJ*, 365, 704
- Schattenburg, M.L., Canizares, C.R. 1986, *ApJ* 301, 759
- Swank et al., 1981, *ApJ*, 246, 214
- Vedder, P.W., Canizares, C.R. 1983, *ApJ*, 270, 666



First Results of the Chandra-LETGS

P. Predehl, B. Aschenbach, H. Bräuninger, W. Burkert, V. Burwitz, G. Hartner, J. Trümper
*Max-Planck-Institut für Extraterrestrische Physik (MPE), Postfach 1603, D-85740 Garching,
Germany*

J.H.M.M. Schmitt
Universität Hamburg, Gojenbergsweg 122, D-21029 Hamburg, Germany

A.C. Brinkman, C.J.T. Gunsing, J.S. Kaastra, R.L.J. van der Meer, R. Mewe, F. Paerels¹,
J.J. van Rooijen
*Space Research Organization of the Netherlands (SRON), Sorbonnelaan 2, 3584 CA Utrecht,
The Netherlands*

J.J. Drake, O. Johnson, M. Juda, S.S. Murray, D. Pease, P. Ratzlaff, B.J. Wargelin
Harvard-Smithsonian Center for Astrophysics, 60 Garden Street, Cambridge, MA 02138, USA

Abstract. We present the first results obtained with the Low Energy Transmission Grating Spectrometer (LETGS) onboard the Chandra X-ray Observatory. The LETGS covers the wavelength range between 5 and 175 Å (2.5–0.07 keV) with a spectral resolution of about 0.06 Å. A number of calibration measurements were carried out in order to determine the instrument's performance, i.e., spectral resolution, the wavelength scale accuracy, and the effective area. The spectral resolution of the instrument, dominated by the angular resolution of the mirror, is as specified and predicted on the basis of preflight measurements. The calibration of the effective area is still an ongoing process. A serious problem for the LETGS is the high background of the HRC-S detector which serves as readout of the grating spectra. The 'First Light' observation of the star Capella shows a beautiful line-rich spectrum. He-like triplet diagnostics could be applied for the first time to a star other than the Sun.

1. Instrument Description

The Chandra X-ray Observatory was successfully launched on July 23, 1999. As the last of four instruments, the Low Energy Transmission Grating Spectrometer (LETGS) was inserted into the telescope beam on September 6, 1999.

The LETGS consists of three subsystems: the High Resolution Mirror Assembly (HRMA) Van Speybroeck et al.(1997), the Low Energy Transmission Grating (LETG) Brinkman et al.(1987), Brinkman et al.(1997), Predehl et al.(1997), and the High Resolution Camera for spectroscopy (HRC-S) Murray et al.(1997). The LETG has been designed and manufactured in Europe in a collaborative effort between SRON in the Netherlands and MPE in Germany, and consists of a toroidally shaped ring-structure, covered with 540 grating elements. Each element with a diameter of 1.5-cm carries a gold-wire grating with a line density of 1008 lines/mm. The grating wires are held only by a coarse support structure but not by a substrate in order to avoid instrumental absorption features. The elements are mounted with their centers on the Rowland torus and with their planes perpendicular to the incoming X-ray beam (the LETG is placed in the convergent beam just behind the mirror system). For X-rays falling onto the center of the grating elements, the dispersed images are sharp. However, the finite size of the elements

¹Present address, Columbia University, New York, NY, USA

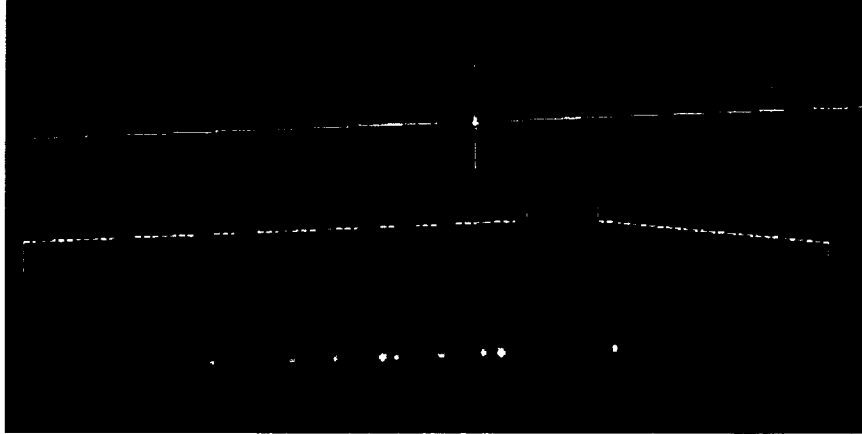


Figure 1. The raw detector image of the HRC-S detector. For the sake of clarity, only the center plate and small parts of the outer plates are shown. The dispersion is along the horizontal direction, and diffraction by the fine support grid is seen in the cross-dispersion direction. The faint hexagonal pattern around the 0th-order is from diffraction by the coarse support grid. Underneath an extracted region from 12 Å to 23 Å with the strong Fe XVII and the oxygen triplet (at the right end) is shown.

causes a slight widening of the image particularly at longer wavelengths. The spectrum dispersed by the LETG behind the telescope forms an image in the focal plane with the zeroth order at the focus position and the plus and minus first and higher orders symmetrically on either side of it (see Figure 1). The prime detector to read out the LETG spectrum is the HRC-S detector. It consists of three flat segments, each 10 cm long and 2 cm wide. The outer segments are tilted with respect to the center one in order to approximate the Rowland circle. The dispersion is 1.15 Å/mm in first spectral order and is determined by the system geometry and the grating line density. Both are optimized in order to cover the wavelength range between 5 and 175 Å (2.5–0.07 keV). The detector can be moved in the cross-dispersion direction and along the optical axis in order to optimize the focus for spectroscopy. The nominal zero order point focus on the central detector plate is displaced by 4 mm with respect to the center along the dispersion direction. This asymmetry is created in order to avoid that the two small dead areas between the center detector strip and the outer plates block the same spectral band.

2. Data Analysis

The spectral width in the cross-dispersion direction is minimal at the zeroth order and fans out towards larger wavelengths, due to the intrinsic astigmatism of a Rowland circle spectrograph. The extraction of the spectrum from the image is done by applying a spatial filter and constructing a histogram of counts vs. position along the dispersion direction. The background of the HRC-S is rather high due to a malfunction of the anti-coincidence circuit in the HRC-S. Fortunately, the background is fairly uniform over the entire detector area. Therefore it can be reliably estimated from areas on the detector away from the spectral image. The width w (in cross dispersion direction) of the spatial filter can be optimized in order to get a maximum signal-to-noise ratio according to

$$\frac{S}{N}(w) = \frac{M - B}{\sqrt{M + B}} \quad (1)$$

with M the measured intensity spatially filtered from the spectrum (source+background) and B the intensity filtered from a background region having the same extent in cross dispersion direction. Both M and B depend, of course, on the width w of the extracted region. The slight influence on the effective area can be easily modeled because the intensity profile in cross dispersion direction is well known: in its outer part it is dominated by the dispersion by the coarse support structure, in its inner part it is simply the point response function of the mirror system.

The detector gain varies strongly over the detector area, a behavior which is not sufficiently well calibrated. We have applied a pulse height filter in order to further suppress the background. However, this has a significant influence on the effective area of the instrument as measured on ground. Therefore, we have done all analyses without applying this filter so far, but work is going on to optimize also this kind of background reduction.

Unlike the High Energy Transmission Grating Spectrometer (HETGS), the LETGS is not able to separate higher diffraction order lines. So far it does not seem to be a serious problem to distinguish between first and higher order lines because of the high spectral resolution of the instrument which allows to separate lines easily and the fact that the relative efficiencies of the higher orders with respect to the first one is well calibrated at several wavelengths.

3. First Light Spectrum

Capella is a binary system at a distance of 12.9 pc comprising G8 and G1 giants with an orbital period of 104 days (Hummel et al. 1994). It is the brightest quiescent coronal X-ray source in the sky after the Sun, and is therefore an obvious line source candidate for first light and for instrument calibration. X rays from Capella were discovered in 1975 by Catura et al.(1975), Mewe et al.(1975) and subsequent satellite observations provided evidence for a multi-temperature component plasma (e.g. Mewe(1991) for references). The most recent prior spectrum was obtained with EUVE, longward of 70 Å with a resolution of about 0.5 Å (Dupree et al. 1993; Schrijver et al. 1995).

The LETG First Light observation on Capella was performed on 6 September 1999 (00h27m UT - 10h04m UT) with LETG and HRC-S. The observation time was ~ 34 ksec (see Figure 1). The HRC-S output was processed through the standard pipeline processing, producing a FITS-file with detector positions, pulse height information, and wavelengths.

Figure 1 shows a detector image after it has been corrected for spacecraft attitude drift and dithering (controlled spacecraft movement in order to avoid that a point source illuminates a single pixel). The bright horizontal line is the dispersed spectrum, which is symmetrical around the zeroth order. Using the procedures described above, we could extract a beautiful, line-rich spectrum of Capella: almost 150 spectral lines (single side, including higher diffraction orders) could be identified. These lines were used for both calibration and scientific purposes (see Figure 2).

4. Wavelength Scale Calibration

For the complete HRC-S, the Capella spectrum has been analyzed in terms of the quantity $m\lambda_{observed} - m\lambda_{predicted}$ as a function of wavelength. The analysis involves 171 lines in the data set, and relates to both positive and negative orders. We tried to analyze the above quantity in terms of decenter (of the 0th order along the dispersion axis), plate scale (conversion pixel or angle to wavelength) for the central detector element, off-sets (jumps) at the detector boundaries, and plate scales (or inclination angles) for the outer elements.

The procedure is as follows. First the centroid of 'unblended lines' was determined by a quasi-automatic fitting procedure. Then, the line was identified using existing literature. In addition to statistical errors on the line centroids, we also included an uncertainty to the theoretical wavelength (0.001 Å for the H and He-like lines, 0.003 Å for other lines with $\lambda < 20$ Å, all other lines 0.01 Å, and for higher orders m times the first order error). We fitted straight lines to the data for each of the three detector elements:

$$m \times (\lambda_{obs} - \lambda_{pred}) = A + B \times \lambda_{pred}, \quad (2)$$

where m is the spectral order, λ_{obs} the measured wavelength, λ_{pred} the theoretical wavelength including errors and with A and B as free parameters. This process was done for six different data sets of Capella. The constant B for the outer detector segments was $(1.32 \pm 0.10) \times 10^{-3}$ Å/Å and for the central segment $(0.56 \pm 0.03) \times 10^{-3}$ Å/Å.

Correction to the gap size between the outer and the central plates had to be applied. They are $(-22 \pm 3) \times 10^{-3}$ Å and $(-41 \pm 3) \times 10^{-3}$ Å, respectively. After applying all corrections, the wavelength uncertainty may be as low as 10 mÅ, supposing that the non-uniformities are stable in time.

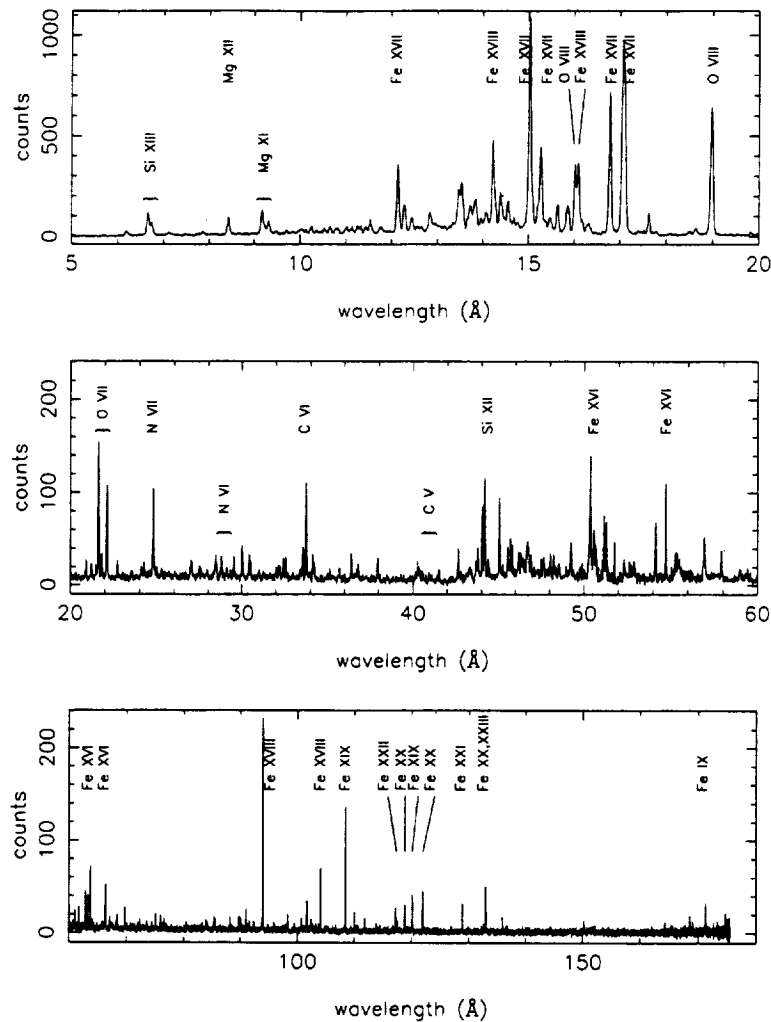


Figure 2. The complete LETGS spectrum of Capella, split into three parts for clarity. Note the difference in x and y scale for the three parts. Indicated in the plot are the triplets discussed in the text and a selection of the Fe lines at longer wavelengths.

5. LETG Efficiency

A much more difficult task is the determination of the effective area. During the telescope calibration performed at NASA-MSFC's long beamline XRCF, the instruments (HRMA, HRC-S, LETG) were calibrated separately but also in combination. In parallel, laboratory measurements together with theoretical models were used in order to improve the results (see Figure 3).

The transmission grating efficiency can be modeled in terms of the geometrical characteristics of the grating as, for instance, grating wire thickness, width, and the refractive index of the grating material. Particularly in wavelength bands where the wires are partially transparent, an exact knowledge of the wire cross section is important. It turns out that the assumption of a rectangular wire cross section (the simplest case) is not sufficient to explain the efficiency of a grating especially for higher diffraction orders. Throughout the whole development phase we have always adopted a trapezoidal rather than rectangular model. Then, depending on the transparency of the grating, the 'effective' width of the wires varies and the efficiency ratios among higher orders vary as well, exactly what is observed. This can

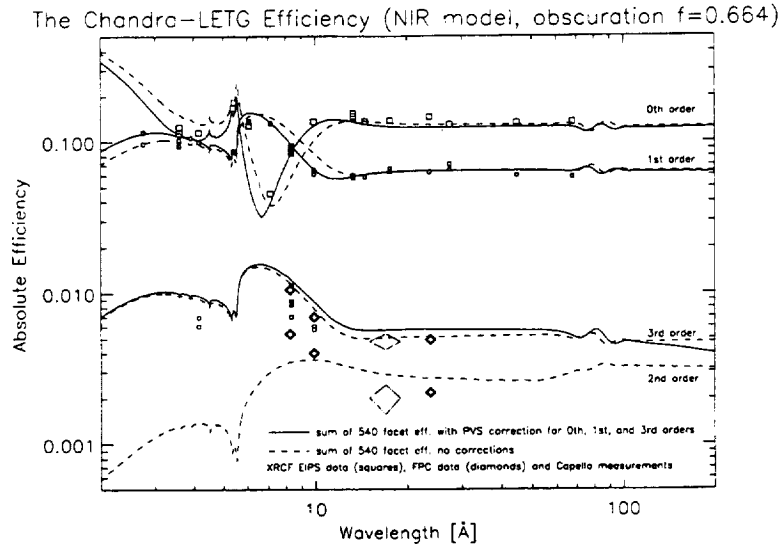


Figure 3. The absolute efficiency of LETG as a function of wavelength. Solid lines represent the theoretical model based on NIR-data of all 540 grating elements, dashed lines include corrections based on recent measurements using the PVS-gratings. Symbols represent XRCF measurements.

lead to a complicated behavior, particularly for those orders which are almost suppressed. The LETG gratings are designed to suppress the even orders which is achieved at a bar-slit ratio of 1:1. Due to uncertainties in the exact determination of the wire cross section and also slight inhomogeneities during the manufacturing process, the suppression works well for the second diffraction order but is extremely difficult to achieve for higher even orders.

At the beginning of the LETG program we realized that the testing of all grating samples (~ 3000 , when AXAF still had 6 mirror shells and we were required to deliver a flight, a flight spare, and an engineering model) in the laboratory X-ray facility would be a horrendous task. Therefore we developed a novel method based on the transmissivity of a grating for polarized light in the so-called resonance domain, i.e., the wavelength range around the grating period (Lochbihler and Predehl 1992). This, in our case, is the NIR-region around $1\ \mu\text{m}$. This method was validated both by electron microscope studies and X-ray measurements on so-called 'Performance Verification Samples', ten randomly selected grating elements. Although the results of the complex tests at XRCF were not always easy to interpret, it became nevertheless apparent that there were significant deviations between model and data particularly at wavelengths between 7 and 10 Å. Deviations of up to 30% occurred. We therefore very accurately re-measured the PVS gratings in X-rays in an effort to re-calibrate the NIR-data. Based on this exercise, we have 'fudged' the NIR-data by adding small constants to the wire width, thickness and slope of the assumed mean trapezoidal cross sections of each grating. The most interesting result was that the thickness seems to depend on diffraction order. This suggests an underlying physical effect not considered so far. Combining all information from NIR, X-ray laboratory measurements, and XRCF calibration, we succeeded to establish an efficiency model for the LETG close to the required level of accuracy.

5.1. LETGS Effective Area

In order to establish the combined HRMA-LETG-HRC effective area, strong point sources with 'known' spectra have been chosen. For the long wavelength band beyond the Carbon edge, Sirius-B was considered to be the best candidate. According to existing white dwarf models (see Brinkman et al. 2000b for details) the flux uncertainty is smaller than 10%. The herewith derived effective area is therefore directly coupled to our knowledge of the Sirius B absolute flux.

The most straightforward way to verify the LETGS effective area is to use a continuum source with a well-defined spectrum. An additional difficulty is that the HRC-S cannot separate the different

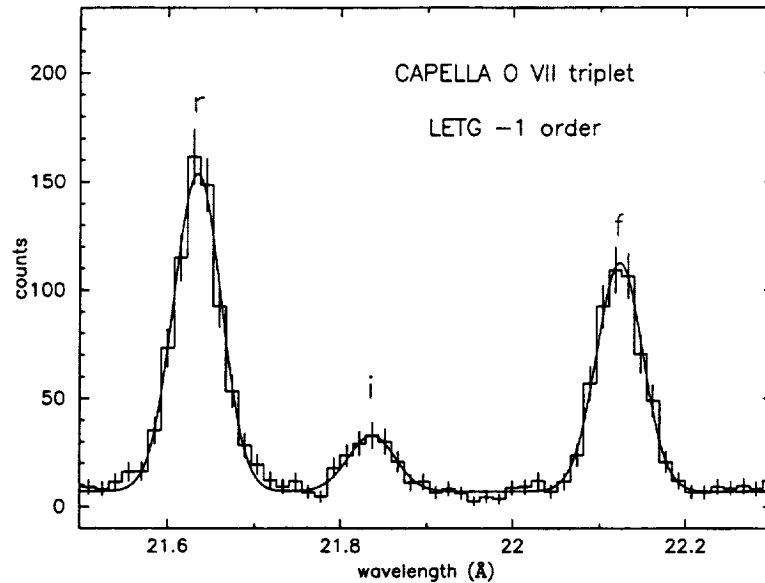


Figure 4. The Oxygen VII triplet in the LETGS -1 order spectrum with the resonance (r), the forbidden (f), and the intercombination (i) line. The measured ratios of these lines (from the fitted curve) are given in the text.

spectral orders. The predicted count rate therefore consists of the contributions of first and higher orders together. We are now in the process of applying this procedure to several celestial sources to look for systematic deviations, which can then be attributed to the LETGS-response. Also the comparison with HETG-ACIS-S measurements as well as observations using other spacecrafts such as XMM, SAX and ASCA are being used to cross calibrate our instrument.

6. Preliminary Capella Results

A quantitative analysis of the spectrum requires the exact knowledge of the effective area of the instrument over the entire wavelength band. However, some diagnostics based on intensity ratios of lines lying closely together could already be applied. A good example for line complexes are the helium-like triplets. Details of this preliminary analysis on this line complex and also on the resonance scattering in the Fe XVII 15 Å lines are given by Brinkman et al. 2000a.

The LETGS wavelength band contains the He-like triplets from C, N, O, Ne, Mg, and Si (wavelengths at roughly 40, 29, 22, 13.5, 9.0, and 6.6 Å, resp.). However, the Si and Mg triplet are not sufficiently resolved and the Ne IX triplet is too much blended with iron and nickel lines. The O VII lines are clean (see Figure 4) and the C V and N VI lines can be separated from the blends by simultaneously fitting all lines. These triplets are suited to diagnose plasmas in the density range $n_e = 10^8$ - 10^{11} cm $^{-3}$ and corresponding temperature range $T \sim 1$ -3 MK. For the C, N, and O triplets the measured i/f ratios are $^1 0.38 \pm 0.14$, 0.52 ± 0.15 , and 0.250 ± 0.35 , respectively, which imply Pradhan(1982) densities n_e (in 10^9 cm $^{-3}$) = 2.8 ± 1.3 , 6 ± 3 , and $\lesssim 5$ (1σ upper limit), respectively, for typical temperatures as indicated by the $(i+f)/r$ ratios of 1, 1, and 3 MK, respectively. The derived densities are comparable to those of active regions on the Sun with temperatures of a few MK. Figure 4 shows a fit to the O VII triplet measured in the -1 order. The He-like triplet diagnostic, which was first applied to the Sun (e.g.,

¹For the analysis we use a composite of six observations obtained in the week after first light, with a total observing time of 95 ksec.

Acton et al.(1972), McKenzie and Landecker(1982), Wolfson et al.(1983)) has now for the first time been applied to a star other than the Sun.

7. Conclusion

The Capella measurements with LETGS show a rich spectrum with excellent spectral resolution ($\Delta\lambda \simeq 0.06\text{\AA}$, FWHM). About 150 lines have been identified of which the brightest hundred are listed (see Brinkman et al. 2000b). The high-resolution spectra of the Chandra grating spectrometers allow us to carry out direct density diagnostics using the He-like triplets of the most abundant elements in the LETGS-band. This was so far only possible for the Sun.

References

- Acton, L.W., Catura, R.C., Meyerott, A., Wolfson, C.J. 1972, *Solar Phys.*, 26, 183
- Brinkman, A.C., et al., 1987, *Astroph. lett. & comm.*, Vol. 26, 73-80
- Brinkman, A.C., et al., 1997, *SPIE*, 3113, 181-192
- Brinkman, A.C., et al., 2000, *ApJ*, 530, 111
- Brinkman, A.C., et al., 2000, *SPIE*, in press
- Catura, R.C., Acton, L.W., and Johnson, H.M. 1975, *ApJ*, 196, L47
- Dupree, A.K., Brickhouse, N.S., Doschek, G.A., Green, J.C., Raymond, J.C., 1993, *ApJ*, 418, L41
- Hummel, C.A., Armstrong, J.T., Quirrenbach, A., Buscher, D.F., Mozurkewich, D., Elias, N.M. II, and Wilson, R.E., 1994, *AJ*, 107, 1859
- Lochbihler H., Predehl P. 1992, *Appl. Opt.* 31, 964
- McKenzie, D.L., Landecker, P.B. 1982, *ApJ*, 259, 372
- Mewe, R., Heise, J., Gronenschild, E.H.B.M., Brinkman, A.C., Schrijver, J., den Bogende, A.J.F. 1975, *ApJ*, 202, L67
- Mewe, R., 1991, *A&A Rev.*, 3, 127
- Mewe, R., Lemen, J.R., and Schrijver, C.J. 1991, *Ap&SS*, 182, 35
- Murray, S.S., et al. 1997, *SPIE*, 3114, 11
- Pradhan, A.K. 1982, *ApJ*, 263, 477
- Predehl, P., et al., 1997, *SPIE*, 3113, 172-180
- Schrijver, C.J., Mewe, R., van den Oord, G.H.J., and Kaastra, J.S. 1995, *A&A*, 302, 438
- Van Speybroeck, L.P., Jerius, D., Edgar, R.J., Gaetz, T.J., and Zhao, P., 1997, *SPIE*, 3113, 89
- Wolfson, C.J., Doyle, J.G., Phillips, K.J.H. 1983, *ApJ*, 269, 319



Chandra and the Emission Line Project

N. S. Brickhouse and J. J. Drake
Smithsonian Astrophysical Observatory
60 Garden Street
Cambridge, MA 02138

Abstract. Calibration data obtained for the Chandra High Energy Transmission Grating and the Low Energy Transmission Grating Spectrometers are allowing us to test plasma spectral models against bright coronal sources with a range of electron temperatures. The three Emission Line Project targets — Capella, Procyon, and HR 1099 — are bright, well-studied X-ray and EUV emitters. The goals of the Emission Line Project are to determine and verify accurate and robust diagnostics; to identify and prioritize problems in fundamental spectroscopy; and to accelerate the improvement of the atomic database needed for modeling.

1. Introduction

The Emission Line Project (ELP) is a collaborative effort, organized by the Chandra X-ray Observatory Center, to improve the plasma spectral models used to analyze and fit X-ray spectral observations. During the first phase of the Emission Line Project we are analyzing the high quality spectra of three stellar coronal targets that are being obtained for the purposes of calibrating the Chandra transmission gratings. For select ELP observations by Chandra, overlapping measurements have been obtained by the Extreme Ultraviolet Explorer (EUVE), the HST Space Telescope Imaging Spectrograph, Beppo-SAX, and the NSF's Very Large Array radio telescope. Broadening the wavelength coverage provides additional important tests for the atomic models.

Stellar coronal spectra are rich in emission lines from high ionization states of cosmically abundant elements. The line source calibration targets — Procyon, Capella, and HR 1099 — were specially chosen because they exhibit emission corresponding to a wide range of plasma temperatures, dominated by $T_e \sim 2 \times 10^6$, 6×10^6 , and 2×10^7 K, respectively (Figure 1). The three sources emit over a continuous range of temperatures, such that most elements and ionization states accessible to the Chandra gratings will be exhibited in these spectra. Current spectral models of collisionally ionized plasmas will be tested against the observations to assess the problem areas and to help set priorities for fundamental theoretical and experimental spectroscopy.

2. Assumptions of Collisional Plasma Emission Models

Given the electron temperature T_e , electron density N_e , and elemental abundances, models of collisionally ionized plasma calculate the power radiated from continuum and line emission processes. A number of assumptions are generally made, particularly that the plasma is optically thin and non-relativistic. Continuum emission from bremsstrahlung, radiative recombination, and 2-photon processes are included. Collisional impact cross sections are integrated over Maxwellian velocity distributions, and it is assumed that the radiation is not affected by electric and magnetic fields. Photoionization and photoexcitation are generally not included.

Often the emission is assumed to be time-independent; however, non-equilibrium ionization models may be constructed using a physical model. For emission lines which may be populated by recombination cascades, it is important to take the ionization balance into account, and thus one must link the ionization and level population calculations. Another common assumption of the "coronal approximation" is that the electron density is low. In that case the population of energy levels is dominated by transitions from the ground state. Generally today, the level populations are calculated using a rate matrix to account for

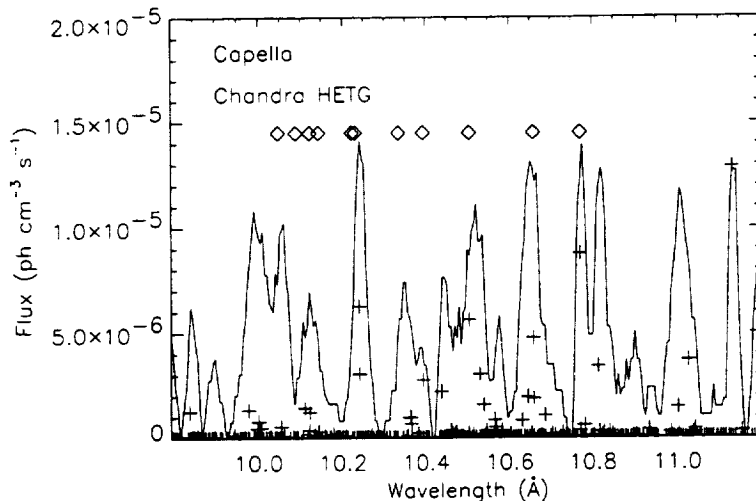


Figure 1. Emission measure distributions for Procyon (Drake, Laming, & Widing 1995), Capella (Dupree et al. 1993; Brickhouse 1996), and HR 1099 (Griffiths & Jordan 1998) compared with that of the quiescent Sun (Raymond & Doyle 1981). Procyon is shown as the solid line, Capella is dash-dotted, HR 1099 is dashed, and the Sun is dotted. The spectral resolution of the EUVE spectrometers allows the measurement of isolated emission lines which have been used to construct the stellar emission measure distributions. ASCA spectra set limits on the highest temperatures in the plasma.

all transitions, such that density effects on the level populations can be properly treated (up to densities $\sim 10^{14} \text{ cm}^{-3}$). Density effects on the ionization balance are still treated crudely, when treated at all.

The physical assumptions of ionization equilibrium and negligible optical depth appear to be good to a first order approximation. Since the coronal emission is weighted by N_e^2 for collisionally excited lines, the observed spectrum (time-averaged over several hours to several days) is naturally biased toward plasma with the shortest equilibration times. The good agreement among lines emitted from the same ionization state with the theoretical predictions, and particularly for branching ratios, can place tight constraints on the optical depths involved. To observe the breakdown of these assumptions, if applicable, will require high spectral resolution, such as provided by the XMM Reflection Grating Spectrometer (RGS) and Chandra Low Energy Transmission Gratings (LETG) and High Energy Transmission Gratings (HETG).

It is interesting to note that most of the simplifying assumptions break down somewhere in the solar corona! Measured particle distributions in the solar wind are non-Maxwellian (Olgvie & Scudder 1978), the strongest X-ray line in the quiescent corona, Fe XVII $\lambda 15.013$, appears optically thick in active region loops (Schmelz et al. 1997), and the He II $\lambda 303.8$ is influenced by recombination following photoionization of He II by the EUV corona (Athay 1988). Nevertheless, the assumptions work well to first order for most emission, thus allowing us to proceed.

In the absence of a significant radiation field, the line intensity I_{line} is the product of the population of the upper level N_k and the atomic transition probability A_{kj} from level k to j .

$$I_{line} = N_k A_{kj} \quad (1)$$

For a two-level atom collisions excite the level and thus I_{line} is proportional to the collisional excitation rate C_{jk} from the lower level j .

$$I_{line} = N_j N_e C_{jk} \quad (2)$$

More generally, the level populations are calculated, such that

$$I_{line} = \frac{1}{4\pi R^2} \epsilon_{At} EM \quad (3)$$

where ϵ_{At} is the atomic emissivity, and EM is the emission measure

$$EM(\Delta T_e) = \int_{V(\Delta T_e)} N_e N_H dV \quad (4)$$

In principle, if the plasma is isothermal and isochoric, line ratio diagnostics provide the cleanest measurements of the physical conditions of the emitting region. In practice the astrophysical plasma is neither, and one must construct multi-component models. A high quality X-ray spectrum (defined as having sufficient bandpass, spectral resolution, signal-to-noise, and calibration) provides a wealth of information to infer the distribution of temperature and possibly density. Emission measure distributions are typically constructed by an inversion of Equation 3, such that a good fit is provided to the spectrum, either globally or to specified emission lines.

The temperatures, densities, emission measures, and abundances derived from such methods are subject to numerous uncertainties beyond the statistical errors associated with the observations, including instrument calibration, line blending, the atomic data, and the simplifying assumptions themselves. The ASCA spectrum of Capella could not be fit by the standard models, and eventually required the examination of all of these issues. The biggest improvement in the fit came with the addition of emission lines from $n > 5$ for Fe XVII to XIX, which had not previously been calculated (Brickhouse et al. 2000; D. A. Liedahl & N. S. Brickhouse 2000, in preparation).

3. Stellar Coronae as Tests of Models

Questions raised over the past several years about the validity of results from moderately resolved spectra from ASCA and EUVE, such as the elemental abundances of elliptical galaxies (Arimoto et al. 1997) and of stellar coronae (Jordan et al. 1998) have led many of us to the conclusion that the models need to be tested and validated; however, given the number of assumptions upon which the spectral models are based, and our limited understanding of stellar coronae, how can we be so confident that the ELP data will provide useful benchmarks?

Before answering that question it is important to emphasize that astrophysical spectra are no substitute for laboratory atomic physics experiments and well calibrated spectroscopic measurements under controlled conditions, and we fully support efforts such as the ones reported in this proceedings; however, the numbers of atomic rates for potentially important emission lines far exceed any conceivable laboratory resources. Moreover, the wide range of temperatures and densities observed in stellar coronae include conditions which are difficult to replicate under laboratory conditions. Thus, high quality astrophysical spectra provide a complementary data set for assessing the quality of the spectral models.

The answer, then, to the question of how useful the ELP data are as benchmarks, is twofold. (1) We begin with the underlying premise that we understand the emission processes in these sources reasonably well. These sources have been well observed with ASCA and EUVE, such that we do not expect gross departures from equilibrium. Since the emission from the strong collisionally excited lines is naturally weighted toward N_e^2 , thermalization and equilibration are most likely to apply for the emission lines that we are most able to observe. Furthermore, EUV branching ratios place tight constraints on the optical depth effects for Capella (Brickhouse, Raymond, & Smith 1995). (2) The breakdown of the classical assumptions would have observable consequences. The Chandra observations (and other coordinated measurements) provide spectra of such high quality that consistency checks are built in. The broad bandpass provides multiple diagnostic lines, such that issues resulting from line blends can be identified. Multiple ionization states of different elements provide a cross-check on the ionization balance models, which underlie the derived shape of the emission measure distributions. While a few lines may have optical depths of order unity, these will easily be identified by line ratio measurements.

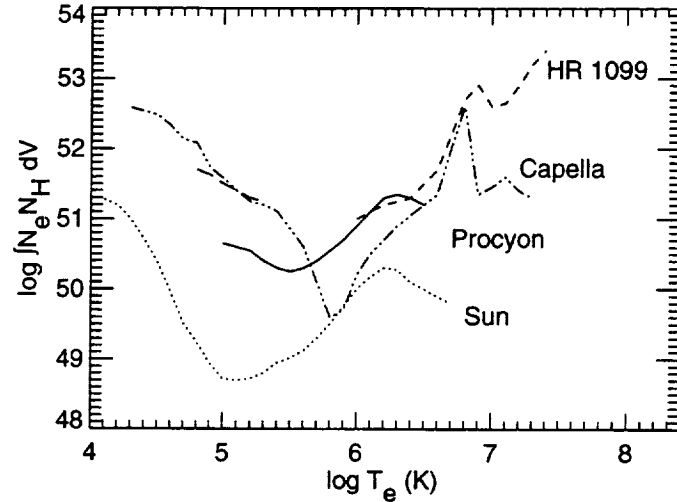


Figure 2. Region of the observed Chandra HETG spectrum of Capella compared with model emission lines, showing the “missing lines.” The smoothed spectrum shown is the Observation Identification 1099, Medium Energy Grating spectrum, minus first order. Plus symbols mark the observed lines calculated using an APEC model (Smith et al. 1999) scaled to the strongest line shown, while diamonds mark the wavelengths of measured Fe XVII lines (Brown et al. 1998) from energy levels with principal quantum numbers $n > 5$. Such lines were estimated to account for nearly 30% of the flux in the waveband between 10 and 11 Å in the ASCA spectrum of Capella (Brickhouse et al. 2000).

4. Preliminary Emission Line Project Data Analysis

The first light papers for the LETG (Brinkman et al. 2000) and for the HETG (C. Canizares et al., in preparation) support the argument above that these data are useful for testing the plasma spectral emission models. Since the instrument calibration and data reduction and processing are still at an early stage, the results reported here are preliminary, and are intended to give an understanding of how the data can be used. We present two examples:

- *Optical depth.* Fe XVII $\lambda 15.014$ is the strongest emission line in the X-ray spectrum of Capella. By comparing its ratio with the optically thin Fe XVII $\lambda 15.265$ one can test the optical depth of $\lambda 15.014$, and thus place constraints on the degree of resonance scattering in the atmosphere. The Capella line ratio appears to be consistent with the assumption of negligible net optical depth (Brinkman et al. 2000; C. Canizares et al., in preparation). While the theoretical predictions tend to be somewhat higher than the laboratory measurements (see Brown et al. 1998), and the jury is still somewhat out on the best data, the Capella measurements provide additional support for the idea that we can neglect optical depth effects in our analysis of these spectra.
- *The identification of spectral regions with “missing lines.”* Figure 2 shows a small section of the Capella spectrum, which had presented modeling difficulties (Brickhouse et al. 2000) for the ASCA analysis. We can clearly identify lines of Fe XVII based on the work of Brown et al. (1998), which are not yet included in the plasma spectral models.

Other tests are planned once the data are felt to be reliable. Collisional ionization equilibrium can be tested by comparing $\Delta n = 0$ transitions in the EUV to $\Delta n = 1$ transitions in the X-ray, exploiting the broad bandpass of the LETG. For example, the ratio of the Fe XVIII $\lambda 93.92$ intensity to the Fe XVIII $\lambda 14.22$ intensity is temperature-sensitive due primarily to the Boltzmann factor in the collision rate. By comparing the line ratio temperature to the temperature derived from the ratios among adjacent ions, one tests the local temperature relative to the degree of ionization. Of course, the underlying

collision strengths and the ionization balance models themselves are also in need of testing for these lines. Ultimately the comparison among several lines from the same ion will help to validate the collision strengths, while comparing lines from different elements will be useful in testing the ionization balance.

5. Conclusions

Our understanding of the coronal spectrum is sufficiently mature that the Emission Line Project will help to identify and solve problems with the plasma spectral emission models. Problems with the models affect both high spectral resolution data, for which the primary analysis will involve the measurement of specific diagnostic lines, and low to moderate resolution data, for which global spectral models are needed. This project has widespread implications for other types of astrophysical sources, including, galaxies, supernova remnants, clusters of galaxies, and stellar coronae.

The Chandra calibration data for Procyon, Capella, and HR 1099 have now been obtained, with many of the data sets available through the Chandra public archives. Preliminary results support the usefulness of these data for testing models. Meanwhile, calibration and processing improvements continue. The ELP website (<http://asc.harvard.edu/elp/ELP.html>) gives information on the distribution, collection, and organization of data as well as links to useful software and plasma models. We are in the process of producing an emission line catalog consisting of measured wavelengths, fluxes, line widths, and identifications.

Broad support in the X-ray astronomy community has made the Emission Line Project possible.

Acknowledgments. We acknowledge the support of Harvey Tananbaum and the Chandra X-ray Observatory Center NAS8-39073. We also appreciate the contributions of the Emission Line Project Core Working Group: Dan Dewey, Richard Edgar, Terry Gaetz, John Houck, David Huenemoerder, Vinay Kashyap, Duane Liedahl, Randall Smith, Doug Swartz, and Brad Wargelin. Some of this material has been presented elsewhere (*Astrophysical Plasmas: Codes, Models, and Observations*, Mexico City, 1999, to be published in the *Revista Mexicana de Astronomia y Astrofisica, Serie de Conferencias*, ed. S. J. Arthur, N. Brickhouse and J. Franco).

References

- Arimoto, N., Matsushita, K., Ishimaru, Y., Ohashi, T., & Renzini, A. 1997, *ApJ*, 477, 128
 Athay, R. G. 1988, *ApJ*, 329, 482
 Brickhouse, N. S. 1996, in *IAU Colloq. 152, Astrophysics in the Extreme Ultraviolet*, ed. S. Bowyer & R. F. Malina (Dordrecht: Kluwer), 105
 Brickhouse, N. S., Dupree, A. K., Edgar, R. J., Liedahl, D. A., Drake, S. A., White, N. E., & Singh, K. P. 2000, *ApJ*, 530, 387
 Brickhouse, N. S., Raymond, J. C., & Smith, B. W. 1995, *ApJS*, 97, 551
 Brinkman, et al. (23 authors) 2000, *ApJ*, 530, L111
 Brown, G. V., Beiersdorfer, P., Liedahl, D. A., Widmann, K. & Kahn, S. M. 1998, *ApJ*, 502, 1015
 Drake, J. J., Laming, J. M., Widing, K. G., 1995, *ApJ*, 443, 393
 Dupree, A. K., Brickhouse, N. S., Doschek, G. A., Green, J. C., & Raymond, J. C. 1993, *ApJ*, 418, L37
 Griffiths, N. W., & Jordan, C. 1998, *ApJ*, 497, 883
 Jordan, C., Doschek, G. A., Drake, J. J., Galvin, A. B., & Raymond, J. C. 1998, in *ASP Conf. Ser. 154, Cool Stars, Stellar Systems, and the Sun, Tenth Cambridge Workshop*, ed. R. A. Donahue & J. A. Bookbinder (San Francisco: ASP), 263
 Ogilvie, K. W., & Scudder, J. D. 1978, *JGR*, 83, 3776
 Raymond, J. C., & Doyle, J. G. 1981, *ApJ*, 247, 686
 Schmelz, J. T., Saba, J. L. R., Chauvin, J. C., & Strong, K. T. 1997, *ApJ*, 477, 509
 Smith, R. K., Brickhouse, N. S., Raymond, J. C., & Liedahl, D. A. 1998, in *Proceedings of the First XMM Workshop on "Science with XMM"*, ed. M. Dahlem (Noordwijk, The Netherlands)

Theoretical Calculations of Atomic Data for Spectroscopy

Manuel A. Bautista

Laboratory for High Energy Astrophysics

NASA Goddard Space Flight Center

Greenbelt, MD 20771, USA

Abstract.

Several different approximations and techniques have been developed for the calculation of atomic structure, ionization, and excitation of atoms and ions. These techniques have been used to compute large amounts of spectroscopic data of various levels of accuracy. This paper presents a review of these theoretical methods to help non-experts in atomic physics to better understand the qualities and limitations of various data sources and assess how reliable are spectral models based on those data.

1. Introduction

Spectroscopic data for atoms and ions fall into the category of fundamental scientific research and this by itself may be good justification for experimental and theoretical work. The data are also essential to the analysis of spectra of laboratory and astronomical plasmas. These applications have been as important motivation as, if not greater than, the fundamental physics. For several decades, theoretical atomic physicists have devoted great effort to the development of methods and computation of vast amounts of data, particularly that needed for the study of optical spectra. On the other hand, the progress of the atomic data sets for X-ray spectroscopy has been much slower, due in part to the scarcity of high quality X-ray spectra to motivate the work. At present, the new generation of observatories (like *Chandra* and *XMM*) and the incoming facilities with the *Constellation-X* program are starting to provide high resolution, high signal-to-noise spectra for which the need of improved atomic data is not just granted but urgent. But the production of high quality atomic data for X-ray spectroscopy is far from simple or routine. The high energy conditions of the emitting plasmas demand the study of large numbers of energy levels as well as inner-shell and Auger processes. Thus, current theoretical methods and computational tools encounter severe difficulties in producing high accuracy data.

The present review of theoretical atomic physics is aimed at astronomers and spectroscopists in general who need to understand the limitations of atomic data. In that sense, the present paper tries to give a general, but relatively simple, overview of the most commonly used approximations and methods for the production of spectroscopic data. The review pays particular attention to the calculation of atomic structure and the spectral processes of photoionization and electron impact excitation. Other processes like collisional ionization and proton impact excitation, although relevant, are not discussed in much detail due to lack of space. For discussions on electron-ion recombination see papers by Nahar and Savin in this volume. Also, the present review emphasizes inner-shell processes that are most relevant to X-ray spectroscopy.

From the point of view of the kinds of atomic data needed for the analysis of spectra there are two general atomic physics problems to be solved:

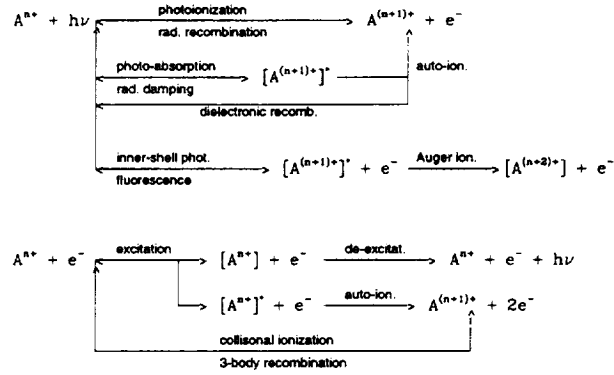


Figure 1. Physical processes after photon-ion and electron-ion scattering. The brackets indicate excited states of the ion and brackets and asterisc indicate autoionizing states.

- 1) Atomic structure
 - Energy Levels
 - Radiative transition rates
 - Autoionization rates
- 2) Scattering
 - ion + photon
 - ion + charged particle

The atomic structure problem is concerned with the computation of energy levels and rates of spontaneous transition rates among levels of the same ion (transition rates or A -values), and from autoionizing levels of one ion to levels of the next ionized species (autoionization rates). The scattering problem, relevant to the formation of spectra of warm and hot plasmas, has to do with all different processes that can occur after a collision of an ion with a photon or with a charged particle. The most important physical processes that occur after ion scattering are illustrated in Figure 1.

2. Atomic Structure Calculations

From the point of view of quantum mechanics the physical representation of ions and spectral processes comes down to the fundamental problem of solving the Schrödinger equation

$$H\Psi_i = E_i\Psi_i. \quad (1)$$

Here, i represents the set of quantum numbers necessary to describe the system, Ψ_i are the wavefunctions of the system, E_i are the eigenvalues, and H is the Hamiltonian which, for a non-relativistic system, can be written as

$$H = \sum_{i=1}^N \frac{p_i^2}{2m_e} - \sum_{i=1}^N \frac{Ze^2}{r_i} + \sum_{i \neq j} \frac{e^2}{|r_i - r_j|}, \quad (2)$$

where the first term is the sum of the kinetic energies of all electrons, the second term is the potential energy due to Coulomb attraction of all electrons by the nucleus, the third term is the energy due to electrostatic repulsion between the electrons, and N is the total number of electrons in the system. The previous equation neglects the spin of the electron, which can be considered separately in non-relativistic systems.

The presence of the two-electron operators $1/|r_i - r_j|$ makes it impossible to obtain exact solutions to the Schrödinger equation for the N -electron system. On the other hand, the two-electron operator should never be neglected as it is often comparable in magnitude to the Coulomb attraction term or one-electron operator. One can show

$$\frac{\text{two-electron term}}{\text{one-electron term}} \equiv \xi \simeq \frac{1}{2} \frac{N(N-1)}{ZN}. \quad (3)$$

For a neutral ion ($Z = N$), $1/4 \leq \xi \leq 1/2$.

Approximate methods for solving Equation (1) replace the two-electron terms by approximate one-electron potentials to give an effective Hamiltonian of the form

$$H^{eff} = \sum_i^N H_i^{eff} = - \sum_{i=1}^N \left[\frac{1}{2} \frac{p_i^2}{m_e} + \frac{Ze^2}{r_i} - V_i^{eff}(r_i) \right]. \quad (4)$$

The exact eigenfunctions of H^{eff} can now be constructed from products of single-electron eigenfunctions of H_i^{eff} . Since H commutes with angular momentum and spin operators (L^2, L_z, S^2, S_z) the eigenfunctions of H^{eff} are required to be eigenfunctions of these operators as well.

For highly ionized ions ($Z \gg N$), the inter-electronic repulsions are only small perturbations relative to the much stronger nuclear central potential. Then, it is a good approximation to choose V_i^{eff} as a *central field potential*. If this can be achieved the orbital wavefunction may be written explicitly as products of spherical harmonics, spin functions, and radial functions. The advantage of using central field orbitals cannot be overestimated. The effect is to reduce the computational problem from solving N coupled integro-partial-differential equations (one for each orbital) in four variables to N coupled integro-differential equations in a single radial variable.

In general V^{eff} does not need to be of central field type, but the advantages of a central potential are so great that essentially all methods for atomic structure calculations use spherically averaged potentials even for neutral and open-shell systems. There are several techniques regularly used in the atomic structure calculations. The most important are: use of model potentials, methods based on the Hartree-Fock theory, semiempirical methods, perturbation methods, and the R-matrix method in the close coupling formalism. These methods, with the exception of the R-matrix, are discussed below followed by a discussion of two particularly important physical effects, i.e. configuration interaction and relativistic effects. The R-matrix method will be described in Section 3.5.

2.1. Model potentials in atomic structure

Alkali atoms and ions are good systems for testing model potentials since, by having a single valence electron, their analysis leads to a single equation for the one-electron wavefunction. For these ions one would expect the potential for large r to approach

$$V^{eff}(r) = -\frac{(Z - N_c)}{r}, \quad (5)$$

where N_c is the number of core electrons. The solution of the Schrödinger equation based on this potential is discussed by Bates and Damgaard (1949). In spite of the simplicity of this potential it gives accurate oscillator strengths in many cases, but it is not always reliable (Bromander et al. 1978).

A large variety of model potentials have been constructed from the assumptions that they behave as shown in Equation (5) for $r > R$, for some suitable R , while for r approaching 0 the potential could be infinite, equal to a finite boundary value, or even zero. For a review of model potentials in atomic structure see Hibbert (1982).

A generally applicable potential is the modified Thomas-Fermi potential by Eissner and Nussbaumer (1969). This potential is implemented in the widely used computer program SUPERSTRUCTURE (Eissner, Jones, and Nussbaumer 1974). This program uses a Thomas-Fermi-Dirac type of central potential to generate one-electron orbitals.

This potential differs from that in Equation (5) not only in the added sophistication of the model, but also in that this one depends on the angular momentum of the valence electrons. SUPERSTRUCTURE is quite efficient and can provide relatively accurate results ($\sim 1\%$ for energy levels and $\sim 10\%$ for oscillator strengths). Recently the code has been extended to calculate autoionization and dielectronic recombination data (AUTOLSJ by Bely-Dubau 1982 and AUTOSTRUCTURE by Badnell 1985, unpublished) has extended the code to calculate autoionization rates and dielectronic recombination.

2.2. Atomic structure calculations base on the Hartree-Fock Formalism

In contrast to the local central-field potentials, the Hartree-Fock (HF) method entails the computation of the one-electron orbitals in the non-local potential (direct and exchange) generated from electronic orbitals in a self-consistent manner using the variational principle. More extensive discussion of the HF method can be found in Hartree (1957), Slater (1960), Froese Fischer (1977), Cohen and McEachran (1980).

Early HF calculations indicated that in going from the ground state of beryllium $1s^2 2s^2 \ ^1S$ to the first excited states $1s^2 2s 2p \ ^1,3P^o$, the $1s$ orbital remains almost unchanged. This led Fock (1933) to realize that accurate wavefunctions could be found by varying only valence orbitals while keeping the orbitals for the core fixed. This approach is known as the *frozen core* (FC) approximation.

In spite of the success of the FC approximation, this is not always directly applicable, such as in the case of configurations containing equivalent electrons. The simplest example of such configurations is the ground state of helium $1s^2 \ ^1S$, which has two equivalent electrons, both described by a single radial function $P_{1s}(r)$. Yet, if one identifies one of the electron as "core" and the other as "valence" they require different radial functions. Evidently, these two $1s$ -orbitals cannot be made orthogonal. The use of nonorthogonal orbitals to solve the atomic structure problem leads to equations much more complex than otherwise. Calculations with such nonorthogonal orbitals have been carried out only for a few systems (e.g. Pratt 1956; Froese 1966; Jucys 1967).

The FC approximation yields goods results for simple systems, but for the majority of cases it is necessary to include electronic configuration interactions like in the multiconfiguration Hartree-Fock (MCHF) or in the superposition of configurations (SOC) methods. For example, for boron-like cores a possible two-configuration core wave function is

$$\Psi(^1S) = c_1 \Psi_1(1s^2 2s^2 \ ^1S) + c_2 \Psi_2(1s^2 2p^2 \ ^1S). \quad (6)$$

Clementi and Veillard (1965) showed that including $\Phi(1s^2 2p^2 \ ^1S)$ accounts for most of the correlation energy error for all values of Z .

The MCHF (e.g. Froese Fischer 1977) method computes orthonormal orbitals self-consistently in an iterative fashion for every choice of the $\{c_i\}$ coefficients. Then, these coefficients are varied and the radial wavefunctions are recomputed until sufficient degree of convergence is achieved. This makes the method potentially very accurate, but computationally lengthy.

Based on the MCHF technique, Hibbert (1975) developed the SOC method in which analytic radial functions depending on variational parameters are used. Core wave functions of the kind shown in Equation (7) are used and the $\{c_i\}$ coefficients are determined for a given choice of the radial wavefunction parameters. Then, the radial wavefunctions are changed and the coefficients determined again until the description of the atom converges satisfactorily. The SOC method is somewhat more efficient than the MCHF technique and is able to provide similarly accurate results. The main implementation of the SOC method is in the computer program CIV3 (Hibbert 1975).

Another approach used to improve calculations of atomic structure arises from the realization that a single valence electron may polarize the spherically symmetric core, including a dipole moment at the nucleus of the form α/r^2 , where α is the dipole polarizability of the core (Hartree 1957). This gives rise to an additional attractive field with a long-range r dependence which is experienced by the valence electron, and at large distances may be represented by a "polarization potential"

$$V_{pol} = -\alpha/2r^4. \quad (7)$$

This potential is singular at $r = 0$, but it can be modified to avoid this singularity as (Biermann and Trefftz 1953)

$$V_{pol} = -(\alpha/2r^4)[1 - \exp(-x^p)], \quad x = r/\rho. \quad (8)$$

The use of a V_{pol} in the orbital equations for valence electrons can be formally justified (Caves and Dalgarno 1972), and it has been shown (e.g. Cohen and McEachran 1980, and references therein) to provide a very satisfactory description of simple spectra. However, the method has the disadvantage that the choice of the parameters p and ρ in Equation (9) remains completely *ad hoc*.

2.3. Semiempirical methods

Semiempirical methods try to compute the atomic structure of ions by solving simplified forms of the HF equations. One of the first examples of this approach is the Hartree-Fock-Slater (HFS) scheme, which consists in replacing the two-electron non-local exchange terms of the Hamiltonian by the statistical potential function

$$V_{xs}(r) = -\frac{3}{2} \left(\frac{24}{\pi} \rho \right)^{1/3}, \quad (9)$$

where ρ is the local electron density $\rho(r)$ of the atom.

Later, Cowan (1967) modified the HFS approach to write the total potential of the ion as

$$V^i(r) = -2Z/r + V_e(r) + V_{xs}(r), \quad (10)$$

where V_e is the potential energy for the density $\rho - \rho_i$ of electrons other than i and V_{xs} is an exchange term of the form

$$V_{xs} = -k_1 f(r) \left[\frac{\rho'}{\rho' + k_2/(n-l)} \right] \left(\frac{\rho'}{\rho} \right) \left(\frac{24}{\pi} \rho \right)^{1/3}, \quad (11)$$

where k_1 and k_2 are constants, ρ' is the electron density less the densities of the electron i and of the electron with which it is paired, and

$$f(r) = \begin{cases} 1 & r \geq r_0 \\ 1 + k(1 - r/r_0) & r < r_0 \end{cases} \quad (12)$$

for suitable k and r_0 .

This definition for the atomic potential is mostly empirically motivated and requires preconceived wave functions with which to construct the electron density functions ρ and ρ' . Once these functions are created the atomic structure equations are solved in an iterative fashion. Then, the accuracy of the results is assessed upon the agreement between obtained energy levels and oscillator strengths with a given sample of experimental values. The method has the advantage of being quite efficient, but it requires a lot of care in the construction of the initial electron density distribution. Further, it is difficult to estimate the accuracy of any given calculation except by the observed agreement of a limited sample of data with experimental values.

The Cowan code has been widely used by many researchers like Kurucz (e.g. Kurucz 1988; Kurucz and Peytremann 1975), who computed millions of energy levels and oscillators strengths for most ions of astrophysical interest.

2.4. Perturbation treatments

Perhaps the best known perturbation treatment is the Z -expansion method which was first introduced by Hylleraas (1930). The main idea behind this method is that one can rewrite the N -electron atom Hamiltonian of Equation (2) in terms of units of length of Z atomic units (au) and unit of energy of Z^2 au (thus different units for each N -electron ion) to obtain

$$H = \left[\frac{1}{2} \sum_i^N \frac{p^2}{m_e} - \sum_i^N \frac{1}{r} \right] + Z^{-1} \left[\sum_{i \neq j} \frac{1}{|r_i - r_j|} \right]. \quad (13)$$

Then, for highly ionized systems ($Z \gg N$) one can divide this Hamiltonian as indicated by the brackets into a one-electron zero order Hamiltonian (H_0) and a two-electron perturbation (H_1) with the expansion parameter Z^{-1} . Perturbation theory leads to the expansion for the energy and wavefunction of the form

$$E = E_0 Z^2 + E_1 Z + E_2 + E_3 Z^{-1} + \dots \quad (14)$$

$$\Psi = \Psi_0 Z^{3/2} + \Psi_1 Z^{1/2} + \Psi_2 Z^{-1/2} + \dots \quad (15)$$

Here, H_0 is the sum of hydrogenic Hamiltonians, so Ψ_0 is a linear combination of Slater determinants of hydrogenic orbitals. Subsequent orders of the Hamiltonian and wavefunctions are found as in standard perturbation theory.

The Z -expansion method is conceptually simple, but computationally lengthy when trying to go beyond the first perturbation term. One advantage of the method is that a single calculation provides results for a whole isoelectronic sequence, but accuracy is normally restricted to highly ionized ions. Another problem occurs in cases of strong configuration interaction (see Section 2.5) where states are labeled by the single configuration with the largest mixing coefficient, thus zero order mixing does not represent the physical state being considered.

Several extensions of the Z -expansion method have been developed (see Cohen 1988, Crossley 1969, and references therein) and a lot of data for astrophysical applications has been published in recent years by Vainshtein, Safronova, and collaborators (e.g. Vainshtein and Safronova 1980; Safronova et al. 1998).

2.5. Additional considerations

Configuration interaction Configuration interaction (CI) can be seen as a way to correct for Hartree's single-electron orbital approximation that pictures each electron moving individually in the field of the nucleus screened by the other electrons. Each electron is described by a single wavefunction and the whole atom is described by the Slater determinant of these wavefunction (e.g. Slater 1960). This model admits the familiar configuration description of, for example, the ground state of Be $1s^2 2s^2 ({}^1S)$. This kind of description is often not very accurate. Much better wavefunctions may be obtained from linear combinations of single configuration wavefunctions of the same total angular momentum and spin symmetry (Condon and Shortley 1935). This approach is named CI.

Going back to the case of the ground state of Be, a good CI description may be

$$\Psi({}^1S) = \alpha \Psi(1s^2 2s^2 {}^1S) + \beta \Psi(1s^2 2p^2 {}^1S), \quad (16)$$

where α and β are the so-called mixing coefficients.

Such CI representation has important effects on atomic quantities like oscillator strengths. For example, in the transition probability of the resonant transition $1s^2 2s^2 ({}^1S) - 1s^2 2s 2p ({}^1P^o)$. In the single configuration model the transition probability is determined by the matrix element $\langle 2s|r|2p \rangle$. On the other hand, in the two-configuration description of the ground 1S state, the matrix element becomes $(\alpha \pm \beta) \langle 2s|r|2p \rangle$. Depending on the relative signs of the mixing coefficients and the \pm sign, the transition may be strengthened or weakened, but which way the value will go is generally impossible to know without a full solution of the atomic structure problem.

CI is very important in the representation of the majority of atomic systems and is a standard capability of codes like SUPERSTRUCTURE, CIV3, Cowan's code, and Froese Fischer's MCHF code.

Relativistic Effects So far we have neglected relativistic effects in atomic structure calculations and we have considered oscillator strengths for dipole allowed transitions under LS coupling. In order to consider forbidden transitions it is necessary to use jj (or at least intermediate) coupling, and this requires some treatment of relativistic effects. For heavy atoms and ions relativistic effects are important even for allowed transitions. There are two ways of treating relativistic effects: by the addition of Breit-Pauli operators to non-relativistic equations, or by the fully relativistic Dirac formalism. The Breit-Pauli operators are seven and each one accounts for a specific physical effect (Bethe and Salpeter 1957). These operators are: (1) the mass operator which gives the correction due to the relativistic variation of mass with velocity; (2) the Darwin term which is characteristic of the Dirac theory but has no obvious physical interpretation; (3) the spin-orbit coupling term which arises from the interaction of spin and orbital magnetic moments of each electron; (4) the spin-other-orbit term which is due to the interaction between the spin of one electron with the orbital magnetic moment of another electron; (5) and (6) are spin-spin coupling terms that describe the interactions between the spin magnetic moments of pairs of electrons; (7) the orbit-orbit coupling term which accounts for the interactions between the orbital magnetic moments of pairs of electrons.

The expectation value of the orbit-orbit coupling term cannot be calculated accurately in the one-electron approximation. Moreover, experience suggests that this term is rather small for all ions of

interest to the present discussion (Ufford and Callen 1958; Cohen and McEachran 1980). The mass and Darwin terms contribute to the overall energy shift, but do not break LS coupling. The spin-spin, orbit-orbit, and spin-other-orbit operators serve to split energy terms into fine structure levels.

Most current codes for atomic structure calculations such as SUPERSTRUCTURE and CIV3 use the Breit-Pauli approximation to account for relativistic effects. A more precise treatment of relativistic effects using the Dirac formalism has been implemented in the computer package GRASP (Dyall et al. 1989).

3. Scattering Calculations

In considering the problems of photoionization and excitation or ionization by electron impact it is customary to think of the residual ion as the "target" or "core" with N electrons and the incoming/outgoing (electron impact/photoionization) as "free electron". Thus, the wavefunctions of the $(N + 1)$ -electron system can be expanded in terms of products of wavefunctions of the core (ϕ_i) and those of the electron (θ_i), i.e.

$$\Psi = \sum_i \phi_i(x_1, \dots, x_N) \theta_i(x_{N+1}). \quad (17)$$

Substitution of (18) in Equation (2) yields the system of coupled equations

$$-(\nabla^2 + k_i^2)\theta_i(x) + \sum_{i'} V_{ii'}\theta_{i'}(x) = 0 \quad (18)$$

where

$$V_{ii'}(x) = -\frac{2Z}{r_1} \delta_{ii'} + \int \phi^*(x_1, \dots, x_N) \times \sum_{n=1}^N \frac{2}{r_{N+1,n}} \phi(x_1, \dots, x_N) dx_1 \dots dx_N \quad (19)$$

and k_i^2 is defined by

$$E = E_i(N) + k_i^2. \quad (20)$$

It is important to notice that these equations have to be solved for every value of the energy (k^2) and of the total angular momentum (L) of the $(N + 1)$ -electron system. This last condition motivates the so-called *partial waves expansion* in which all states of definite angular momentum of the free electron are considered separately. Furthermore, the calculated collision strength is divided into partial waves as

$$\Omega = \sum_{l=0}^{\infty} \Omega_l \quad (21)$$

There are several methods to solve the scattering problem and calculate the cross sections necessary for practical applications. Below is a discussion of the most widely used methods ordered according to their level of sophistication, starting with the simplest method. This discussion is followed by a study of several physical effects that affect the cross sections. The techniques are: the central field approximation, used in photoionization calculations; the Gaunt factor and the Coulomb-Born approximation, used for electron impact excitation; and the Distorted Wave and the R-matrix methods, used for both photoionization and electron impact excitation and ionization, as well as atomic structure.

3.1. The central field approximation

This is the simplest approximation used to solve the multi-electron problem. As discussed above, in the context of atomic structure calculations, it is assumed that inter-electronic couplings are small and can be treated as small perturbations with respect to an effective central field potential that includes the attraction by the nucleus less the screening by the core electrons. A further substantial simplification of the problem results by treating *subshells* of equivalent electrons (having the same values of n and l , but different values of m and s) by means of a single radial function. This has the effect of reducing the number of coupled radial equations to only one for each subshell.

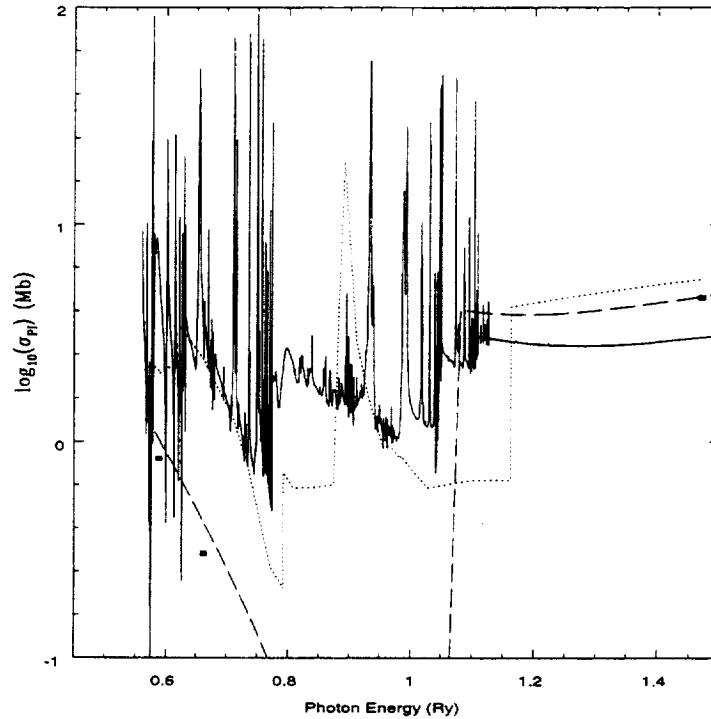


Figure 2. Photoionization cross section of the ground state $3d^6 4s^2 \ ^5D$ of Fe I. The full curve represents the R-matrix results of Bautista and Pradhan (1995); the dotted curve shows the results of Kelly and Ron (1972) and Kelly (1972) using the many-body perturbation method; the dashed curve and the square dot represent the central-field results of Verner et al. (1993) and Reilman and Manson (1979) respectively.

Central field type calculations of photoionization cross sections have been carried out by Reilman and Manson (1979), who adopted Hartree-Slater wave functions (Herman and Skillman 1963), and Verner et al. (1993), using the Dirac-Slater potential (Slater 1960; Band et al. 1979). These cross sections are reasonable accurate at high photon energies, but often give poor results near the threshold, particularly where CI is strong. For example, in the photoionization of Fe I the central field cross section from the threshold to the $3d$ subshell is underestimated by more than three orders of magnitude, as seen in Figure 2 (Bautista and Pradhan 1995). Similar errors of up to orders of magnitude are found in Fe II through Fe V (Bautista and Pradhan 1998).

Other problems with central field cross sections are that they neglect resonances and, because only degenerate subshells of equivalent electrons rather than individual energy levels are considered, the utility of these cross sections in detailed spectral modeling is limited.

3.2. The Gaunt factor

Burgess, Seaton, and Van Regemorter (Burgess 1961; Seaton 1962, Van Regemorter 1962) suggested an approximate formula to obtain near threshold collision strengths for optically allowed transitions. The formula is based on the Kramers approximation and the Gaunt factor, g , and is usually accurate within a factor of a few. Later, the formula was modified to replace g , which is a varying function with energy, by an empirical parameter $\bar{g} \sim 0.2$. The formula is

$$\Omega(i, i') = \frac{8\pi}{3\sqrt{3}} S(i, i') \bar{g}, \quad (22)$$

where $S(i, i')$ is the line strength, which relates to the absorption oscillator strength as $g_{i'} f_{i'i} = (2/3)(E_{i'} - E_i)S(i, i')$

At high energies \bar{g} increases logarithmically and the collision strength takes the form (Seaton 1962)

$$\Omega(i, i') = \frac{4}{3} S(i, i') \ln[4k^2 / (r_0 \Delta E)^2], \quad (23)$$

where $\Delta E = E_{i'} - E_i$, and r_0 is the distance of closest approach given by

$$\frac{2z}{r_0} - \frac{l(l+1)}{r_0^2} + k^2 = 0. \quad (24)$$

3.3. The Coulomb-Born approximation

In the Coulomb-Born (CB) approximation $V_{ii'}$ is replaced by its asymptotic form at large r , $2z/r$, where $z = Z - N + 1$. In doing this the solutions to the scattering problem are known analytically. The CB approximation is best for highly charged ions and transitions not affected by channel coupling and large partial waves (e.g. Seaton 1975; Van Regemorter 1960).

3.4. The Distorted Wave approximation

The Distorted Wave (DW) method assumes the coupling between different target states to be weak ($V_{ii'} = 0$, for $i \neq i'$ in Equation 19). Then, the system of coupled equations is reduced to

$$\{-(\nabla^2 + k_i^2) + V_{ii}\}\theta_i = 0. \quad (25)$$

Some of the most refined forms of the method were developed by Saraph, Seaton, and Shemming (1969) and Eissner and Seaton (1972) including exchange, which is important in many cases, like in intercombination transitions. In addition, *correlation functions*, χ_i , which are wavefunctions of the $(N + 1)$ -electron system, were introduced to modify the wavefunctions as

$$\Psi = \sum_i \phi_i(x_1, \dots, x_N) \theta_i(x_{N+1}) + \sum_{j=1} c_j \chi_j(x_1, \dots, x_{N+1}), \quad (26)$$

where the coefficients c_j are determined variationally. This form of expansion of the wavefunction is known as the close-coupling (CC) expansion (Seaton 1953).

The DW method usually gives accurate collision strengths in the absence of resonances for systems more than a few times ionized (see paper by Bhatia in this volume). Hershkowitz and Seaton (1973) showed that the DW method could also provide information about bound states of the $(N + 1)$ -electron system, and hence obtain resonance structures. However, for detailed calculations of cross sections including resonances it is usually preferred to use the R-matrix method.

3.5. The R-matrix method

The R-matrix method is the most sophisticated of the techniques discussed here and is also the most accurate. The method takes into account nearly all of the physical effects that contribute to cross sections for astrophysical applications and is applicable to all kinds of ions, from neutral to highly ionized species. Of course, with the increased complexity of the calculations the R-matrix method can be computationally very intensive.

The R-matrix theory starts by dividing the configuration space by a sphere of radius a centered on the target nucleus. In the internal region, $r < a$, where r is the relative coordinate of the free electron, electron exchange and correlation between the scattered electron and the target are important. Thus a CC expansion like that in Equation (27) is adopted for the system. In the external region, $r > a$, electron exchange between the free electron and the target can be neglected if a is large enough to contain the charge distribution of the target. Then the scattered electron moves in the long-range multipole potentials of the target ion. The internal and external regions are linked by the R-matrix on the boundary, $r = a$.

Following the theory from Burke et al. (1971), and Burke and Robb (1975), the total wavefunction Ψ in the inner region for any energy E can be written in terms of the basis states set $\{\psi_k\}$ as

$$\Psi = \sum_k A_{Ek} \psi_k \quad (27)$$

where the ψ_k functions are energy independent and are expanded as shown in Equation (27), and the energy dependence is carried through the A_{Ek} coefficients.

Then, the R matrix is defined as

$$R_{ij}(E) = \frac{1}{2a} \sum_k \frac{w_{ik}(a)w_{jk}(a)}{E_k - E}, \quad (28)$$

where

$$\frac{1}{r} w_{ik}(r) = \langle \chi_i | \psi_k \rangle \quad (29)$$

This R matrix is the basic solution of the electron-scattering problem as it allows one to determine the atomic structure of the $(N + 1)$ system, the collision strengths, and photoionization cross sections. The R matrix, the amplitude of the wavefunctions at the $r = a$ boundary, and the poles E_k are obtained from the eigenvalues and eigenvectors of the Hamiltonian matrix. Further, quantitative results for physical parameters of interest are obtained by matching the solutions with those in the outer region which are known analytically.

One important point to note is that in the R-matrix method the solution inner region is obtained only once, then cross sections for any number of energy points are readily available. Furthermore, although the basic computations in this method are lengthy, it turns out to be a very efficient technique as it provides results for large numbers of points which allow complex resonance structures in the cross sections to be delineated.

The R-matrix method has been implemented in the RMATRIX package of codes (Berrington, Eissner, and Norrington 1995) which has been widely used by several groups like the Opacity Project, that carried out extensive atomic structure and photoionization calculations of astrophysically important ions, and the Iron Project, and the RmaX Project (see papers by Pradhan and Berrington in this volume).

3.6. Important physical effects

There are several specific physical effects that should be taken into account when calculating or evaluating cross sections for photoionization or collisional excitation/ionization. These are: target CI, resonances, convergence of the wavefunction expansion, convergence of partial waves expansion, relativistic effects, and radiation damping.

Configuration interaction The first requirement in any scattering calculation is a good representation of the target, i.e. accurate wavefunctions for the target ion. Such representation usually requires the inclusion of CI in the atomic structure model, which as we saw in Section 2.5.1 affects the calculated energy levels and oscillator strengths of the ion. Furthermore, comparisons between calculated and experimental energies and oscillator strengths of the target are important indicators of the quality of the target representation and the overall accuracy of the obtained cross sections.

Resonances Resonances are an important part of collisional excitation/ionization and photoionization cross sections. Physically, resonances occur when the incoming particle (electron or photon) with just the right kinetic energy gets trapped into an autoionizing state¹ of the $(N + 1)$ -electron system. Then, as the electron remains trapped for a time before autoionization occurs, the time delay yields a phase shift in the wavefunction that manifests itself in sharp peaks or troughs in the cross sections (resonances).

Resonances appear as Rydberg series converging onto the various excitation thresholds of the target. In complex ions with many levels close in energy the series of resonances often overlap and interference

¹Autoionizing states are compound states of the (electron+ion) system located above the ionization potential. These states result from the excitation of two or more electrons of the system or by excitation of inner-shell electrons.

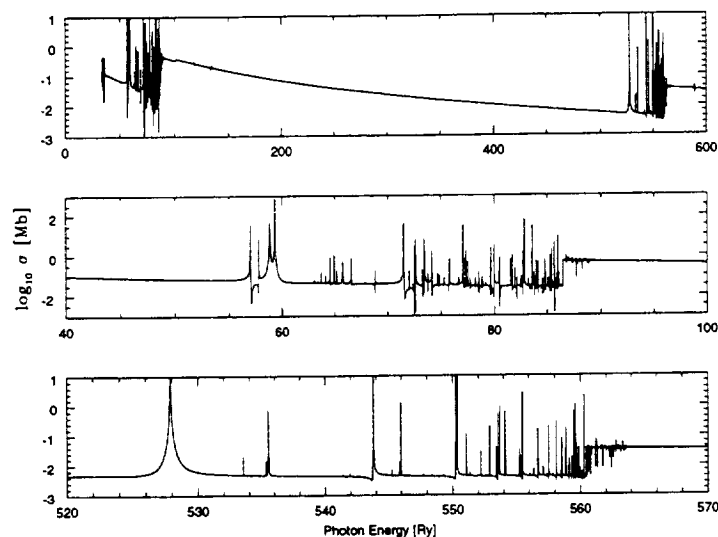


Figure 3. Photoionization cross section of the Fe XV $2p^6 3s^2(^1S)$ ground state from the R-matrix calculation of Bautista (2000a). The top panel shows the full cross sections and the lower panels present close-ups of the cross section around the L- and K-inner shell thresholds.

effects can occur which makes the resonances inseparable from the background cross section. An example of this is the photoionization cross section of the ground state of Fe I (Figure 2). The R-matrix cross section (Bautista and Pradhan 1995) given by the solid line is over three orders of magnitude greater than the central field results without resonances. Similar discrepancies with respect to central field photoionization cross section are found for all iron ions up to Fe V (Bautista and Pradhan 1998). Like in the case of photoionization near the inner $3d$ subshell of Fe I, resonances are a general phenomenon near inner-shell ionization thresholds. Figure 3 shows the photoionization cross section of Fe XV from the first ionization threshold to just above the K-shell threshold (Bautista 2000a). Complex resonance structures are seen converging onto both L and K-shell thresholds. The enhancement of the cross section due to resonances near the L-shell threshold was first pointed out by Hanque and Pradhan (1999). These resonances can change the appearance of the thresholds from sharp edges to more complex and continuous transitions. The resonances also enhance the photoionization rates. For example, assuming a power law continuum of the kind $F \propto E^{-\alpha}$ for E from 500 to 700 Ry, the resonances near the K-shell threshold of Fe XV enhance the ionization rate of this ion by factors of 1.7 for $\alpha = 1$, 1.8 for $\alpha = 2$, and 2.9 for $\alpha = 3$.

Resonances in the collision strengths are known to enhance the excitation rates by up to several factors in the case of valence electron excitation. In the case of inner-shell excitation, Bautista (2000b) carried out R-matrix calculations for Fe XVI and compared the results with earlier DW results. In the region free of resonances the agreement is generally very good, but huge numbers of near threshold narrow resonances are found from the R-matrix calculation (see Figure 4). These resonances enhance the effective collision strengths by up to three order of magnitude, as shown in Table 1.

Convergence of the partial waves expansion It is a standard approach to expand the collision strengths in partial waves from 0 to infinity from every possible value of the angular momentum of the free electron. Clearly, infinite expansion terms cannot be computed in practice and one takes only the lowest dominant partial waves and extrapolate through infinity. The convergence of the partial waves expansion is usually rapid for forbidden transitions, but it can be quite slow for allowed transitions. Also, the number of partial waves needed for convergence increases with increasing energy of the free electron. Thus, the convergence of the partial waves expansion becomes a difficult practical problem, and a possible source

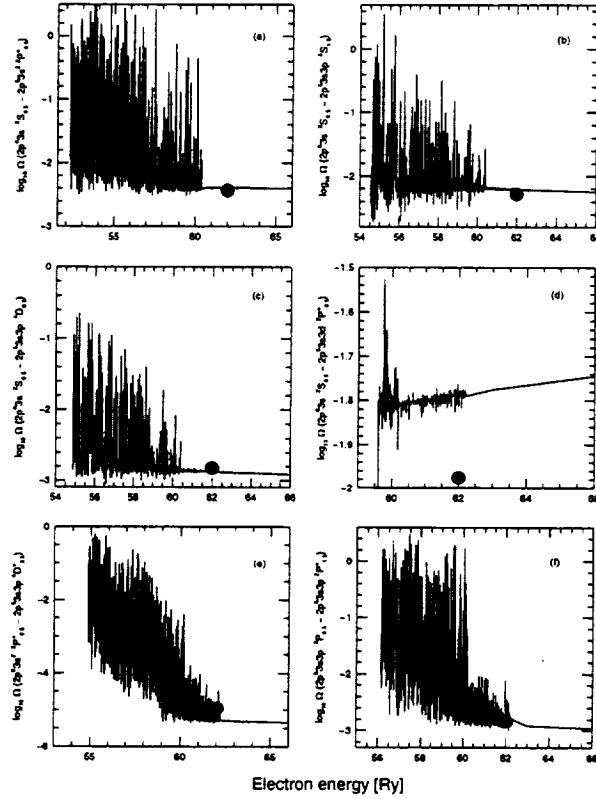


Figure 4. Comparison between R-matrix collision strengths from Bautista (2000b) and distorted wave results by Phillips et al. (1997).

of error in the collision strengths for highly ionized systems for which very high collision energies need to be considered (e.g. Burke and Seaton 1986; Chidichimo 1988, 1989; Eissner et al. 1999)

Convergence of the close coupling expansion The general form of the CC expansion for the radial wavefunction Ψ in terms of a N -electron target basis χ_i and the scattering electron function θ_i is

$$\Psi = \sum_i^{\infty} \chi_i \theta_i + \int_{\epsilon} \chi_{\epsilon} \theta_{\epsilon}. \quad (30)$$

In the DW and the standard R-matrix approach, however, the integral term that accounts for the target continuum is neglected or replaced by a discrete sum over bound correlation functions (Equation 27) and the sum over the infinite number of target states is truncated to a small number of strongly coupled states. This approximation is usually good when considering valence electron excitations among the lowest energy levels of the ion. However, for excitations to highly excited levels and inner-shell excitations the convergence of the CC expansion must be looked at in great detail. For example, Sawey and Berrington (1993) showed that in order to obtain accurate collision strengths for the $n = 4$ levels

Table 1. Comparison between effective collision strengths from Bautista (2000b) and the DW results of Phillips et al. (1997). The results are given for temperatures of $5 \cdot 10^4$, 10^5 and 10^6 K. The last column indicates the maximum factor of enhancement over the DW results.

Lower level	Upper Level	$\Upsilon(5 \cdot 10^4 \text{K})$	$\Upsilon(10^5 \text{K})$	$\Upsilon(10^6 \text{K})$	Phillips et al.	max. ratio
$2p^5 3s^2 S_{0.5}$	$2p^5 3s^2 P_{1.5}^o$	4.02(-2)	4.37(-2)	1.99(-2)	3.70(-3)	12
	$2p^5 3s^2 P_{0.5}^o$	2.01(-2)	2.18(-2)	9.96(-3)	1.96(-3)	11
	$2p^5 3s3p^4 D_{2.5}$	4.10(-2)	3.43(-2)	1.24(-2)	2.10(-4)	236
	$2p^5 3s3p^4 D_{3.5}$	2.92(-2)	2.36(-2)	5.36(-3)	1.10(-5)	2660
	$2p^5 3s3p^4 P_{2.5}$	2.17(-2)	1.87(-2)	6.76(-3)	6.60(-5)	380
	$2p^5 3s3p^2 D_{2.5}$	1.18(-1)	9.92(-2)	2.74(-2)	1.21(-3)	105
$2p^5 3s3p^4 S_{1.5}$	$2p^5 3s3p^4 P_{1.5}$	3.05(-1)	3.46(-1)	1.22(-1)	5.38(-3)	64
$2p^5 3s3p^4 D_{2.5}$	$2p^5 3s3p^2 D_{1.5}$	5.93(-2)	5.66(-2)	1.79(-2)	2.03(-4)	292
$2p^5 3s3p^4 D_{0.5}$	$2p^5 3s3p^4 D_{3.5}$	5.41(-1)	4.61(-1)	1.24(-1)	3.40(-3)	159
$2p^5 3s3p^4 D_{3.5}$	$2p^5 3s3p^2 P_{0.5}$	1.69(-2)	1.52(-2)	6.83(-3)	6.12(-4)	30
$2p^5 3s3p^4 D_{1.5}$	$2p^5 3s3p^2 D_{1.5}$	5.23(-2)	4.95(-2)	1.57(-2)	3.24(-4)	161
$2p^5 3s3p^4 P_{2.5}$	$2p^5 3s3p^2 P_{1.5}$	1.05(-1)	9.25(-2)	3.84(-2)	3.22(-3)	38
	$2p^5 3s3p^2 D_{1.5}$	4.84(-2)	4.15(-2)	1.31(-2)	1.47(-4)	329
$2p^5 3s3p^4 P_{1.5}$	$2p^5 3s3p^2 D_{1.5}$	4.02(-2)	3.47(-2)	1.18(-2)	2.82(-4)	143
$2p^5 3s3p^4 P_{0.5}$	$2p^5 3s3d^4 F_{4.5}^o$	1.04(-2)	9.27(-3)	3.03(-3)	7.00(-5)	162
	$2p^5 3s3p^2 D_{2.5}$	1.47(-1)	1.14(-1)	3.11(-2)	9.72(-4)	224
	$2p^5 3s3p^2 P_{0.5}$	2.19(-1)	1.93(-1)	5.23(-2)	1.43(-3)	154
$2p^5 3s3p^2 P_{1.5}$	$2p^5 3s3p^2 D_{2.5}$	3.46(-1)	2.80(-1)	7.80(-2)	2.98(-3)	161
	$2p^5 3s3p^2 P_{1.5}$	6.01(-1)	5.40(-1)	1.51(-1)	1.85(-3)	325

of He I one must include target states in the CC expansion up to at least $n = 5$. Otherwise, if the CC expansion is too small the obtained collision strengths tend to be severely overestimated.

The use of pseudo-orbitals to accelerate the convergence of CC expansions was first introduced by Burke, Gallagher, and Geltman (1969). Recent developments are the convergent close-coupling (CCC) and R-matrix with pseudo-states (RMPS) methods (see the review by Gorczyca et al. in this volume).

Relativistic effects If relativistic corrections are small, one can carry out the scattering calculation in LS coupling and then perform an algebraic transformation of the K (reactance) matrices to fine structure (Saraph 1972, Luo and Pradhan 1990).

As the relativistic effects become significant one must allow for the fine structure splitting of the target by using the so-called term-coupling-coefficients (TCCs) to diagonalize the Hamiltonian with the inclusion of relativistic corrections.

For more complete and proper treatment of relativistic effects it is necessary to use either the Breit-Pauli or the Dirac formulations. The Breit-Pauli operators have been implemented into the RMATRIX package of codes by the Iron Project (Hummer et al. 1993). One limitation with relativistic calculations is that by splitting the structure of the core into fine structure the size of the computation often exceeds the capacity of modern vectorized supercomputers. Perhaps, this problem may be solved in the near future with the use of massively parallel computers.

Radiation damping Radiation damping of resonances can be an important effect for highly charged ions. When the radiative de-excitation rates of autoionizing states are comparable to the autoionization rates the resonances associated with these states become damped. In the case of photoionization damping of resonances occurs because as the target is photo-excited to an autoionizing state radiative de-excitation competes with autoionization. In collisional excitation damping of resonances indicates a competition between dielectronic recombination and autoionization.

Radiation damping in electron-ion scattering were studied by Pradhan (1981, 1983a, 1983b) using the branching ratios between autoionization and radiative rates and more recently by Zhang and Pradhan (1995) employing the detailed Bell and Seaton (1985) theory of dielectronic recombination. Radiation

damping was found to be important in reducing the strength of resonances in boron-like Fe XXII and helium-like Fe XXV. As expected, radiation damping increases with the principal quantum number n within a given Rydberg series of resonances. This is because autoionization rates typically decrease as n^{-3} while radiative rates remain approximately constant.

Robicheaux et al. (1995) and Gorczyca and Badnell (1996) have studied radiation damping in photoionization cross sections. However, in practical applications of photoionization and scattering the overall radiation damping effect may be not so great in most cases. This is because while the higher n resonances can be highly damped, the lower resonances in the series, which are usually dominant, are not affected significantly, except in highly charged ions (Pradhan and Zhang 1997; Robicheaux 1998).

4. Conclusions

A number of methods for atomic structure and electron-ion scattering calculations have been developed, which are able to provide atomic data for spectroscopic applications. These methods vary in complexity and accuracy of the results in such a way that one must often decide between promptly available and highly accurate data to fulfill current spectroscopic needs. In the case of X-ray spectroscopy most of the atomic data currently available have been produced using some of the simplest techniques described here, while improved data such as that from the IRON Project (see review by Pradhan) is slowly being calculated. In some cases, new more elaborate calculations will help in refining the spectral models, while in other cases the new atomic data could vastly change the previous results leading to dramatic changes in the spectral models. Therefore, it is of prime importance to researchers trying to analyze and/or model spectra to have at least some basic understanding of the quality of the data being used.

References

- Band, I.M., Kharitonov, Y.I., and Trzhaskovskaya, M.B. 1979, *Atom. Data Nucl. Data Tables* 23, 443.
- Bates, D.R. and Damgaard, A. 1949, *Philos. Trans. R. Soc. London, Ser. A* 242, 101.
- Bautista, M.A. 2000a, *J. Phys. B: Atom., Mol. & Optic. Physics*, (submitted).
- 2000b, *J. Phys. B: Atom., Mol. & Optic. Physics* 33, 71.
- Bautista, M.A. and Pradhan A.K. 1995, *J. Phys. B: Atom., Mol. & Optic. Physics* 28, L173.
- 1998, *Astrophys. J.* 492, 650
- Bell, R.H. and Seaton, M.J. 1985, *J. Phys. B: Atom., Mol. & Optic. Physics* 18, 1589.
- Bely-Dubau, F., Fuacher, P., Dubau, J., Gabriel, A.H. 1982, *MNRAS* 198, 239.
- Berrington, K.A., Eissner, W.B., and Norrington, P.H. 1995, *Comput. Phys. Commun.* 92, 290.
- Bethe, H.A. and Salpeter, E.E. 1957, "Quantum Mechanics of One- and Two-electron Atoms." Springer-Verlag, Berlin and New York.
- Biermann, L. and Treffitz, E. 1953, *Z. Astrophys.* 30, 275.
- Bromander, J., Durić, N., Erman, P., and Larsson, M. 1978, *Phys. Scr.* 17, 119.
- Burgess, A. 1961, *Mem. Soc. Roy. Sci. Liege* 4, 299.
- Burke, P.G., Gallagher, D.F., and Geltman, S. 1969, *J. Phys. B: Atom., Mol. & Optic. Physics* 2, 1142.
- Burke, P.G., Hibbert, A., and Robb, W.D. 1971, *J. Phys. B: Atom., Mol. & Optic. Physics* 4, 153.
- Burke, P.G., and Robb, W.D., 1975, *Adv. Atom. Mol. Phys.* 11, 143.
- Burke, V.M. and Seaton M.J. 1986, *J. Phys. B: Atom., Mol. & Optic. Physics* 19, L527.
- Caves, T.C. and Dalgarno, A. 1972, *J. Quantum Spectrosc. Radiat. Transfer* 12, 1539.
- Chidichimo, M.C. 1988, *Phys. Rev. A* 37, 4097.
- 1989, *Phys. Rev. A* 38, 6107.
- Clementi, E. and Veillard, A. 1965, *J. Chem. Phys.* 44, 3050.
- Cohen, M. 1988, *Adv. Atom. Mol. Phys.* 25, 195.
- Cohen, M. and McEachran, R.P. 1980, *Adv. Atom. Mol. Phys.* 16, 1.

- Condon, E.U. and Shortley, G.H. 1935, "The Theory of Atomic Spectra." Cambridge Univ. Press, London and New York.
- Cowan R.D. 1967, *Phys. Rev.* 163, 54.
- Crossley, R.J.S. 1969, *Adv. Atom. Mol. Phys.* 5, 237.
- Dyall, K.G., Grant, I.P., Johnson, C.T., Parpia, F.A., and Plummer, E.P. 1989, *Comput. Phys. Commun.* 55, 425,
- Eissner, W., Galavís, M.E., Mendoza, C., and Zeippen, C.J. 1999, *Astron. and Astrophys. Suppl. Ser.* 136, 394.
- Eissner, W. and Nussbaumer, H. 1969, *J. Phys. B: Atom., Mol. & Optic. Physics* 2, 1028.
- Eissner, W., Jones, M., and Nussbaumer, H. 1974, *Comput. Phys. Commun.* 8 271.
- Eissner, W. and Seaton, M.J. 1972, *J. Phys. B: Atom., Mol. & Optic. Physics* 5, 2187.
- Fock, V. 1933, *Z. Phys.* 81, 195.
- Froese, C. 1966, *Phys. Rev.* 150, 1.
- Froese Fischer, C. 1977 "The Hartree-Fock Method for Atoms." Wiley, New York.
- Gorczyca, T.W. and Badnell, N.R. 1996, *J. Phys. B: Atom., Mol. & Optic. Physics* 29, L283.
- Hanque, N. and Pradhan, A.K. 1999, *Phys. Rev. A* 60, R4221.
- Hartree, D.R. 1957, "The Calculation of Atomic Structures." Wiley, New York.
- Hershkowitz, M.D. and Seaton, M.J. 1973, *J. Phys. B: Atom., Mol. & Optic. Physics* 6, 1176.
- Herman, F. and Skillman, S. 1963, "Atomic Structure Calculations." Englewood Cliffs, NJ: Prentice-Hall.
- Hibbert, A. 1975, *Comput. Phys. Commun.* 9, 141.
- 1982, *Adv. in Atom. and Mol. Phys.* 18, 309.
- Hylleras, E.A. 1930, *Z. Physik* 65, 209.
- Jucys, A.P. 1967, *Int. J. Quantum Chem.* 1, 311.
- Kelly H.P. 1972, *Phys. Rev. A* 6, 1048.
- Kelly, H.P. and Ron, A. 1972, *Phys. Rev. A* 5, 168.
- Kurucz, R.L. 1988, *Trans. IAU, XXB*, M. McNally, ed., Dordrecht: Kluwer, pp. 168.
- Kurucz, R.L. and Peytremann, E. 1975, *SAO Special Report* 362.
- Luo, D. and Pradhan, A.K. 1990, *Phys. Rev. A* 41, 165.
- Phillips K.J.H., Greer C.J., Bhatia A.K., Coffey I.H., Barnsley R., and Keenan F.P. 1997, *Astron. & Astrophys.* 324, 381.
- Pradhan, A.K. 1981, *Phys. Rev. Letters* 47, 79.
- 1983a,b, *Phys. Rev. A* 28, 2113; 2128.
- Pradhan, A.K. and Zhang, H.L. 1997, *J. Phys. B: Atom., Mol. & Optic. Physics* 30, L571.
- Pratt, G.W. 1956, *Phys. Rev.* 102, 1303.
- Reilman, R.F. and Manson S.T. 1979, *Astrophys. J. Supp. Ser.* 40, 815.
- Robicheaux, F. 1998, *J. Phys. B: Atom., Mol. & Optic. Physics* 31, L109.
- Robicheaux, F., Gorczyca, T.W., Pindzola, M.S., and Badnell, N.R. 1995, *Phys. Rev. A* 52, 1319.
- Safronova, U.I., Shlyaptseva, A.S., Cornille, M., and Dubau, J. 1998, *Physica Scripta* 57, 395.
- Saraph, H.E. 1972, *Comput. Phys. Commun.* 3, 256.
- Saraph H.E., Seaton, M.J. and Shemming, J. 1969, *Phil. Trans. Roy. Soc. London, Ser. A* 264, 77.
- Sawey, P.M.J. and Berrington, K.A. 1993, *Atom. Data Nucl. Data Tables* 55, 81.
- Seaton, M.J. 1953, *Proc. Roy. Soc. Lond. Ser. A* 218, 400.
- 1962, in "Atomic and Molecular Processes." (D.R. Bates, ed.), p.374, Academic Press, New York.
- 1975, *Adv. Atom. Mol. Phys.* 11, 83.
- Slater, J.C. 1960, "Quantum Theory of Atomic Structure." McGraw-Hill, New York.
- Ufford, C.W. and Callen, H.B. 1958, *Phys. Rev.* 110, 1352.
- Vainshtein, L.A. and Safronova, U.I. 1980, *Atom. Data and Nucl. Data Tables* 25, 311.

Van Regemorter, H. 1960, *Mon. Notic. Roy. Astron. Soc.* 121, 213.

—, 1962, *Astrophys. J.* 136, 906.

Verner, D.A., Yakovlev, D.G., Brand, I.M., and Trzhaskovskaya, M.B., 1993, *At. Data. Nucl. Data Tables* 55, 233.

Zhang, H.L. and Pradhan, A.K. 1995, *J. Phys. B: Atom., Mol. & Optic. Physics* 28, L285.

Distorted Wave Calculations and Applications

A. K. Bhatia

Laboratory for Astronomy and Solar Physics
NASA/Goddard Space Flight Center
Greenbelt, Maryland 20771
USA

Abstract. Physical properties such as temperature and electron density of solar plasma and other astrophysical objects can be inferred from EUV and X-ray emission lines observed from space. These lines are emitted when the higher states of an ion are excited by electron impact and then decay by photon emission. Excitation cross sections are required for the spectroscopic analyses of the observations and various approximations have been used to calculate the scattering functions. One of them which has been widely used is a distorted wave approximation. This approximation, along with its applications to solar observations, is discussed. The Bowen fluorescence mechanism and optical depth effects are also discussed. It is concluded that such calculations are reliable for highly charged ions and for high electron temperatures.

1. Introduction

Since this workshop is dedicated to X-ray astronomy it is appropriate to mention that solar X-rays were first detected on August 5, 1948 from a V2 rocket and the first nonsolar X-ray source was also discovered from a rocket flight in 1962. Since then a number of satellites have been launched to study X-ray sources, the most recent satellites being the *Chandra* and the *XMM-Newton* observatories. Photons from the Sun and other astrophysical objects are messengers bearing information about the plasma properties of these objects. The purpose of the distorted wave (DW) calculations is to provide atomic data required to infer the plasma properties such as electron density, temperature, and elemental abundances (which in the solar corona and solar winds are different from their photospheric values). This difference in elemental abundances seems to be a function of the first ionization potential (FIP) of the elements and can vary from region to region of the Sun. Other properties of interest are heating of stellar coronae, magnetic fields, and acceleration of stellar winds.

Photons are emitted when the upper levels of an ion excited by electron impact decay to the lower levels. Some of the high-lying levels can be populated by charge exchange and some levels can be populated by the dielectronic recombination of electrons with ions. Excitation by heavy particles like protons can be important for the fine-structure levels but most of the time electron impact excitations dominate. This is called "the coronal condition", i.e. electron impact excitation is balanced by radiative decay. For an optically thin plasma, the intensity of the observed line due to the transition from level j to level i is given by

$$I_{ji} = N_j A_{ji} \Delta E_{ij} \quad (1)$$

where N_j is the population of the upper level and depends on the electron density N_e , A_{ji} is the spontaneous radiative transition rate, and ΔE_{ij} is the energy separation between the two levels. In general, the ionization and recombination processes are very slow compared to excitation processes. This implies that excitation processes can be considered separately from ionization and recombination processes. Therefore, assuming ionization equilibrium, the level population of a multi-level ion excited by electron impact is obtained by solving the statistical equilibrium equations

$$\frac{dN_i}{dt} = -N_e N_i \sum_{j>i} C_{ij}^e + \sum_{j>i} N_j A_{ji} - N_i \sum_{j<i} A_{ij} + N_e \sum_{j>i} N_j C_{ji}^d \quad (2)$$

$$\frac{dN_i}{dt} = 0 \quad \text{for steady state} \quad (3)$$

where C_{ij}^e , for an assumed Maxwellian electron velocity distribution at temperature T_e for an isothermal plasma, is the excitation rate coefficient from level i to level j and is given by

$$C_{ij}^e = \frac{8.63 \times 10^{-6}}{\omega_i k T_e^{1.5}} \int_{\Delta E_{ij}}^{\infty} \Omega_{ij}(E) \exp\left(-\frac{E}{k T_e}\right) dE \quad (4)$$

where k is the Boltzmann constant and the units are $\text{cm}^3 \text{sec}^{-1}$. The thermally averaged collision strength is called the effective collision strength Υ_{ij} defined as

$$\Upsilon_{ij} = \int_0^{\infty} \Omega_{ij}(E) \exp\left(-\frac{E}{k T_e}\right) d\left(\frac{E}{k T_e}\right) \quad (5)$$

so that

$$C_{ij}^e = \frac{8.63 \times 10^{-6}}{\omega_i T_e^{0.5}} \Upsilon_{ij}(T_e) \exp\left(-\frac{\Delta E_{ij}}{k T_e}\right) \quad (6)$$

The deexcitation rate coefficient C_{ji}^d is obtained by the principle of detailed balance:

$$C_{ji}^d = \frac{\omega_i}{\omega_j} \exp\left(\frac{\Delta E_{ij}}{k T_e}\right) C_{ij}^e \quad (7)$$

The dimensionless quantity $\Omega_{ij} = \Omega_{ji}$ is the collision strength which we want to calculate. This is related to the excitation cross section σ_{ij} for exciting the target state i to the state j

$$\sigma_{ij} = \frac{\pi a_0^2}{\omega_i k_i^2} \Omega_{ij} \quad (8)$$

at wave number k_i of the incident electron; ω_i is the statistical weight of the initial target state and Ry units are used throughout. At low electron density most of the population is in the ground level $i=1$ and if only one level is excited then $j=2$, and Equations (2) and (3) reduce to

$$N_e N_1 C_{12}^e = N_2 A_{21} \quad (9)$$

where C_{12}^d has been neglected because it is very small compared to A_{21} . The radiative transition rates due to dipole-allowed transitions are much higher than electric quadrupole, magnetic dipole, and quadrupole transition rates. The observed transitions are classified as resonance or dipole-allowed transitions (spin-allowed and angular momentum changes by 1), forbidden transitions (spin-forbidden and no change in angular momentum), and intercombination transitions (spin-forbidden and the angular momentum changes). For a known Z dependence, the radiative rates can be scaled along the isoelectronic series. The rates for the electric-dipole, electric-quadrupole, and magnetic-dipole are proportional to Z^4 , Z^6 , and Z^{10} , respectively. The magnetic-dipole rates can become comparable to the electric-dipole rates at high Z . This then gives lines due to magnetic-dipole transitions as intense as the lines due to electric-dipole transitions for high Z ions.

If the density is very low then the collisional excitation becomes less important and recombination of electrons and ions in high-lying levels becomes more important. Emission lines are then due to cascades to lower levels.

If the electron density is very high ($N_e > 10^{18} \text{cm}^{-3}$) as in stellar envelopes, then Equations (2) and (3) in the two-level model give

$$N_1 C_{12}^e = N_2 C_{21}^d \quad (10)$$

which is the condition for thermodynamic equilibrium. Using Equation (7), Equation (10) reduces to

$$\frac{N_2}{N_1} = \frac{\omega_2}{\omega_1} \exp\left(-\frac{\Delta E_{12}}{k T_e}\right) \quad (11)$$

This is the Saha-Boltzmann distribution indicating that at very high electron densities the level populations are proportional to their weights. This can be generalized to all the levels of the ion. At such high densities the optical properties of the plasma can be considered separately because the statistical equilibrium equations need not be solved for the level populations. This condition is called local thermodynamic equilibrium (LTE).

2. Calculations

The simplest approximation is to use Coulomb waves for the incident and scattered electron in the expression for the transition matrix element

$$f_{ij} \propto \langle \Psi_j | V | \Psi_i \rangle \quad (12)$$

where f_{ij} is the transition amplitude, Ψ_i and Ψ_j are the initial and final state wavefunctions, and V is the perturbing potential. In general, the electrons in the ions are moving faster than the incident electron and Born-type approximations are not valid. The next step is to solve the scattering problem accurately. The total wave function is of the form

$$\Psi_i = A \Phi_i(1, 2, \dots, N) F_i(N+1) \quad (13)$$

where Φ_i is the target function, F_i represents the incident or the scattered electron, and A is the antisymmetrization operator. The Hamiltonian of the $(N+1)$ -electron system is given by

$$H_{N+1} = - \sum_i (\nabla_i^2 + \frac{2Z}{r_i}) + \sum_{i>j} \frac{2}{r_{ij}} \quad (14)$$

The wave function Ψ_i satisfies the Schrödinger equation

$$H_{N+1} \Psi_i = E \Psi_i \quad (15)$$

In the DW approximation the coupling between the channels (target+scattered electron) is neglected. For this reason resonances, representing compound states of the target and the electron, cannot be included in such calculations, and a close-coupling approximation is required to include resonances, but then the scattering equations are coupled integro-differential equations. The solution of integral equations requires a lot more computer time than is required by DW equations. Since the resonance contribution cannot be scaled along the isoelectronic series, it is not possible to scale effective collision strengths obtained in the close-coupling or R-matrix approximations while those obtained in the DW approximation can be scaled. The resonance contribution to the effective collision strength is often more important for the forbidden and intercombination transitions than for the dipole-allowed transitions. For the latter transitions the contribution from the incident partial waves can be much more substantial than the contribution from resonances.

In the DW approximation, the scattering function satisfies the equation

$$\left[\frac{d^2}{dr^2} - \frac{l_i(l_i+1)}{r^2} + \frac{2z}{r} + V_i(r) + k_i^2 \right] F_i(r) = 0 \quad (16)$$

where $z=Z-N$ is the ion charge, Z being the nuclear charge and N the number of electrons, and $V_i(r)$ is a central potential. The $F_i(r)$ satisfies the boundary conditions

$$F_i(0) = 0 \quad (17)$$

$$F_i(r \rightarrow \infty) = \frac{1}{k_i^{0.5}} \sin[k_i r - \frac{l_i \pi}{2} + \frac{z}{k_i} \ln(2k_i r) + \arg \Gamma(l_i + 1 - \frac{iz}{k_i}) + \delta_{l_i}] \quad (18)$$

where δ_{l_i} is the phase shift in addition to the Coulomb phase shift.

Along these lines DW programs (Eissner and Seaton 1979; Eissner 1998) have been developed at University College London (UCL), and in these programs $V_i(r)$ is chosen as a scaled Thomas-Fermi-Dirac-Amaldi potential. There are a number of excited states of the target and equations like Equation (16) have to be solved for each state. The reaction matrix is given by

$$K_{ij} = - \langle \Psi_j | H_{N+1} - E | \Psi_i \rangle \quad (19)$$

and the T-matrix is given by

$$T = - \frac{2iK}{1 + iK} \quad (20)$$

The collision strength for total angular momentum L , spin S , and parity π is given by

$$\Omega_{ij}^{LS\pi} = \frac{(2L+1)(2S+1)}{2} \sum_{l_i, l_j} |T|^2 \quad (21)$$

and the total collision strength, symmetric in i and j , is given by

$$\Omega_{ij} = \sum_{LS\pi} \Omega_{ij}^{LS\pi} \quad (22)$$

which, for incident energy $E \rightarrow \infty$, behaves like $\log(E)$, $1/E^2$, and constant for dipole allowed, spin forbidden, and non-dipole allowed transitions, respectively.

The target functions should be such that all the configurations in the complex (the same quantum number and parity) are included; e.g. to calculate 2^1S state of a He-like ion, $2s^2$ and $2p^2$ configurations should be included. We will see below that a large number of configurations are required to obtain a good representation of the bound state wavefunction. Along these lines the program Superstructure (Eissner et al. 1972) developed at UCL takes into account configuration interaction and also includes relativistic corrections using the Breit-Pauli Hamiltonian as a perturbation to the nonrelativistic Hamiltonian. The target functions are expanded in terms of Slater states and the same type of potential $V_i(r)$ as in Equation (16) is used to calculate the radial functions. The potential $V_i(r)$ depends upon parameters λ_i which are determined variationally by optimizing the weighted sum of the term energies. Atomic data such as energy levels, oscillator strengths, and radiative transition rates are calculated in LS and in intermediate coupling. Term coupling coefficients required to transform LS K-matrices to intermediate coupling in the recoupling program JAJOM (Saraph 1978), which calculates collision strengths between the levels, are also calculated in the Superstructure program. Since only a finite number of incident partial waves can be included in the calculation of collision strengths, the contribution from higher partial waves is included using the Coloumb-Bethe approximation (CBe; Burgess and Sheorey 1974) for dipole-allowed transitions and geometric progression for non-dipole allowed transitions. This is referred to as a top-up. The program JAJOM has been modified (Saraph and Eissner 2000) recently to include these contributions in the final results.

Collision strengths have been calculated for a number of ions and before we discuss their applications, we consider one ion, say O III, and illustrate the convergence of collision strengths with the incident partial waves for allowed and forbidden transitions. Energy levels, oscillator strengths, transition rates, and collision strengths for O III have been calculated by using $2s^22p^2$, $2s2p^3$, $2p^4$, $2s^22p3s$, $2s^22p3p$, and $2s^22p3d$ configurations in the Superstructure and DW programs and they are given by Bhatia and Kastner (1993). These configurations give rise to 46 fine-structure levels. Collision strengths have been calculated at five incident energies (4, 6, 8, 10, and 12 Ry) and up to total angular momentum $L^T=21$.

$$\vec{L}^T = \vec{l}_i + \vec{l}_t \quad (23)$$

where \vec{l}_i is the incident angular momentum and \vec{l}_t is the target angular momentum. For allowed transitions, we compare in Table 1 some increments in collision strengths, at the highest incident energy 12 Ry, with increasing incident partial wave l_i obtained in the DW calculation and in the CBe approximation. It is seen that for $l_i \geq 19$ the CBe approximation can be used to calculate contributions from higher incident partial waves to collision strengths.

Table 1. Comparison of DW and CBe collision strength increments $\Delta\Omega$ for allowed transitions at incident electron energy=12 Ry.

Transition	$l_i \rightarrow l_i+1$	increments $\Delta\Omega$	
		DW	CBe
$2s^2 2p^2 \ ^3P_0 \rightarrow 2s 2p^3 \ ^3D_1$	14 15	0.048877	0.048395
	15 16	0.043548	0.043203
	16 17	0.038977	0.038635
	17 18	0.034909	0.034601
$2s^2 2p^2 \ ^3P_0 \rightarrow 2s 2p^3 \ ^3P_1$	14 15	0.050030	0.049471
	15 16	0.043854	0.043446
	16 17	0.038622	0.038213
	17 18	0.034014	0.033654
$2s^2 2p 3p \ ^3D_2 \rightarrow 2s^2 3p 3d \ ^3F_2$	14 15	2.908503	3.041705
	15 16	2.780783	2.854956
	16 17	2.652672	2.688366
	17 18	2.519384	2.538703

The convergence is quite rapid for the forbidden transitions as indicated in Table 2 and, in general, not many incident partial waves are needed for such transitions. The convergence should be even more rapid for ions ionized more than two times.

Table 2. Comparison of DW and CBe collision strength with increasing number of partial waves l_i for forbidden transitions at incident electron energy=12 Ry

Spin-forbidden			Spin-allowed		
Transition	l_i	Ω_{DW}	Transition	l_i	Ω_{DW}
$2s^2 2p^2 \ ^3P_1 \rightarrow 2s^2 2p 3p \ ^1P_1$	14	0.008192	$2s^2 2p^2 \ (^3P_0 \rightarrow ^3P_1)$	14	0.080818
	15	0.008196		15	0.080818
	16	0.008199		16	0.080818
	17	0.008202		17	0.080818
	18	0.008204		18	0.080818
$2s^2 2p^2 \ ^1S_0 \rightarrow 2s^2 2p 3p \ ^3D_1$	14	0.001836	$2s^2 2p^2 \ (^3P_0 \rightarrow ^3P_2)$	14	0.145157
	15	0.001836		15	0.146256
	16	0.001836		16	0.147157
	17	0.001836		17	0.147904
	18	0.001836		18	0.148534

3. Applications

There are a number of electron density sensitive lines emitted from excited states of various ions. This sensitivity is due to the presence of metastable levels among the excited states. In general most of the levels are populated due to excitation from the ground state but a metastable level, e.g. the 3P_0 level in Be-like systems, does not decay rapidly by radiative transition and thus can have a substantial population so that the higher levels could be excited from it too. Since the population of the metastable level depends upon electron density, other level populations could also be density sensitive. The critical

electron density above which a metastable level population becomes important is given by

$$N_e(\text{critical}) = \frac{\sum_i A_{ji}}{\sum_i C_{ji}} \quad (24)$$

where j represents the metastable level and i all other levels to which radiative, collisional excitation, and deexcitation take place.

A number of DW calculations have been carried out on various systems and some comparisons with solar and laboratory observations are available. Line ratios

$$R = \frac{(2s2p^3P_2 - 2p^2^3P_2)}{(2s^2^1S_0 - 2s2p^1P_1)} \quad \text{and} \quad R^* = \frac{(2s^2^1S_0 - 2s2p^3P_1)}{(2s^2^1S_0 - 2s2p^1P_1)} \quad (25)$$

have been measured in the emission spectra of the Texas experimental tokamak plasma (Huang et al. 1987) for beryllium-like Ti XIX and Sc XVIII for various electron densities, and these ratios agree very well with the DW calculations of Bhatia, Feldman, and Seely (1986). A similar comparison has been made for other beryllium-like ions at electron density of $3.5 \times 10^{13} \text{cm}^{-3}$ (cf. Figures 6 and 7 of Huang et al. 1987). A comparison of DW calculations with solar and astrophysical observations is expected to be as good as for the tokamak plasma.

Bhatia, Feldman, and Seely (1986a) give atomic data and spectral line intensities for the beryllium sequence. The atomic data consisting of energy levels, oscillator strengths, transition rates, and collision strengths were calculated using $2s^2$, $2s2p$, $2p^2$, $2s3s$, $2s3p$, $2s3d$, $2p3s$, $2p3p$, and $2p3d$ configurations giving rise to 20 fine-structure levels. Proton collisions for the transitions $2s2p(^3P_0 - ^3P_2)$ and $2s2p(^3P_1 - ^3P_2)$ have been included using the semiclassical theory of Kastner and Bhatia (1979).

With the DW calculations established as reasonably accurate, results of such calculations are compared with solar observations for a few ions giving emission lines from the visible to the X-ray region. Identifications of optically thin as well as optically thick lines are discussed and wherever possible electron densities in the plasma are inferred from intensity ratios.

4. O IV and Mg VIII

Observations of solar flares on 1973 August 9 and September 7 were obtained by the Naval Research Laboratory's SO82B spectrograph on board Skylab. Since the instruments covered the 960-1600 Å wavelength range, spectra of allowed and intersystem lines of O IV became visible at high electron densities. These lines have been used for density diagnostics. Cook, Keenan, and Bhatia (1994) analyzed these observations using atomic data obtained with the configurations $2s^22p$, $2s2p^2$, and $2p^3$. The intensity ratio of the lines at 1342.99 and 1338.61 Å, due to the transitions $2p^3^2D_{3/2} \rightarrow 2s2p^2^2P_{3/2,1/2}$, was found not in the ratio of transition rates expected; the lines have the same upper level. This is due to the contamination of H₂ lines at 1342.88 and 1338.57 Å. However, the intensity ratio of the allowed line at 1343.51 Å due to $2p^3^2D_{5/2} \rightarrow 2s2p^2^2P_{3/2}$ and the intercombination line at 1407.39 Å, due to $2s2p^2^4P_{1/2} \rightarrow 2s^22p^2P_{3/2}$, was found to be density sensitive, but not temperature sensitive, as shown in Figure 1 of Cook, Keenan, and Bhatia (1994). The observed ratio in the two flares is 0.89 and 0.90 giving an electron density of $1.6 \times 10^{12} \text{cm}^{-3}$ at $\log(T_{max}) = 5.2$ K, where T_{max} is the temperature of maximum abundance of O IV.

EUV spectral lines of Mg VIII have been observed from the solar corona by Skylab, the Solar EUV Rocket Telescope and Spectrograph (SERTS), and more recently by Solar and Heliospheric Observatory (SOHO). SERTS flights (Thomas and Neupert 1994) in 1989, 1991, and in 1993 measured intensities for lines at 311.78, 313.74, 315.02, 317.01, 339.00, 430.44, and 436.73 Å. All these lines with the exception of 430.44 and 436.73 Å have been measured by SOHO (Harrison et al. 1995) launched in December 1995. Figure 1 taken from Bhatia and Thomas (1998) shows a comparison of solar active region spectra taken by SERTS-89 and by the Coronal Diagnostic Spectrometer (CDS) on SOHO.

Bhatia and Thomas (1998) carried out a calculation using the configurations $2s^22p$, $2s2p^2$, $2p^3$, $2s^23s$, $2s^23p$, and $2s^23d$ in the Superstructure program. These configurations give rise to 20 fine-structure levels. The energy levels, oscillator strengths, and radiative rates have been calculated in intermediate coupling. These are given in Tables 1 and 2 of Bhatia and Thomas (1998). Collision strengths are calculated at five

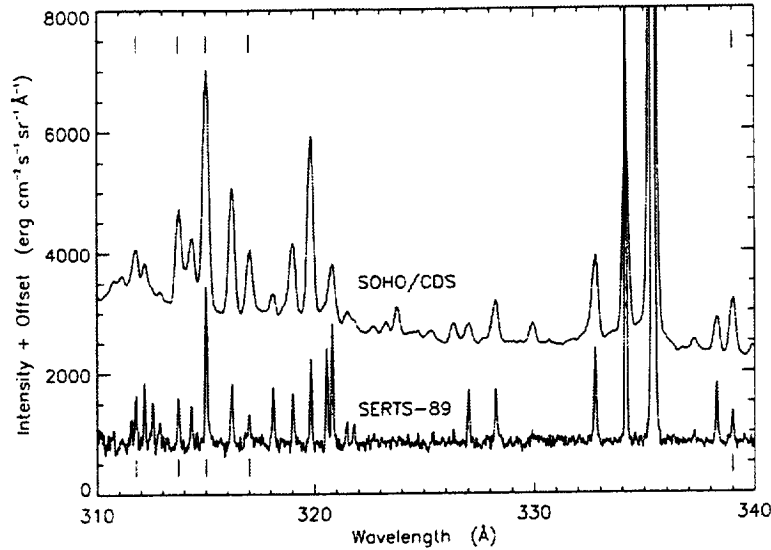


Figure 1. Comparison of average active region spectra taken at different times by SERTS 89 and by CDS on SOHO. The tick marks indicate Mg VIII lines.

incident energies (15.0, 22.5, 30.0, 37.5, and 45 Ry); these are given in Table 2 of Bhatia and Thomas. The temperature of maximum abundance for this ion is $\log(T_e)=5.9\text{K}$. Level populations are calculated by solving the statistical equilibrium equations at a number of electron densities, and intensity ratios are then calculated using Equation (1).

A comparison with relative intensities in an active region observed by SERTS-89 is given in Table 3. The calculated intensity ratio $I(313.74)/I(317.01)=1.69$ agrees reasonably well with the observed value 1.40. The inclusion of 3 more configurations, $2s3p3s$, $2s3p3p$, and $2s3p3d$, does not change the above calculated ratio appreciably. These lines originate from the same upper level and therefore the ratio depends only on radiative transition rates. The agreement indicates that the calculated radiative rates are reliable. The relative intensities of 436.73 and 430.44 Å remain in some disagreement with the calculated values. However, the intensity ratio $I(436.73)/I(430.44)$ is found to be density sensitive, and at $N_e = 10^{9.2} \text{ cm}^{-3}$ (interpolated), its value is 1.68, which is the observed value from SERTS-89 (Thomas and Neupert 1994). This density is comparable to the value of $N_e = 10^{9.6} \text{ cm}^{-3}$ derived by Brickhouse, Raymond, and Smith (1995) from the same SERTS-89 spectrum, but using Fe IX line ratios formed at temperatures similar to those of Mg VIII.

Atomic data and spectral line intensities for the boron isoelectronic sequence (Ar XIV through Kr XXXII) are given by Bhatia, Feldman, and Seely (1986). The calculations were carried out using $2s^22p$, $2s2p^2$, $2p^3$, $2s^23s$, $2s^23p$, and $2s^23d$ configurations.

5. O III and Fe XXI

Emission lines of carbon-like ions are present in various wavelength ranges, e.g. Fe XXI has emission lines in the ranges 1-25, 90-200, and 300-2500 Å. The Fe ions are of particular interest because Fe is the most abundant element in the solar atmosphere. Many of these lines have been used for electron density diagnostics. Mason et al. (1979) calculated energy levels, oscillator strengths, transition rates, and collision strengths using configurations $2s^22p^2$, $2s2p^3$, and $2p^4$ in the Superstructure and DW programs. The levels in the ground configuration $2s^22p^2$ are $^3P_{0,1,2}$, 1D_2 , and 1S_0 . Level populations and intensity ratios were calculated at various electron densities and at $T_e = 10^7 \text{ K}$. The intensity ratios $I(142.14)/I(128.73)$, $I(121.22)/I(128.73)$, $I(102.23)/I(128.73)$, and $I(97.89)/I(128.73)$ are sensitive to N_e as shown in Table 4.

Table 3. Relative intensities observed by SERTS-89 compared to calculated values at $\log(T_e)=5.9$

Transition		$\lambda(\text{\AA})$	I_{Obs}	I_{cat}					
				$\log N_e(\text{cm}^{-3})$					
i	j			6	7	8	9	10 ^c	
$2s^2 2p^2 P_{1/2}$	$- 2s2p^2 P_{3/2}$	311.778	$0.313^a \pm 0.056$	0.199	0.199	0.199	0.199	0.199	
$2s^2 2p^2 P_{1/2}$	$- 2s2p^2 P_{1/2}$	313.736	0.317 ± 0.049	1.380	1.062	0.540	0.395	0.378	
$2s^2 2p^2 P_{3/2}$	$- 2s2p^2 P_{3/2}$	315.024	1.000 ± 0.123	1.000	1.000	1.000	1.000	1.000	
$2s^2 2p^2 P_{3/2}$	$- 2s2p^2 P_{1/2}$	317.008	0.227 ± 0.052	0.816	0.628	0.319	0.233	0.223	
$2s^2 2p^2 P_{1/2}$	$- 2s2p^2 S_{1/2}$	335.230	— ^b	0.437	0.357	0.225	0.188	0.184	
$2s^2 2p^2 P_{3/2}$	$- 2s2p^2 S_{1/2}$	339.000	0.213 ± 0.033	0.627	0.511	0.322	0.269	0.263	
$2s^2 2p^2 P_{1/2}$	$- 2s2p^2 D_{3/2}$	430.445	0.159 ± 0.019	1.614	1.208	0.542	0.356	0.334	
$2s^2 2p^2 P_{3/2}$	$- 2s2p^2 D_{5/2}$	436.726	0.267 ± 0.032	0.108	0.255	0.498	0.566	0.574	

^a Blended with Ni XV, see Thomas and Neupert (1994)

^b Masked by Fe XVI 335.40 \AA

^c Above $\log(N_e)=10$, ratios do not change

Table 4. Theoretical intensity ratios as a function of electron density

$\lambda(\text{\AA})$	Theoretical intensity ratios for $\log(N_e(\text{cm}^{-3}))$						
	11.0	11.5	12.0	12.5	13.0	14.0	15.0
142.14	0.013	0.023	0.055	0.147	0.379	1.246	1.465
128.73	1.000	1.000	1.000	1.000	1.000	1.000	1.000
121.22	0.015	0.044	0.118	0.271	0.538	1.422	1.836
102.23	0.228	0.254	0.321	0.469	0.753	1.720	2.144
97.89	0.099	0.110	0.139	0.204	0.327	0.747	0.930

This sensitivity can easily be understood. Let us consider the lines at 142.14 and 128.73 \AA due to the transitions $2s2p^3 D_2 \rightarrow 2s^2 2p^2 P_1$ and $2s2p^3 D_1 \rightarrow 2s^2 2p^2 P_0$, respectively. The level 3D_2 is mainly excited from 3P_1 while 3D_1 is excited from the ground level 3P_0 . This is because the collision strengths between 3P_1 and 3D_2 are much larger than between 3P_0 and 3D_2 as indicated in Table 5.

This implies that at low electron densities most of the population is in the ground level 3P_0 as shown in Table 6. Since we are interested mostly in intensity ratios, absolute level populations are not needed. Therefore, N_j in Equation (1) represents fractional level population which is defined as the level population divided by the total population in the ion. The sum of the five fractional level populations is equal to 1.0. As the electron density increases the population of 3P_1 increases, the 142.12 line increases in intensity, and therefore the ratio becomes density sensitive.

These calculations were applied to flare spectra obtained from OSO-5. From the $I(142.14)/I(128.73)$ intensity ratios, Mason et al. (1979) concluded that N_e was $< 2 \times 10^{12} \text{cm}^{-3}$ in flare B (1969 Feb. 25) and $< 5 \times 10^{12} \text{cm}^{-3}$ in flare E (1969 March 12).

Other C-like ions for which atomic data have been calculated are Ne V (Bhatia and Doschek 1993a), Mg VII (Bhatia and Doschek 1995), Si IX (Bhatia and Doschek 1993b), and Ca XV (Bhatia and Doschek 1993c), in addition to OIII (Bhatia and Kastner 1993) as mentioned earlier. The configurations used in the Superstructure and DW programs are $2s^2 2p^2$, $2s2p^3$, $2p^4$, $2s^2 2p3s$, $2s^2 2p3p$, and $2s^2 2p3d$. This set of configurations give rise to 46 fine-structure levels.

O III is particularly interesting because the He II 303.8 \AA resonance line, He II Ly α , coincides with the energy difference between the $2s^2 2p^2 P_2$ and $2s^2 2p3d P_2$ levels. Therefore, the He II line photoexcites the $2s^2 2p3d P_2$ from the lower 3P_2 level, producing a fluorescent cascade of visible and ultraviolet lines due to the decay of the photoexcited level. This cascade is through the levels of the $2p3p$

Table 5. Collision strengths between the levels of 142.14 and 128.73 Å

Transition	Collision strength		
	20 Ry	50 Ry	100 Ry
$^3P_0 \rightarrow ^3D_1$	0.1832	0.2157	0.2520
$^3P_1 \rightarrow ^3D_1$	0.0199	0.0222	0.0248
$^3P_0 \rightarrow ^3D_2$	0.0025	0.0019	0.0013
$^3P_1 \rightarrow ^3D_2$	0.3506	0.4116	0.4784

Table 6. Populations of levels in the ground configurations as a function of electron density^a

Level	Level population for $\log(N_e(\text{cm}^{-3})) =$						
	11.0	11.5	12.0	12.5	13.0	14.0	15.0
3P_0	9.67-1	9.06-1	7.75-1	5.80-1	3.77-1	1.45-1	9.84-2
3P_1	7.40-3	2.17-2	5.73-2	1.27-1	2.25-1	3.05-1	2.52-1
3P_2	2.56-2	7.16-2	1.66-1	2.86-1	3.71-1	3.95-1	3.68-1
1D_2	9.72-5	3.86-4	1.73-3	7.44-3	2.65-2	1.42-1	2.45-1
1S_0	5.34-6	1.84-5	6.90-5	2.73-4	1.10-3	1.34-2	3.72-2

^a Throughout in the tables, $a+b = a \times 10^b$

and 2p3s configurations. This is known as the Bowen fluorescence mechanism (Bhatia, Kastner, and Behring 1982). The statistical equilibrium equations are solved in the presence of the He II radiation field to obtain level populations and then intensities of various lines are calculated using Equation (1). A convincing proof of this process comes from the fact that the 303.63 Å line in the spectra of the Sun obtained by Behring et al. (1976) and the multiplet at 644 Å in the Skylab spectra obtained by Vernazza and Reeves (1978) would not have been seen in the absence of this mechanism (see Figure 4 in Bhatia et al. 1982). Also, the calculated intensity of the multiplet at 644 Å in the presence of photoexcitation agrees with the observed intensity. The primary cascade lines (i.e. lines originating from $2p3d\ ^3P_2$ to the levels of $2p3p$) are 3444.10, 3132.84, 2837.17, and 2819.57 Å and the secondary cascade lines (i.e. lines between the levels of $2p3p$ and $2p3s$) are 3759.87, 3340.75, 3312.30, 3299.36, 3047.13, and 3023.45 Å (Kastner et al. 1983).

There are non-photosensitive multiplets and their calculated intensities agree with the observations: the multiplet components at 508.18 and 703.85 Å agree with the observations of Behring et al. (1976) and the multiplets at 508, 526, 703, and 835 Å agree with the observations of Vernazza and Reeves (1978).

The ratio $I(3444)/I(5007)$ in planetary nebulae can be used to infer the photoexcitation rate P of the He II resonance line, the 3444 Å line being a Bowen line and the 5007 Å line an optically thin forbidden non-Bowen line. The line at 3444 Å is due to $2s^22p3d\ ^3P_2 \rightarrow 2s^22p3p\ ^3P_2$ and the line at 5007 Å is due to $2s^22p^2(^1D_2 \rightarrow ^3P_2)$. Having established P the electron density can be determined from the density sensitive infrared line ratio $I(88.3\mu\text{m})/I(51.8\mu\text{m})$. The line at 88.3 μm is due to $2s^22p^2(^3P_1 \rightarrow ^3P_0)$ and the 51.8 μm line due to $2s^22p^2(^3P_2 \rightarrow ^3P_1)$. Since 3P_2 is the upper level of the 51.8 μm line and the lower level of the pumped transition, the ratio is sensitive to P as well as to N_e which can both be determined by comparing calculated intensity ratios with observations (see Figures 1 and 2 in Bhatia and Kastner 1987).

The O III 374.436 Å line due to $2s^22p3s\ ^3P_1 \rightarrow 2s^22p^2\ ^3P_2$ can photoexcite the N III 374.441 and 374.434 Å lines but a comparison with solar and nebular observations indicates that this process plays a small role, unlike in O III. The quenching of the infrared 57.3 μm line, emitted in the ground configuration transition $2s^22p(^2P_{3/2} \rightarrow ^2P_{1/2})$, is due to photoexcitation from the $2s^22p\ ^2P_{3/2}$ level to

$2s^23d^2D_{5/2,3/2}$ levels. This is an indication of the presence of Bowen fluorescence in N III (Kastner and Bhatia 1984).

There are a number of ions for which Bowen fluorescence is possible and Kastner and Bhatia (1986) have suggested a general name of PAR-Photoexcitation by Accidental Resonance. This mechanism can be used to identify the presence of other ions, e.g. in the above case He II.

In the X-ray region, the Fe XXI emission lines in the 9.4 – 9.8 Å range were observed during an intense (GOES class M4.5) flare on 1985 July 2 with the Flat Crystal Spectrometer (FCS) on the Solar Maximum Mission (SMM) satellite (Fawcett et al. 1987). To infer electron density, Phillips et al. (1996) carried out a calculation using configurations $2s^22p^2$, $2s2p^3$, $2p^4$, $2s^22p4s$, $2s^22p4d$, $2s^22p5s$, and $2s^22p5d$. These configurations give rise to 42 fine-structure levels. The transitions for these X-ray lines along with their wavelengths, oscillator strengths, radiative transition rates, and collision strengths at three incident energies are given in Table 7, where 1, 2, and 3 refer to the levels $^3P_{0,1,2}$ arising from the $2s^22p^2$ configuration and 26, 27, 28, 30, and 31 refer to 1D_2 , 3F_3 , and $^3D_{1,2,3}$ arising from the $2s^22p4d$ configuration. Since the observed wavelengths are accurate to 0.001 Å, 0.049 Å has been added to the calculated wavelengths in order to identify the observed lines.

Table 7. Atomic data for Fe XXI X-ray lines.

Tr.(i-j)	$\lambda(\text{Å})$	$\omega_i f_{ij}$	$A_{ji}(\text{s}^{-1})$	$\Omega(110)$	$\Omega(220)$	$\Omega(330)$
1-28	9.476	2.55-1	6.37+12	0.0091	0.0150	0.0187
2-26	9.546	3.30-1	4.88+12	0.0132	0.0202	0.0250
2-28	9.541	4.01-2	9.91+11	0.0028	0.0027	0.0031
2-30	9.457	1.29-1	1.95+12	0.0051	0.0077	0.0095
3-27	9.585	3.50-1	3.67+12	0.0151	0.0215	0.0265
3-31	9.489	5.36-1	5.73+12	0.0201	0.0318	0.0397

A useful relation between the oscillator strength f_{ij} and the transition rate A_{ji} is given by

$$A_{ji} = \frac{6.670 \times 10^{15} \omega_i f_{ij}}{\lambda^2(\text{Å}) \omega_j} \quad (26)$$

where ω_i is the weight factor of the level i .

The complete atomic data set obtained for 42 fine-structure levels is used to solve the statistical equilibrium equations. The level populations of the lowest five levels $^3P_{0,1,2}$, 1D_2 , and 1S_0 agree very well with the close-coupling results of Conlon et al. (1992) as indicated in Figure 1 of Phillips et al. (1996). The calculated intensity ratios are compared with the observations in Table 8.

Table 8. Observed and theoretical wavelengths and intensities for Fe XXI

Let.	Observed			Calculated				
	$\lambda(\text{Å})$	Ident.	Int. Ratio	$\lambda(\text{Å})$	Ident.	Electron Density (cm^{-3})		
						10^{11}	10^{12}	10^{13}
A	9.455	—	0.080	9.457	2-30	0.003	0.014	0.087
B	9.476	1-28	1.000	9.476	1-28	1.001	1.005	1.032
C	9.482	3-31	0.163	9.489	3-31	0.015	0.088	0.408
D	9.542	2-28	0.138	9.541	2-28	0.155	0.155	0.159
E	9.548	2-30	0.146	9.546	2-26	0.100	0.133	0.370
F	9.587	3-27	0.080	9.585	3-27	0.078	0.127	0.346

The relative intensities of lines C and E are best fitted by a theoretical spectrum with electron density N_e more than 10^{12}cm^{-3} and a comparison of the calculated line spectra with the observed spectrum, given in Figure 5 of Phillips et al. (1996), also indicates a good fit at $N_e = 10^{12} \text{cm}^{-3}$.

The fact that the electron density in a flare can be so high is also borne out by Fe XXII lines at 8.976 Å (P) and 9.073 Å (Q and R) observed by the SMM FCS (Fawcett et al. 1987). The line P is due to the transition $2s^2 4d^2 D_{3/2} \rightarrow 2s^2 2p^2 P_{1/2}$, the line Q due to $2s^2 4d^2 D_{5/2} \rightarrow 2s^2 2p^2 P_{3/2}$, and the line R due to $2s^2 4d^2 D_{3/2} \rightarrow 2s^2 2p^2 P_{3/2}$. These lines are not blended with other lines. The observed intensity ratio $[I(Q)+I(R)]/I(P)=0.54\pm 0.03$. Mason and Storey (1980) carried out a DW calculation and concluded that $N_e=10^{13} \text{cm}^{-3}$.

Atomic data and spectral line intensities for the carbon isoelectronic sequence (Ar XIII through Kr XXXI) using $2s^2 2p^2$, $2s^2 2p^3$, $2p^4$, $2s^2 2p^3 s$, $2s^2 2p^3 p$, and $2s^2 2p^3 d$ configurations are given by Bhatia, Seely, and Feldman (1987).

6. Mg VI

Eight lines of Mg VI in the EUV range have been identified in the SERTS-89 data (Thomas and Neupert 1994). To identify these lines and also X-ray lines observed earlier by Behring et al. (1972), Bhatia and Young (1998) extended the earlier calculations of Bhatia and Mason (1980) who dealt with Mg VI, Si VIII, S X, Ar XII, and Ca XIV, by adding another configuration $2s^2 2p^2 3s$ to the configurations $2s^2 2p^3$, $2s^2 2p^4$, and $2p^5$. Collision strengths are calculated at five incident energies, 7, 10, 35, 50, and 85 Ry, and for incident partial waves up to 19. Proton rates within five levels, $^4S_{3/2}$, $^2D_{3/2,5/2}$ and $^2P_{1/2,3/2}$, of the $2s^2 2p^3$ configuration have been included in the calculation of intensities for $N_e=10^8$, 10^{10} , and 10^{12}cm^{-3} and $\log(T_e)=5.45$, 5.60, and 5.75K.

This model predicts lines at 387.77, 387.93, and 388.00 Å. Since the 388.00 Å line is the most intense of these three, the line observed at 387.955 Å is identified with the predicted 388.00 Å line due to $2s^2 2p^4^2 D_{1/2} \rightarrow 2s^2 2p^3^2 P_{3/2}$. The line observed at 349.162 Å is identified as a blend of the four predicted lines at 349.11, 349.12, 349.16, and 349.18 Å. Similarly, the observed line at 270.401 Å is identified with a blend of 270.39 and 270.40 Å. The observed intensity ratio of the lines 399.275 and 403.296 Å agrees with the predicted intensity ratio.

The observed X-ray lines (Behring et al. 1972) are 111.557 and 111.724 Å, 111.557 Å being the stronger of the two, in agreement with the calculations.

Atomic data for Ne IV have been calculated by Bhatia and Kastner (1988) by including configurations $2s^2 2p^3$, $2s^2 2p^4$, $2p^5$, $2s^2 2p^2 3s$, $2s^2 2p^2 3p$, and $2s^2 2p^2 3d$. These configurations give rise to 72 fine-structure levels. The multiplets at 358.7, 421.6, and 469.8 Å are found to be density sensitive at $\log(N_e(\text{cm}^{-3}))=6$ to 12 (see Figure 5 in Bhatia and Kastner 1988). The PAR process (Kastner and Bhatia 1986) mentioned above is possible in this ion because of excitation by a coincident wavelength of Fe XI.

Atomic data and spectral line intensities for the nitrogen isoelectronic sequence (Ar XII through Kr XXX) are given by Bhatia, Seely, and Feldman (1989). The calculations were carried out by including the configurations $2s^2 2p^3$, $2s^2 2p^4$, $2p^5$, $2s^2 2p^2 3s$, $2s^2 2p^2 3p$, and $2s^2 2p^2 3d$. This set of configurations gives rise to 72 fine-structure levels.

7. Fe XVII and resonance scattering

Neon-like Fe XVII is present in flares and solar active regions in a broad temperature range $(2-10)\times 10^6$ K because of the filled 2p shell. Strong resonance lines in the range 15-17 Å have been observed by McKenzie et al. (1980) and Phillips et al. (1982). The transitions of interest are $2s^2 2p^5 3d^1 P_1 \rightarrow 2s^2 2p^6^1 S_0$ at 15.02 Å and $2s^2 2p^5 3d^3 D_1 \rightarrow 2s^2 2p^6^1 S_0$ at 15.26 Å along with subordinate lines in the extreme-ultraviolet (EUV) region.

There have been a number of theoretical studies of the expected spectrum assuming optically thin conditions. Bhatia and Doschek (1992) carried out a DW calculation using seven configurations, $2s^2 2p^6$, $2s^2 2p^5 3s$, $2s^2 2p^5 3p$, $2s^2 2p^5 3d$, $2s^2 2p^6 3s$, $2s^2 2p^6 3p$, and $2s^2 2p^6 3d$, giving rise to 37 fine-structure levels. Collision strengths were calculated at five incident energies: 76.83, 91.53, 120.93, 179.73, and 253.23 Ry. Their collision strengths are in good agreement with those of Zhang et al. (1987), Zhang and Sampson (1989), and Hagelstein and Jung (1987). The level populations and intensity ratios were calculated as a function of electron density and temperature.

The Fe XVII level structure is distinguished in having all the excited levels much higher than the single ground level 1S_0 , implying that even at high electron densities most of the ion population is in the ground level. The EUV lines have been observed in solar flare spectra recorded by a Naval Research Laboratory slitless spectrograph flown on the Skylab manned space station in 1973 (Feldman et al. 1985; Doschek, Feldman and Bhatia 1991). The predicted relative intensities of these lines at $N_e=10^{11} \text{ cm}^{-3}$ and $T_e=4 \times 10^6 \text{ K}$ agree fairly well with the observed relative intensities, which are accurate to within 30%.

For optically thin plasma, the ratio $I(15.02)/I(15.26)$ according to the calculation is 4.8, while the observed (McKenzie et al. 1980; Phillips et al. 1982) ratio is 2.75 ± 0.7 and the experimental value of Brown et al. (1998) using Electron Beam Ion Trap (EBIT) is 3.04 ± 0.12 . The observed intensity ratios of various lines do not agree with the optically thin calculated intensity ratios and it is clear that these lines suffer resonance scattering as suggested by Rugge and McKenzie (1985). Resonance scattering implies that the emitted photon is absorbed and reemitted but not necessarily in the line of sight, so, there can be an apparent loss of flux although the total flux integrated over 4π remains unchanged.

The optical depth at the line center is given by

$$\tau_0 = \int k_0 dl = \frac{\pi e^2}{m_e c} f(N_1 L) \phi(\nu) \quad (27)$$

where k_0 is the absorption coefficient, f the oscillator strength, $N_1(\text{cm}^{-3})$ the population of the ground state, $L(\text{cm})$ the path length; neglecting nonthermal velocities, the Gaussian line profile function at the line center is

$$\phi(\nu) = \lambda(\text{cm}) \sqrt{\frac{m_{ion}}{2\pi k T_{ion}}} = \frac{1}{\sqrt{\pi} \Delta \nu_{thin}} = \frac{1}{\sqrt{\pi} \Delta \nu_D} \quad (28)$$

where m_{ion} is the ion mass in amu units and T_{ion} is the ion temperature which can be taken equal to T_e .

$$\tau_0 = \frac{\sqrt{\pi} e^2}{m_e c} f \lambda \sqrt{\frac{m_{ion}}{2k T_e}} (N_1 L) \quad (29)$$

$N_1 L(\text{cm}^{-2})$ is the column length, which can be taken out of the integral for the uniform case. It can be shown that

$$\tau_0 = 1.161 \times 10^{-14} f \lambda (\text{\AA}) \sqrt{\frac{M}{T_e}} (N_1 L) \quad (30)$$

It should be noted that τ_0 is a function of electron temperature and M is the atomic mass number. For $T_e=4 \times 10^6 \text{ K}$ and $M=56$ for Fe, we find

$$\frac{\tau_0}{(N_1 L)} = 4.35 \times 10^{-17} f \lambda \quad (31)$$

Table 9 from Table 3 of Bhatia and Kastner (1999) gives λ , f , A , and $\tau_0/N_1 L$ for transitions originating from the $3s$, $3p$, and $3d$ levels at $T_e = 4 \times 10^6 \text{ K}$.

The forbidden magnetic quadrupole line $2p^5 3s(^3P_2) \rightarrow 2p^6(^1S_0)$ at 17.10 \AA has been included because it can be intense due to overpopulation of the 3P_2 level. It is seen from the table that the 15.02 \AA line has $\tau_0 \simeq 2$ for $N_1 L = 10^{15} \text{ cm}^{-2}$ due to the large oscillator strength, and therefore can suffer resonance scattering, i.e. loss of flux.

The simplest way to take into account optical depth effects is to multiply the transition rates by constant escape probabilities. Various approximate treatments, e.g. Phillips et al. (1996) and Saba et al. (1999) have been carried out to interpret observations of the disk center to limb intensity variation. Saba et al. used the escape probability method of Kastner and Kastner (1990) and concluded that the intensity of the 15.02 \AA line is a factor of 2 to 3 lower than the predicted optically thin value. It is very unlikely that other processes like dielectronic recombination, inner-shell ionization, polarization of lines, etc. will remove the discrepancy between observations and calculations.

These studies indicate that the strongest line at 15.02 \AA can have significant optical depth in solar active regions and in flares.

Table 9. Fe XVII Resonance lines and forbidden line 17.10 Å

Upper Level ^a	$\lambda(\text{Å})$	f	$A(s^{-1})$	τ_0/N_1L
$2p^53s^3P_2$	17.10	4.8	1.69+5	0.0
$2p^53s^1P_1$	17.05	0.123	9.44+11	7.50-17
$2p^53s^3P_1$	16.78	0.101	8.00+11	8.98-17
$2p^53d^3P_1$	15.45	0.089	8.27+10	5.96-18
$2p^53d^3D_1$	15.26	0.593	5.69+12	3.94-16
$2p^53d^1P_1$	15.02	2.662	2.64+13	1.74-15
$2s2p^63p^1P_1$	13.82	0.275	3.21+12	1.66-16

^a Lower level is ground level $2p^6^1S_0$.

Recently, Bhatia and Kastner (1999) solved Equation (2) for $T_e = 4 \times 10^6 \text{K}$ and $N_e = 10^{11} \text{cm}^{-3}$ iteratively by multiplying transition rates by escape factors appropriate to the chosen geometry and emergent intensities by monodirectional escape probabilities.

The Doppler-profile escape factor for slab geometry has been given by Capriotti (1965) as

$$SEF(\tau) = 1 - (0.8293)\tau + (0.7071)\tau \ln(2\tau) + \sum_{k=1}^{\infty} \frac{(-1)^k (2\tau)^{2k+1}}{k(k+2)!(k+2)^{1/2}} \quad (32)$$

for $\tau \leq 2.5$, and

$$SEF(\tau) = \frac{((\ln(2\tau))^{1/2} + 0.25(\ln(2\tau))^{-1/2} + 0.14)}{(2\sqrt{\pi}\tau)} \quad (33)$$

for $\tau > 2.5$. The monodirectional single-flight or free-flight photon escape probability, assuming a constant source function, is given by (Kastner and Kastner 1990) as

$$p_f(D, \tau; 1) = (\sqrt{\pi}\tau)^{-1} \int_{-\infty}^{\infty} (1 - \exp(-\tau \exp(-x^2))) dx \quad (34)$$

where the dimensionless frequency variable $x = (\nu - \nu_0)/\Delta\nu_D$. The escape probability, expressed as a logistic function, is given by

$$p_f(D, \tau; 1) = \frac{1}{1 + \exp(b(\log(\tau) - c))} \quad (35)$$

where $b=2.410527$ and $c=0.3950445$. The present analysis is valid for lines which are not self-reversed, i.e. $0 < \tau < 10$. Similar expressions are given for cylindrical geometry by Bhatia and Kastner (1999) and in this case $b=2.3212136$ and $c=0.22335545$ in expression (35). The emergent intensity for an optically thick plasma is decreased from the optically thin value and is now given by

$$I_{ji} = N_j A_{ji} \Delta E_{ij} p_f(D, \tau; 1) = I_{ji}(\text{optically thin}) p_f(D, \tau; 1) \quad (36)$$

Equation (2) becomes nonlinear (see Equations (1) and (2) in Bhatia and Kastner 1992) in level populations when the optical depth effects are included and then the equations have to be solved non-iteratively or by the Newton-Raphson method (Bhatia and Kastner 1992). Both the methods give the same results. It is found that the upper level populations of the resonance lines increase with the column length; variation of the upper level $2p^53d^1P_1$ of the most optically thick resonance line at 15.02 Å at $T_e=4 \times 10^6 \text{K}$ and for $N_e=10^9, 10^{10}$, and 10^{11}cm^{-3} is shown in Figure 2 taken from Bhatia and Kastner (1999).

The level population increases by a factor of 1000 at a column length of 10^{21}cm^{-2} compared to its optically thin value.

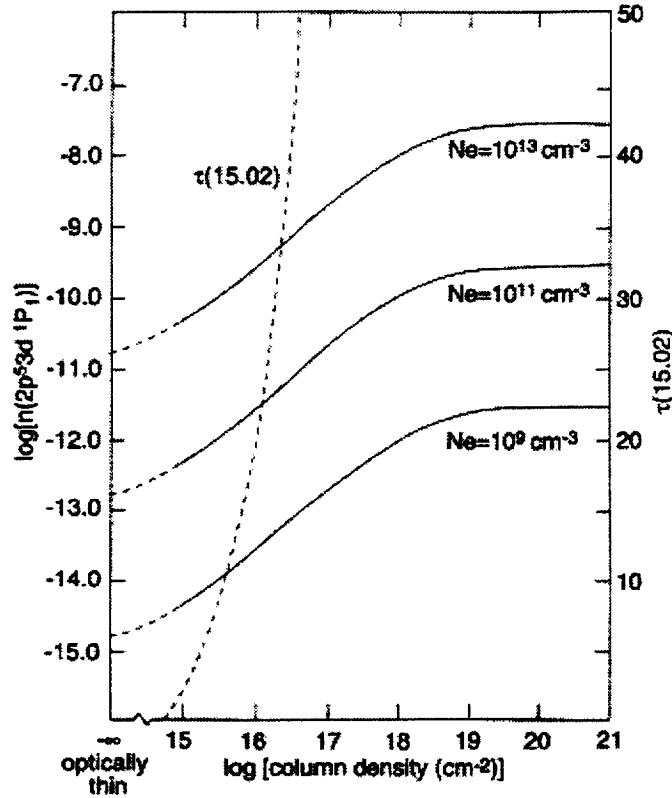


Figure 2. Variation of the population of the upper level $2p^5 3d(^1P_1)$ of the 15.02 Å resonance line, with increasing column density of Fe XVII.

The calculated photon fluxes of the six resonance lines listed in Table 9 relative to the reference line at 17.10 Å are given in Table 10 for active regions ($T_e=4 \times 10^6$ K and $N_e=10^{11}$ cm $^{-3}$) for the plane-parallel (slab) geometry.

Similar tables are given in (Bhatia and Kastner 1999) for flare temperatures and cylindrical geometry. It is seen from Table 10 that all resonance lines show an initial increase in flux relative to the forbidden line as the column density increases. Also, intensities of the 15.02 and 15.26 Å lines with respect to the 16.78 Å line, due to $2p^5 3s\ ^3P_1 \rightarrow 2p^6\ ^1S_0$, first increase with column density and then decrease (see Figures 3 and 4 from Bhatia and Kastner 1999), contrary to conventional wisdom which holds that the intensities of resonance lines always decrease with an increase of optical depth. This should be relevant for interpretation of future observations.

As expected, all the EUV lines originating from 3d levels are also affected by the opacity as indicated in Table 11 (for $T_e=4 \times 10^6$ K and $N_e=10^{11}$ cm $^{-3}$; see also Figure 4 of Bhatia and Kastner 1999). Eleven lines at 193.7, 226.1, 240.4, 243.0, 295.98, 324.5, 340.1, 351.6, 358.24, 373.41, and 387.23 Å increase in intensity with respect to the 254.9 Å line with an increase in column length, reaching saturation values at a column length of 10^{21} cm $^{-2}$. The magnetic dipole transition $2p^5 3s(^3P_0 - ^1P_1)$ at 1153.2 Å is also enhanced by opacity.

Wood and Raymond (2000), using a 3D Monte Carlo radiation transfer code, have investigated the effects of resonance scattering of emission lines on the emergent fluxes from coronal loop structures. They find, depending on viewing angle, the emergent flux may be lower or higher than the optically thin prediction due to scattering out of or into the line of sight.

For a source which is uniform over the field of view and along the line of sight, an estimate of the electron density can be made from the decrease in the flux of the resonance line (Schmelz et al. 1992).

Table 10. X-ray photon flux ratios^a in slab geometry.

$\log(N_1 L(\text{cm}^{-2}))$	17.05	16.78	15.45	15.26	15.02	13.82
$-\infty$	0.176	0.0992	-0.933	-0.157	0.453	-1.086
13	0.177	0.100	-0.933	-0.153	0.465	-1.085
14	0.183	0.105	-0.932	-0.135	0.514	-1.076
15	0.216	0.134	-0.929	-0.0563	0.654	-1.032
16	0.336	0.243	-0.911	+0.0811	0.713	-0.921
17	0.473	0.378	-0.852	0.0698	0.689	-1.044
18	0.597	0.465	-0.958	-0.147	0.466	-1.652
19	0.712	0.551	-1.589	-0.808	-0.169	-2.572
20	0.727	0.561	-2.461	-1.705	-1.069	-3.517
21	0.733	0.566	-3.406	-2.657	-2.066	< -4

^a Entries are $\log[F(\lambda)/F(17.10)]$; column headings are line wavelengths (\AA)

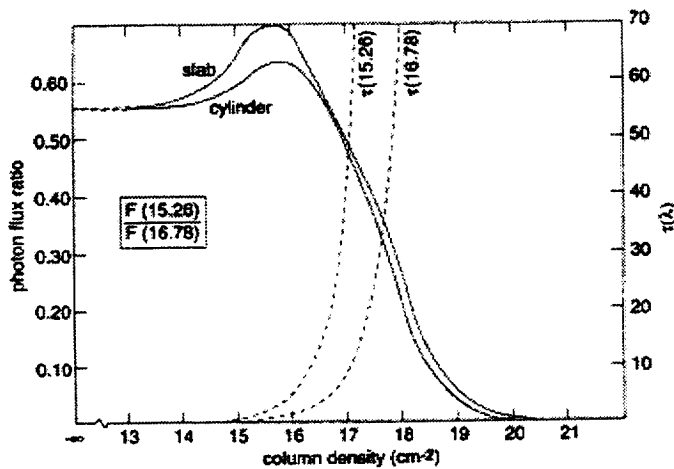


Figure 3. Column density dependence of the the 15.02 \AA resonance line photon flux in slab and cylindrical geometry, relative the flux of the 16.78 \AA line.

The number density can be written as

$$N_1 = \frac{N_1}{N(\text{FeXVII})} \frac{N(\text{FeXVII})}{N(\text{Fe})} \frac{N(\text{Fe})}{N(\text{H})} \frac{N(\text{H})}{N_e} N_e \quad (37)$$

Since most of the population is in the ground state, $N_1/N(\text{FeXVII}) = 1$; taking $N(\text{FeXVII})/N(\text{Fe}) = 0.776$ (Arnaud and Rothenflug 1985), $N(\text{Fe})/N(\text{H}) = 10^{-4}$ (which is 4 times the photospheric abundance; Feldman 1992), and $N(\text{H})/N_e = 0.8$ in regions where hydrogen is mostly ionized, Equation (37) gives

$$N_1 = 0.6208 \times 10^{-4} N_e \quad (38)$$

Using Equation (31), we have for the 15.02 \AA line

$$\tau_0 = 1.080 \times 10^{-19} N_e L = 1.080 \times 10^{-19} \frac{EM}{N_e} \quad (39)$$

where the column emission measure EM is defined as

$$EM = \int N_e^2 dl \quad (40)$$

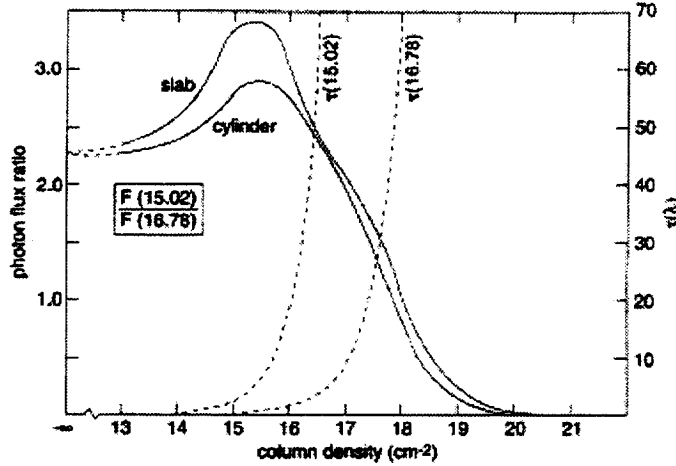


Figure 4. Column density dependence of the the 15.26 Å resonance line photon flux in slab and cylindrical geometry, relative the flux of the 16.78 Å line.

From Schmelz et al. (1992), for NOAA active region 4891, $\log(\text{EM})=29.17$. This gives

$$\tau_0 = 1.598 \times 10^{10}/N_e \quad (41)$$

A flux decrease of a factor of 2 implies that the monodirectional escape probability=0.5 which from Kastner and Kastner (1990) or Equation (35) means $\tau_0=2.512$. This gives $N_e = 6.36 \times 10^9 \text{cm}^{-3}$, a plausible value for the electron density.

We considered here only monodirectional escape probability $p_f(D, \tau; 1)$ from a uniformly emitting source (homogeneous) while there is a corresponding escape probability $p_f(D, \tau; 0)$ for a source in which emitting and absorbing ions are spatially separated (inhomogeneous), see Kastner and Kastner (1990) for more details.

Even though $I(15.02)/I(17.10)$ and $I(15.02)/I(17.05)$ are sensitive to electron temperature they cannot be used for temperature diagnostics because of the resonance scattering of the 15.02 Å line. Instead, Fe XVII X-ray lines in conjunction with Fe XVIII lines have been used for temperature diagnostics (Phillips et al. 1997). The relative abundance of Fe XVII to Fe XVIII required in the intensity ratio for temperature diagnostics (see Equations (2) and (8) in Phillips et al. 1997) is known. The intensity ratio of the strong Fe XVIII line at 16.073 Å due to $2p^4 3s^4 P_{5/2} \rightarrow 2p^5 \ ^2P_{3/2}$ to the Fe XVII 16.773 Å line is sensitive to T_e as indicated in Figure 5 of Phillips et al.

An unidentified line in the solar spectra of Parkinson (1975) was identified by Bhatia and Kastner (1985) as the electric quadrupole line at $2s^2 2p^5 3p \ ^3P_2 \rightarrow 2s^2 2p^6 \ ^1S_0$ at 16.33 Å in Fe XVII; this has been confirmed by Brown et al. (1998).

Atomic data and spectral line intensities for the neon isoelectronic sequence (Si V through Kr XXVII) are given by Bhatia, Feldman and Seely (1986b). The calculations included configurations $2s^2 2p^6$, $2s^2 2p^5 3s$, $2s^2 2p^5 3p$, and $2s^2 2p^5 3d$. These configurations give rise to 27 fine-structure levels.

8. Fe XV

Fe XV is of interest because X-ray lines in the range 53.07 to 73.94 Å from an M-class solar flare have been observed by Acton et al. (1985) with a high-resolution rocket-borne grazing incidence spectrograph telescope (XSST). Bhatia, Mason, and Blancard (1997) carried out a DW calculation using configurations $3s^2$, $3s3p$, $3p^2$, $3s3d$, $3p3d$, $3s4s$, $3s4p$, $3s4d$, $3s4f$, $3p4s$, $3p4p$, $3p4d$, and $3p4f$, giving rise to 78 fine-structure levels. Energy levels, transition rates, and collision strengths at incident electron energies of 25, 50, and 75 Ry were calculated and statistical equilibrium equations were solved for level

Table 11. Relative intensities^a of EUV lines enhanced by opacity^b.

$\lambda(\text{\AA})$	$-\infty$	16	17	18	19	20
193.7	<-4.0	-2.143	-1.219	-0.532	-0.276	-0.288
226.1	<-4.0	-1.785	-0.929	-0.232	+0.045	+0.092
240.4	<-4.0	-2.051	-1.127	-0.441	-0.217	-0.196
243.0	<-4.0	-2.193	-1.342	-0.663	-0.407	-0.419
296.0	-0.982	-0.965	-0.854	-0.560	-0.383	-0.395
324.5	<-4.0	-2.180	-1.256	-0.570	-0.313	-0.325
340.1	-1.038	-1.022	-0.915	-0.631	-0.428	-0.469
351.6	-1.293	-1.276	-1.170	-0.886	-0.712	-0.724
358.2	-0.905	-0.880	-0.733	-0.397	-0.290	-0.221
373.41	-1.235	-1.204	-1.017	-0.617	-0.438	-0.421
387.2	-1.138	-1.107	-0.920	-0.520	-0.341	-0.324
1154	-1.346	-1.325	-1.22	-0.865	-0.758	-0.689

^a Entries are $\log[F(\lambda)/F(254.9)]$; column headings are $\log(\text{column density})(\text{cm}^{-2})$

^b Cylindrical geometry

populations to calculate intensity ratios at $N_e=10^8, 10^9, 10^{10}, 10^{11},$ and 10^{12} cm^{-3} and $\log(T_e)=6.7\text{K}$. Results for four transitions are given in Table 12.

Table 12. Collision strengths and intensity ratios for a few transitions in Fe XV.

Transition	Collision Strengths			Intensity $\log T_e=6.7$
	25	50	75(Ry)	
$3s^2 \ ^1S_0 - 3s4s \ ^3S_0$	2.169-3	8.830-4	4.730-4	
$3s^2 \ ^1S_0 - 3s4s \ ^1S_0$	9.506-2	1.054-1	1.088-1	
$3s4s \ ^1S_0 - 3s3p \ ^1P_1$	1.739-2	3.646-2	5.179-2	3.88
$3s^2 \ ^1S_0 - 3s4p \ ^1P_1$	1.052-2	2.786-2	4.457-2	1.00

This calculation shows that the collision strengths for the monopole transition $3s^2 \ ^1S_0$ to $3s4s \ ^1S_0$ are very large. This results in appreciable intensity of the dipole-allowed line $3s4s \ ^1S_0$ to $3s3p \ ^1P_1$ at 69.74 \AA , consistent with the observed intensity of the unidentified line at 69.644 \AA .

The emission lines in Fe XV have also been observed by SERTS in an active region on the Sun. The 13-configuration calculation of Bhatia, Mason, and Blancard (1997) did not include $3d^2$ which resulted in a poor representation of the $3p^2 \ ^1S_0$ level. Therefore, Bhatia and Mason (1997) calculated atomic data using configurations $3s^2, 3s3p, 3p^2, 3s3d, 3p3d,$ and $3d^2$. Recently, Eissner et al. (1999) have carried out an R-matrix calculation using exactly the same set of configurations. The two calculations agree so far as the energy levels and transition rates are concerned because the same set of configurations was used in the Superstructure program. A comparison between collision strengths at 50 Ry, obtained in the DW approximation and R-matrix approach, for a few transitions chosen at random indicated in Table 13, shows that DW results are reliable.

The inclusion of resonances will certainly not give the same rate coefficients. But it is known that at high temperatures the contribution of resonances becomes less important and it can be seen in Figure 5 (taken from Eissner et al. 1999) that the effective collision strengths are not too different at the temperature of maximum abundance ($\log(T_e) = 6.4\text{K}$) of Fe XV compared to the DW results.

The level populations obtained using the DW and R-matrix rates agree very well. Using the DW atomic data, we calculated the intensity ratios of various extreme-ultraviolet (EUV) lines in Fe XV at $N_e=10^{11}, 10^{12},$ and 10^{13} cm^{-3} and compare them with those observed in active regions of the Sun by SERTS in Table 14.

Table 13. Comparison of collision strengths in Fe XV from DW and R-matrix calculations.

Transition	Bhatia and Mason	Eissner et al.
$3s^2\ ^1S_0 - 3s3p\ ^1P_1$	4.135	4.176
$3s3p\ ^3P_0 - 3s3d\ ^3D_1$	1.171	1.164
$3s3p\ ^3P_1 - 3p^2\ ^3P_2$	1.566	1.551
$3s3p\ ^3P_2 - 3s3d\ ^3D_3$	5.015	4.976
$3s3p\ ^1P_1 - 3p^2\ ^1S_0$	1.961	1.910

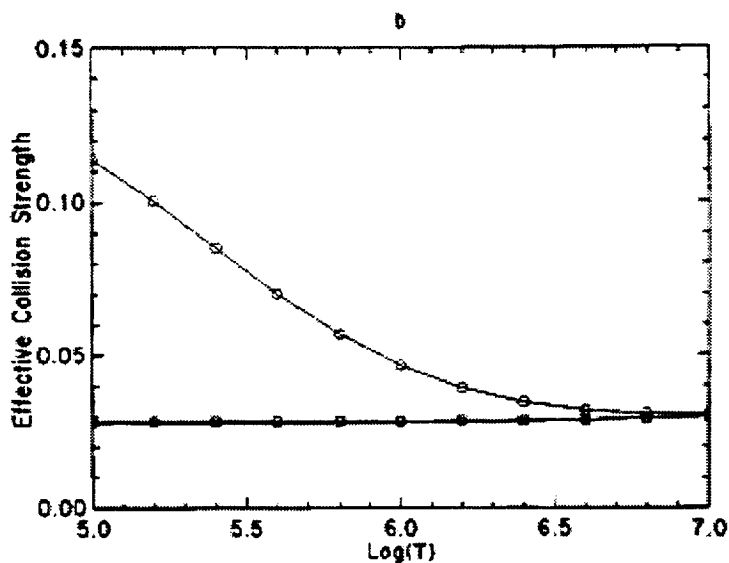


Figure 5. Comparison of the R-matrix (upper curve) and DW (lower curve) effective collision strengths of Fe XV vs. temperature.

The lines at 292.251 and 321.782 Å indicate a density of $N_e = 10^{11} \text{ cm}^{-3}$. It should be noted that, although Thomas and Neupert (1994) identified the 292.251 Å line as Si X, Young et al. (1998) have recently ascribed it to the Fe XV transition used in our analysis. The agreement with electron density we find using other Fe XV lines would tend to confirm this later identification.

9. Fe X

There are three famous lines: "green line" at 5303 Å in Fe XIV, "yellow line" at 5694 Å in CA XV, and "red line" at 6374 Å in Fe X in the Sun. The latter is a visible forbidden line in the ground configuration $3s^23p^5$ due to the transition $^2P_{1/2} \rightarrow ^2P_{3/2}$. Edlén, comparing such lines in the solar spectra to the laboratory spark spectra, concluded that the temperature of the solar corona is of the order of a million degrees. Strong EUV lines of Fe X have been observed in the solar spectrum of the full Sun obtained by Malinovsky and Heroux (1973) during a sounding rocket flight. Thomas and Neupert (1994) identified lines at 257.26 and 345.72 Å as Fe X lines in SERTS-89 flight. The most recent observations are the lines at 174.526, 175.265, 177.240, 184.534, 190.046, 220.862, and 257.246 Å from the SERTS-95 (Brosius et al. 1998), and with improved calibration of the lines at 174.5338 and 177.2477 Å (Brosius et al. 1999).

Bhatia and Doschek (1995a) calculated atomic data using $3s^23p^5$, $3s3p^6$, $3s^23p^43d$, and $3s3p^53d$ configurations in the SUPERSTRUCTURE and DW programs. These configurations give rise to 54 fine-

Table 14. Comparison of calculated intensities at $\log(T_e)=6.4\text{K}$ with observations^a.

Transition	$\lambda(\text{\AA})$	Observed	$\log N_e(\text{cm}^{-3})$		
			11	12	13
$3s3d\ ^1D_2 - 3s3p\ ^1P_1$	243.780	7.21-2	4.79-2	4.79-2	4.79-2
$3s3p\ ^1P_1 - 3s^2\ ^1S_0$	284.158	1.000	1.000	1.000	1.000
$3p^2\ ^3P_2 - 3s3p\ ^3P_1$	292.251	5.78-3	6.85-3	7.37-3	7.44-3
$3p^2\ ^3P_1 - 3s3p\ ^3P_2$	321.782	4.68-3	5.11-3	5.53-3	5.59-3
$3p^2\ ^1D_2 - 3s3p\ ^3P_2$	327.030	1.16-2	9.95-3	1.01-2	1.01-2
$3s3d\ ^3F_4 - 3s3d\ ^3D_3$	372.758	2.14-2	1.01-3	1.10-3	1.11-3
$3s3p\ ^3P_1 - 3s^2\ ^1S_0$	417.245	4.48-2	2.59-2	2.58-2	2.75-2

^aThomas and Neupert, ApJ Suppl. **91**, 461 (1994)

structure levels. Collision strengths were calculated at five incident energies (9, 18, 27, 36, and 45 Ry) and up to the total angular momentum $L^T=21$. They calculated level populations (at $\log(N_e(\text{cm}^{-3}))=8-12$ and $\log(T_e)=6\text{K}$) and intensity ratios of various lines by including proton impact excitation rates and solar background radiation.

They suggested that the four unidentified lines at 220.86, 238.71, 257.26, and 324.71 Å in the representative spectra in the atlas published by Feldman et al. (1987) as Fe X lines. A number of UV forbidden lines in the range 1000 to 3000 Å have been observed in solar spectra. In the line list published by Feldman and Doschek (1977a), the lines at 1582.60, 1603.31, 1611.7, and 1918.27 Å have been identified as Fe X lines. These identifications have been further confirmed by Bhatia and Doschek as Fe X lines from the intensity ratios they calculated.

The line at 257.26 Å is a blend of two lines from the transitions $3p^43d(^4D_{7/2,5/2} \rightarrow ^2P_{3/2})$ and the $\Delta J=2$ transition is a magnetic quadrupole transition. Therefore, the $^4D_{7/2}$ level can get much more populated than the $^4D_{5/2}$ level as indicated in Table 15 which gives level populations of the lowest five levels. This is a good example of a metastable level mentioned earlier.

Table 15. Level populations of the lowest five levels in Fe X.

configuration	Density Level	10^8	10^9	10^{10}	10^{11}	10^{12}
		Population				
$3s^23p^5$	$^2P_{3/2}$	0.983+00	0.912+00	0.708+00	0.600+00	0.585+00
	$^2P_{1/2}$	0.113-01	0.435-01	0.152+00	0.216+00	0.226+00
$3s3p^6$	$^2S_{1/2}$	0.213-10	0.205-09	0.187-08	0.179-07	0.178-06
	$^4D_{5/2}$	0.127-07	0.137-06	0.146-05	0.124-04	0.115-03
	$^4D_{7/2}$	0.106-02	0.843-02	0.289-01	0.318-01	0.295-01

These calculations did not included the resonance contribution. Young et al. (1996), including the resonance contribution for the ground transition $^2P_{3/2} \rightarrow ^2P_{1/2}$ from Pellan and Berrington (1995) in the above data, calculated the $I(257.26)/I(354.72)$ ratio at various N_e . Comparing to the observed ratio 1.2 (subflare) and 2.5 (active region loops) in the SERTS-89 spectra, they concluded that $N_e=2.5 \times 10^{10}$ and $2.0 \times 10^9 \text{ cm}^{-3}$ for the subflare and active region loops, respectively.

10. Fe VIII

A number of Fe VIII spectral lines in the range 130 to 190 Å have been observed under quiet solar conditions by a grazing-incidence spectrograph with a spectral resolution of 0.06 Å flown on Aerobee-200 rockets (Behring et al. 1972, 1976). The lines at 185.221 and 187.247 Å have been observed from

SERTS-95 flight (Brosius et al. 1998), the former is blended with a Ni XVI line. The same line has also been observed with the RES-K spectrograph on board KORONAS-I satellite (Zhitnik et al. 1998). Bhatia and Eissner (2000) have calculated atomic data using configurations $3p^6 3d$, $3p^5 3d^2$, $3p^6 4s$, $3p^6 4p$, and $3p^6 3d 4s$. These configurations give rise to 73 fine-structure levels. Collision strengths are calculated at 10, 30, 50, 70 Ry and for the total angular momentum L^T up to 33.

The level populations and intensities of various lines have been calculated at $\log(N_e(\text{cm}^{-3}))=8-14$ and $\log(T_e)=5.57\text{K}$. It is found that the forbidden infrared $5.447 \mu\text{m}$ line is a density insensitive line and is due to the transition $3p^6 3d(^2D_{5/2}) \rightarrow ^2D_{3/2}$. This line should be useful to determine properties of coronal magnetic fields by measuring the Zeeman effect or Faraday rotation. Such infrared lines are called coronal lines because they originate in the ground levels of ions produced at very high, i.e. coronal, temperatures.

The observed lines at 168.170 and 168.546 Å are due to the transitions $3p^5 3d^2 ^2D_{5/2} \rightarrow 3p^6 3d ^2D_{5/2}$ and $3p^5 3d^2 ^2P_{3/2} \rightarrow 3p^6 3d ^2D_{5/2}$ and their observed intensity ratio is $12/7=1.7$ which agrees well with the calculated ratio $0.0991/0.0527=1.9$ at $N_e=10^8 \text{cm}^{-3}$. The observed line at 168.929 Å due to the transition $3p^5 3d^2 ^2P_{1/2} \rightarrow 3p^6 3d ^2D_{3/2}$ has intensity comparable to that of the line at 168.546 Å but appears to be blended with a 2nd order line at 84.491 Å. The calculated intensity at $N_e=10^8 \text{cm}^{-3}$ is 0.035 which is less than the calculated value 0.0527 of the 168.546 Å line, in agreement with the observations that the line is blended. These line ratios are not sensitive to electron densities.

The lines at 159.705, 168.929, 186.599, and 256.981 Å with respect to the line at 168.173 Å are sensitive to electron density in the range $\log(N_e(\text{cm}^{-3}))=8$ to 10. The intensity ratio of the lines at 195.972 and 194.661 Å is sensitive to electron density in the same range.

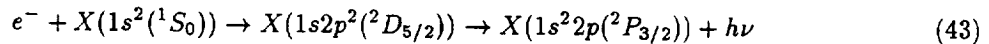
11. Determination of T_e

So far it has been assumed that T_e is known from the ionization balance. It is also possible to infer electron temperatures from temperature-sensitive allowed lines when they are observed for the same ion and do not differ too much in wavelength (to avoid large calibration uncertainties). Such lines, for example, are present in Mg II. Indicating $3s$, $3p$, and $3d$ levels by 1, 2, and 3, the intensity ratio of two emission lines from $3d \rightarrow 3p$ and $3p \rightarrow 3s$ in the absence of chromospheric radiation can be written as

$$\frac{I_{32}}{I_{21}} = \frac{\Delta E_{13} C_{13}}{\Delta E_{12} C_{12}} \propto \exp\left(\frac{\Delta E_{12} - \Delta E_{13}}{kT_e}\right) \quad (42)$$

Since $\Delta E_{13} \approx 2 \times \Delta E_{12}$ the ratio is sensitive to T_e . Feldman and Doschek (1977b) analyzed the Mg II spectra recorded by the NRL normal-incidence slit spectrograph on Skylab. These lines are emitted around 2800 Å within a few Å of each other. A comparison with observations indicates $T_e \leq 1.8 \times 10^4 \text{K}$ in the quiet Sun and active regions. This is in agreement with the predicted temperature of formation of Mg II based on the ionization equilibrium calculation of Jordan (1969).

Also, the intensity ratio of a satellite line formed due to dielectronic recombination to the allowed line can be used for temperature determination (Doschek 1985). The allowed line $w(1s2p ^1P_1 \rightarrow 1s^2 ^1S_0)$ is due to electron impact excitation of $1s^2 ^1S_0$ in He-like ions and the line $j(1s2p^2 ^2D_{5/2} \rightarrow 1s^2 2p^2 ^2P_{3/2})$ is a satellite line formed due to dielectronic recombination of an electron with a He-like ion:



The electron impact excitation of $^2D_{5/2}$ from the ground levels is not significant for Li-like ions. The intensity ratio is given by

$$\frac{I_j}{I_w} = \beta \frac{\exp((\Delta E_w - \Delta E_j)/kT_e)}{T_e} \quad (44)$$

where β is a function of transition rates, autoionization rates, and effective collision strength. ΔE_w is the energy separation between the levels of the line w and ΔE_j is the energy separation of the levels of the line j .

12. Database

Most of the atomic data calculated using the Superstructure and DW programs are available in the CHIANTI database (Young et al. 1998; Dere et al. 1997). Effective collision strengths for a number of ions obtained from DW or R-matrix calculations are given in Lang (1994).

13. Conclusions

A large number of DW calculations have been carried out over the years and just a few have been mentioned here. As the computational facilities improve so does the scope of the calculations: a larger number of configurations and incident partial waves can now be used in computing atomic data for an ion of interest. We have assumed a constant element abundance and a steady state coronal equilibrium condition in the calculations of intensities of various emission lines in spite of the doubts expressed by Feldman (1993). This is an interesting paper and questions the validity of a few other assumptions too. Physical properties can be inferred from a comparison of the calculated intensities with the observed ones. It is clear that the DW calculations are reasonably accurate for highly charged ions and at high electron temperatures. The Bowen fluorescence mechanism and optical depth effects can be considered in the calculation of line intensities. Unidentified lines in observed spectra can also be identified using such calculations. Most EUV and X-ray lines are emitted only when the plasma is at high temperatures and therefore the DW calculations should be suitable in such cases. Moreover, such calculations as discussed here are always required in the absence of experimental determination of all the enormous data needed to analyze the solar and astrophysical observations.

Acknowledgments. Thanks are extended to Dr. W. Eissner who, over the years, has been generous in making available to me the updated programs, and to Dr. J. L. R. Saba for helpful comments. This paper is dedicated to the memory of Dr. S. O. Kastner with whom I collaborated for a quarter of a century. His death in August, 1999 brought to an end a very fruitful association.

References

- Acton, L.W., Bruner, M.E., Brown, W.A., Fawcett, B.C., Schweizer, W., and Spear, R.J. 1985, *ApJ* 291, 965.
- Arnaud, M. and Rothenflug, R. 1985, *ApJS* 60, 425.
- Behring, W.E., Cohen, L. and Feldman, U. 1972, *ApJ* 175, 493.
- Behring, W.E., Cohen, L., Feldman, U. and Doschek, G.A. 1976, *ApJ* 203, 521.
- Bhatia, A.K. and Doschek, G.A. 1992, *ADNDT* 52, 1.
- 1993, *ADNDT* 53, 195.
- 1993a, *ADNDT* 55, 315.
- 1993b, *ADNDT* 55, 281.
- 1993c, *ADNDT* 55, 195.
- 1995, *ADNDT* 60, 145.
- 1995a, *ADNDT* 60, 97.
- Bhatia, A.K. and Eissner, W. 2000, *ADNDT* (submitted)
- Bhatia, A.K., Feldman, U., and Seely, J.F. 1985, *ADNDT* 32, 435.
- 1986, *ADNDT* 35, 319.
- 1986a, *ADNDT* 35, 449.
- 1987, *ADNDT* 36, 453.
- Bhatia, A.K. and Kastner, S.O. 1985, *Solar Phys.* 96, 11.
- 1988 *ApJ* 332, 1063.
- 1992, *ApJS* 79, 139.
- 1993, *ADNDT* 54, 133.

- 1999, *ApJ* 516, 482.
- Bhatia, A.K., Kastner, S.O. and Behring, W.E. 1982, *ApJ* 257, 998.
- 1983, *ApJS* 53, 129.
- Bhatia, A.K. and Mason, H.E. 1980, *MNRAS* 190, 925.
- 1997, *ADNDT* 66, 119.
- Bhatia, A.K., Mason, H.E., and Blancard, C. 1997, *ADNDT* 66, 83.
- Bhatia, A.K. and Thomas, R.J. 1998, *ApJ* 497, 483.
- Bhatia, A.K., Seely, J.F. and Feldman, U. 1987, *ADNDT* 36, 453.
- 1989, *ADNDT* 43, 99.
- Bhatia, A.K. and Young, 1998, *ADNDT* 68, 219.
- Brickhouse, N.S., Raymond, J.C. and Smith, B.W. 1995, *APJS* 97, 551.
- Brosius, J.W., Davila, J.M., and Thomas, R.J. 1998, *ApJS* 119, 225
- Brosius, J.W., Thomas, R.J. and Davila, J.M. 1999, *ApJ* 526, 494
- Brown, G.V., Beiersdorfer, P., Liedahl, D.A., and Widman, K. 1998, *ApJ* 502, 1026.
- Burgess, A. and Sheorey, V.B. 1974, *J. Phys. B* 7, 2403.
- Capriotti, E.R. 1965, *ApJ* 142, 1101.
- Colon, E.S. Keenan, F.P. and Aggarwal, K.M. 1992, *Phys. Scripta* 46, 518.
- Cook, J.W., Keenan, F.P., Bhatia, A.K. 1994, *ApJ* 425, 861.
- Dere, K.P., Landi, E., Mason, H.E., Monsignori Fossi, B.C., and Young, P.R. 1997, *A&AS* 125 149.
- Doschek, G.A. 1985, in "Autoionization, Recent Developments and Applications" (A. Temkin ed.), Chap. 6, Plenum Press, New York.
- Doschek, G.A., Feldman, U. and Bhatia, A.K. 1991, *Phys. Rev. A* 43, 2565
- Eissner, W. 1998, *Compt. Phys. Commun.* 114, 295.
- Eissner, W., Galavis, M.E., Mendoza, C. and Zeippen, C.J. 1999, *A&AS* 137, 165.
- Eissner, W., Jones, M. and Nussbaumer, H. 1972, *Compt. Phys. Commun.* 8, 270.
- Eissner, W. and Seaton, M.J. 1979, *J. Phys. B* 5, 2187.
- Fawcett, B.C., Jordan, C., Lemen, J.R., and Phillips, K.J.H. 1987, *MNRAS* 225, 1013.
- Feldman, U. 1992, *Physica Scripta* 46, 202.
- 1993, *Physica Scripta* T47, 128.
- Feldman, U. and Doschek, G.A. 1977a, *J. Opt. Soc. Am.* 67, 726.
- 1977b, *ApJ* 212, L147.
- Feldman, U., Doschek, G.A. and Seely, J.F. 1985, *MNRAS* 212, 41P
- Feldman, U., Purcell, J.D. and Dohne, B. 1987, Special NRL publication, available from NRL, Library of Congress Card Catalog No. 87-63602
- Hagelstein, P.L. and Jung, R.K. 1987, *ADNDT* 37, 121.
- Harrison, R.A. et al. 1995 *Solar Phys.* 162, 233.
- Huang, L.K., Lippman, S., Yu, T.L., Stratton, B.C., Moos, H.W., Finkenthal, M., Hodge, W.L., Rowan, W.L., Richards, B., Phillips, P.E. and Bhatia, A.K. 1987, *Phys. Rev. A* 35, 2919.
- Jordan, C. 1969, *MNRAS* 142, 501.
- Judge, P.G. 1998, *ApJ* 500, 1009.
- Kastner, S.O. and Bhatia, A.K. 1979, *A&A* 71, 211.
- 1984, *ApJ* 287, 945.
- 1986, *Comments on Atomic and Molecular Physics* 18, 39.
- 1987, *Physical Scripta* RS5, 76.
- Kastner, S.O., Behring, W.E. and Bhatia, A.K. 1983, *ApJS* 53, 129.
- Kastner, S.O. and Kastner, R.E. 1990, *JQSRT* 44, 275.
- Lang, J. 1994, (Special Editor), *ADNDT* 57, 1.

- Mason, H.E. Doschek, G.A., Feldman, U. and Bhatia, A.K. 1979, *A&A* 73, 74.
Mason, H.E. and Storey, P.J. 1980, *MNRAS* 191, 631.
McKenzie, D.L., Landecker, P.B., Broussard, R.M., Rugge, H.R. and Young, R.M. 1980, *ApJ* 241, 409.
Molinovsky, M. and Heroux, L. 1973, *ApJ* 181, 1009.
Parkinson, J.H. 1975, *Solar Phys.* 42, 183.
Pellan, J. and Berrington, K.A. 1995, *A&AS* 110, 209.
Phillips, K.J.H., Bhatia, A.K., Mason, H.E. and Zarro, D.M. 1996, *ApJ* 466, 549.
Phillips, K.J.H., Greer, C.J., Bhatia, A.K., Coffey, I.H., Barnsley, R. and Keenen, F.P. 1997, *A&A* 324, 381.
Phillips, K.J.H., et al. 1982, *ApJ* 256, 774.
Phillips, K.J.H., Greer, C.J., Bhatia, A.K. and Keenen, F.P. 1996, *ApJ* 469, L57.
Rugge, H.R. and McKenzie, D.L. 1985, *ApJ* 297, 338.
Saba, J.L.R., Schemlz, J.T., Bhatia, A.K. and Strong, K.T. 1999, *ApJ* 510, 1064.
Saraph, H.E. 1978, *Compt. Phys. Commun.* 15, 247.
Saraph, H.E. and Eissner, W. 2000, *Compt. Phys. Commun.* (to be published)
Schmelz, J.T., Saba, J.L.R. and Strong, K.T. 1992, *ApJ* 398, L118.
Thomas, R.J. and Neupert, W.M. 1994, *ApJS* 91, 461.
Vernazza, J.E. and Reeves, E.M. 1978, *ApJS* 37, 485.
Wood, K. and Raymond, J. 2000, *ApJ* (accepted)
Young, P.R., Landi, E., and Thomas, R.J. 1998, *A&A* 329, 291.
Young, P.R., Mason, H.E., Bhatia, K.A., Doschek, G.A. and Thomas, R.J. 1996, *Proceedings of IAU* No. 152, Eds. Bowyer and Malina, p.583
Zhang, H. and Sampson, D.H. 1989, *ADNDT* 43, 1.
Zhang, H., Sampson, D.H., Clark, R.E.H., and Mann, J.B. 1987, *ADNDT* 37, 17.
Zhitnik, I.A., Kuzin, S.V., Oraevskii, V.N., Pertsov, A.A., Sobel'man, I.I., and Urnov, A.M. 1998, *Astron. Lett.* 24, 819.



The RmaX Network: R-matrix calculations for X-ray atomic processes

Keith A Berrington¹

School of Science and Mathematics,

Sheffield Hallam University, Sheffield S1 1WB, UK.

Abstract. The RmaX network ('R-matrix for X-rays') has been formed to calculate using ab-initio R-matrix techniques electron and photon collisional properties to higher precision than hitherto for transitions in the soft X-ray region, to improve understanding of the dynamics of X-ray transitions in astrophysical plasmas.

New opportunities are arising with the launch of the new generation X-ray observatories such as *Chandra* and *XMM*. A significant amount of theoretical work on atomic collisional processes is in train for these major space projects. Such work includes gathering and assessing existing data, and the generation of atomic data to higher accuracy and new data where appropriate.

The RmaX Network is an international partnership formed to manage the calculation of the new data, and follows previous successful projects, namely the Opacity Project (OP) for calculating radiative opacities (The Opacity Project Team 1995) and the Iron Project (IP) for collisional data for metal ions (Hummer et al. 1993). The name 'RmaX' refers to the use of ab-initio R-matrix methods (Burke and Berrington 1993) in the computation of atomic data for X-ray transitions.

What atomic data are required? X-ray emitting plasmas may be divided into two broad categories:

- Hot ($10^6 - 10^8\text{K}$), and maintained at a high degree of ionization by electron collisions (e.g. stellar coronae and shocked regions). In a 'coronal' plasma, line excitation is principally by electron collisions while the ionization state is determined by collisional ionization and dielectronic recombination. In this case K- and L-shell collisional processes predominate, although excitation to higher valence shells may be important also.
- Cool ($10^4 - 10^5\text{K}$) and ionized by some energetic photon source (e.g. AGN, XRB, CV). In these X-ray photoionized plasmas, line excitation is by a mixture of collisional excitation and recombination and cascading, while the ionization state depends upon photoionization by energetic photons and low temperature recombination. For this case, K- and L-shell photoionization predominates and excited state recombination coefficients may be derived from valence shell photoionization cross-sections. The ionization of metallic ions by energetic photons is also important in understanding the opacity of the ISM to X-rays, and in this case the absorption may be by inner-shell processes in near neutral species.

How are these data to be calculated?

One of the most widely used, and perhaps most fully developed, of the sophisticated models available to atomic physics today is the R-matrix approach. This is essentially a basis function approach, in which the wavefunction $\Psi(E)$ for an electron interacting with an N-electron target is expanded in a many-electron basis in a local region, while outside the system is reduced to a simple potential scattering

¹On behalf of the Iron Project and RmaX teams: N Badnell (Strathclyde University), M Bautista (NASA GSFC), K A Berrington (Sheffield Hallam University), K Butler (Munich University), M Chidichimo (Waterloo University), W Eissner (Stuttgart University), D G Hummer (Boulder), H E Mason (Cambridge University), M E Galavis and C Mendoza (IVIC Caracas), S N Nahar and A K Pradhan (Ohio State University), H E Saraph, M J Seaton and P J Storey (University College London), J A Tully (Observatoire de la Côte d'Azur Nice), C J Zeippen (Observatoire de Paris Meudon)

problem. In each case the Schrödinger equation is used:

$$\Psi(E) = \sum_k A_k(E) \psi_k, \quad H_{N+1} \Psi(E) = E \Psi(E)$$

$$H_{N+1} = \sum_{n=1}^{N+1} \left[\frac{1}{2} \nabla_n^2 - \frac{Z}{r_n} + \sum_{m>n}^{N+1} \frac{1}{|r_n - r_m|} \right] + H_{\text{Breit-Pauli}}$$

The strength of the R-matrix method is that the ψ_k basis is energy independent, so that a single diagonalization of the internal-region Hamiltonian in this basis yields the expansion coefficients and wavefunctions at all energies – a vital advantage when physical properties are required over a large energy range. The R-matrix method is therefore an accurate general purpose method for the calculation of optical and electron-ion properties, including collisional excitation, photoionization and bound-state properties such as energy levels and transition probabilities. All of these properties can be obtained in intermediate coupling, incorporating relativistic effects through the use of the Breit-Pauli R-matrix method, as implemented in the R-matrix programs (Hummer et al 1993; Scott and Taylor 1982; Berrington et al 1995).

New directions in R-matrix models are concerned with ‘discretising’ the continuum, such that ionization can be described as an excitation process involving discrete states in the continuum (Berrington et al. 1997; Berrington and Nakazaki 1998). In the case of photoionization, these procedure allows for the investigation of soft X-ray ionization of atoms by ejection of the inner-shell electron(s).

Indeed, the optical properties of atoms and ions in X-ray fields are dominated by the inner-shell ‘edge’, where the cross section for photoionization for example can rise abruptly, often by at least an order of magnitude. The usefulness of the R-matrix method is that resonances, which modify the inner-shell ‘edge’ with quantum mechanical interference, are modelled ab initio, giving a highly accurate picture of the edge. In laboratory experiments on simple atoms R-matrix calculations are already modelling experiments to high accuracy (Berrington et al. 1997; Berrington and Nakazaki 1998). This confirmation by benchmarking of theory against experiment and observation is an essential part of the RmaX network, for scientific reliability.

We have identified four main tasks which define the goals of this proposal.

1. Electron impact excitation involving K- and L-shells of Fe ions. This includes inner-shell excitation as well as excitation to higher valence shells, neither of which was included in the Iron Project (which dealt with atomic data for IR, optical, UV and EUV transitions). These data will treat the problem of excitation in the “coronal” plasmas.
2. Photoionization of K- and L-shell electrons in light elements, C, N, O and Ne as well as in Fe ions. These data are required to treat the problems of ionization in the X-ray photoionized plasmas (e.g. AGN), as well as that of the X-ray opacity of the ISM.
3. Radiation damping and total dielectronic photorecombination rates. The aim here is two-fold: to include radiation damping in the excitation and photoionization cross sections obtained as above and to provide photorecombination data for Fe ions for use in calculating the ionization equilibrium of the ‘coronal’ plasmas.
4. Radiative transitions for fine-structure levels. We are extending our Opacity Project techniques to intermediate coupling, to obtain accurate and complete data sets of transition probabilities for fine-structure levels for the ions referred to above. These data are needed to carry out accurate level population calculations for heavy, or highly-ionized systems.

Finally, we aim to interface with the needs of the X-ray astrophysical community, in the provision of the new atomic data to the community via atomic databases and inclusion of the data in emission analysis codes.

References

Berrington, K.A., Eissner, W., and Norrington, P.H. 1995, *Comput. Phys. Commun.* 92, 290.

- Berrington, K.A. and Nakazaki, S. 1998, *J. Phys.* B31, 313.
- Berrington, K.A., Pelan, J.C., and Quigley, L. 1997, *J. Phys.* B30, 4973.
- Burke, P.G. and Berrington, K.A. (eds) 1993, "Atomic and molecular processes: an R-matrix approach" (Institute of Physics Publishing) ISBN 0-7503-0199-6.
- Hummer, D.G., Berrington, K.A., Eissner, W., Pradhan, A.K., Saraph, H.E., and Tully, J.A. 1993, *A&A* 279, 298.
- The Opacity Project Team, *The Opacity Project Volumes 1 & 2* (Institute of Physics Publishing) ISBN 0 7503 0288 7 (1995)
All data are available from TOPbase, access via web or telnet: european site at CDS Strasbourg, telnet 130.79.128.5; american site at the HEASARC GSFC, telnet 128.183.126.111; at either site, username=topbase, password=Seaton+
- Scott, N.S. and Taylor, K.T. 1982, *Comput. Phys. Commun.* 25, 347.

The IRON Project

Anil K. Pradhan

*Department of Astronomy, The Ohio State University,
Columbus, Ohio, USA 43210*

Abstract. Recent advances in theoretical atomic physics have enabled large-scale calculation of atomic parameters for a variety of atomic processes with high degree of precision. The development and application of these methods is the aim of the Iron Project. At present the primary focus is on collisional processes for all ions of iron, Fe I – FeXXVI, and other iron-peak elements; new work on radiative processes has also been initiated. Varied applications of the Iron Project work to X-ray astronomy are discussed, and more general applications to other spectral ranges are pointed out. The IP work forms the basis for more specialized projects such as the RmaX Project, and the work on photoionization/recombination, and aims to provide a comprehensive and self-consistent set of accurate collisional and radiative cross sections, and transition probabilities, within the framework of relativistic close coupling formulation using the Breit-Pauli R-Matrix method. An illustrative example is presented of how the IP data may be utilised in the formation of X-ray spectra of the $K\alpha$ complex at 6.7 keV from He-like Fe XXV.

1. Introduction

The main purpose of the Iron Project (IP; Hummer et al. 1993) is the continuing development of relativistic methods for the calculations of atomic data for electron impact excitation and radiative transitions in iron and iron-peak elements. Its forerunner, the Opacity Project (OP; Seaton et al. 1994; The Opacity Project Team 1995), was concerned with the calculation of radiative parameters for astrophysically abundant elements, oscillator strengths and photoionization cross sections, leading to a re-calculation of new stellar opacities (Seaton et al. 1994). The OP work, based on the non-relativistic formulation of the close coupling approximation using the R-matrix method (Seaton 1987, Berrington et al. 1987), was carried out in LS coupling, neglecting relativistic fine structure that is not crucial in the calculation of mean plasma opacities. Also, collisional processes were not considered under the OP. The IP collaboration seeks to address both of these factors, and with particular reference to iron and iron-peak elements. The collaboration involves members from six countries: Canada, France, Germany, UK, US, and Venezuela.

The relativistic extension of the R-matrix method is based on the Breit-Pauli approximation (Berrington et al. 1995). Collisional and radiative processes may both be considered. However, the computational requirements for the Breit-Pauli R-matrix (hereafter BPRM) calculations can be orders of magnitude more intensive than non-relativistic calculations. Nonetheless, a large body of atomic data has been obtained and published in a continuing series under the title **Atomic Data from the Iron Project** in *Astronomy and Astrophysics Supplement Series*, with 43 publications at present. A list of the IP publications and related information may be obtained from the author's Website: www.astronomy.ohio-state.edu/~pradhan.

The earlier phases of the Iron Project dealt with (a) fine structure transitions among low-lying levels of the ground configuration of interest in Infrared (IR) astronomy, particularly the observations from the Infrared Space Observatory, and (b) excitation of the large number of levels in multiply ionized iron ions (with $n = 2, 3$ open shell electrons, i.e. Fe VII – Fe XXIV) of interest in the UV and EUV, particularly for the Solar and Heliospheric Observatory (SOHO), the Extreme Ultraviolet Explorer (EUVE), and Far Ultraviolet Spectroscopic Explorer (FUSE). In addition, the IP data for the low ionization stages of iron (Fe I – Fe VI) is of particular interest in the analysis of optical and IR observations from ground

based observatories. In the present review, we describe the IP work within the context of applications to X-ray spectroscopy, where ongoing calculations on collisional and radiative data for H-like Fe XXVI, He-like Fe XXV, and Ne-like Fe XVII are of special interest.

The sections of this review are organised as follows: 1. Theoretical, 2. collisional, 3. radiative, 4. collisional-radiative modeling of X-ray spectra, 5. atomic data, 6. Discussion, and 7. Conclusion.

2. The Close Coupling approximation and the Breit-Pauli R-matrix Method

In the close coupling (CC) approximation the total electron + ion wave function may be represented as

$$\Psi = A \sum_{i=1}^{NF} \psi_i \theta_i + \sum_{j=1} C_j \Phi_j, \quad (1)$$

where ψ_i is a target ion wave function in a specific state $S_i L_i$ and θ_i is the wave function for the free electron in a channel labeled as $S_i L_i k_i^2 \ell_i (SL\pi)$, k_i^2 being its incident kinetic energy relative to $E(S_i L_i)$ and ℓ_i its orbital angular momentum. The total number of free channels is NF ("open" or "closed" according to whether $k_i^2 <$ or $> E(S_i L_i)$). A is the antisymmetrization operator for all $N + 1$ electron bound states, with C_j as variational coefficients. The second sum in Eq. (1) represents short-range correlation effects and orthogonality constraints between the continuum electron and the one-electron orbitals in the target.

The target levels included in the first sum on the RHS of Eq. (1) are coupled; their number limits the scope of the CC calculations. Resonances arise naturally when the incident electron energies excite some levels, but not higher ones, resulting in a coupling between "closed" and "open" channels, i.e. between free and (quasi)bound wavefunctions. The R-matrix method is the most efficient means of solving the CC equations and resolution of resonance profiles (see reviews by K.A. Berrington and M.A. Bautista). The relativistic CC approximation may be implemented using the Breit-Pauli Hamiltonian.

Both the continuum wavefunctions at $E > 0$ for the (e + ion) system, and bound state wavefunctions may be calculated. Collision strengths are obtained from the continuum (scattering) wavefunctions, and radiative transition matrix elements from the continuum and the bound wavefunctions that yield transition probabilities and photoionization and (e + ion) photo-recombination cross sections (see the review by S.N. Nahar).

Recent IP calculations for the $n = 3$ open shell ions include up to 100 or more coupled fine structure levels. Computational requirements for such radiative and collisional calculations may be of the order of 1000 CPU hours even on the most powerful supercomputers.

3. Electron Impact Excitation

Collision strengths and maxwellian averaged rate coefficients have been or are being calculated for all ions of iron. While some of the most difficult cases, with up to 100 coupled fine structure levels from $n = 3$ open shell configurations in Fe VII – Fe XVII, are still in progress, most other ionization stages have been completed. In particular fine structure collision strengths and rates have been computed for thousands of transitions in Fe II – Fe VI. For a list of papers see "Iron Project" on www.astronomy.ohio-state.edu/~pradhan.

Work on K-shell and L-shell collisional excitations, beginning with the H-like and the He-like ions will be continued under the new RmaX project, which is part of the IP and is focused on X-ray spectroscopy. Work is in progress on He-like Fe XXV (Mendoza et al.) and Ne-like Fe XVII. Fig. 1 presents the collision strength for a transition in Fe XVII from the new 89-level BPRM calculation including the $n = 4$ complex (Chen and Pradhan 2000). The extensive resonance structure is due to the large number of coupled thresholds following L-shell excitation.

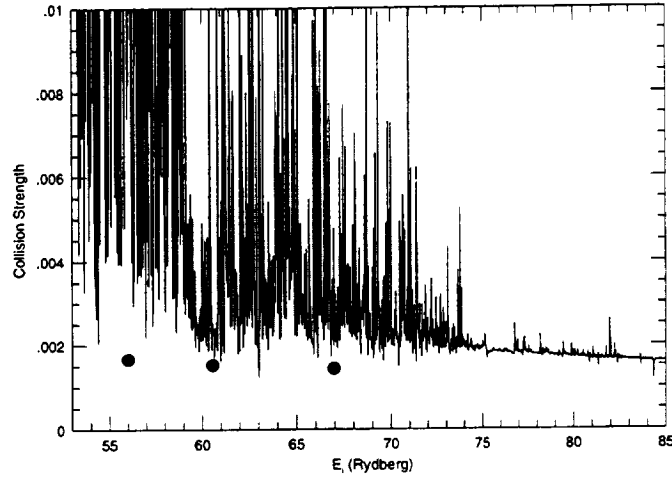


Figure 1. The BPRM collision strength $\Omega(2p^6 \ ^1S_0 \rightarrow 2p^5 3s \ ^3P_2)$ (Chen and Pradhan 2000); the relativistic distorted wave values are denoted as filled circles (H.L. Zhang, in Pradhan and Zhang 2000)

4. Radiative transition probabilities

There are two sets of IP calculations: (i) with atomic structure codes CIV3 (Hibbert 1973) and SUPERSTRUCTURE (Eissner et al. 1974), and (ii) BPRM calculations. Of particular interest to X-ray work are the recent BPRM calculations for 2,579 dipole (E1) oscillator strengths for Fe XXV, and 802 transitions in Fe XXIV (Nahar and Pradhan 1999), extending the available datasets for these ions by more than an order of magnitude. Also, these data are shown to be highly accurate, 1 – 10%.

5. Collisional-Radiative model for He-like ions: X-ray emission from Fe XXV

Emission from He-like ions provides the most valuable X-ray spectral diagnostics for the temperature, density, ionization state, and other conditions in the source (Gabriel 1972, Mewe and Schrijver 1981, Pradhan 1982).

The $K\alpha$ complex of He-like ions consists of the principal lines from the allowed (w), intersystem (x,y), and the forbidden (z) transitions $1^1S \leftarrow 2(1^1P^o, 3^3P_2^o, 3^3P_1^o, 3^3S_1)$ respectively. (These are also referred as the R,I,F lines, where the I is the sum (x+y); we employ the former notation). Two main line ratios are particularly useful, i.e.

$$R = \frac{z}{x+y}, \quad (2)$$

and

$$G = \frac{x+y+z}{w}. \quad (3)$$

R is the ratio of forbidden to intersystem lines and is sensitive to electron density N_e since the forbidden line z may be collisionally quenched at high densities. G is the ratio of the triplet-multiplicity lines to the ‘resonance’ line, and is sensitive to (i) electron temperature, and (ii) ionization balance. Condition (ii) results because recombination-cascades from H-like ions preferentially populate the triplet levels, enhancing the z line intensity in particular (the level $2(3^3S_1)$ is like the ‘ground’ level for the triplet levels). Inner-shell ionization of Li-like ions may also populate the $2(3^3S_1)$ level ($1s^2 2s \rightarrow 1s2s + e$)

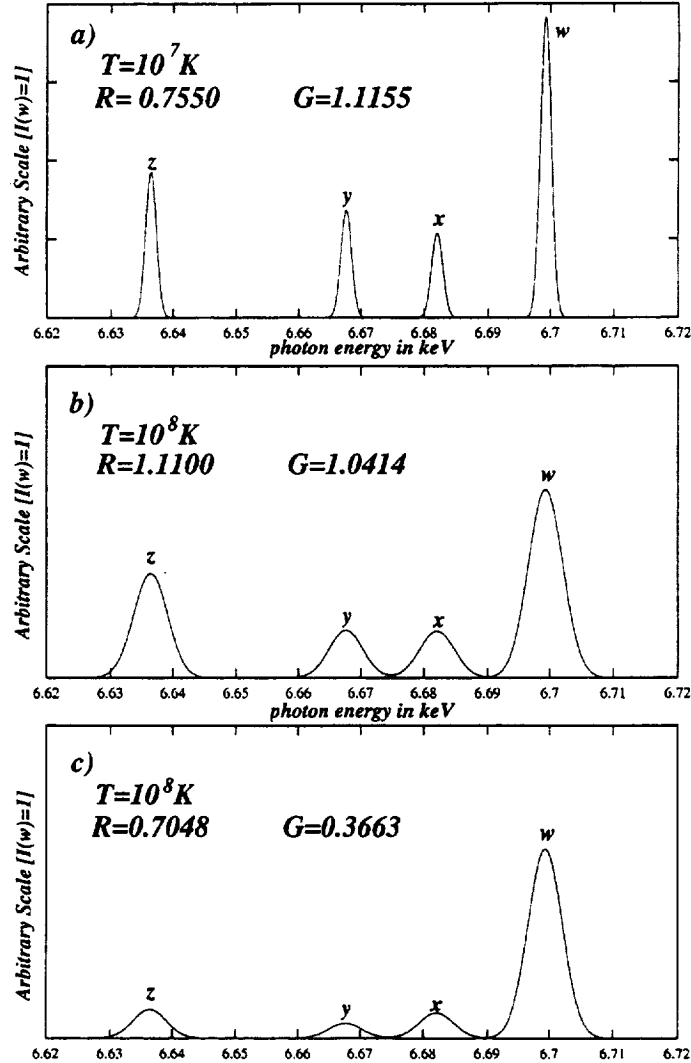


Figure 2. X-ray spectra of Fe XXV (Oelgoetz and Pradhan 2000). The principal lines w,x,y,z and the line ratios R and G are computed at plasma electron temperatures shown. The lines are Doppler broadened. $I(w)$ is normalized to unity.

enhancing the z line. The line ratio G is therefore a sensitive indicator of the ionization state and the temperature of the plasma during ionization, recombination, or in coronal equilibrium.

For Fe XXV the X-ray lines w,x,y,z are at $\lambda\lambda$ 1.8505, 1.8554, 1.8595, 1.8682 \AA , or 6.700, 6.682, 6.668, 6.637 keV, respectively. A collisional-radiative model (Oelgoetz and Pradhan, in progress) including electron impact ionization, recombination, excitation, and radiative cascades is used to compute these line intensities using rates given by Mewe and Schrijver (1978), Bely-Dubau et al. (1982), and Pradhan (1985a). New unified electron-ion recombination rates (total and level-specific) are being calculated by S.N. Nahar and collaborators, and electron excitation rates are being recalculated by C. Mendoza and collaborators; these will be employed in a more accurate model of X-ray emission from He-like ions.

Fig. 2 shows illustrative results for doppler broadened line profiles under different plasma conditions (normalized to $I(w) = 1$). All are at $N_e = 10^{10} \text{ cm}^{-3} \ll N_c$, so that the R dependence is only on T_e .

Figs. 2(a) and 2(b) are in coronal equilibrium, but differing widely in T_e , $10^7 - 10^8$ K, as reflected in the broader profiles for the latter case. The ratios R and G show a significant (though not large) temperature dependence in this range. The ionization fractions Fe XXIV/FeXXV and Fe XXVI/FeXXV for the two cases are such that the Li-like iron dominates at 10^7 K and the H-like at 10^8 K. Figs. 2(a) and (b) illustrate a general property of the He-like line ratios: $G \approx 1$ in coronal equilibrium (for other He-like ions it may vary by 10-20%).

On the other hand, the situation is quite different when the plasma is out of equilibrium. In particular, it is known that the forbidden line z is extremely sensitive to the ionization state since it is predominantly populated via recombination-cascades (Pradhan 1985b). Fig. 2(c) illustrates a case where recombinations are suppressed, and the plasma is at $T_e = 10^8$ K. The total G value is now only a third of its coronal value, with the z/w ratio being considerably lower. Although the new recombination and excitation rates may change the number somewhat, it is seen that $G \approx 0.37$ is a lower limit on an ionization dominated plasma.

A reverse situation occurs in a recombination dominated plasma. It is known from tomakak studies (Kallne et al. 1984, Pradhan 1985b) that the z/w ratio, and hence G, increases practically without limit, as T_e decreases much below the coronal temperature of maximum abundance. $G \gg 1$ observed values imply a recombination dominated source. However, the z/w ratio may also be enhanced by inner-shell ionization through the Li-like state. More detailed calculations are needed to distinguish precisely between the two cases, and to constrain the temperature and ionization fractions.

Di-electronic satellite intensities (Gabriel 1972) may also be computed using BPRM data for the autoionization and radiative rates of the satellite levels from recombination of $e + \text{FeXXV} \rightarrow \text{Fe XXIV}$ (Pradhan and Zhang 1997). This work is in progress.

6. Atomic Data

The atomic data from the OP/IP is available from the Astronomy and Astrophysics library at CDS, France (Cunto et al. 1993). The data is also available from a Website at NASA GSFC linked to the author's Website (www.astronomy.ohio-state.edu/~pradhan).

A general review of the methods and data, ("Electron Collisions with Atomic Ions - Excitation", Pradhan and Zhang 2000) is available from the author's website. The review contains an evaluated compilation of theoretical data sources for the period 1992-1999, as a follow-up of a similar review of all data sources up to 1992 by Pradhan and Gallagher (1992) - a total of over 1,500 data sources with accuracy assessment. Also contained are data tables for many Fe ions, and a recommended data table of effective collision strengths and A-values for radiative-collisional models for ions of interest in nebular plasmas.

The collisional data from the IP is being archived in a new database called TIPBASE, complementary to the radiative database from the OP, TOPBASE (see the review by C. Mendoza).

7. Discussion

An overview of the work under the Iron Project collaboration was presented. Its special relevance to X-ray astronomy was pointed out since the IP, and related work, primarily aims to study the dominant atomic processes in plasmas, and to compute extensive and accurate set of atomic data for electron impact excitation, photoionization, recombination, and transition probabilities of iron and iron-peak elements. The importance of coupled-channel calculations was emphasized, in particular the role of autoionizing resonances in atomic phenomena. (A new project RmaX, a part of IP focused on X-ray spectroscopy, is described by K.A. Berrington in this review).

During the discussion, a question was raised regarding the resonances in Fe XVII collision strengths (e.g. Fig. 1), and it was mentioned that new experimental measurements appear not to show the expected rapid variations in cross sections. A possible explanation may be that there are numerous narrow resonances in the entire near-threshold region, without a clearly discernible background or energy gap. The measured cross sections are averages over the resonances corresponding to the experimental beam-width. These averaged cross sections themselves may not exhibit sharp variations, unlike more

highly charged He-like ions where the the non-resonant background and the resonance complexes are well separated in energy (e.g. He-like Ti XXI, Zhang and Pradhan 1993).

8. Conclusion

Nearly all of the atomic data (with the exception of measured energy levels) in astrophysical models are obtained from theoretical atomic physics. It is therefore important to advance and enhance the scope of these methods continually in order to meet the needs of current and future space observatories with high throughput and resolution, particularly in X-ray astronomy. To that end the Iron Project work encompasses, and has been extended to, the following general areas.

- *Photoionization*: Charge balance models of radiatively ionized plasmas require photoionization cross sections for all abundant elements in all ionization states. All these data must be obtained theoretically. Recently, pioneering work has begun on the measurements of a few ions at the Advanced Light Source in Berkeley by R. Phaneuf and collaborators at the University of Nevada (Reno) and in Aarhus Denmark (see review by Nahar). These experiments establish the accuracy of the Opacity Project and the Iron Project data (the latter with relativistic effects).
- *Electron-Ion Recombination*: It is necessary to obtain non-resonant and resonant (i.e. radiative and di-electronic) recombination cross sections at all energies to derive rate coefficients at all temperatures needed in the models (up to 10^9 K). A unified method using the BPRM method, as developed for the Iron Project, has been described by Nahar in this review. Whereas experiments are now being done for several ions, the high-energy cross sections and thresholds are not accessible. Also, the very high- n and ℓ resonances are field ionized, and consequently the peak values of DR may be reduced to varying extent. Since experiments can not be done for all physical conditions in various astrophysical situations, theoretical calculations (with field effects) are essential in order to simulate plasma conditions.
- *Level-Specific photoionization/recombination rates*: These are needed not only for low-lying metastable levels, but also for high- n Rydberg levels in order to construct recombination-cascade matrices for Non-LTE models. Theoretical calculations are now under way for ions of interest in X-ray work, especially the He-like ions (Nahar et al. 2000).
- *Electron Impact Excitation*: Rate coefficients are obtained from theoretical cross sections for all ions and many transitions including a large number of excited states. For example, the 89-level calculations for Fe XVII up to the $n = 4$ levels yields cross sections for 3,916 transitions (Chen and Pradhan 2000). Calculations are also nearing completion for He-like ions including all $n = 4$ levels (Mendoza et al. 2000). Experimental measurements have been done for a few of the low-lying transitions in some ions and good agreement has been found with theory.
- *Radiative transition probabilities*: The new BPRM calculations, together with ongoing studies of relativistic effects, afford the possibility of accurate large-scale datasets of millions of transitions for complex iron ions that can not be obtained experimentally, but are needed for opacities calculations and in extended Non-LTE models of X-ray sources.

Acknowledgments. This work was partially supported by the NASA Astrophysical Theory Program and the National Science Foundation.

References

- Bely-Dubau, F. Dubau, J., Faucher, P. and Gabriel, A.H. 1982, MNRAS, 198 239
 Berrington, K.A., Burke, P.G., Butler, K., Seaton, M.J., Storey, P.J., Taylor, K.T., & Yan, Yu. 1987, J. Phys. B20, 6379
 Berrington K.A., Eissner W.B., Norrington P.H., 1995, Comput. Phys. Commun. 92, 290
 Cunto, W.C., Mendoza, C., Ochsenbein, F. and Zeippen, C.J., 1993, A&A 275, L5

- Eissner W, Jones M and Nussbaumer H 1974 *Comput. Phys. Commun.* 8 270
- Gabriel, A.H., *MNRAS* 1972, 160, 99
- Hibbert A., 1975, *Comput. Phys. Commun.* 9, 141
- Hummer, D.G., Berrington, K.A., Eissner, W., Pradhan, A.K., Saraph, H.E., & Tully, J.A. 1993, *Astron. Astrophys.* 279, 298
- Kallne, E, Kallne, J., Dalgarno, A., Marmar, E.S., Rice, J.E. and Pradhan, A.K. 1984, *Phys.Rev.Lett* 52, 2245
- Mewe, R. and Schrijver, J. 1978, *A&A* , 65, 99
- Nahar, S.N. and Pradhan, A.K. 1999, *A&AS* 135, 347
- Pradhan, A.K. 1982 *ApJ* , 263, 477
- Pradhan, A.K. 1985a *ApJS* , 59, 183
- Pradhan, A.K. 1985b *ApJ* , 288, 824
- Pradhan, A.K. and Gallagher, J.W. 1992, *ADNDT* , 52, 227
- Pradhan, A.K. and Zhang, H.L. 1997, *J. Phys. B*, 30, L571
- Pradhan, A.K. and Zhang, H.L. 2000, "*Electron Collisions with Atomic Ions*", In *LANDÖLT-BORNSTEIN Volume "Atomic Collisions"*, Ed. Y. Itikawa, Springer-Verlag (in press).
- The Opacity Project Team, *The Opacity Project*, Vol.1, 1995, Institute of Physics Publishing, U.K.
- Seaton, M.J. 1987, *J. Phys.* B20, 6363
- Seaton, M.J., Yu, Y., Mihalas, D. and Pradhan, A.K. 1994, *MNRAS* , 266, 805
- Zhang H.L. and Pradhan A.K. 1995, *Phys.Rev.A*, 52, 3366

Photoionization and Recombination

Sultana N. Nahar

Department of Astronomy, The Ohio State University
Columbus, Ohio, USA 43210

Abstract. Theoretically self-consistent calculations for photoionization and ($e + \text{ion}$) recombination are described. The same eigenfunction expansion for the ion is employed in coupled channel calculations for both processes, thus ensuring consistency between cross sections and rates. The theoretical treatment of ($e + \text{ion}$) recombination subsumes both the non-resonant recombination (“radiative recombination”), and the resonant recombination (“di-electronic recombination”) processes in a unified scheme. In addition to the total, unified recombination rates, level-specific recombination rates and photoionization cross sections are obtained for a large number of atomic levels. Both relativistic Breit-Pauli, and non-relativistic LS coupling, calculations are carried out in the close coupling approximation using the R-matrix method. Although the calculations are computationally intensive, they yield nearly all photoionization and recombination parameters needed for astrophysical photoionization models with higher precision than hitherto possible, estimated at about 10-20% from comparison with experimentally available data (including experimentally derived DR rates). Results are electronically available for over 40 atoms and ions. Photoionization and recombination of He-, and Li-like C and Fe are described for X-ray modeling. The unified method yields total and complete ($e + \text{ion}$) recombination rate coefficients, that can not otherwise be obtained theoretically or experimentally.

1. Introduction

Although photoionization and recombination are direct opposite processes as they occur in nature, they are usually treated in independent theoretical frameworks. This basic inconsistency, directly related to ionization balance in radiatively ionized media, and consequent inaccuracies, propagate through the photoionization models employed in astrophysics. A further division, largely artificial, is made in theoretical methods used to compute electron-ion recombination rates. Two sets of data are usually calculated: (i) “radiative recombination” (RR), calculated using background, or non-resonant, photoionization cross sections, and (ii) “di-electronic recombination” (DR) representing the contribution of autoionizing resonances, first shown to be important by Burgess (1964). That this procedure is not only theoretically unsatisfactory, but also impractical in most cases, as seen from both theoretical calculations and experimental measurements of photoionization and recombination cross sections. The simple reason is that the resonances are inseparable from the background. The cross sections contain, in general, extensive and interacting Rydberg series of resonances; the non-resonant and resonant contributions are not accurately separable (except, possibly, for few-electron, highly charged ions). The large number of photoionization cross sections computed under the Opacity Project exhibit these features in detail (*The Opacity Project Team* 1995, 1996 - compiled publications and data). In addition, the cross sections for photoionization and recombination of excited states, particularly metastable levels, may contain even more complicated resonances than the ground state (Luo et al. 1990). Experimentally, of course, the measurements *always* yield a combined (RR + DR) cross section (albeit in limited energy ranges usually accessible in experimental devices).

Therefore a theoretical method that accounts for both the resonant and the non-resonant recombination in a unified manner is desirable, and has been developed (e.g. Nahar and Pradhan 1994, Zhang et al. 1999), based on the close coupling (CC) approximation using the R-matrix method (Burke and Seaton 1984, Berrington et al. 1987, Hummer et al. 1993) as used in the Opacity Project and the Iron Project (hereafter OP and IP). Photoionization cross sections may be computed essentially for all bound

states, level of excitation ($n, \ell, SL\pi, SLJ\pi$), energy range, and with energy resolution to delineate resonances. In principle, the cross section for the inverse photo-recombination process is given by detailed balance. However, since recombination takes place to an infinite number of bound states of ($e + \text{ion}$) system, it becomes impractical (and as it turns out, unnecessary) to do so for the very highly excited levels above a certain n -value (chosen to be 10 in practice). For recombination into levels with $n > 10$, the non-resonant contribution, relative to the resonant contribution per unit energy is negligible owing to the density of resonances as $n \rightarrow \infty$. In that range we employ a precise theoretical treatment of DR based on multi-channel quantum defect theory and the CC approximation (Bell and Seaton 1985, Nahar and Pradhan 1994) to compute the recombination cross section.

Among the problems that manifest themselves in the CC photoionization/recombination calculations are: the accuracy and convergence of the eigenfunction expansion for the ion, relativistic fine structure effects, the contribution from non-resonant recombination into high- n levels as $E \rightarrow 0; n \rightarrow \infty$, resolution of narrow resonances with increasing n and/or ℓ , and radiation damping thereof.

Experimental work is of importance in ascertaining the accuracy of theoretical calculations and the magnitude of various associated effects, since most of the photoionization/recombination data can only be calculated theoretically. In recent years there has also been considerable advance in the measurements of ($e + \text{ion}$) recombination cross sections on ion storage rings (e.g. Kilgus et al. 1990, 1993, Wolf et al. 1991), and photoionization cross sections using accelerator based photon light sources (R. Phaneuf et al., private communication). We compare the CC calculations for both atomic processes with the latest experimental data.

2. Theory

The CC approximation takes account of the important coupling between the energetically accessible states of the ion in the ($e + \text{ion}$) system. The target ion is represented by an N -electron system, and the total wavefunction expansion, $\Psi(E)$, of the $(N+1)$ electron-ion system of symmetry $SL\pi$ or $J\pi$ may be represented in terms of the target eigenfunctions as:

$$\Psi(E) = A \sum_i \chi_i \theta_i + \sum_j c_j \Phi_j, \quad (1)$$

where χ_i is the target wavefunction in a specific state $S_i L_i \pi_i$ or $J_i \pi_i$ and θ_i is the wavefunction for the $(N+1)$ -th electron in a channel labeled as $S_i L_i (J_i \pi_i) k_i^2 \ell_i (SL\pi \text{ or } J\pi)$; k_i^2 being its incident kinetic energy. Φ_j 's are the correlation functions of the $(N+1)$ -electron system. Bound and continuum wavefunctions for the ($e + \text{ion}$) system are obtained on solving the CC equations at any total energy $E < 0$ and $E > 0$ respectively. The coupling between the eigenfunctions of the energetically inaccessible states of the ion ('closed channels'), and the accessible states ('open channels'), gives rise to resonance phenomena, manifested as infinite Rydberg series of resonances converging on to the excited states of the target ion.

With the bound and the continuum (free) states of the ($e + \text{ion}$) system, atomic cross sections may be calculated for electron impact excitation (EIE), photoionization, and recombination — the free and the bound-free processes. Radiative transition (bound-bound) probabilities may also be obtained.

The R-matrix method, and its relativistic extension the Breit-Pauli R-matrix method (BPRM), are the most efficient means of solving the CC equations, enabling in particular the resolution of the resonances in the cross sections at a large number of energies.

3. Photoionization

Photoionization calculations are carried out for all levels

($n, \ell, SL\pi, SLJ\pi$), with $n \leq 10, \ell < n - 1$. Typically this means several hundred bound levels of each atom or ion. The cross section for each level is delineated at about thousand energies, or more, to map out the resonance structure in detail. In recent studies, photoionization cross sections of all ions of C, N, and O were computed (Nahar and Pradhan 1997, Nahar 1998) with more extended eigenfunction expansions, resolution of resonances, and number of levels, than the earlier OP data. Overall, new

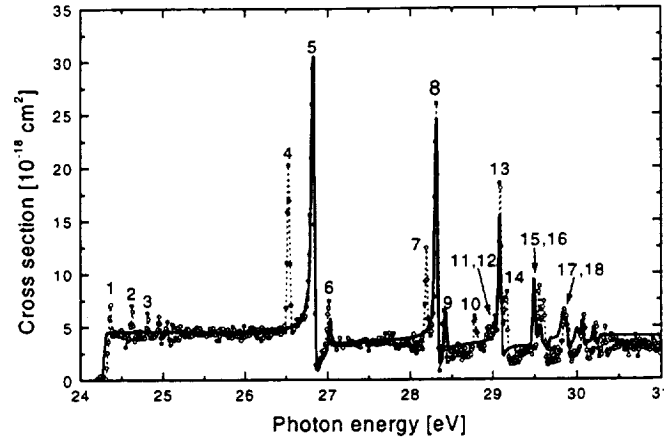


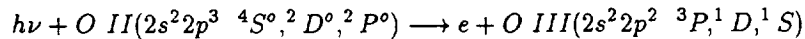
Figure 1. Photoionization cross sections of the ground state of C II: experiment (open circle, Kjeldsen et al. 1999), theory (solid curve, Nahar 1995)

photoionization data for over 40 atoms and ions, with improvements over the OP data (e.g. currently in TOPbase, Cunto et al. 1993), has now been calculated for: low ionization stages of iron: Fe I, II, III, IV, and V (references in Bautista and Pradhan 1998), Ni II (Bautista 1999), the C-sequence ions (Nahar and Pradhan 1991,1992), the Si-sequence ions (Nahar and Pradhan 1993). Unified ($e + \text{ion}$) photo-recombination cross sections and rates (total and level-specific) have also been obtained, as discussed below.

3.1. Comparison with experiments

The recent ion-photon merged beam experiment by Kjeldsen et al. (1999) on the photoionization cross sections of the ground state of C II shows an extremely rich and detailed resonance structures (Figure 1). There is excellent agreement between the theory and experiment, both in terms of magnitude and details of the background and resonances. However, the theoretical calculations were in LS coupling, neglecting fine structure, that clearly manifests itself in the additional peaks seen in the experimental cross sections (new relativistic calculations are in progress).

New photoionization experiments have been carried out for positive atomic ions at the Advance Light Source (ALS) in Berkeley, where a photon light source is used on an accelerator that produces the ion beams. These extremely high resolution measurements provide an unprecedented check on the details of the theoretical cross sections, particularly resonance structures and fine structure effects. Figure 2 compares the O II cross section from theory (Nahar 1998), and experiments at the ALS done by the Reno group headed by R. Phaneuf. The experimental cross sections include not only the photoionization of the ground state $2s^2 2p^3$ ($^4S^o$) but also the metastable excited states $2s^2 2p^3$ ($^2D^o, ^2P^o$).



The complicated features arise from several series of resonances converging on to the excited states of the residual ion O III. There is very good agreement between the CC calculations and experiment, verifying the often expressed, but not heretofore established, claim of about 10% accuracy of the theoretical cross sections. The situation may be more complicated, and the uncertainties larger, for more complex atomic systems.

These results also show that metastable states may need to be included in atomic photoionization models of astrophysical sources.

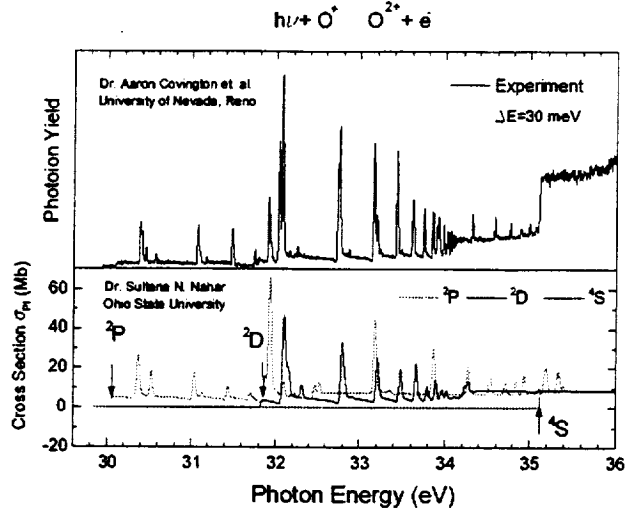


Figure 2. Photoionization cross sections of the ground and metastable states, $2s^22p^3(^4S^{\circ}, ^2D^{\circ}, ^2P^{\circ})$, of O II: experiment (upper panel, summed σ_{PI} , Phaneuf et al.), theory (lower panel, Nahar 1998). The arrows in the lower panel indicate the threshold cross section for each state.

4. Unified method for (e + ion) recombination

Photoionization calculations described above are for total photoionization from a given level into all excited levels of the residual ion. However, for photo-recombination the calculations must be repeated to obtain the cross section into the ground state of the ion alone. Detailed balance then applies as

$$\sigma_{RC}(\epsilon) = \frac{\alpha^2 g_i (\epsilon + I)^2}{4 g_j \epsilon} \sigma_{PI}, \quad (2)$$

where $\sigma_{RC}(i_o)$ is the photo-recombination cross section, σ_{PI} is the photoionization cross section into the ground state i_o , α is the fine structure constant, ϵ is the photoelectron energy, and I is the ionization potential in Rydberg atomic units. Recombination can take place into the ground or any of the excited recombined (e+ion) states. The contributions of these bound states to the total σ_{RC} are obtained by summing over the contributions from individual cross sections. σ_{RC} thus obtained from σ_{PI} , including the autoionizing resonances, corresponds to the total (DR+RR) unified recombination cross section in an ab initio manner.

Recombination into the high- n states, i.e. $n_{\max} < n \leq \infty$, is computed assuming DR to dominate over the non-resonant background contribution. The CC approximation can then be used to calculate DR collision strengths Ω_{DR} , as an extension of the theory of DR by Bell and Seaton (1985). These two main parts of the unified recombination calculations, and other parts, are described in detail in Zhang et al. (1999). For very highly charged ions, such as the H- and He-like ions with large radiative decay rates for core transitions, radiation damping effects can be significant. As in other CC calculations for excitation and photoionization, resonances are resolved at a suitably fine mesh to enable perturbative radiative damping, and to ensure that the neglected resonances do not significantly affect the computed rates. Relativistic fine structure is considered in the BPRM calculations for highly charged ions.

4.1. Comparison with experiments

Although experimental results are available for relatively few ions in limited energy ranges, and mostly for simple atomic systems such as the H-like and He-like ions, they are useful for the calibration of theoretical

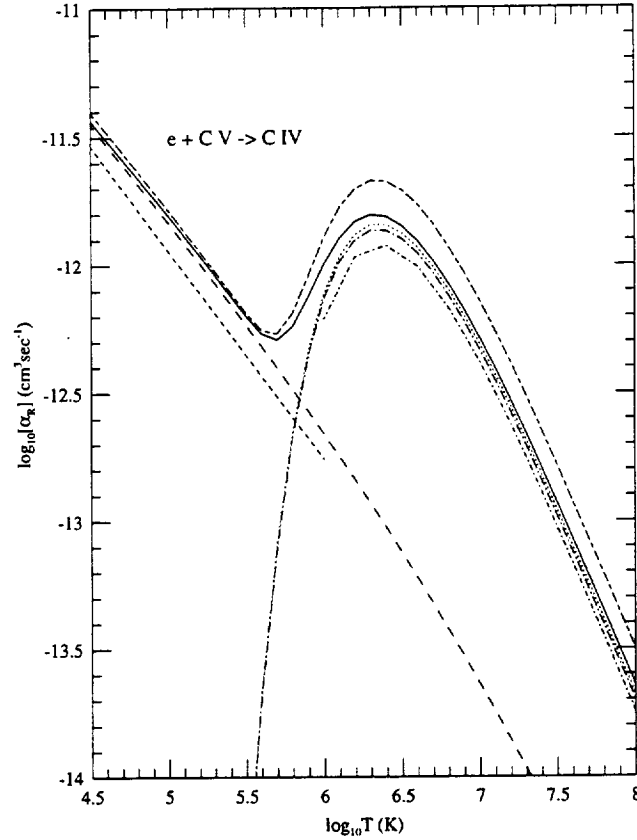


Figure 3. $e + C V \rightarrow C IV$. Total unified rate coefficients: BPRM with fine structure – solid curve, LS coupling – short and long dashed curve; using cross sections from Zhang et al. (1999) – dotted; Savin (1999) – dot-long dash curve; DR rates by Badnell et al. (1990) – dot dash curve; RR rates: Aldrovandi and Pequignot (1973) – short-dash; Verner and Ferland (1996) – long-dash

cross sections. Zhang et al. (1999) have compared in detail the BPRM cross sections with experimental data from ion storage rings for $e + C V \rightarrow C IV$, $e + C VI \rightarrow C V$, $e + O VIII \rightarrow O VII$, with close agreement in the entire range of measurements for both the background (non-resonant) cross sections and resonances. The reported experimental data is primarily in the region of low-energy resonances that dominate recombination (mainly DR) with H- and He-like ions. The recombination rate coefficients, α_R , obtained using the cross sections calculated by Zhang et al. agree closely with those of Savin (1999) who used the experimental cross sections to obtain 'experimentally derived DR rates'. However, these rates do not include contributions from much of the low energy non-resonant RR and very high energy regions. The total unified $\alpha_R(T)$ which includes all possible contributions is, therefore, somewhat higher than that obtained from limited energy range. In Figure 3, the solid curve corresponds to the total unified α_R . The dotted curve and the dot-long-dash curves are the rates using cross sections from Zhang et al. (1999) and Savin (1999) respectively, in the limited energy range in experiments (the two curves almost merge). The short-and-long dash curve is the total α_R in LS coupling (Nahar and Pradhan 1997) which, at high temperatures, is higher than the new BPRM rates including fine structure and radiation

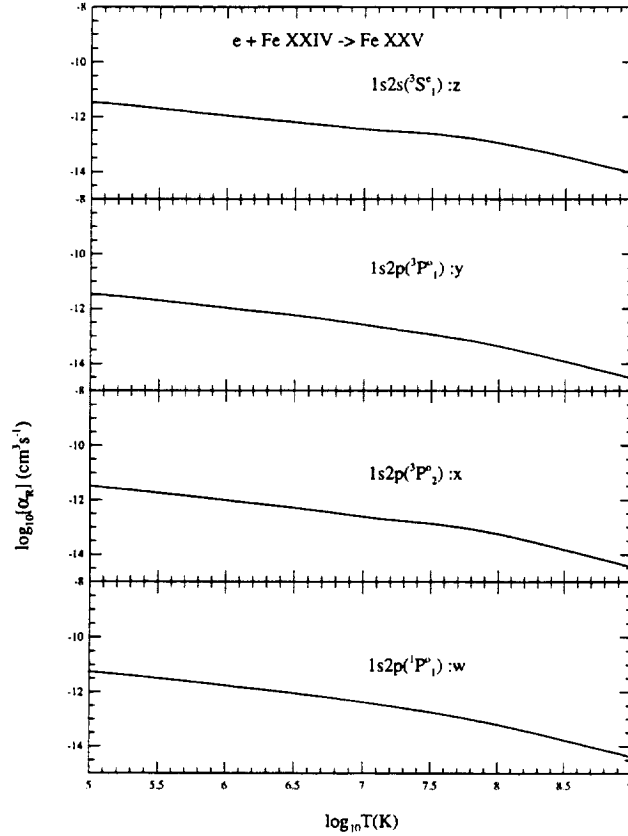


Figure 4. Level specific recombination rate coefficients for the K- α lines of Fe XXV.

damping (solid curve). The dot-dash curve is the DR rate by Badnell et al. (1990), which is lower than the others. The dashed and the long-dashed curves are RR rates by Aldrovandi and Pequignot (1973), and Verner and Ferland (1996); the latter agrees with the present rates at lower temperatures.

4.2. Photoionization/recombination of Fe XXV

Fe XXV is one of the most important ions in X-ray spectroscopy (see the review article by Pradhan in this volume). We have completed the calculations for: (i) photoionization cross sections for fine structure levels up to $n = 10$, including those for ionization into the ground level, and (ii) total and level-specific unified recombination cross sections and rate coefficients.

The most commonly observed lines of Fe XXV correspond to the K- α transitions between the $n=1$ and 2 levels: (1) the 'z' line $1s2s(^3S_1) - 1s^2(^1S_0)$, (2) the 'y' line, $1s2p(^3P_1^o) - 1s^2(^1S_0)$, (3) the 'x' line, $1s2p(^3P_2^o) - 1s^2(^1S_0)$, and (4) the 'w' line $1s2p(^1P_1^o) - 1s^2(^1S_0)$. Recombination rate coefficients into these levels are given in Figure 4; these vary smoothly with temperature, except a slight "shoulder" at high temperature due to DR.

5. Ionization equilibrium

The new photoionization/recombination data should enable more accurate calculations for photoionization equilibrium

$$\int_{\nu_0}^{\infty} \frac{4\pi J_{\nu}}{h\nu} N(X^z) \sigma_{PI}(\nu, X^z) d\nu = \sum_j N_e N(X^{z+1}) \alpha_R(X_j^z; T), \quad (3)$$

and, coronal equilibrium

$$C_I(T, X^z) N_e N(X^z) = \sum_j N_e N(X^{z+1}) \alpha_R(X_j^z; T), \quad (4)$$

where $\alpha_R(X_j^z; T)$ is the total electron-ion recombination rate coefficient of the recombined ion of charge z , X_j^z , to state j at electron temperature T , C_I is the rate coefficient for electron impact ionization, and σ_{PI} is the photoionization cross section evaluated at photon frequency ν and convoluted with the isotropic radiation density J_{ν} of the source; N_e , $N(X^{z+1})$, and $N(X^z)$ are the densities for the free electrons, and the recombining and recombined ions respectively.

Coronal ionization fractions for C,N,O using the unified recombination rates are also computed (Nahar and Pradhan 1997; Nahar 1999).

6. Conclusion

We carry out ab initio large scale close coupling R-matrix calculations for (i) photoionization cross sections, and (ii) electron-ion recombination rate coefficients. The predicted theoretical features in σ_{PI} are being observed in the recent sophisticated experiments.

The unified method for (e+ion) recombination has been benchmarked with available experimental measurements. Our study of unified electron-ion recombination rates exhibit a general pattern with temperature. Although generally applicable to all systems, the close coupling unified method is especially suitable for the strong coupling cases where the broad and overlapping resonances dominate the near-threshold region in the electron-ion recombination process, and other methods may not be accurate.

Total and state-specific unified recombination rate coefficients and photoionization cross sections are available for about 40 atoms and ions:

Carbon: C I, C II, C III, C IV, C V, C VI (Nahar and Pradhan 1997)

Nitrogen: N I, N II, N III, N IV, N V, N VI, N VII (Nahar and Pradhan 1997)

Oxygen: O I, O II, O III, O IV, O V, O VI, O VII, O VIII (Nahar 1999)

C-like: F IV, Ne V, Na VI, Mg VII, Al VIII, Si IX, S XI (Nahar 1995,1996)

Silicon and Sulfur: Si I, Si II, S II, S III, Ar V, Ca VII (Nahar 2000)

Iron: Fe I (Nahar et al. 1997), Fe II (Nahar 1997), Fe III (Nahar 1996b), Fe IV (Nahar et al 1998), Fe V (Nahar and Bautista 1999), Fe XIII (Nahar 2000), Fe XXIV, Fe XXV (Nahar et al. 2000)

Nickel: Ni II (Nahar and Bautista 2000).

These photoionization/recombination datasets are self-consistent, and should yield more accurate astrophysical photoionization models.

Acknowledgments. This work is supported partially by the NSF and NASA.

References

- Aldrovandi, S.M.V. and Pequignot, D. 1973, *Astron. Astrophys.* 25, 137.
 Badnell, N.R., Pindzola, M.S., and Griffin, D.C. 1990, *Phys. Rev. A* 41, 2422
 Bautista, M.A. 1999, *Astron. Astrophys. Suppl.* 137, 529
 Bautista, M.A. and Pradhan A.K. 1988, *Astrophys. J.* 492, 650
 Bell, R.H. and Seaton, M.J. 1985, *J. Phys. B*, 18, 1589
 Berrington K.A., Burke P.G., Butler K., Seaton M.J., Storey P.J., Taylor K.T., Yu Yan, 1987, *J.Phys.B* 20, 6379

- Burgess, A. 1964, *Astrophys. J.* 141, 1588
- Burke P.G. and Seaton M.J. 1984, *J. Phys. B* 17, L683
- Cunto W C, Mendoza C, Ochsenbein F and Zeippen C J, 1993. *A&A* 275, L5
- Hummer D.G., Berrington K.A., Eissner W., Pradhan A.K, Saraph H.E., Tully J.A., 1993, *A&A* 279, 298
- Kilgus G, Berger J, Blatt P, Grieser M, Habs D, Hochadel B, Jaeschke E, Krämer D, Neumann R, Neureither G, Ott W, Schwalm D, Steck M, Stokstad R, Szmola R, Wolf A, Schuch R, Müller A and Wägner M 1990 *Phys. Rev. Lett.* 64, 737
- Kilgus G, Habs D, Schwalm D, Wolf A, Schuch R and Badnell N R 1993 *Phys. Rev. A* 47, 4859
- Kjeldsen H., Folkmann F., Hensen J.E., Knudsen H., Rasmussen M.S., West J.B., Andersen T., 1999, *ApJ* 524, L143
- Luo D., Pradhan A.k., Saraph H.E., Storey P.J., Yan Y. 1989, *J. Phys. B* 22, 389
- Nahar, S.N. 1995, *ApJS* 101, 423.
- 1996, *ApJS* 106, 213.
- 1996b, *Phys. Rev. A* 53, 2417
- 1997, *Phys. Rev. A* 55, 1980
- 1998, *Phys. Rev. A* 58, 4593
- 1999, *ApJS* 120, 131.
- 2000, *ApJS* 126, 537.
- Nahar, S.N., & Bautista M.A. 1999, *ApJS* 120, 327
- 2000 (in preparation).
- Nahar, S.N., Bautista M.A., & Pradhan, A.K. 1997, *ApJ* 479, 497
- 1998, *Phys. Rev. A* 58, 4593
- Nahar, S.N., & Pradhan, A.K. 1991, *Phys. Rev. A* 44, 2935
- 1992, *Phys. Rev. A* 45, 7887
- 1991, *Phys. Rev. A* 44, 2935
- 1992, *Phys. Rev. A* 45, 7887
- 1993, *J. Phys. B* 26, 1109
- 1994, *Phys. Rev. A* 49, 1816
- 1997, *ApJS* 111, 339
- Savin, D.W. 1999, *Astrophys. J.* 523, 855 *The Opacity Project 1 & 2*, compiled by the Opacity Project team (Institute of Physics, London, UK, 1995,1996)
- Wolf A, Berger J, Bock M, Habs D, Hochadel B, Kilgus G, Neureither G, Schramm U, Schwalm D, Szmola E, Müller A, Waner M, and Schuch R 1991 *Z. Phys. D Suppl.* 21, 569
- Verner, D.A. & Ferland G. 1996, *ApJS* 103, 467
- Zhang, H.L., Nahar, S.N., & Pradhan, A.K. 1999, *J. Phys. B* 32, 1459

K-Shell Photoionization of Fe

B M McLaughlin¹, D Donnelly¹, K L Bell¹, M P Scott¹ and F P Keenan²

¹*Department of Applied Mathematics and Theoretical Physics*

²*Department of Pure and Applied Physics*

The Queen's University of Belfast, Belfast BT7 1NN, N. Ireland

Abstract. The status of K-shell photoionization of neutral iron has been reviewed. A comparison with the available experimental data and existing theoretical work is made for this important element. Several anomalies and features are illustrated and future directions of theoretical work are indicated.

1. Introduction

The *Ginga* satellite, launched in 1987, provided the first indication that the X-ray spectra of active galactic nuclei (AGN) were not featureless continua, but also contained structure associated with various atomic processes. Iron Fe-K emission lines (H-like, FeXXVI and He-like, FeXXV) with wavelengths of 1.936 Å and 1.940 Å were observed (Mushotzky et al. 1993). These lines are characteristic of X-ray illuminated cold material, and act as an indication of the amount of cool material illuminated by the AGN. More recently launched X-ray satellites, *Chandra*, July 23, 1999 and *XMM*, December 10, 1999 for the first time provide the ability to do X-ray spectroscopy in very high resolution. Elements of prime interest are C, N, O, Ne, Mg, Si, S, Ca, Ar, Fe and Ar, primarily at the K and L-edge energies for a number of ionization stages and a wide range of energies (0.1 - 12 keV). With the advent of such high resolution spectra there is an urgent need for high quality atomic data for photon and electron collisional excitation on the atomic species of interest together with their respective transitions probabilities.

Fe-K lines are observed in solar flares and are produced within the solar photosphere by the hot plasma in the corona (Bai 1979; Parmar et al. 1984; Phillips et al. 1994) and in active galactic nuclei (AGN). The appearance of these lines is due to the $2p \rightarrow 1s$ transition, which spontaneously occurs as a result of the instability of the $1s$ hole states generated from the K-shell photoionization of neutral iron. This instability is due to the large binding energy of the Fe $1s$ shell (~ 7 keV), the magnitude of which presents a major obstacle to determining accurate experimental or theoretical data for the K-shell photoionization of neutral iron.

The importance of understanding what occurs when high energy photons collide with neutral iron have many applications. It is known that in the interstellar medium, iron (Fe), silicon (Si) and magnesium (Mg) appear mainly at the same order of abundance in silicate grains. All Fe ions can emit K-shell photons in the region around the Fe-K emission region, the average energy of which moves from 6.4 keV to 6.7 keV as the ionization stage increases. Only in high resolution with statistics folded in will it confirm if neutral Fe K-shell lines are present in the spectra. Furthermore, X-ray Fluorescence in dark clouds (that is secondary emitted photons as a result of inner shell rearrangements by the incident photon) is important to understand so as to build accurate theoretical models. Figure 1 illustrates the presence of the Fe (K_{α}) line and its bremsstrahlung continua, in the spatial resolution of the ground based detector calibration for the *Chandra* satellite. The results are for a non-flight camera, the High Speed Imager (HSI) which shows a quasi-Gaussian peak with the approximate width for the telescope point spread function. The Fe (K_{α}) line is clearly visible as is the corresponding weaker bremsstrahlung continua (Edgar 1999, private communication). The setup includes an electron-ion point source (EIPS) with an iron anode which produces neutral Fe K and L lines and a bremsstrahlung continuum, and a filter of Mn with a thickness of about 2 mean free paths at 6.4 keV which has its K-edge between Fe K_{α} and K_{β} . The Mn filter also cuts out a large part of the continuum making a source spectrum strongly dominated by the one line, in this case the Fe K_{α} at 6.4 keV. Finally another interesting quantity to

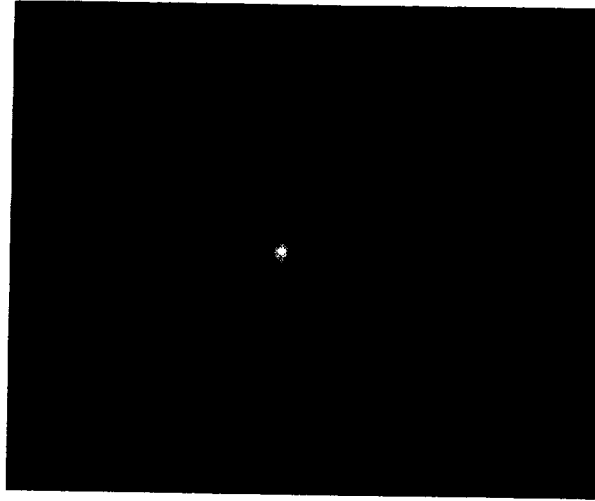


Figure 1. Ground base calibration of the detector for the Chandra satellite. The neutral iron (Fe) K_{α} line is clearly visible (bright spot) as is the corresponding weaker continuum bremsstrahlung tail to its right; courtesy of the SAO/MIT/Marshall Space Flight Center calibration group (Edgar 1999, private communication).

know is what is the total Fe abundance. Astrophysically, neutral iron is rare. However in the ultra-violet (UV) region singly ionized iron (Fe^{+}) has been observed in the Gas Phase but in the solid state phase the amount of Fe present is very much open to interpretation and speculation (Raymond and Smith 1999, private communication).

2. Overview of previous work

In order to assess the level of sophistication required in a theoretical model of neutral iron one first has to assess the status of theoretical work on this complex element. The first calculations on this complex system were made using the relativistic central field Dirac-Slater approximation (Verner et al. 1993; Verner and Yakovlev 1995). Verner and co-workers calculated the cross-section for the $1s$ -photoionization of neutral iron (Fe) as part of a more general study of photoionization from each individual sub-shell of ions of elements between helium and zinc. The results were found to have an approximate linear dependence on the photon energy. For valence shell photoionization the first attempt to treat this complex at the ab initio level was carried out by Bautista and Pradhan (Bautista and Pradhan 1995). These photoionization calculations catered only for the outer (valence) shell electrons of Fe but however showed a discrepancy of several orders of magnitude compared with the results relativistic central field approximation (Verner et al. 1993).

Recently ab initio work on inner shell photoionization of this complex system was carried out by Black and co-workers (Black et al. 1998) within the context of the R-matrix approach (Burk and Berrington 1993). In that work nine $1s^{-1}$ target hole states of Fe^+ were used obtained from the base configuration $1s^{-1}3d^64s^2$ for the photoionization calculations. Each of the nine-states were represented by a single configuration and electron correlation effects from configuration interaction mixing were neglected. The ground state of neutral iron was represented by a single configuration and no autoionizing states were considered. The results showed (as illustrated in Figure 2) that the relativistic central field approximation were essentially ‘duplicated’ at an energy of 1.25 keV above the lowest $1s^{-1}3d^64s^2$ hole state of Fe^+ included. The ab initio R-matrix method was used in order to test the viability of including $1s$ hole states of Fe^+ only in the calculation of K-shell photoionization cross sections. Despite the requirement of a large (sixty-four) number of continuum orbitals, the results were highly satisfactory with excellent agreement with the work of Verner and co-workers (Verner et al. 1993) occurring at higher photon energies as is seen from Figure 2. The results of Black and co-workers (Black et al. 1998) demonstrated an unusually rapid growth near the threshold which appeared to be inconsistent with the cross sections found experimentally for structurally similar neutral nickel (Parthasaradhi et al. 1998).

3. Ab initio Work

Following the work of Black and co-workers further investigations were carried out (Donnelly et al. 1999, 2000). Many sophisticated theoretical approaches have difficulties in dealing with such deep inner shell electron excitation. In particular, the R-matrix method encounters problems in so far as the number of continuum orbitals required to span the energy range between the the neutral Fe ground state and the $1s$ hole states of Fe^+ is quite considerable. A further difficulty in applying any close-coupling approximation to this problem is in the determination of the actual target $1s^{-1}$ hole states of Fe^+ to be included in the wavefunction expansion. A more realistic description of the process is attempted by including the ‘ground’ $1s^{-1}$ hole Fe^+ state together with excited hole states, each target state being represented by a configuration interaction type wave function, in an attempt to either confirm or refute the rapid growth feature in the calculations of Black and co-workers (Black et al. 1998). Sixteen $1s^{-1}$ -hole Fe^+ target states are utilized, with each one represented by an extensive configuration interaction. Electron correlation effects significantly alter the magnitude of the background cross section in comparison with earlier work and extensive resonance structure is resolved near the lowest threshold of the $1s^{-1}$ -hole Fe^+ state as is illustrated in Figure 3. The ground state of the neutral Fe is represented in this manner so that one keeps the Fe and Fe^+ systems ‘balanced’ by treating the neutral Fe ground state as a bound state of the $\{Fe^+ + e^-\}$ system.

3.1. Target States of Fe^+

Our calculations adopt a similar approach to the one used by Black and co-workers (Black et al. 1998) where the Fe^+ ground state is omitted and only a selected number of $1s^{-1}$ hole states of Fe^+ as target states are included. This choice of target states requires consideration of the following inner-shell processes:

$$\begin{aligned}
 h\nu + Fe \{ 1s^2 2s^2 2p^6 3s^2 3p^6 3d^6 4s^2 \ ^5D \} \\
 \downarrow \\
 Fe^+ \left\{ \begin{array}{l} 1s 2s^2 2p^6 3s^2 3p^6 3d^8 \ ^{2S+1}L \\ 1s 2s^2 2p^6 3s^2 3p^6 3d^7 4s \ ^{2S+1}L \\ 1s 2s^2 2p^6 3s^2 3p^6 3d^6 4s^2 \ ^{2S+1}L \end{array} \right\} + e^- \quad (1)
 \end{aligned}$$

In total twenty-three target states result from the photon ejection processes outlined in 1. From the work of Black and co-workers (Black et al. 1998) which included only the hole states $1s^{-1}3d^64s^2$, it was demonstrated that $1s^{-1}3d^6(^5D)4s^2$ 6D and 4D states only contribute significantly to the cross section. Hence of the nine-states of this type, only these two states are included leaving a total of sixteen target hole states. The configurations used to represent these target state wave functions are generated from the set of one-electron orbitals $\{1s, 2s, 2p, 3s, 3p, 3d, 4s, \overline{4p}, \overline{4d}, \overline{5s}, \overline{5d}\}$, whose radial part is represented

by a linear combination of Slater-type orbitals. The $1s$, $2s$, $2p$, $3s$ and $3p$ orbitals are the Hartree-Fock ground state orbitals of Fe^+ (Clementi and Roetti 1974), while the remaining orbitals were generated by energy optimizing the radial functions using the atomic structure code CIV3 (Hibbert 1975).

The $3d$ and $4s$ orbitals were energy optimized on the $\text{Fe}^+ 1s^{-1}3d^74s$ 6F state. The optimal $3d$ orbital obtained in this manner is highly satisfactory for all $1s$ hole states with a valence electron arrangement of $1s^{-1}3d^74s$. However it differs significantly from the optimal form of the $1s$ hole states, with the valence electron arrangement of $1s^{-1}3d^8$. Consequently, we optimize a $\overline{4d}$ orbital on $1s^{-1}3d^8$ 4F using two configurations: $1s^{-1}[3d^8 + 3d^7\overline{4d}]$ 4F . Furthermore it is also observed that the $3d$ orbital being used differs from the optimal $3d$ found in states which are of the form $1s^{-1}3d^64s^2$, while the $4s$ also differs from the optimal $4s$ of these types of states. We thus determine further corrector orbitals for each of these cases, by simultaneously optimizing a $\overline{5s}$ and $\overline{5d}$ corrector orbital on the $1s^{-1}3d^64s^2$ 6D state using the following set of configurations: $1s^{-1}[3d^64s^2 + 3d^64s\overline{5s} + 3d^64s\overline{4d} + 3d^64s\overline{5d} + 3d^54s^2\overline{4d} + 3d^54s^2\overline{5d}]$ 6D . Finally, further valence shell correlation is introduced by using a $\overline{4p}$ pseudo orbital which is optimized on the $1s^{-1}3d^64s^2$ 6D state also, but this time we only use the following two configurations: $1s^{-1}[3d^64s^2 + 3d^6\overline{4p}^2]$ 6D . The resulting parameters for this and the other optimized orbitals are given in Table 1.

Table 1. Radial function parameters for Fe^+ orbitals.

nl	c_j	I_j	ζ_j	$\langle r \rangle$	nl	c_j	I_j	ζ_j	$\langle r \rangle$		
$3d$	0.03953	3	11.71760	0.96202	$4p$	0.13463	2	11.63605	2.68050		
	0.31529	3	6.21570			-0.33988	3	4.93808			
	0.32377	3	4.06451			1.00840	4	1.66329			
	0.39096	3	2.54111			$\overline{4d}$	0.45825	3		5.44096	2.50343
	0.08377	3	1.60897				-0.94999	4		1.62731	
$4s$	0.00469	1	39.07900	2.81236	$\overline{5s}$	0.28429	1	10.52423	2.68076		
	-0.04064	1	25.59940			-0.65984	2	10.43637			
	-0.01141	2	21.70570			0.77988	3	6.09671			
	0.11936	2	10.88620			-1.08361	4	2.64182			
	0.06587	3	9.40162			0.89168	5	1.45405			
	-0.06104	3	7.05231		$\overline{5d}$	0.54078	3	6.73270	2.57939		
	-0.30777	3	4.71260			-7.66811	4	1.39691			
	0.03839	4	3.83931			7.99473	5	1.61600			
	0.67820	4	1.86530								
	0.40217	4	1.19327								
	-0.02782	4	0.83151								

With this set of atomic orbitals, the configuration state functions (CSF's) are generated by adding one electron from the orbital basis set, with the exception of the $1s$ orbital, to the following basis distributions; $1s^{-1}3d^7$, $1s^{-1}3d^64s$, $1s^{-1}3d^54s^2$ and the $1s^{-1}3d^6\overline{4p}^2$ hole states configurations for electron correlation purposes. Only the even configurations are considered from this procedure, since all of our target states are of that parity which results in a total of 763 configurations. The eigenenergies of the target states were determined using the atomic structure computer code CIV3 (Hibbert 1975) and are presented in Table 2 relative to the lowest Fe^+ hole state. To our knowledge, no experimental data exist for comparison purposes of all these states and in particular the excited hole states of Fe^+ . We note it is essential to include pseudo-orbitals in order to achieve an accurate description of the target states and that the use of spectroscopic orbitals only cannot fully account for the various correlations occurring in the states resulting from the different core rearrangements.

3.2. Photoionization Calculations

The electron configurations for the neutral Fe in the present calculation are generated by the addition of one electron from the orbital basis set to the target state configurations included in the calculations. Here

Table 2. Fe⁺ term energies relative to the lowest 1s⁻¹3d⁸ hole state

Target State	Energy (a.u.)	Energy (Ryd)	Energy (eV)
1s ⁻¹ 3d ⁸ ⁴ F	0.000000	0.000000	0.0000000
1s ⁻¹ (3d ⁷ ⁴ F)(⁵ F)4s ⁶ F	0.058532	0.117064	1.5927374
1s ⁻¹ (3d ⁷ ⁴ F)(³ F)4s ⁴ F	0.066235	0.132470	1.8023468
1s ⁻¹ 3d ⁸ ⁴ P	0.070907	0.141814	1.9294785
1s ⁻¹ (3d ⁷ ⁵ F)4s ⁴ F	0.088616	0.177232	2.4113651
1s ⁻¹ (3d ⁷ ⁴ P)(⁵ P)4s ⁶ P	0.140332	0.280664	3.8186296
1s ⁻¹ (3d ⁷ ⁴ P)(³ P)4s ⁴ P	0.148154	0.296308	4.0314772
1s ⁻¹ (3d ⁷ ² G)(³ G)4s ⁴ G	0.157481	0.314962	4.2852779
1s ⁻¹ (3d ⁷ ⁴ P)(⁵ P)4s ⁴ P	0.171142	0.342284	4.6570127
1s ⁻¹ (3d ⁷ ² H)(³ H)4s ⁴ H	0.184958	0.369916	5.0329654
1s ⁻¹ (3d ⁷ ² P)(³ P)4s ⁴ P	0.185816	0.371632	5.0563128
1s ⁻¹ (3d ⁷ ² D)(³ D)4s ⁴ D	0.195742	0.391484	5.3264131
1s ⁻¹ (3d ⁶ ⁵ D)(⁶ D)4s ² ⁶ D	0.266753	0.533506	7.2587215
1s ⁻¹ (3d ⁷ ² F)(³ F)4s ⁴ F	0.268866	0.537732	7.3162192
1s ⁻¹ (3d ⁶ ⁵ D)(⁴ D)4s ² ⁴ D	0.271122	0.542244	7.3776081
1s ⁻¹ (3d ⁷ ² D)(³ D)4s ⁴ D	0.384466	0.768932	10.461857

we allow the addition of a 1s orbital, which results in the generation of the 1s²2s²2p⁶3s²3p⁶3d⁷4s ⁵D ground state configuration of neutral Fe and its associated electron correlation configurations, as well as the 1s⁻¹ hole states of both even and odd parity generated by the addition of the other orbitals in the basis set. These odd parity configurations are bound state configurations which are used in the representation of the autoionizing states have *LS*π symmetry values of ⁵P^o, ⁵D^o and ⁵F^o. This approach results in a 'balanced' set of configurations for the neutral and single ionized Fe systems. With a R-matrix boundary radius of 12.3 Bohr it required a minimum of sixty-continuum orbitals for each value of the free electron orbital angular momentum *l* (*l* ≤ 8), to span the outgoing electron energy range of ~ 1.65 keV relative to the lowest lying 1s⁻¹3d⁸ hole state. The K-edge energy for neutral Fe was calculated to be 7.084 keV in suitable agreement with the 7.083 keV theoretical estimate of Verner and

Table 3. K-edge energies for neutral Fe.

Method	Energy (keV)	Energy (Ryd)
9CC ¹	7.1112	522.69
16CC ²	7.0840	520.69
DS ³	7.0830	520.61
EXPT ⁴	7.1240	523.63
EXPT ⁵	7.1160	523.04
EXPT ⁶	7.1120	522.75
EXPT ⁷	7.1150	522.97
EXPT ⁸	7.1140	522.89

¹ Theory: 9-state R-matrix LS coupling

² Theory: 16-state R-matrix LS coupling

³ Theory: DS Central Field Approximation (Verner et al. 1993)

⁴ Experiment (Gas) (Servier 1979)

⁵ Experiment (Solid) (Servier 1979)

⁶ Experiment (Solid) (Servier 1979)

⁷ Experiment (Oxide) (Servier 1979)

⁸ Henke's Tables (Henke et al. 1993)

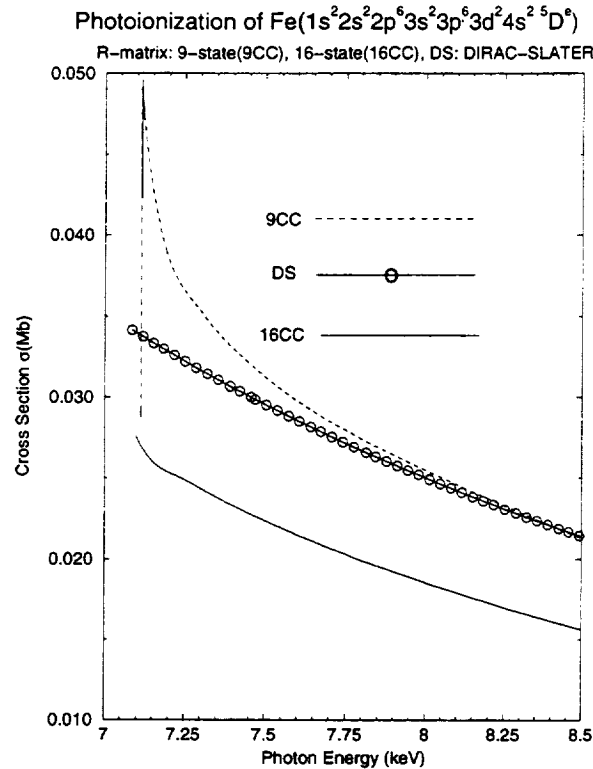


Figure 2. Total cross sections for the $1s$ photoionization of the ground state of neutral iron. Solid line is the 16-state results, for energies (keV) above the hole states, dashed line is that from the 9-state work (Black et al. 1998) and the open circles are those from the relativistic central field approximation (Verner et al. 1993).

co-workers (Verner et al. 1993) and in respectable accord with the available experimental measurements of Servier and co-workers (Servier 1979) and that given in Henke's tables (Henke et al. 1993) and are presented in Table 3.

4. Results

The total $1s^{-1}$ photoionization cross section is calculated by summing the individual contributions from each of the inner-shell processes in equation (1) and including only the two dominant contribution from the $1s^{-1}3d^6 4s^1$ hole states. For the photon energy region from threshold to the highest hole-state included in the calculation an energy resolution of 1.36 meV (10^{-4} Rydbergs) is used to fully resolve the expected resonance structure. Above this region a larger step length of 0.136 eV (10^{-2} Rydbergs) is employed. The sixteen-state results using the length formulation are given in Figures 2 and 3 and are compared with the nine-state results of Black and co-workers (Black et al. 1998) and those from the relativistic central field Dirac-Slater approximation of Verner and co-workers (Verner et al. 1993).

Some striking differences are evident among the three sets of results. The sixteen-state results are unique in that they demonstrate very extensive resonance structure in photon energy region the 7084.351 eV (~ 520.69 Rydbergs) to 7094.827 eV (~ 521.46 Rydbergs) as is illustrated in Figure 4. All three symmetries ($^5F^o$, $^5D^o$ and $^5P^o$) that contribute to the total inner-shell photoionization cross section exhibit strong resonance structure with autoionizing resonance series approaching the $1s^{-1}$ hole state thresholds. These autoionization resonances are of the form $1s^{-1}3d^7 4snp, nf, \dots$, $1s^{-1}3d^6 4s^2 np, nf, \dots$ and $1s^{-1}3d^8 np, nf, \dots$ caused by the electron being able to attach itself to the $1s^{-1}$ hole states. These

resonances represent the autoionizing states as generated by the method described previously. Figure 2 illustrates the region above all the hole states included in the 16-state work whereas Figure 3 displays the photoabsorption cross section for the entire energy region studied, where the energy unit is now given in Rydbergs, From Figures 2, 3 and 4 some striking differences are evident among the three sets of results. Firstly, the sixteen-state results demonstrate extensive resonance structure in the photon energy region 7.084 keV to 7.095 keV as seen in Figure 4. We note that, while of a smaller magnitude, the large jump in the cross section which occurs in the nine-state work at the $1s^{-1}3d^64s^2$ 6D and 4D thresholds (photon energy 7091.562 eV and 7091.698 eV respectively) is also present in the sixteen-state calculation (see Figure 4). It was found that with the exception of some resonance structure, the remaining target states of the form $1s^{-1}3d^8$ and $1s^{-1}3d^74s$ had a negligible contribution to the total background cross section. The $1s^{-1}3d^64s^2$ target states by far give the major contribution to the background cross section as illustrated in Figure 5 compared to the $1s^{-1}3d^8$ states (cf Figure 6) or the $1s^{-1}3d^74s$ states (cf Figure 7). Of consequence to astrophysical modelers, is the fact that throughout the energy range considered the present background cross section lies at best $\sim 20\%$, and at worst $\sim 30\%$, lower than the work of Verner and co-workers (Verner et al. 1993). However, the energy difference between the two sets of data is slowly decreasing, so that at much higher photon energies the two calculations will converge. At higher energies the results of Black and co-workers (Black et al. 1998). and the present work differ roughly by the same amount. Close to threshold, however, the sixteen-state calculations show no sign of the rapid rise (cf Figure 3) demonstrated by Black and co-workers (Black et al. 1998) which appears

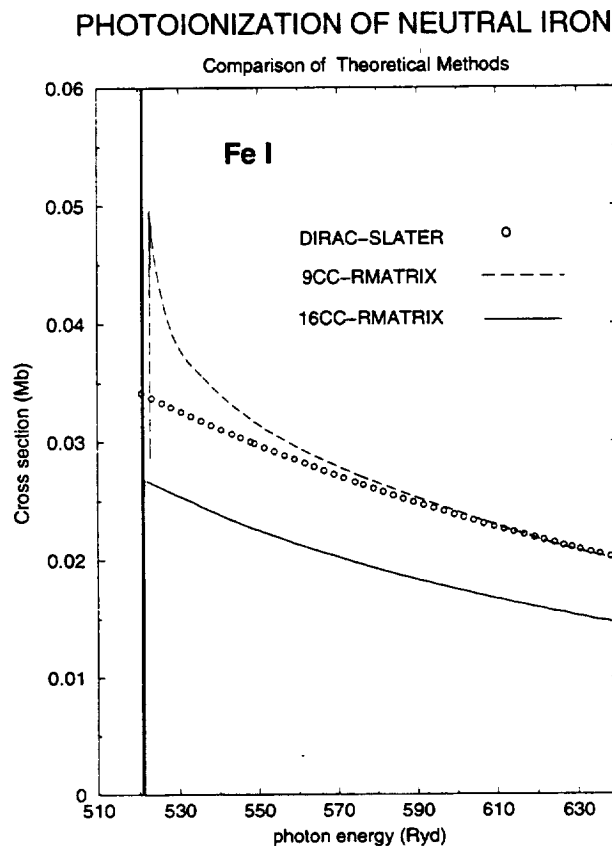


Figure 3. Total cross sections for the $1s$ photoionization of the ground state of neutral iron. Solid line is the 16-state results, at all energies (Rydbergs), dashed line is that from the 9-state work (Black et al. 1998) and the open circles are those from the relativistic central field approximation (Verner et al. 1993).

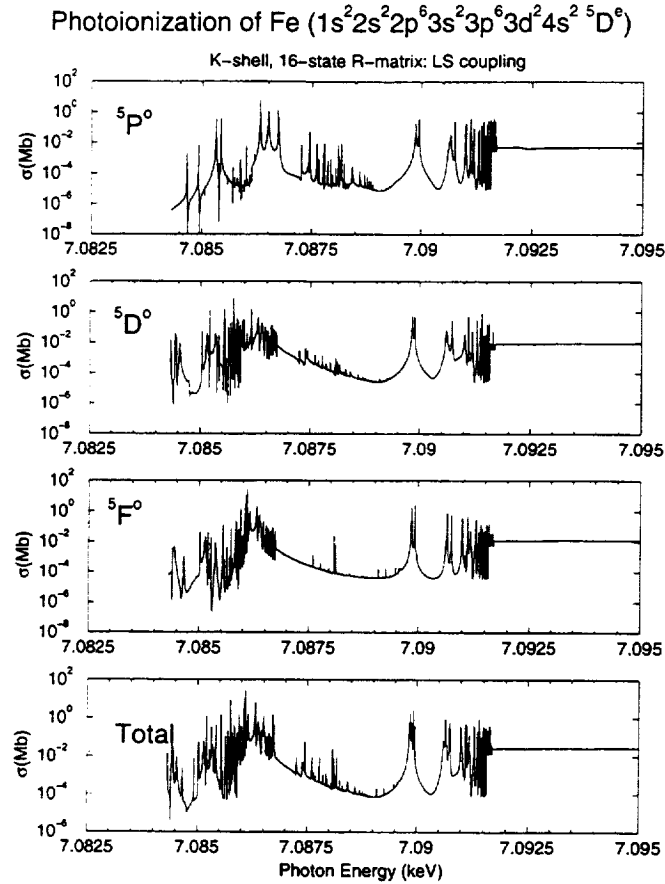


Figure 4. Partial and total cross sections from the sixteen-state R-matrix results performed in LS-coupling. The wealth of resonance structure in the photon region above the K-edge is clearly illustrated.

to have been replaced by the resonance structure as illustrated in Figure 4. The explanation for this significant reduction in the background cross section is related to the degree of configuration interaction included in the various calculations and it should be stressed that the nine-state calculation includes the $1s^{-1}3d^6 4s^2 \ ^6D$ and $1s^{-1}3d^6 4s^2 \ ^6D$ by only a single configuration and neglected any electron correlation effects which are deemed to be important.

We note that the inclusion of configuration interaction gives rise to eigenvector coefficients corresponding to the configurations (i.e. $1s^{-1}3d^6 4s^2 \ ^6D$ and $1s^{-1}3d^6 4s^2 \ ^4D$) which are substantially less than unity. The remaining configurations in the eigenvector expansions do not contribute significantly to the partial cross section. Configuration interaction effects gives rise to the reduction in the total cross section. The agreement between the length and velocity formulations is highly satisfactory but this is not a fool proof method for verifying the accuracy of the cross sections. A rough estimate of the accuracy of the present work can be gauged from the experimental work on the structurally similar neutral nickel system (Parthasaradhi et al. 1998). The spectrum of neutral Ni near its K-edge is similar to that resolved in the present work. Secondly, Wang Dachun and co-workers (Wang et al. 1992) have experimentally determined the X-ray attenuation coefficients for neutral Fe which allow the calculation of the *total* cross section at the threshold. Examination of the neutral Fe experimental data before and after threshold gives us a rough value of the *1s* cross section which unfortunately also includes electron scattering contributions. While experimental results are within 20% of the present work, it is not possible to draw conclusions from these data about the accuracy of our calculation.

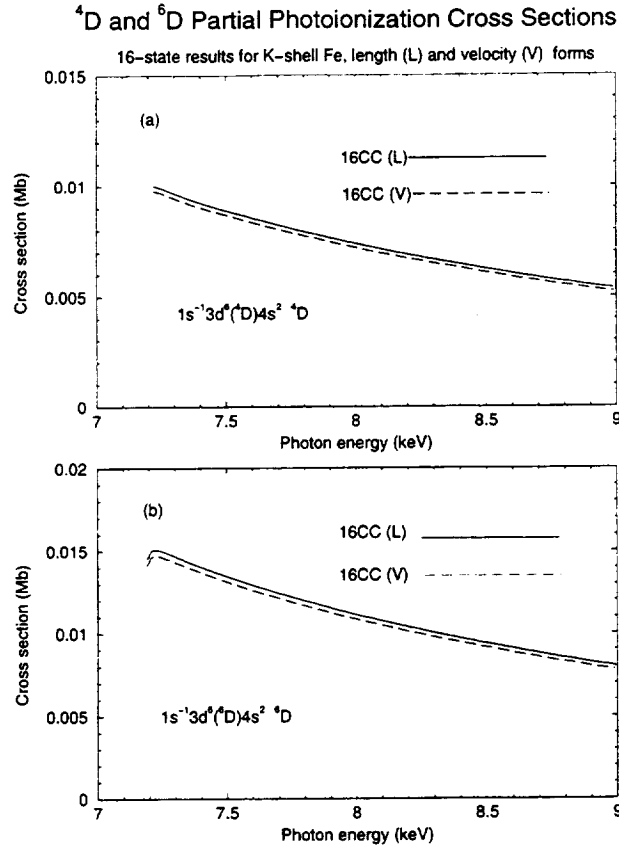


Figure 5. Length and velocity forms of the partial cross sections for the $1s$ photoionization of the ground state of neutral iron, leaving the resulting Fe^+ ion in the (a) $1s^{-1}3d^6 4s^2 \ ^4D$ and (b) $1s^{-1}3d^6 4s^2 \ ^6D$ hole states.

5. Future Work

The discussion on the K-shell photoionization of neutral Fe presented above concentrated on including only the $1s^{-1}$ hole states. It is clear from the various investigations presented above that there are many limitations of these calculations. First and foremost is the fact that only the Fe^+ $1s^{-1}$ hole states are included in both the nine and sixteen-state R-matrix calculations, whereas the valence states of Fe^+ are totally neglected. This may be suitable if one is primarily interested in energies above the K-edge. However neglecting the valence states effectively discounts the structure approaching the K-edge from below. Their inclusion is of importance if one is interested in calculating the optical constants f_1 and f_2 from the photoabsorption cross sections for applications (Henke et al. 1993). The majority of ab initio calculations to date have been carried out in LS - coupling. There is very limited work which takes into account relativistic effects, which are clearly important for the neutral iron system. The work of Verner and co-workers (Verner et al. 1993) attempts to cater for relativistic effects admittedly within the confines of the Dirac-Slater approach at the single configuration level but this work totally neglects any resonances effect. A thorough study where both relativistic and correlation effects are included in the theoretical model is required. Such relativistic effects can be investigated within the context of the R-matrix approach, either at the Breit-Pauli level or within a fully Dirac approach and are presently being investigated. If one envisages including valence and hole states of Fe^+ other than $1s^{-1}$ then the limitations of present day computer architectures will be the major factor which curtails the number of states included in any calculation. Furthermore, investigation into the size of the basis set required has

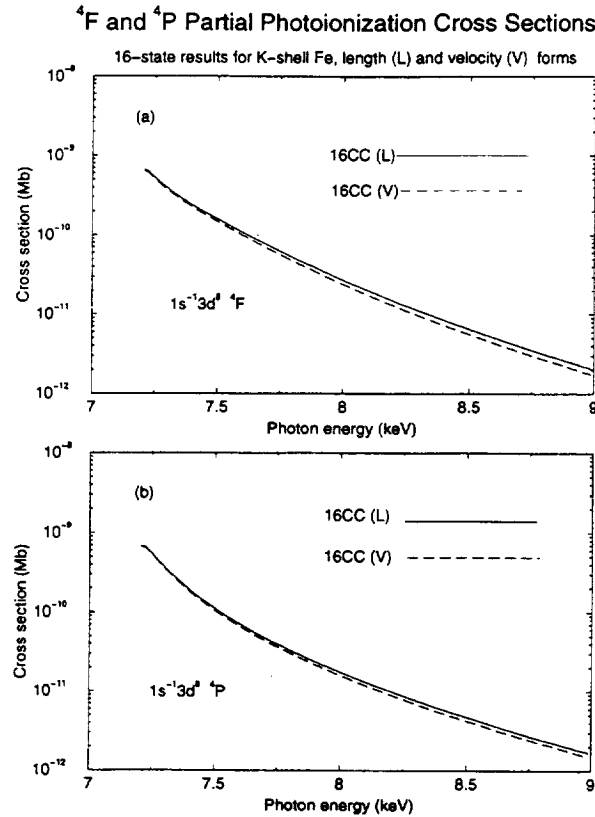


Figure 6. Length and velocity forms of the partial cross sections for the $1s$ photoionization of the ground state of neutral iron, leaving the resulting Fe^+ ion in the (a) $1s^{-1}3d^8 {}^4F$ and (b) $1s^{-1}3d^8 {}^4P$ hole states.

to be addressed so that highly correlated targets state of Fe^+ can be included, when additional hole and valence states are included. Finally the numerical stability of the continuum basis regarding the number of terms required to span the 7 keV range between the ground state and the $1s^{-1}$ hole states of singly ionized iron is another fundamental problem to be addressed.

6. Summary

The status of K-shell photoionization of neutral iron has been reviewed. A comparison with the available (although limited) experimental data and existing theoretical work is made for this important element. Several anomalies and features are illustrated and future directions of theoretical work are indicated. We have presented the results from the current ‘*state of the art*’ ab initio R-matrix calculations for K-shell photoionization of neutral iron. Resonance structure near threshold has been fully resolved and a background approximately 25% lower than previous work has been determined, the difference being attributed to correlation effects in the target. It should be emphasized that the results reported are not definitive and more extensive calculations are still required. A more *definitive* calculation would ideally include a large number of ‘hole’-states together with valence states. However, we have shown the importance of including correlation effects on the background total cross section.

Acknowledgments. The work reported on here was supported by grants from the UK PPARC program. BMMCL would like to thank a number of people; Dick Edgar, Douglas Swartz, John Houck, John Raymond and Randall Smith for many intensive discussions which contributed to this article.

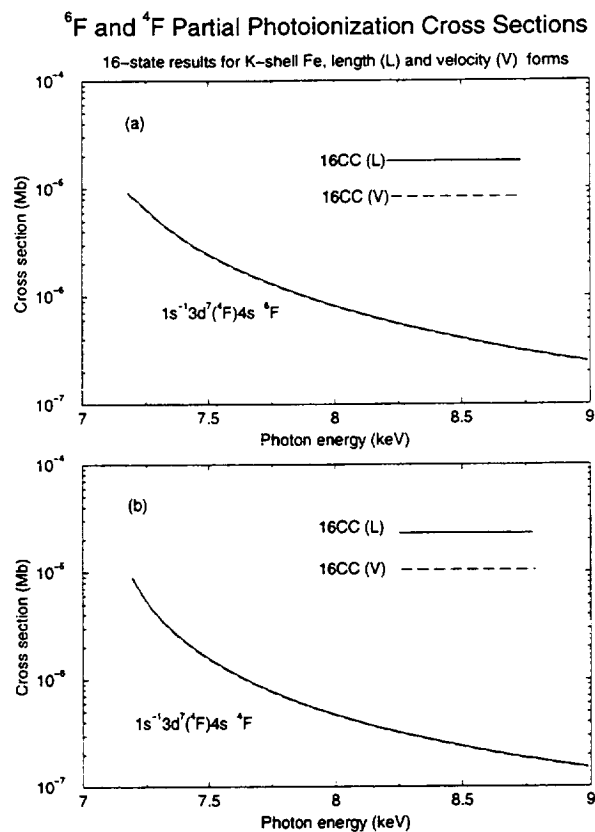


Figure 7. Length and velocity forms of the partial cross sections for the $1s$ photoionization of the ground state of neutral iron, leaving the resulting Fe^+ ion in the (a) $1s^{-1}3d^7 4s\ {}^6F$ and (b) $1s^{-1}3d^7 4s\ {}^4F$ lowest hole states.

References

- Bai, T. 1979, *Sol. Phys.* 62, 113, *erratum Sol. Phys.* 64, 417.
- Bautista, M.A. and Pradhan, A.K. 1995, *J. Phys. B: At. Mol. & Opt. Phys.* 28, L173.
- Black, G.M., Donnelly, D., Bell, K.L., Scott, M.P., and Keenan, F.P. 1998, *Astron. and Astrophys.* 337, L21.
- Burke, P.G. and Berrington, K.A. (eds.) 1993, "Atomic and Molecular Processes an R-matrix Approach" (Bristol : IOP Publishing).
- Clementi, E. and Roetti, C. 1974, *At. Data Nucl. Data Tables* 14, 177.
- Donnelly, D., Bell, K.L., Scott, M.P., Keenan, F.P., and McLaughlin, B.M. 1999, X99 contributed papers: (<http://www.phy.anl.gov/X99>), *X-ray and Inner-shell Processes*, 154.
- Donnelly, D., Bell, K.L., Scott, M.P., and Keenan, F.P. 2000, *ApJ* 531, 1168.
- Henke, B.L., Gullikson, E.M., and Davis, J.C. 1993, *At. Data. Nucl. Data Tables* 54, 181.
- Hibbert, A. 1975, *Comput. Phys. Commun.* 11, 141.
- Mushotzky, R.F., Done, C. and Pounds, K.A. 1993, *Ann. Rev. Astron. and Astrophys.* 31, 717.
- Parmar, A.N., Wolfson, C.J., Culhane, J.L., Phillips, K.J.H., Acton, L.W., Dennis, B.R., and Rapley, C.G. 1984, *ApJ* 279, 866.
- Parthasaradhi, K., Esposito, A., Mobilio, S., and Pelliccioni, M. 1998, *Phys. Rev. A* 38, 1608.

- Phillips, K.J.H., Pike, C.D., Lang, J., Watanabe, T., and Takahashi, M. 1994, *ApJ* 435, 888.
- Servier, K.D. 1979, *At. Data Nucl. Data Tables* 24, 323.
- Verner, D.A. and Yakovlev, D.G. 1995, *Astron. and Astrophys. Suppl.* 109, 125.
- Verner, D.A., Yakovlev, D.G., Band, I.M., and Trzhaskovskaya, M.B. 1993, *At. Data Nucl. Data Tables* 55, 233.
- Wang, D., Ding, X., Wang, X., Yang, H., Zhou, H., Shen, X., and Zhu, G. 1992, *Nucl. Instr. Meth. Phys. Res. B* 71, 241.

The R-matrix with Pseudostates Method

T. W. Gorczyca,¹ N. R. Badnell,² D. C. Griffin,³ D. M. Mitnik,⁴ and M. S. Pindzola⁴

¹Department of Physics, Western Michigan University, Kalamazoo, Michigan 49008-5151

²Department of Physics and Applied Physics, University of Strathclyde, Glasgow G4 0NG, UK

³Department of Physics, Rollins College, Winter Park, Florida 32789

⁴Department of Physics, Auburn University, Auburn, Alabama 36849-5311

Abstract. We review the development of pseudostate methods for treating electron-ion collision processes. We describe our implementation of these methods within the Wigner–Eisenbud R-matrix method. We present recent results for photoionization, electron-impact excitation, and electron-impact ionization, which demonstrate the importance of properly accounting for the two-electron continuum. The comparison with experimental, as well as other theoretical, electron-impact ionization results suggests that there may be inaccuracies in the overall normalization of earlier measurements. This is confirmed in the case of Al²⁺ by a more recent experimental study. The implications regarding the use of excitation and ionization rates from existing databases for modeling astrophysical plasmas are discussed.

1. Introduction

The close-coupling method (Massey and Mohr 1932), as developed for continuum Hartree-Fock solutions by Seaton (1953), has proven to be a practical means for studying electron-ion collision phenomena because the individual behavior of both the colliding and ionic electrons is revealed. In its most general form, the close-coupling wavefunction for a quasi two-electron system can be expanded as the sum of product wavefunctions (angular coupling and antisymmetrization are assumed):

$$\Psi(\vec{r}_1, \vec{r}_2) = \sum_i \Phi_i(\vec{r}_1) f_i(\vec{r}_2) + \int d\vec{k} \Phi_{\vec{k}}(\vec{r}_1) f_{\vec{k}}(\vec{r}_2). \quad (1)$$

In this close-coupling expansion, Φ_i and $\Phi_{\vec{k}}$ are the (denumerably infinite) bound and (indenumerably infinite) continuum wavefunctions of the one-electron ion, and f_i and $f_{\vec{k}}$ are the wavefunctions for the scattering electron, which are determined by solving the close-coupling equations. The R-matrix method (Burke and Berrington 1993), in particular, is widely used for this purpose.

Of course, only a finite close-coupling expansion can be used in any numerical treatment. It is the choice of which terms to retain that truly defines the art of performing electron-ion collision calculations within basis expansion methods. The earliest close-coupling calculations for electron-hydrogen collisions could only include the lowest six states (1s, 2s, 2p, 3s, 3p, 3d), given the computational power available at the time. However, it was pointed out by Castillejo et al. (1960) that the atomic polarizability, which is given by

$$\alpha = \sum_{n>1} \frac{\langle \Phi_{1s} | \vec{r} | \Phi_{n\ell} \rangle \langle \Phi_{n\ell} | \vec{r} | \Phi_{1s} \rangle}{E_{n\ell} - E_{1s}} + \sum_{\vec{k}} \int dk \frac{\langle \Phi_{1s} | \vec{r} | \Phi_{k\ell} \rangle \langle \Phi_{k\ell} | \vec{r} | \Phi_{1s} \rangle}{E_{k\ell} - E_{1s}}, \quad (2)$$

received an 18.4% contribution from the second term in Equation (2). This means that the two-electron continuum must be included in order to accurately describe the polarization of the hydrogen atom by an incoming electron. Indeed, the seminal close-coupling calculations on $e^- - \text{H}$ by Burke et al. (1963) found a major disagreement with experimental results for the 1s \rightarrow 2p excitation. Burke and coworkers had truncated their atomic expansion to the $n = 3$ states and they concluded that “these discrepancies probably can not be reconciled by any close-coupling expansion”, referring to the denumerably infinite number of bound terms Φ_i in Equation (1).

In subsequent studies, and following the Sturmian basis set ideas of Rotenberg (1962), Burke et al. (1969) introduced into the close-coupling expansion the so-called *pseudostates*. These are unphysical orbitals which in general overlap with both the bound and continuum hydrogenic orbitals $\Phi_{n\ell}$ and $\Phi_{k\ell}$. A distinctly improved convergence over the earlier e^- -H results was obtained but non-trivial discrepancies with experiment remained. Despite remarkable advances in computational power over the next two decades, and the development of more sophisticated pseudostate methods (e.g. Scott et al. 1989, and reference therein) the disagreement between theory and experiment for e^- -H collisions remained unresolved.

Then, in 1992, Bray and Stelbovics (1992) resolved the discrepancy by performing *Converged Close-Coupling* (CCC) calculations. They solved the Lippmann-Schwinger (momentum-space) equations with a large expansion of Laguerre pseudoorbitals and obtained e^- -H elastic and excitation cross sections that were in good agreement with experiment. This was an important triumph for it indicated that the indenumerably infinite two-electron continuum expansion in Equation (1) could be adequately represented by a finite pseudostate expansion. Furthermore, it was found that electron-impact ionization cross sections could be extracted by analyzing the excitation to pseudostates Bray and Stelbovics (1993).

Following up on this encouraging breakthrough, Meyer and Greene (1994) applied a large pseudostate expansion within their (position-space) Eigenchannel R-matrix method and were able to calculate helium photo-double-ionization cross sections in excellent agreement with the latest experimental results (Meyer et al. 1997). This achievement was particularly important because it demonstrated that the R-matrix method could be used to perform converged pseudostate calculations, at least in principle.

The Belfast (Wigner-Eisenbud) R-matrix codes (Burke and Berrington 1993; Berrington 1995) are extremely robust in that they can be used to study electron-ion systems of arbitrary complexity. Having found essentially equivalent results using two separate R-matrix codes in a joint study (Bartschat and Green 1993) the success of the Eigenchannel R-matrix method for treating the two-electron continuum suggested that the Wigner-Eisenbud R-matrix method should be capable of the same. Indeed, after overcoming some tricky issues dealing with non-orthogonal orbitals and unphysical R-matrix poles, Bartschat et al. (1996) developed the *R-matrix with Pseudostates* (RMPS) method for use within the Belfast R-matrix codes. Bartschat and coworkers have successfully applied their RMPS method to treat two-electron processes in the photoionization and electron-impact excitation and ionization of numerous atomic systems (Bartschat 1998).

2. Two-Electron Photoionization Processes

The present implementation of the RMPS method (Gorczyca and Badnell 1997) arose independently from that of Bartschat and coworkers in response to a void of theoretical calculations for the higher- n photoionization-excitation of helium:



In particular, the effective angular distribution parameter β_n^{eff} , which characterizes the differential photoionization-excitation cross section via

$$\frac{d\sigma_{n\ell}}{d\Omega} = \frac{\sigma_{n\ell}}{4\pi} [1 + \beta_{n\ell} P_2(\cos\theta)] , \text{ and } \beta_n^{eff} = \frac{\sum_{\ell=0}^{n-1} \sigma_{n\ell} \beta_{n\ell}}{\sum_{\ell=0}^{n-1} \sigma_{n\ell}} , \quad (4)$$

had been measured for $n = 2-6$, yet theoretical calculations only existed for $n = 2$ (Wehlitz et al. 1993). It was immediately found that a standard R-matrix approach for treating the $n = 3$ processes which used only physical orbitals (basis set 1) showed major qualitative differences from the observed behavior (see Figure 1), especially on using the length form of the dipole operator (this places more emphasis on the large- r portion of the wavefunction). Whereas the angular distribution should have the high-energy behavior $\frac{d\sigma_3}{d\Omega} \approx \cos^2\theta$ ($\beta \rightarrow 2$) due to the dominance of the 3s excitation, the length form using basis 1 shows a nearly isotropic result ($\beta \approx 0$) at 200 eV. The use of physical states alone seriously fails to describe even the qualitative nature of the ionized electron's angular distribution.

On first introducing pseudoorbitals into the close-coupling expansion, we encountered severe difficulties with regards to the issues of the non-orthogonality of basis functions and unphysical R-matrix

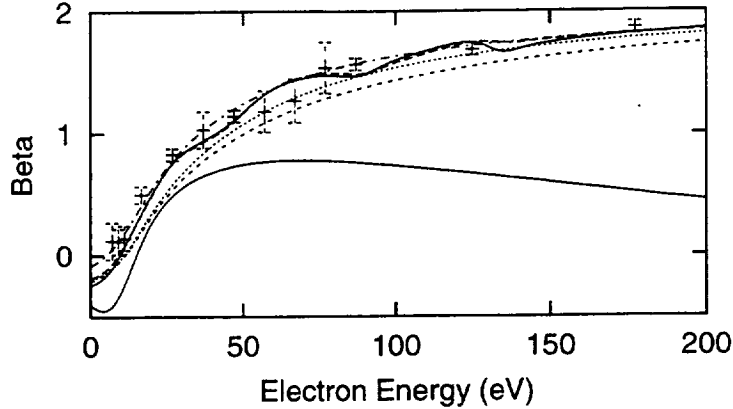


Figure 1. RMPS asymmetry parameters for $h\nu + \text{He}(1s^2) \rightarrow \text{He}^+(3\ell) + e^-$: basis 1, length (full curve) and velocity (chain curve), basis 2, length (dashed curve) and velocity (broken curve), and basis 3, length (full curve) and velocity (long broken curve) results. The basis 1 length curve invariably shows the poorest overall behavior compared to the others. The experimental values (\diamond) are from Wehlitz et al. (1993).

poles. We found it essential to modify the codes in order to 1) implement a stable Gram-Schmidt orthogonalization procedure for overlapping basis sets which retained only the minimum set of linearly independent orbitals, and 2) use a *different* Buttle correction (Burke and Berrington 1993) which takes into account the use of non-orthogonal orbitals (Gorczyca and Badnell 1997). The agreement obtained with experiment is much better on using pseudoorbitals to improve the ground-state wavefunction (basis set 2), but there is still a noticeable split between the length and velocity results. The two are finally brought into close agreement when pseudoorbitals are used to describe the final continuum state as well. We point out that, on using several pseudoorbitals — even in the ground state description alone, the above two modifications were crucial for obtaining meaningful scattering information.

3. Double Continuum Effects in Electron-Impact Excitation

In a recent study (Griffin et al. 2000), the RMPS method was used to study electron-impact excitation in C^{3+} and O^{5+} . A comparison of results from a standard R-matrix calculation and an RMPS one are shown in Figure 2. It is seen immediately that the effect of the double continuum is to cause a reduction, by as much as a factor of two, in the computed cross section over a wide range of energies. Of course, this level of correction due to the double continuum occurs only for excitation to the $n = 4$ states and higher; excitation to the lower terms show smaller effects. Still, this suggests that many electron-impact excitation rates currently in data bases that are used by plasma modelers may be an overestimate since they are normally computed using standard close-coupling (i.e. non-pseudostate) methods.

4. Electron-Impact Ionization

The sum of electron-impact excitation cross sections to pseudostates that lie above the ionization limit can be interpreted as an ionization cross section, since the pseudostates have predominantly continuum character. Together with two completely independent approaches — the well-known *Distorted Wave* (DW) method and the *Time-Dependent Close-Coupling* (TDCC) method — we performed RMPS calculations for three ions of the Li-like sequence, Be^+ (Pindzola et al. 1997), B^{2+} (Woitke et al. 1997; Marchalant et al. 1997), and C^{3+} (Mitnik et al. 1999). We compared our calculated ionization cross sections to existing experimental results — for Be^+ (Falk and Dunn 1983), B^{2+} (Crandall et al. 1986; Experiment (b) in Figure 3), and C^{3+} (Crandall et al. 1982), and a new experimental result for B^{2+} (Woitke et al. 1997) (Experiment (b) in Figure 3). An important trend is highlighted in the figures: (1)

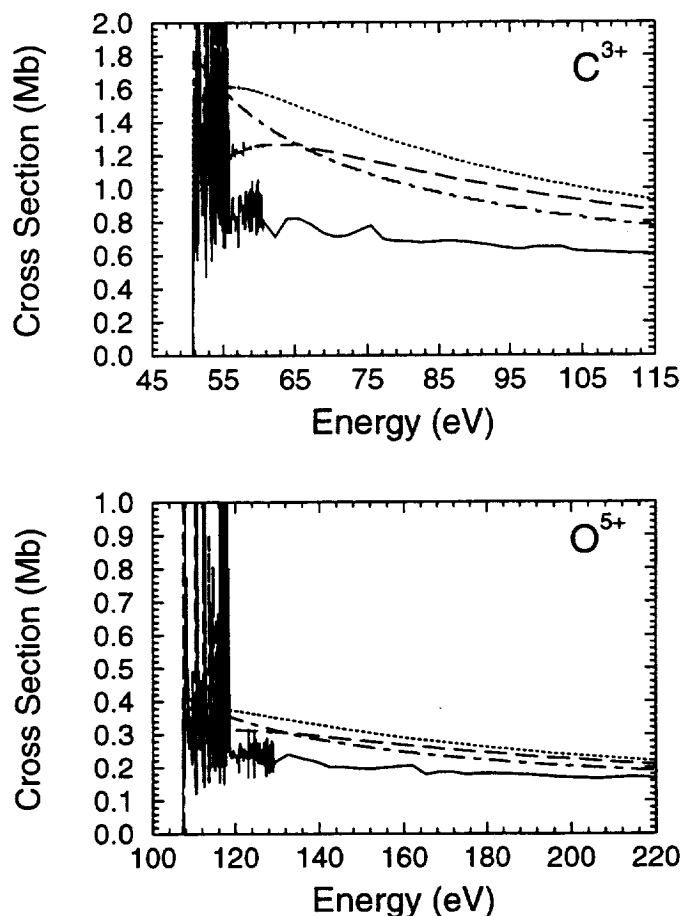


Figure 2. Electron-impact excitation cross sections for the $2s \rightarrow 4d$ transition in C^{3+} and O^{5+} . The dotted curves are from a 9-state non-pseudostate R-matrix calculation; the dashed curves are from a 13-state non-pseudostate R-matrix calculation; the solid curves are from a 41-state RMPS calculation; and the dot-dashed curves are from the fitting formula of Fischer et al. (1997).

the experimental results are much larger than the theoretical ones for Be^+ ; (2) the experimental and theoretical results are about the same for B^{2+} ; (3) the experimental results are significantly less than the theoretical results for C^{3+} .

The excellent agreement between the RMPS and TDCC results tends to suggest that the disagreement with experiment is due to an uncertainty in the normalization of the experiment. This is supported somewhat by the improved agreement between theory and experiment found in the more recent measurements (Woitke et al. 1997; Marchalant et al. 1997), but even more so from a comparison between theoretical and experimental results in another system. In a joint study that used the RMPS, TDCC, and CCC methods to compute the electron-impact ionization cross section of Al^{2+} (Badnell et al. 1998), it was found that, whereas all three *completely independent* theoretical methods gave results in excellent agreement with each other, they were all much larger than the experimental results that existed at that time (Crandall et al. 1998; see Figure 4). As a result of these findings, a new measurement was performed (Thomason and Peart 1998) which gave a cross section that is in much better agreement with the theoretical results, as seen in Figure 4. This is a particularly important example where the theoretical electron-ion studies were able to detect a probable error in the experimental normalization.

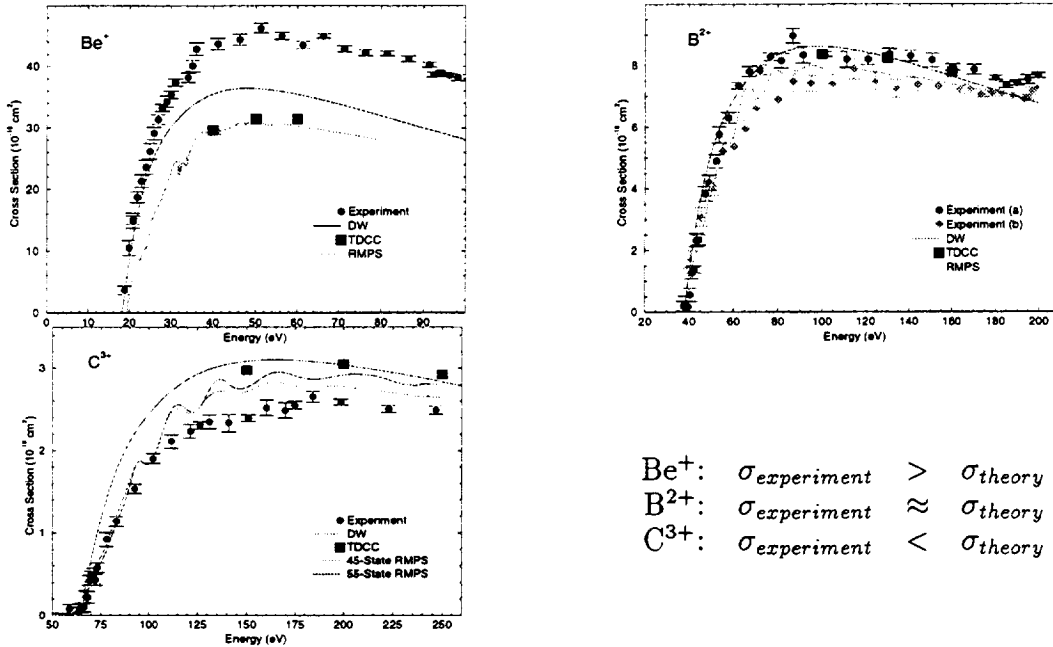


Figure 3. Electron-impact ionization of Li-like ions: comparison between theoretical and experimental results.

5. Conclusion

We have presented a brief review of the history leading up to recent pseudostate work in order to highlight the main ideas behind the RMPS method, and to elucidate the importance of double continuum processes in electron-ion collisions. It has been demonstrated that the use of pseudoorbitals is necessary even just to reproduce the gross features of photoionization angular distributions involving two

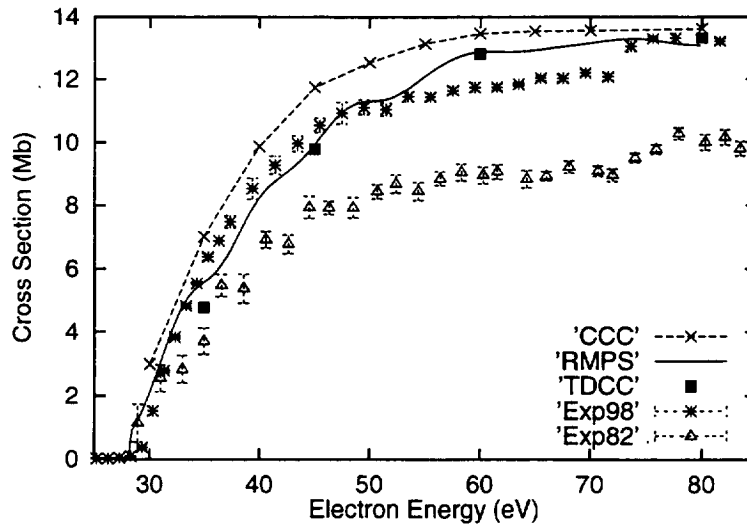


Figure 4. Electron-impact ionization of Al²⁺: comparison of various theoretical (Badnell et al. 1998), earlier experimental (Crandall et al. 1982) and more recent experimental (Thomason and Peart 1998) results.

electrons. The two-electron continuum was also shown to play an important role in electron-impact excitation, significantly reducing the cross section (by as much as a factor of two) over a wide range of energies. Furthermore, electron-impact ionization cross sections can be extracted from pseudostate calculations. Of particular importance, the results from the RMPS calculations and two other independent state-of-the-art calculations, which are all in excellent agreement with each other, have shown large differences when compared to experimental results, suggesting that the experimental normalization may be incorrect. Indeed, a more recent experimental study in Al^{2+} reported absolute ionization cross sections that are in good agreement with the latest theoretical calculations, and which are much larger than the results of earlier measurements. These findings have important implications for the modelers of astrophysical plasmas since they indicate that many of the atomic rates that exist in databases at present are subject to larger uncertainties than may have been realized in the past.

References

- Badnell, N.R., Pindzola, M.S., Bray, I., and Griffin, D.C. 1998, *J. Phys.* B31, 911.
- Bartschat, K. 1998, *Comput. Phys. Commun.* 114, 168.
- Bartschat, K., Hudson, E.T., Scott, M.P., Burke, P.G., Burke, V.M. 1996, *J. Phys.* B29, 115.
- Burke, P.G. and Berrington, K.A. 1993, "Atomic and Molecular Processes: An R-matrix Approach" (IOP, Bristol).
- Bray, I. and Stelbovics, A.T. 1992, *Phys. Rev. A* 46, 6995.
- 1993, *Phys. Rev. Lett.* 70, 746.
- Burke, P.G., Gallaher, D.F., and Geltman, S. 1969, *J. Phys.* B2, 1142.
- Berrington, A.K., Eissner, W.B., and Norrington, P.H. 1995 *Comput. Phys. Commun.* 92, 290.
- Burke, P.G., Schey, H.M., and Smith, K. 1963, *Phys. Rev.* 129, 1258.
- Castillejo, L., Percival, I.C., and Seaton, M.J. 1960, *Proc. Roy. Soc. A* 254, 259.
- Crandall, D.H., Phaneuf, R.A., Falk, R.A., Belić, D.S., and Dunn, G.H. 1982, *Phys. Rev. A* 25, 143.
- Crandall, D.H., Phaneuf, R.A., Gregory, D.C., Howald, A.M., Mueller, D.W., Morgan, T.J., Dunn, G.H., Griffin, D.C., and Henry, R.J.W. 1986, *Phys. Rev. A* 34, 1757.
- Crandall, D.H., Phaneuf, R.A., Hasselquist, B.E. and Gregory, D.C. 1979 *J. Phys.* B12, L831.
- Falk, R.A. and Dunn, G.W. 1983, *Phys. Rev. A* 27, 754.
- Fisher, V.I., Ralchenko, Y.V., Bernshtam, V.A., Goldgirsh, A., Maron, Y., Vainshtein, L.A., and Bray, I. 1997, *Phys. Rev. A* 56, 4821.
- Gorczyca, T.W. and Badnell, N.R. 1997, *J. Phys.* B30, 3897.
- Griffin, D.C., Badnell, N.R., and Pindzola, M.S. 2000, *J. Phys.* B33, 1013
- Marchalant, P.J., Bartschat, K., and Bray, I. 1997 *J. Phys.* B30, L435.
- Massey, H.S.W. and Mohr, C.B.O. 1932, *Proc. R. Soc. A* 136, 289.
- Meyer, K.W. and Greene, C.H. 1994, *Phys. Rev. A* 50, R3573.
- Meyer, K.M., Greene, C.H., and Esry, B.D. 1997, *Phys. Rev. Lett.* 78, 4902.
- Mitnik, D.W., Pindzola, M.S., Griffin, D.C. and Badnell, N.R. 1999, *J. Phys.* B32, L479.
- Pindzola, M.S., Robicheaux, F., Badnell, N.R., and Gorczyca, T.W. 1997, *Phys. Rev. A* 56, 1994.
- Rotenberg, M. 1962, *Ann. Phys. N. Y.* 19, 262.
- Scott, M.P., Scholz, T.T., Walters, H.R.J. and Burke, P.G. 1989, *J. Phys.* B22, 3097.
- Seaton, M.J. 1953, *Proc. R. Soc. Lond. Ser. A* 218, 400.
- Thomason, J.W.G. and Peart, B. 1998, *J. Phys.* B31, L201.
- Wehlitz, R., Langer, B., Berrah, N., Whitfield, S.B., Viehhaus, J. and Becker, U. 1993, *J. Phys.* B26, L783.
- Woitke, O., Djurić, N., Dunn, G.H., Bannister, M.E., Smith, A.C.H., Wallbank, B., Badnell, N.R., Pindzola, M.S. 1997, *Phys. Rev. A* 58, 4512.

Laboratory Data for X-Ray Astronomy

P. Beiersdorfer¹, G. V. Brown¹, H. Chen¹, M.-F. Gu², S. M. Kahn²
J. K. Lepson³, D. W. Savin², S. B. Utter¹

¹*High Temperature and Astrophysics Division, Lawrence Livermore National Laboratory
7000 East Ave., Livermore, CA 94550, USA*

²*Department of Physics, Columbia University, 538 W 120th St., New York, NY 10027, USA*

³*Space Sciences Laboratory, University of California, Berkeley, CA 94720, USA*

Abstract. Laboratory facilities have made great strides in producing large sets of reliable data for X-ray astronomy, which include ionization and recombination cross sections needed for charge balance calculations as well as the atomic data needed for interpreting X-ray line formation. We discuss data from the new generation sources and pay special attention to the LLNL electron beam ion trap experiment, which is unique in its ability to provide direct laboratory access to spectral data under precisely controlled conditions that simulate those found in many astrophysical plasmas. Examples of spectral data obtained in the 1–160 Å wavelength range are given illustrating the type of laboratory X-ray data produced in support of such missions as *Chandra*, *XMM*, *ASCA* and *EUVE*.

1. Introduction

The field of X-ray astronomy has shifted from simple source detection to detailed spectroscopic investigation. The culmination of mapping out X-ray sources came with *ROSAT*, which provided a catalogue of over 60,000 detected sources, covering nearly all categories of X-ray emitting astrophysical objects. Subsequent observations conducted with *ASCA* have demonstrated the great spectral diversity among the different objects. The X-ray band from 0.1 to 10 keV is rich in discrete spectral line emission and comprises the K-shell emission from carbon through nickel, the L-shell emission from neon through nickel, and the M-shell emission from iron and nickel. The *ASCA* observations have thoroughly demonstrated that X-ray emission line spectroscopy represents an indispensable tool for understanding the physical conditions in high-temperature cosmic plasmas.

Although *ASCA* observations provided a wealth of new information, they were limited by the relatively low resolving power of *ASCA*'s energy dispersive instrumentation. Present satellite missions, such as *Chandra* and *XMM*, have overcome this limitation using high-resolution dispersive gratings, and now have the spectral resolution to discern individual spectral features and thus to resolve many of the lines important for plasma diagnostics. This opens the X-ray band to scientific scrutiny in unprecedented fashion.

Successful and reliable interpretation of these X-ray spectra requires an adequate understanding of the atomic data underlying the emission. Cosmic X-ray sources are never in local thermodynamic equilibrium. Calculations of the spectral emission, therefore, must be based on detailed accounting of all microphysical processes that feed and deplete a given quantum level in ions that more often than not have a complex atomic structure. Temperature gradients, transient phenomena, photon fields, flows and shocks further complicate the picture and require atomic data valid also for plasmas outside equilibrium.

The atomic data needs can be grouped into two categories. The first comprises the ionization and recombination data needed for determining the proper ionization structure of the emitting sources. These data determine the relative abundances of each ionization stage of a given element in the plasma. The second comprises the data needed to describe the radiation produced by a given ionization state. These data determine what lines are produced given the properties of the ambient plasma and their relative intensities. Clearly, both types of atomic data are needed to describe the observed line features. The first provides the particle, the second the photon mix.

Calculation of the atomic data in many cases is difficult or very time consuming. Relativity cannot be neglected in intermediate- Z ions so that intermediate coupling must be used to describe the atomic structure. The proper predictions of ionization and recombination rates involve many processes such as resonant excitation-autoionization, recombination into metastable levels, etc, that are more often than not missing from calculations. Nevertheless, these calculations are arguably still less complex than those necessary for proper prediction of the X-ray emission from a given ion species. The latter not only must include line formation by recombination and ionization phenomena, but also radiative cascades from higher-lying levels, resonance excitation, radiative decay by higher-order multipoles, and collisional deexcitation, among others. Because of this complexity, most calculations compute only a fraction of the entire problem. Even then, they must rely on approximations.

The need for laboratory measurements is clear. Again and again laboratory data have shown that calculations are incomplete, i.e., that they are missing crucial physics left out as part of the approximations. And laboratory data provide the yard stick by which to determine the accuracy of calculations. They are used as means to decide when a given calculational result is "good enough", i.e., when to break off a time-consuming calculation.

The conventional approach in laboratory measurements has been to measure a given cross section, wavelength, or rate and compare it with theory. While this approach, which simply isolates a single piece of a very complex puzzle, is standard in atomic physics, it does not work for laboratory astrophysics. Approaches are needed that address a whole set of processes working together and cover the whole spectrum. Advances in experimental design during the past decade have allowed such measurements. New generation atomic physics devices have been developed that act as "analog computers" providing the data needed to describe X-ray spectra in detail. These devices are: (1) merged and crossed beam facilities for the measurement of ionization cross sections, (2) ion storage ring facilities for the measurement of ionization cross sections and low-energy dielectronic recombination resonances, (3) late-generation synchrotrons for photoionization measurements, and (4) electron beam ion traps for measurements of electron-ion excitation cross sections and high-energy dielectronic recombination resonances.

The new laboratory devices have in common that large sets of atomic data can be generated in a rather short amount of time. No longer is it necessary to measure one small piece of the puzzle over a long period of time. Once the experimental conditions are set up, say for measuring dielectronic recombination, much of the same data can be produced in a relatively short time. For example, by sweeping the energy of the electron cooler in a storage ring all dielectronic resonances can be measured for a given ion that fall into the energy range accessible with the electron beam. Similarly, by sweeping the beam energy in the electron beam ion trap all excitation processes contributing to a given line can be measured. The new generation machines thus contrast starkly with older plasma sources such as sparks and lasers, where most of the experimental time is spent understanding the source itself. The new devices are ready to go on demand and can thus truly function as analog computers that can generate the desired data more accurately than computer codes do. Moreover, the new sources operate in a low-density regime so that the data are directly applicable to most astrophysical plasmas.

Unlike computer codes, controlled measurements can in principle account for all processes. None of the physics is left out. For example, if the Breit-interaction is relevant for a given dielectronic resonance, it is included when the resonance is measured. If quantum electrodynamics shifts a given line position, it will show up in the spectrum. If relativity turns on a particular radiative decay mode, the line will automatically appear in the spectrum. If configuration interaction influences the line intensity, the line intensity will reflect that intensity. If cascade contributions from thousands of levels need to be summed to get the correct flux of a line, the sum will automatically be "computed" in the measurement.

Of course, no measurement is perfect. Setting up the appropriate measurement technique is paramount to measuring the correct quantities with the desired accuracy. When done appropriately, serious measurements provide an invaluable parameter: reliable uncertainty limits. Uncertainty limits are something very few calculations can provide.

One may argue that the combination of being able to generate large amounts of experimental data on demand and to give uncertainty estimates reduces the reliance on calculations and in many cases eliminates it. For example, by using the merged beam technique ionization cross sections for virtually all charge states of iron have been measured in the range below 2 keV and for some as high as 5 keV (Müller 1991, Stenke et al. 1999a,b). Storage rings have refined such measurements so that even minute contributions from exotic processes are included with high accuracy in the measurements

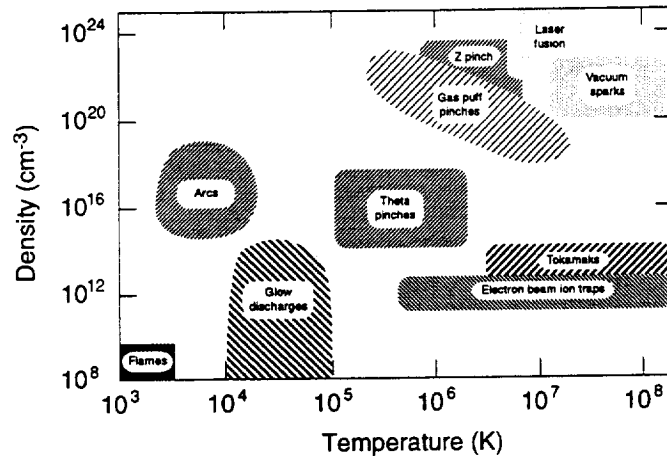


Figure 1. Density and temperature space sampled by different spectroscopic light sources. The EBIT source provides the appropriate charge states found in astrophysical plasmas at densities comparable to stellar atmospheres. Storage rings and merged beam apparatuses are not shown, as they do not generally provide spectroscopic data.

(Linkemann et al. 1995). Similarly, storage rings can measure low-energy recombination rates, both due to dielectronic and radiative capture, for virtually all ions (Andersen et al. 1992; Schuch et al. 1997; Müller et al. 1998). The electron beam ion trap can measure virtually all high-energy dielectronic recombination rates (Beiersdorfer et al. 1992a,b; Knapp et al. 1993). Although not all of these rates have indeed been measured, this nevertheless means that the relevant cross sections and rates that enter charge balance calculations can be measured with existing laboratory apparatuses. Reliance on theoretical cross section calculations could be eliminated in the near future, provided resources were focused on making the necessary measurements.

In the following, we describe measurements performed with the electron beam ion trap (EBIT) at Livermore. Unlike merged beams and storage rings, which measure ionization and recombination by detecting changes in the ion charge, the EBIT measures the radiation emitted by the ions. The data produced by EBIT is thus most closely related to that observed by X-ray missions. In fact, among laboratory sources of X radiation, the EBIT source is the closest in parameter space to those of hot astrophysical X-ray emitting plasmas, as illustrated in Figure 1. Only tokamak sources produce similarly high charge states at relatively low densities; but these plasmas lack the control afforded by the EBIT source. The conditions under which astrophysical spectra are produced can vary considerably – from ionizing plasmas in super nova remnants to stellar coronae in equilibrium and recombining photoionized plasmas surrounding accretion sources. Similarly, spectra at the LLNL EBIT source can be produced under many different conditions that simulate those of astrophysical sources. This allows us not only to measure specific atomic rates but also to test the interplay of different line formation processes. The source thus offers tremendous versatility not found in other laboratory plasmas.

2. The EBIT Source

The electron beam ion trap was designed and implemented at the Lawrence Livermore National Laboratory. It was specifically developed and built for studying the interactions of electrons with highly charged ions using X-ray spectroscopy (Levine et al. 1989). A schematic of the device is shown in Figure 2. Neutral atoms or ions with low charge are injected into a nearly monoenergetic beam where they are collisionally ionized and excited by an electron beam. The beam electrons are confined and focused by a 3 Tesla magnetic field, generated by a pair of superconducting Helmholtz coils. As the beam passes through the trap region of 2-cm length, it is compressed to a diameter of approximately 60 μm . Ions are longitudinally confined in the trap by applying the appropriate voltages to a set of three drift tubes



Figure 2. Artist's view of the EBIT device developed and deployed at Livermore.

through which the beam passes. Radial confinement is provided by electrostatic attraction of the electron beam, as well as flux freezing of the ions within the magnetic field. All three drift tube voltages float on top of a common potential that is supplied by a fast-switching high-voltage amplifier. The electron beam energy is determined by the sum of these potentials and may range between about 150 and 20,000 eV for most measurements of interest. The electron beam density at a given beam energy can be selected by varying the beam current. It typically is in the range of $2 \times 10^{11} - 5 \times 10^{12} \text{ cm}^{-3}$, i.e., in the range of many stellar coronae.

Six axial slots cut in the drift tubes and aligned with six vacuum ports permit direct line-of-sight access to the trap, as shown in Figure 3. One port is used for introducing atomic or molecular gases into the trap by means of a ballistic gas injection system. The remaining five ports are used for spectroscopic measurements. A seventh port on the top of EBIT permits axial access to the trap and is used for the injection of singly charged metal ions into the trap from a metal vapor vacuum arc source.

In over a decade of operation, spectroscopic instrumentation has been developed that matches the unique properties of the source. This instrumentation now provides measurements that span the 1 - 7000 Å region, i.e., the region from X rays to the visible. Special emphasis was placed on the X-ray and EUV regions to provide laboratory data for astrophysics missions such as *ASCA*, *Chandra*, *EUVE*, *DXS*,

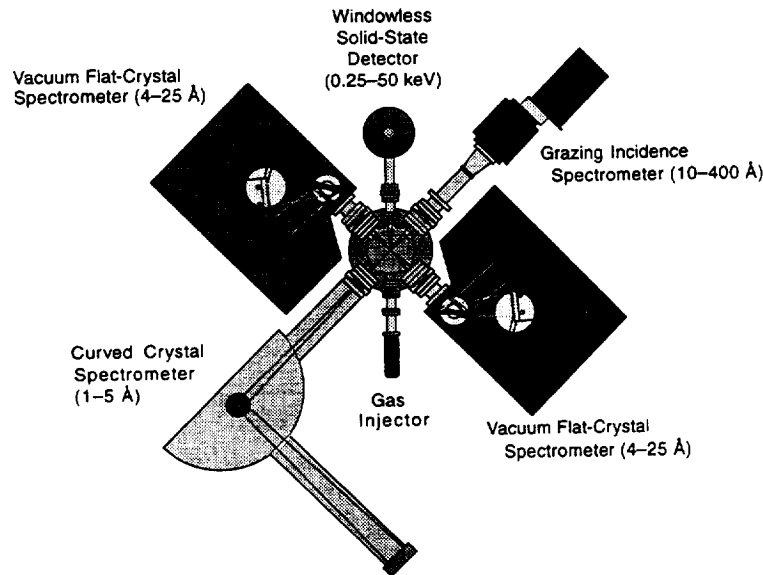


Figure 3. Radial cut through EBIT showing the six ports that provide access to the trap. Five ports are used for spectroscopy. The sixth port is used to inject gases into the trap.

and *XMM*. A typical arrangement for X-ray astrophysics is shown in Figure 3. A windowless high-purity Ge detector monitors the overall X-ray emission from the ions. This signal is used for tuning the facility, for count rate normalization, and for monitoring the presence of impurity ions. Two high-resolution bent-crystal spectrometers are available to provide detailed information on K-shell line emission spectra below 5 Å (Beiersdorfer et al. 1990). Two flat-crystal spectrometers operating *in vacuo* provide detailed L-shell and K-shell spectra in the 4 – 25 Å region (Brown et al. 1999). Two flat-field spectrometers, one with a 1200 ℓ/mm , the other with 2400 ℓ/mm grating are used to study the 10 – 400 Å extreme ultraviolet region (Beiersdorfer et al. 1999a). An X-ray calorimeter with parameters identical to those of the X-Ray Spectrometer (XRS) that had been part of the *Astro-E* mission will commence operation in summer 2000.

We use multichannel detection to increase efficiency and provide data of the highest level of reliability. X-ray detectors include gas-proportional counters, CCD cameras, and microchannel plates. Data are recorded with a multi-parameter data acquisition system.

A very important feature of EBIT is the ability to produce ions of a desired charge state. We do so by relying on the fact that we can choose the energy of the electron beam. This provides us with a powerful technique to determine which line comes from which ionization state. A calculation of the iron ionization balance as a function of electron beam energy based on electron-impact ionization and radiative recombination is shown in Figure 4.

Proper selection of the beam energy also allows us to select a specific line formation process. In fact, excitation processes are best studied by sweeping the energy of the electron beam in a continuous fashion after the desired ion balance has been established. The multi-parameter data acquisition system allows us to tag each X-ray event with the energy of the electron beam. This procedure correlates the line emission to specific beam energies and to determine the excitation function of a given spectral line. Resonant enhancement in the line emission, onsets of radiative cascades from higher levels, and dielectronic satellite features blending with a given line can thus be measured and the relative magnitude of each process assessed for different electron energies, as discussed in subsequent sections.

A novel and very useful feature is the ability to sweep the electron beam energy in time so as to reproduce a Maxwellian electron distribution function. To do so we have developed a procedure for rapidly changing the energy of the electron beam using a programmable arbitrary function generator. At the same time the current is adjusted to keep the electron density constant. Typical traces of electron

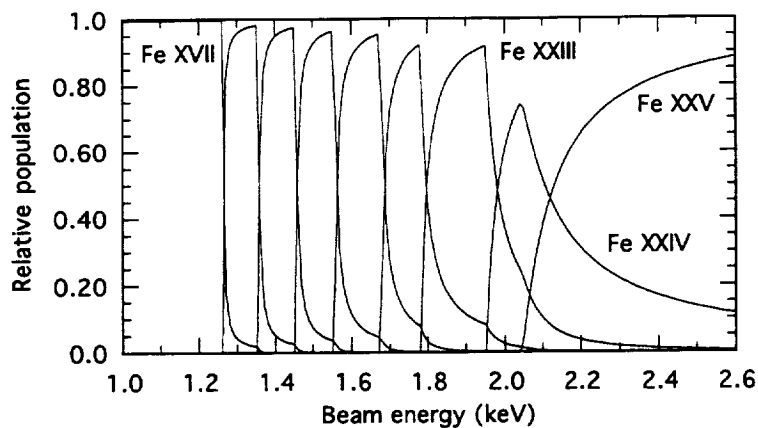


Figure 4. Calculated iron ionization balance in EBIT as a function of electron beam energy.

beam energy and beam current are given in Figure 5. When integrated over one sweep period this provides nearly the same electron energy distribution function as that found in a Maxwellian plasma of a given temperature. Missing are only very low and very high energy electrons, as we can set the beam energy neither to zero nor to infinity. Luckily such truncations are unimportant for most X-ray applications (cf. Savin et al. 1999). The sweeping is done fast enough so that the ionization equilibrium has no time to adjust to the instantaneous beam conditions but sees only the average that represents the Maxwellian temperature. The great advantage of this procedure is that we can dial up any given

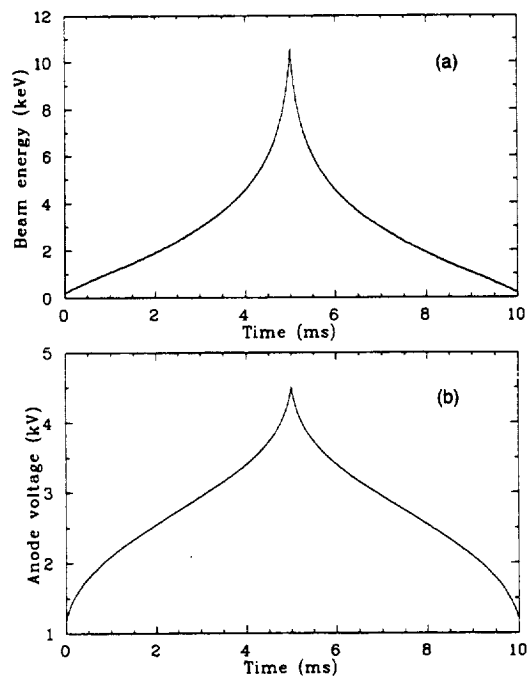


Figure 5. Timing patterns used to simulate a Maxwellian plasma with EBIT: (a) electron beam voltage, (b) voltage on the electron gun anode producing the beam current. The traces simulate a 2.0 keV plasma.

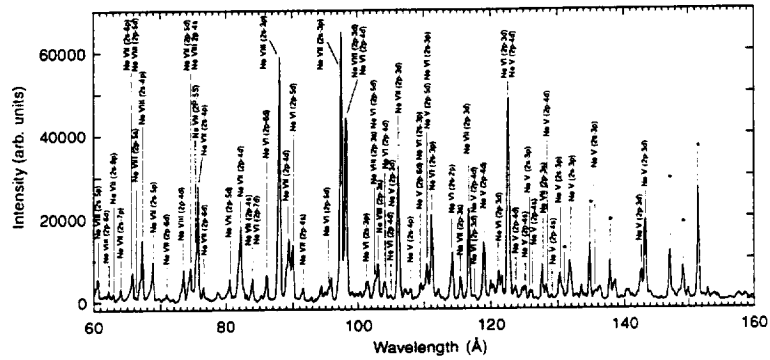


Figure 6. Spectrum of Ne v - Ne VIII. Lines are identified by the charge state and the transition. Lines marked (*) are second order lines.

temperature and produce the relevant spectra. EBIT truly acts as an analog computer that calculates the spectra for us.

3. Representative EBIT Measurements of M-shell, L-shell, and K-shell Spectra

The extreme ultraviolet wavelength band can be observed with *Chandra* up to 200 Å. This overlaps with the range covered by the short-wavelength spectrometer aboard the *EUVE* satellite. Using our 1200 ℓ/mm grating spectrometer we have surveyed the emission from four charge states of neon in this wavelength band. A typical spectrum is shown in Figure 6. The spectrum shows the sheer wealth of lines. Clearly, these lines represent a great potential for detailed plasma diagnostics provided all lines are properly accounted for in the spectral models.

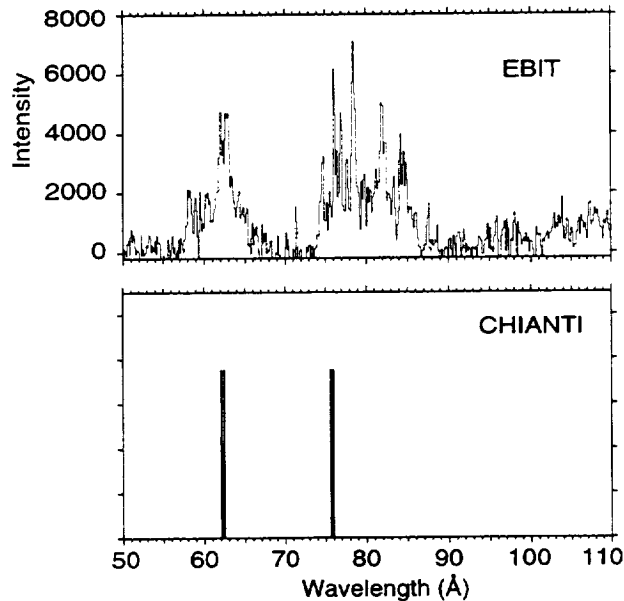


Figure 7. Spectrum of Fe XIII in the extreme ultraviolet: (a) measurement on EBIT; (b) predictions from the CHIANTI data base. CHIANTI does not give intensities for the four lines it lists, so the lines shown indicate no more than their positions.

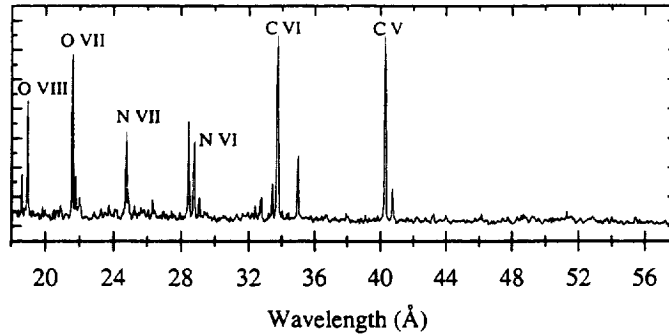


Figure 8. K-shell emission from carbon, nitrogen, and oxygen in the extreme ultraviolet recorded with EBIT.

Using the same instrumentation, we have performed systematic measurements of the M-shell emission of Fe VII through XVI in the 60–140 Å region. Much of this emission is unknown. To illustrate this point, we show a spectrum of Fe XIII in Figure 7 and compare it to the data found in CHIANTI (Dere et al. 1997). The comparison demonstrates the incompleteness of the modeling data base. This lack of data is not just a problem of CHIANTI; it extends to all data bases, including MEKA (Kaastra et al. 1993) and the Arcetri model (Landini and Monsignori Fossi 1990). The problem spans across all charge states of iron from Fe XIII and below (Lepson et al. 2000). In fact, many of the problems in performing global fits to the short-wavelength spectra obtained by the *EUVE* mission (Mewe et al. 1995) appear to be attributable to the fact that many of the lines are simply missing from the models used for the fits (Beiersdorfer et al. 1999b).

The shorter wavelength region below 60 Å is accessed with our 2400 ℓ/mm grating. A spectrum of the K-shell emission from heliumlike and hydrogenic ions of the CNO group is shown in Figure 8. This region is especially important for such missions as *DXS*, *Chandra*, and *XMM*.

Yet shorter wavelengths are analyzed on EBIT with crystal spectrometers. Using our two flat crystal spectrometers, we are able to measure the entire emission from L-shell iron ions in the 10 – 18 Å region simultaneously (Brown et al. 1998, 1999). A spectrum of the Fe XVII emission is shown in Figure 9. Although the spectrum is better known than M-shell, new lines are identified. The new lines are relatively weak and are mostly transitions from levels with high principal quantum number n . However, because most of these lines are clustered near the ionization limit for Fe XVII, these high- n L-shell transitions contribute to a narrow part of the spectrum between about 10 – 11 Å. The combined flux of these lines is about 13 % of that of the strong $3d \rightarrow 2p$ resonance line at 15.0 Å. This is a considerable

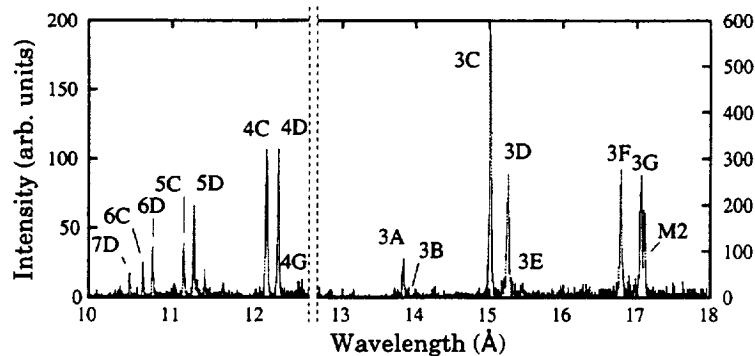


Figure 9. L-shell emission spectrum of Fe XVII. The range shown is the full range simultaneously accessible with our flat-crystal spectrometers. Note that there are different vertical scales associated with the left and right halves of the spectrum.

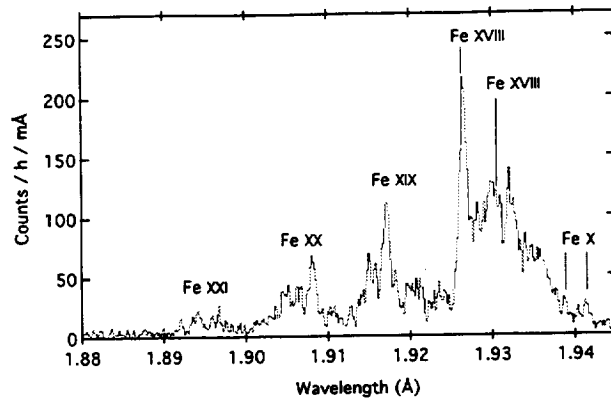


Figure 10. K-shell spectrum of Fe x - Fe xx. The emission in the range from 1.925 to 1.940 Å is comprised of K-shell lines from all charge states of iron between Fe xvii and Fe x. Individual contributions cannot be resolved and are not marked except for the four features shown.

amount of flux that has not been included in most spectral codes. A study of the contributions from these high- n transitions on the spectrum of Capella observed with *ASCA* was made recently (Brickhouse et al. 2000) and found to be a significant effect.

Spectra have also been measured for all higher charge states of iron in this wavelength band. Many lines have been identified for the first time (e.g., Drake et al. 1999). A preliminary line list of the L-shell

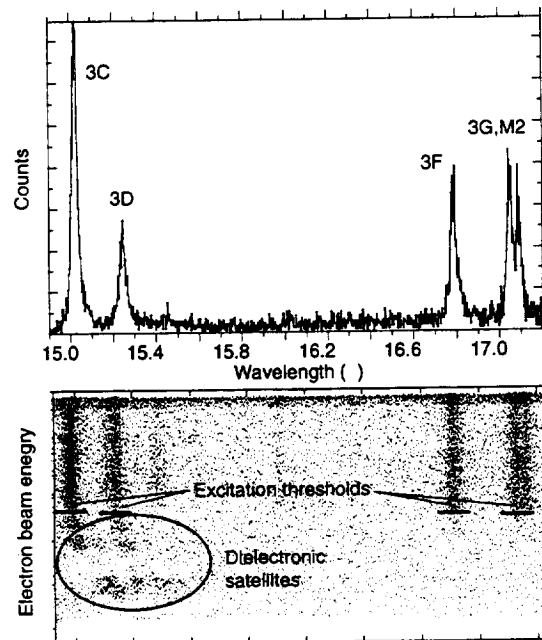


Figure 11. Emission of the $3d \rightarrow 2p$ and $3s \rightarrow 2p$ transitions in neonlike Fe xvii. The bottom figure shows the emission as a function of electron energy. The threshold for direct electron-impact excitation is marked. Emission below threshold is due to dielectronic satellites.

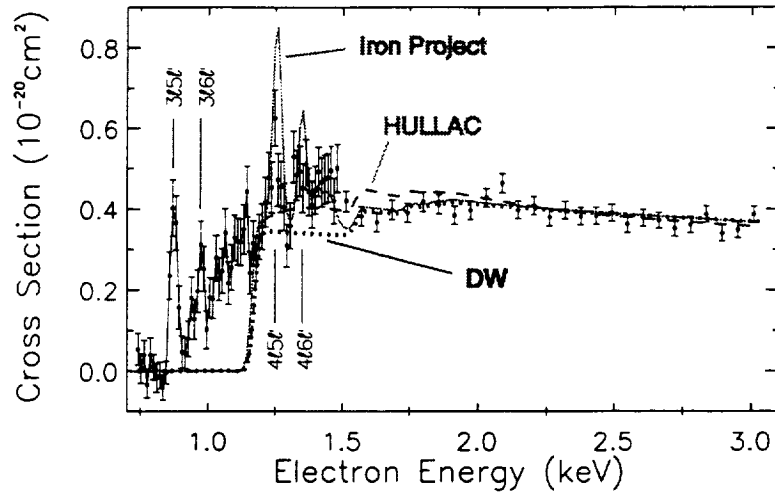


Figure 12. Emission of the $3p_{3/2} \rightarrow 2s_{1/2}$ transition in lithiumlike Fe^{23+} as a function of electron energy showing dielectronic satellite contributions below threshold and resonance excitation contributions above threshold for electron-impact excitation. Different theoretical predictions are indicated: HULLAC (Gu et al. 1999); Iron Project (Berrington and Tully 1997); DW (Zhang et al. 1990).

iron lines from Fe XVIII through Fe XXIV was published in (Phillips et al. 1999). A more comprehensive list is in preparation (Brown et al. 2000). This list now contains about twice as many lines as were used in the MEKA model or were given in standard line lists.

The K-shell iron emission is very important for hot astrophysical sources such as galaxy clusters and supernova remnants. Using our high-resolution bent crystal spectrometers we have made numerous observations of the K-shell spectrum of iron. The spectral resolving powers in these measurements range from 800 to 20,000. Most of the lines from the higher charge states of iron in this spectrum are known. However, many of the lines from the lower charge states are not as well known, mostly because it is very difficult to produce low charge states of iron in the laboratory yet have the high electron energies needed to excite the K-shell lines. We have overcome these problems and measured the K-shell emission from very low charge states of iron, ranging from Fe XX to as low as Fe IX. A typical spectrum of the K-shell emission from low charge state iron ions is shown in Figure 10. Line lists resulting from our K-shell measurements can be found in (Beiersdorfer et al. 1993, Decaux et al. 1995, 1997).

4. Determination of Line Formation Processes and Excitation Cross Sections

Line identification is only a small, albeit important, part of our measurements. Using the ability to quickly switch the electron beam energy, we map out different line formation processes. Such processes include both direct electron-impact excitation as well as indirect line formation processes, such as those associated with resonance excitation and high- n dielectronic satellite contributions.

As an example of the different line formation processes contributing to a given line we show in Figure 11 the L-shell lines from Fe XVII in the 15 – 18 Å range. By sweeping the electron beam energy from as low as 200 eV to well above 2000 eV, the measurement identifies the different contributions to the lines: direct electron-impact excitation and resonance excitation above the threshold for excitation, and dielectronic-recombination satellite lines below threshold. While the latter are technically lines different from their parent line, they cannot be resolved and contribute to the line intensity observed in a plasma source. The figure immediately shows that dielectronic resonances are important for the $3d \rightarrow 2p$ lines. But dielectronic resonances are not important for the $3s \rightarrow 2p$ lines.

Based on such energy-dependent measurements the excitation cross section contributing to given line as a function of energy can be readily extracted. An example for the $3d_{5/2} \rightarrow 2p_{3/2}$ transition in lithiumlike Fe XXIV is shown in Figure 12.

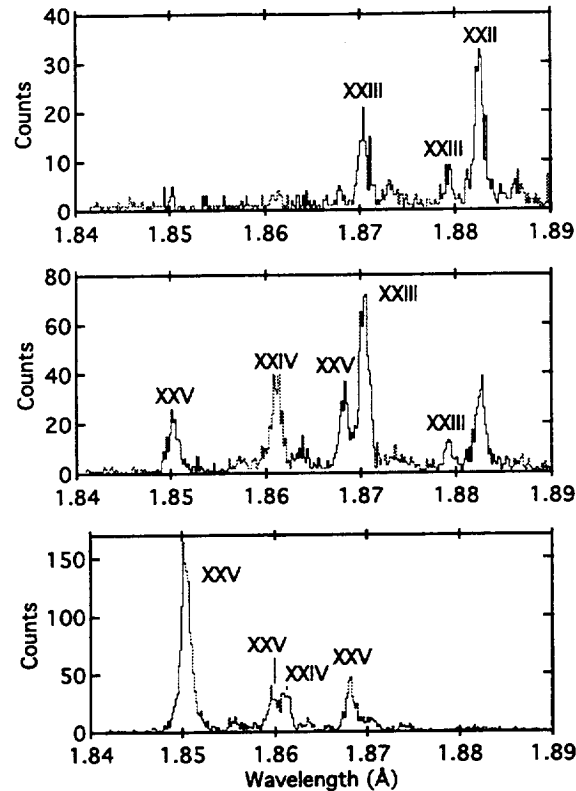


Figure 13. K-shell emission from iron ions for different values of the ionization parameter $\eta = n_e t$: (a) $\eta = 5 \times 10^{10} \text{ cm}^{-3}$, (b) $\eta = 20 \times 10^{10} \text{ cm}^{-3}$, (c) $\eta = 50 \times 10^{10} \text{ cm}^{-3}$. Lines strongly enhanced by innershell ionization are the Fe xxiii line at 1.879 Å and the Fe xxv line at 1.868 Å. These can be used as markers for ionizing plasmas for high values of η .

As noted, the contributions from the dielectronic satellite lines, especially those that are unresolved in wavelength from their parent line, are important for accounting for all of the flux. Our measurements show that such satellites can enhance some L-shell lines in Fe xxiv by 20 % (Gu et al. 1999) or more, especially in colder plasmas. As already illustrated in Figure 12, we stress that not all lines are enhanced by such contributions. Each line must be treated individually. This counters the assumptions made in the MEKA model, for example, where essentially every electron-dipole-allowed line is assumed to have a given percentage of the flux emanating from dielectronic satellites.

5. Nonequilibrium Processes

Many astrophysical plasmas are not in charge-balance equilibrium. Our capabilities that allow us to rapidly switch the energy of the electrons also let us simulate nonequilibrium conditions. For example, we have simulated ionizing plasmas found in super nova remnants by studying the time dependence of the spectral emission as charge state equilibrium is reached (Decaux et al. 1997). Such a simulation allows us to identify various markers for ionizing plasmas among the iron K lines. Typical spectra of the K-shell iron emission for different values of the ionization parameter $\eta = n_e t$ are shown in Figure 13.

Recombining plasmas are another area of investigation. In photo-ionized plasmas, high charge state ions are produced in intense photon fields. The electron temperature is rather low, and the role of electrons in X-ray line formation is purely limited to recombination. We have simulated such conditions

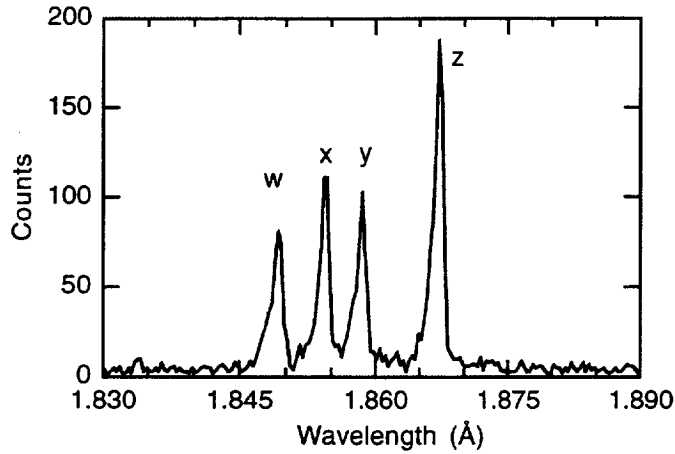


Figure 14. K-shell emission from iron produced by electron capture. All emission is from Fe XXV ions. The lines are labeled in the following notation: $w - 1s2p\ ^1P_1 \rightarrow 1s^2$, $y - 1s2p\ ^3P_1 \rightarrow 1s^2$, $x - 1s2p\ ^3P_2 \rightarrow 1s^2$, $z - 1s2s\ ^3S_1 \rightarrow 1s^2$. No lower charge states may contribute. Such spectra are produced in photo-ionized plasmas.

by first producing a given ionization state, then switching the energy of the electrons to values where recombination is the only line formation process. A typical K-shell spectrum of Fe XXV produced by electron capture into hydrogenic Fe XXVI ions is shown in Figure 14. The spectrum looks very different from that produced in a hot electron plasma. The triplet lines are much stronger than the singlet lines, which is in stark contrast to spectra produced by electron-impact excitation. Furthermore, no satellite transitions, neither collisional nor dielectronic, from lower charge states are visible. The latter is the result of the fact that none of the lower charge states has a K-shell vacancy, thus precluding the possibility that a K-shell transition takes place during the recombination process. This makes the spectra unique for identifying recombination dominated plasmas.

6. Conclusion

Facilities nowadays exist that can produce much of the atomic data needed for the proper and reliable interpretation of astrophysical X-ray data. Ionization and recombination cross sections for all astrophysically relevant ions can be measured by using particle-counting techniques on storage rings and crossed and merged beam facilities. Such measurements include resonance phenomena that may lead to double ionization or that enhance recombination. Similarly, X-ray excitation cross sections can be measured by observing the spectra of interest directly in the laboratory by using photon counting techniques on the EBIT. X-ray spectroscopic measurements at the Livermore EBIT have been optimized over the past decade to provide definitive values of electron-impact excitation, dielectronic and resonance excitation cross sections. By looking directly at the processes that produce line emission, the EBIT measurements can assess whether or not a particular process is relevant and which lines need to be included in spectral models. The Livermore measurements now cover the entire K-shell or L-shell complex in essentially one experimental setup and can provide the atomic data needed for synthesizing accurate spectral models. Most importantly, the spectral and collisional data provided by the new facilities provide uncertainty limits that are invaluable in establishing believable bounds on the physical parameters inferred from spectroscopic observations of astrophysical data.

Acknowledgments. Discussions with Duane Liedahl, Nancy Brickhouse, and Mau Chen are gratefully acknowledged. This work was supported by NASA grants NAG5-6731 and NAG5-5123 and work order W-19127 and was performed under the auspices of the Department of Energy by the University of California Lawrence Livermore National Laboratory under contract No. W-7405-ENG-48.

References

- Andersen, L. H., Pan, G. Y., Schmidt, H. T., Pindzola, M. S., and Badnell, N. R. 1992, *Phys. Rev. A* 45, 6332.
- Beiersdorfer, P., Lepson, J. K., Brown, G., Utter, S. B., Kahn, S., Liedahl, D., and Mauche, C. W. 1999b, *Astrophys. J.* 519, L185.
- Beiersdorfer, P., López-Urrutia, J. R. C., Springer, P., Utter, S. B., and Wong, K. L. 1999a, *Rev. Sci. Instrum.* 70, 276.
- Beiersdorfer, P., Marrs, R. E., Henderson, J. R., Knapp, D. A., Levine, M. A., Platt, D. B., Schneider, M. B., Vogel, D. A., and Wong, K. L. 1990, *Rev. Sci. Instrum.* 61, 2338.
- Beiersdorfer, P., Phillips, T., Jacobs, V. L., Hill, K. W., Bitter, M., von Goeler, S., and Kahn, S. M. 1993, *Astrophys. J.* 409, 846.
- Beiersdorfer, P., Phillips, T. W., Wong, K. L., Marrs, R. E., and Vogel, D. A. 1992a, *Phys. Rev. A* 46, 3812.
- Beiersdorfer, P., Schneider, M. B., Bitter, M., and Von Goeler, S. 1992b, *Rev. Sci. Instrum.* 63, 5029.
- Berrington, K. A., and Tully, J. A. 1995, *Astron. & Astrophys.* 126, 105.
- Brickhouse, N. S., Dupree, A. K., Edgar, R. J., Liedahl, D. A., Drake, S. A., White, N. E., and Singh, K. P. 2000, *Astrophys. J.* 530, 387.
- Brown, G., Beiersdorfer, P., Kahn, S., Liedahl, D., and Widmann, K. 1998, *Astrophys. J.* 502, 1015.
- Brown, G. V., Beiersdorfer, P., Liedahl, D. A., Widmann, K., and Kahn, S. M. 2000 (in preparation; available as LLNL preprint UCRL-JC-136647).
- Brown, G. V., Beiersdorfer, P., and Widmann, K. 1999, *Rev. Sci. Instrum.* 70, 280.
- Decaux, V., Beiersdorfer, P., Kahn, S. M., and Jacobs, V. L. 1997, *Astrophys. J.* 482, 1076.
- Decaux, V., Beiersdorfer, P., Osterheld, A., Chen, M., and Kahn, S. M. 1995, *Astrophys. J.* 443, 464.
- Dere, K. P., Landi, E., Mason, H. E., Fossi, B. C. M., and Young, P. R. 1997, *A&AS* 125, 149.
- Drake, J. J., Swartz, D. A., Beiersdorfer, P., Brown, G. V., and Kahn, S. M. 1999, *Astrophys. J.* 521, 839.
- Gu, M., Kahn, S., Savin, D., Beiersdorfer, P., Brown, G., Liedahl, D., Reed, K., Bhalla, C., and Grabbe, S. 1999, *Astrophys. J.* 518, 1002.
- Kaastra, J.S., and Mewe, R. 1993, *Legacy* 3, 16.
- Knapp, D. A., Marrs, R. E., Schneider, M. B., Chen, M. H., Levine, M. A., and Lee, P. 1993, *Phys. Rev. A* 47, 2039.
- Landini, M., and Monsignori Fossi, B. C., *Astron. Astrophys. Suppl.* 82, 229 (1990).
- Lepson, J. K., Beiersdorfer, P., Brown, G. V., Kahn, S. M., Liedahl, D. A., Mauche, C. W., and Utter, S. B. 2000, *Revista Mexicana de Astronomia y Astrofisica* 9, 137.
- Levine, M. A., Marrs, R. E., Bardsley, J. N., Beiersdorfer, P., Bennett, C. L., Chen, M. H., Cowan, T., Dietrich, D., Henderson, J. R., Knapp, D. A., Osterheld, A., Penetrante, B. M., Schneider, M. B., and Scofield, J. H. 1989, *Nucl. Instrum. Methods B* 43, 431.
- Linkemann, J., Müller, A., Kenntner, J., Habs, D., Schwalm, D., Wolf, A., Badnell, N. R., and Pindzola, M. S. 1995, *Phys. Rev. Lett.* 74, 4173.
- Mewe, R., Kaastra, J.S., Schrijver, C.J., van den Oord, G.H.J., and Alkemade, F.J.M. 1995, *Astron. Astrophys. Suppl.* 296, 477.
- Müller, A. 1991, *Physica Scr.* T37, 14.
- Müller, A., Bartsch, T., Brandau, C., Hoffknecht, A., Knopp, H., Schippers, S., Uwira, O., Linkemann, J., Saghiri, A. A., Schmitt, M., Schwalm, D., Wolf, A., Bosch, F., Franzke, B., Kozhuharov, C., Mokler, P. H., Nolden, F., Steck, M., Stohlker, T., Winkler, T., Danared, H., DeWitte, D. R., Gao, H., Lebius, H., Schuch, R., Spies, W., Zong, W., Dunn, G.H., Graham, W. G., Tanis, J. A., Doerfert, J., Savin, D., and Stachura, Z. 1998, *Hyperf. Inter.* 114, 229.
- Phillips, K. J. H., Mewe, R., Harra-Murnion, L. K., Kaastra, J. S., Beiersdorfer, P., Brown, G. V., and Liedahl, D. A. 1999, *Astron. Astrophys. Suppl.* 138, 381.

- Savin, D. W., Beck, B., Beiersdorfer, P., Kahn, S. M., Brown, G. V., Gu, M. F., Liedahl, D. A., and Scofield, J. H. 1999, *Phys. Scripta* T80, 312.
- Schuch, R., DeWitt, D. R., Gao, H., Mannervik, S., Zong, W., and Badnell, N. R. 1997, *Physica Scr.* T73, 114.
- Stenke, M., Aichele, K., Hartenfeller, U., Hathiramani, D., Steidl, M., and Salzborn, E. 1999a, *J. Phys. B* 32, 3627.
- Stenke, M., Hartenfeller, U., Aichele, K., Hathiramani, D., Steidl, M., and Salzborn, E. 1999b, *J. Phys. B* 32, 3641.
- Zhang, H. L., Sampson, D. H., and Fontes, C. J. 1990, *Atom. Data Nucl. Data Tables* 44, 31.

Time-resolved atomic spectroscopy with fast-ion beams, heavy-ion storage rings and ion traps

Elmar Träbert

*Institut de Physique Nucléaire Expérimentale, Université de Liège, B-4000 Liège, Belgium, and
Fakultät für Physik und Astronomie, Ruhr-Universität Bochum, D-44780 Bochum, Germany*

e-mail: traebert@ep3.ruhr-uni-bochum.de

Abstract.

The understanding of the light received from astrophysical sources requires knowledge of atomic structure and dynamics, or of excitation cross sections and conditions, wavelengths and transition probabilities, f -values, branching ratios and level lifetimes. Fast ion beams (by beam-foil spectroscopy) and ion traps, as well as their cross-breed, the heavy-ion storage ring, can contribute to the field of X-ray astronomy. Fast-ion beam spectroscopy has a long track record in all spectral ranges, including XUV and X-ray, with a plethora of data supporting astrophysics. In contrast, most of the time-resolved work with the ion trap techniques has been done in the UV and VUV/EUV above 100 Å, but it can be extended into the region of interest.

1. Introduction

X-ray spectroscopy at wavelengths of below 100 Å and in an astrophysical context is the topic of this conference. My field of interest for about a quarter century now has been the study of ions with a time resolution that permits the investigation of atomic properties, that is level lifetimes, branching ratios, multiplet mixing and the like. Most of my (and everybody else's) work in this field was not in the aforementioned wavelength band. However, at least some of it was, and that work demonstrates what can be done. Moreover, there is a lot of interesting work that has been done in other wavelength ranges and that paved the way for future work in the desired region. Some of the work was done in the near-ultraviolet, some in the vacuum-UV (VUV), most in the extreme-UV (EUV), and also some in the very range to be discussed at this meeting. My presentation is structured by the techniques and devices used, and it lists the particular properties and advantages. With such a catalog, it should become possible to identify the most suitable technique and the probably best-versed laboratory for soliciting specific information when it will be needed to interpret the data from future soft-X-ray astronomical work. As I am presenting my views, I found it easiest (for me) in several cases to offer entries for the search into the vast further literature on the subject (in particular beam-foil spectroscopy, a field that has been covered in a sequence of topical conferences) via my own work, although, of course, that represents only a fraction of all the work done. An "executive-style" summary of lifetime measurements and capabilities is presented in Table 1.

2. Beam-foil spectroscopy

Beam-foil spectroscopy, the study of light emitted by fast ion beams after being sent through a thin foil of solid material (Figure 1), has been invented in the early 1960s. One of the very first papers in the field claimed the "Laboratory excitation of the emission spectrum of a Nova", stressing the fact that the optical spectrum of an energetic nitrogen ion beam looked very different from that of ordinary (thermal, dense) light sources and that it contained lines that also appeared in astrophysical data, but that had not been seen in other terrestrial light sources (Bashkin and Meinel 1964). This feature is just one of many interesting ones of the beam-foil technique (Träbert 1997).

Table 1. Examples of lifetime studies

<p>Beam-Foil work at Bochum, Lund, Oxford, Argonne, RIKEN (and many other places): Allowed transition rates in Li-, Be-, B-, Ne-, and Na-like ions Intercombination transition rates in He-, Mg-, Al-, and Si-like ions (Träbert et al. 1988) High-J level identification and lifetimes in Si-, P-, and S-like ions (Träbert 1999) Lifetimes 1 ps to 30 ns, typical precision 5 - 10%</p> <p>Heavy-ion storage ring at Heidelberg: Intercombination transition rate in C^{2+} to $\pm 0.14\%$ (Doerfert et al. 1997) Systems investigated: B^+ (Träbert et al. 1999b), C^{2+} (Doerfert et al. 1997), C^+, N^{2+} (Träbert et al. 1999c), N^+ (Träbert et al. 1998), O^{2+} (Träbert et al. 2000a), Al^+ (Träbert et al. 1999b) Lifetimes 0.3 ms to 100 ms</p> <p>M1/E2 transition rates to $\pm 0.2\%$ to $\pm 5\%$ Systems investigated: F^+ (Calamai et al. 2000), O^{2+}, F^{3+} (Träbert et al. 2000a), Si^{6+}, Si^{8+} (Träbert et al. 1998a), S^{9+} (Träbert et al. 2000a), Sc^{12+} (Träbert et al. 1999), Ti^{13+}, Ti^{17+} (Träbert et al. 2000b), B^{3+}, C^{4+}, N^{5+} (Schmidt et al. 1994) Lifetimes 0.5 ms to 500 ms</p> <p>Livermore EBIT: M1 transition rates in B- and F-like ions of Ar (UV) to $\pm 2\%$ (Träbert et al. 2000c) Lifetimes up to 15 ms M1 transition rates in He-like ions (soft-X-ray) to $\leq 1\%$: N^{5+} (Neill et al. 2000), O^{6+} (Crespo López-Urrutia et al. 1998), F^{7+} (Neill et al. 2000), and Ne^{8+} (Träbert et al. 1999a) Lifetimes 30 μs to 4 ms</p>

The beam-foil excitation process largely takes place in a dense medium. It is violent, non-thermal and non-selective, and it reaches high-lying levels in ordinary atomic level systems as well as core-excited states. In stark contrast, de-excitation of the ions, after leaving the bulk of the foil, takes place in good vacuum without further collisions, and the light source is optically thin. Magnetic and electrical fields guide the ion beams to the experimental site; consequently the beams are isotopically pure, and it can be ascertained that a specific spectral line in a beam-foil spectrum belongs to a specific element. The charge state distribution of the ions after the foil is a function of the ion beam energy; the beam energy can be varied in order to identify the ion charge state that gives rise to a given spectral line. With a suitable accelerator, any charge state of any element is accessible. For data to compare with the solar chromosphere (singly charged ions), a few hundred keV of ion energy are ample (see the ion-beam laser work at Edmonton (Pinnington et al. 1992, 1993) and at various other places that helped to check on solar abundances). For ions and charge states typical of the solar corona, accelerators are needed that provide ion beams of up to about 30 MeV, while for the reproduction of some solar flare data, an ion energy of order 100 MeV is necessary.

Fast-ion beam spectroscopy works in all spectral ranges; there are X-ray spectra, EUV, UV, visible and infrared studies, as well as laser-assisted investigations in the near-UV to the IR, and some long-wavelength laser resonance experiments exploit X-ray detection schemes. From neutral atoms to hydrogen-like Fe, all ions of primary astrophysical interest have already been studied (though far from exhaustively). For the wavelength range of present interest, that is on the short side of 100 Å, grazing-incidence spectrometers with concave gratings ($R=2.2$ m or 1.5 m, angle of incidence 86° to 88°) and channeltron detectors have been successfully employed down to about 10 Å (Möller et al. 1998). Multichannel detection nowadays is feasible, but it has not yet been used on many "astrophysical" ions in the present range of interest. For beam-foil spectroscopy in the true X-ray range, $R=5''$ curved-crystal

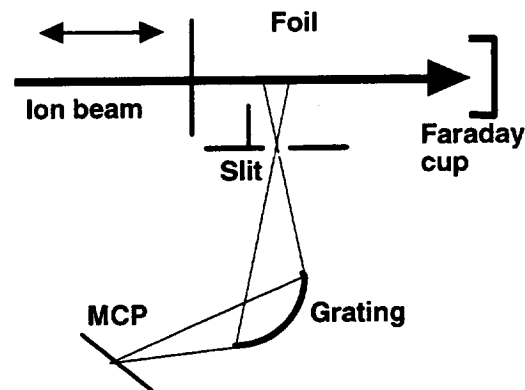


Figure 1. Schematics of beam-foil spectroscopy, with a grating spectrometer that is equipped with a microchannelplate (MCP) multiplex detector. The foil can be moved with respect to the viewing region of the detection system, and thus time-resolved spectra of different delay time after excitation, or decay curves for lifetime measurements, can be recorded.

spectrometers proved their value in survey spectra down to about 2 \AA (Träbert et al. 1979; Armour et al. 1980). The results compared well with X-ray spectra from early sounding rockets and satellite missions.

Interestingly, there are satellite lines on the short-wavelength side of the resonance lines in He-like ions that have been seen by beam-foil spectroscopy some 20 years ago (Träbert et al. 1979; Armour et al. 1980). Meanwhile such lines from multiply-excited few-electron atoms are being subsumed in the fashionable field of "hollow atoms" that links fields seemingly as far apart as ion-surface interactions and plasma pinches. The resolving power of the experiments that observed fast-ion beams with curved-crystal spectrometers, equipped with commercial crystals (RAP, EDT and the like) and with proportional counter detectors, was sufficient at the time. However, significant improvements in spectral resolution, at the cost of accelerator time, would clearly be feasible, as is the use of multichannel detectors. Some of the satellite line structure can be reduced by using a dilute gas target instead of a foil target. An extended gas target, however, takes away most of the geometry-related intrinsic time resolution, but it can be beneficial for high spectral resolution work on the diagram lines. Earlier attempts at precision spectroscopy on H-like and He-like Ar ions in a gas target ran aground with the problem of modeling the satellite line intensity distribution for $n > 2$.

A very interesting and unique feature of the beam-foil light source is the already mentioned intrinsic time resolution. Close to the foil, the spectrum is full of lines and dominated by the decays of very many short-lived levels. Observing the ion beam farther away (centimeters) from the foil corresponds to an observation at times of nanoseconds after excitation. Short-lived levels (picosecond-range), like the resonance levels in ordinary ions or levels in core-excited ions, are depleted by then, and the emphasis in the spectra shifts to long-lived levels (nanosecond range). Typical levels of such lifetimes in multiply charged ions are the upper levels of intercombination transitions, or levels that otherwise only weakly couple to lower-lying levels. An upper limit of the level lifetimes in such observations is given by geometry: With ever longer lifetimes, the decay lengths (ion velocity times lifetime) grow beyond the

size of practical vacuum chambers and laboratories, and the signal per unit length of ion beam observed drops below the noise level of the detector. In any case, such studies need powerful ion sources that are not available at or compatible with every type of ion accelerator.

The “delayed” spectra (Träbert et al. 1988) resemble solar coronal spectra in several ways. It has thus been possible to identify a number of intercombination transitions (Mg-, Al-, Si-, S-like ions of Ti to Cu) (Träbert et al. 1987, 1988) as well as the decays of some low-lying high-J levels ($J=3$ in Si-, $J=7/2$ in P-, $J=5/2$ in Cl-like ions) (Träbert et al. 1993, 1996; Jupén et al. 1993; Träbert 1996, 1998), first in the delayed beam-foil spectra of iron group elements, and then, often with the benefit of better wavelength numbers, also in solar spectra that existed much earlier. In the latter spectra, many of the lines had either not yet been identified at all, or, because of the incompleteness of information in the atomic data bases, they had been assumed to originate from other ions. Obviously, these delayed spectra are a valuable ingredient in the analysis of the $n=3$ shell structure that draws on complementary data from laser-produced plasmas, tokamaks, the sun, and foil-excited ion beams. (On the not quite funny side, I am not going to cite a 1999 Ap.J. paper that claims that the ground state intercombination transitions in Al-like Fe XIV are not yet known, giving as evidence for this claim a NIST bibliography of 1988 (10 years old at the time!). That bibliography, indeed, did not yet cite the aforementioned 1987 publication (Träbert et al. 1987) of those very lines and their re-identification in spectra of the solar corona. However, other colleagues spotted that paper within a few years, and nowadays it is easily found using the ASD abstract service. I am afraid that in many cases a “has not been measured” ought to read as “has possibly been measured, but has not on its own account reached the eyes of a given person yet”.)

Last, but not least, by observing the light of a given wavelength as a function of distance from the foil (time after excitation), it is possible to derive level lifetimes and transition probabilities. In practice, the longest lifetimes measured reasonably well by beam-foil spectroscopy are of order 30 ns (special cases reach up to a few hundred nanoseconds). The measurement of short lifetimes with this technique is also limited by geometry, the width and shape of the field of view of the detection system at the position of the ion beam, the displacement of the foil along the ion beam (a matter of μm precision) and the foil properties (Engström 1993; Engström and Bengtsson 1991). Although lifetimes of less than 1 ps have been reported, routine work starts from a few picoseconds up. In this usual working range, a precision of typically 5 to 10% is generally being reached. In a few cases, correlating the decay curve of a given level with transitions feeding it, even smaller lifetime uncertainties have been demonstrated.

For unbranched decays, the inverse of the upper level lifetime is the transition probability. In case of branched decays, transition probabilities of individual lines can be derived from the combination of a lifetime measurement with a determination of branching fractions (which may be based on the wavelength dependence of the relative detection efficiency). This has been demonstrated by a fast-beam experiment in the EUV (Träbert et al. 1983). An extension of this technique to the wavelength range below 100 Å is difficult because of the often poor and irregular performance of grazing-incidence optics.

The light observed from a fast ion beam is Doppler shifted and broadened. While for normal-incidence spectrometers “refocusing” techniques are known that can reduce the Doppler width of spectral lines in fast-beam observations, the same refocusing techniques affect the dispersion and make lines from stationary calibration light sources appear broadened. Furthermore, the geometry of grazing-incidence spectrometers is not compatible with these known schemes. Hence in most cases, EUV/XUV wavelength data from solar spectra will be available with a higher accuracy than those from fast ion beams. However, with appropriate precautions (often reducing the solid angle of observation) and employing a high-groove density diffraction grating, precise wavelengths can be obtained with fast ion beams, too (Mannervik et al. 1989). Line widths (FWHM) as small as 0.1 Å have been reached for beam-foil spectra below 200 Å, as has been demonstrated at Bochum, for example, for the H_{β} line of O VIII (Müller et al. 1982) and for the 3d-4f array in Ne-like Ti XIII (Jupén et al. 1996). This particular spectrum, by the way, is very similar in appearance to what has been observed at a tokamak plasma.

Much of this work has been done at the superbly suited Bochum accelerator facility where, alas, atomic physics is presently being phased out. Comparable spectroscopic facilities with grazing-incidence spectrometers (with a more limited accelerator performance for the ions of X-ray - astrophysical interest) are available, for example, at Université Laval (Québec, Canada; Lapierre and Knystautas 1999), Lund University (Sweden; Engström 1993), Argonne National Laboratory, Notre Dame (IN), and RIKEN (Japan; Hutton et al. 1997).

3. Ion traps

Ion traps aim at keeping ions contained in a small volume, for extended observation times. They come in many flavors or operating principles (Ghosh 1995), using electrostatic (Kingdon), magnetic (Penning) or radiofrequency electromagnetic field (Paul) confinement, or derivatives thereof, like the heavy-ion storage ring and the electron-beam ion trap (EBIT). One of the decisive factors in doing reliable lifetime measurements in such traps is the background pressure that limits the storage time because of collisional losses, including scattering and charge exchange reactions. For a long time, low-charge state ions have been produced from gas inside the trap (under high vacuum conditions, but nevertheless expecting the more signal from the more gas). This ambient gas then remains in the trap volume while the decay curve measurement takes place. Evidently, with less gas in the trap, less perturbation and fewer charge exchange collisions would occur. Pressure variation and decay-rate extrapolation towards zero pressure are regularly done, but they often remain unsatisfactory. It would obviously be much cleaner to produce the ions in one place, select the right species and transfer only that sample to a storage trap that runs under clean ultrahigh vacuum conditions.

One such approach at separating ion production and ion storage has been the combination of an electron cyclotron resonance ion source (ECRIS) with a Kingdon trap (electrostatic ion trap, at Texas A&M (Church 1993; Yang 1994), Reno (Moehs et al. 1991; Moehs and Church 1988, 1999a, 1999b), and Caltech (Smith et al. 1999). When the ion trap potentials are switched on, a fraction of the keV-ion beam that has been passing through the trap volume may be captured. The optical emission of this sample of trapped ions is then monitored, and the optical decay curve corrected for the ion losses from the trap. A number of cases in Ar, Mn and Fe, including some of astrophysical interest, has been treated this way, and the more recent lifetime results bear error bars of 1% to 15%. The authors, however, state that the comparison with theory remains largely inconclusive (although the very fact of these measurements marks a considerable step forward).

In a case (Ar^{14+}) where extensive theoretical calculations corroborate earlier calculations rather than the Kingdon trap lifetime measurements, a renewed discussion by the experimental authors (Church et al. 1999) has not brought to light any likely cause of the present disagreement which various parties would like to blame on the experimental side. Meanwhile an EBIT experiment done at Livermore (Träbert et al. 2000d) supports the theoretical claims rather than the Kingdon trap results. In another Kingdon trap experiment, on C^+ (Smith et al. 1999), the results initially came close to earlier radiofrequency ion trap data rather than to the concurrent, much more precise results from a heavy-ion storage ring experiment (Träbert et al. 1999c), but have shifted closer to the latter since. In this case, three exponential components have to be fitted to a spectrally unresolved decay curve that represents the superposition of lines from three closely-spaced levels ($^4\text{P}_{1/2,3/2,5/2}$), and good statistics are of utmost importance. Some extra caution seems warranted with data that required many weeks of collection at a Kingdon trap and then still remained poorer in statistics by about an order of magnitude in comparison to the data from a two-day experiment at the storage ring! Elaborate statistical tests cannot overcome poor data statistics in first place.

4. Heavy-ion storage rings

Another approach to separating ion storage from ion production is the heavy-ion storage ring (Müller and Wolf 1997), as available at Heidelberg, Stockholm, Aarhus, Darmstadt - none in the USA (Figure 2). In such a storage ring, the vacuum beam pipe and magnetic guidance system of an accelerator system are being turned into a ring into which an ion beam is injected and then left circulating. Ion production (in an ion source that is feeding an ion accelerator), charge-state selection (by the magnets in the ion beam transport system) and storage (in the storage ring) are spatially separated from each other (by 10 to 100 m) and can be optimized individually. Detection can exploit the change of ion trajectory after a change of ion charge state, for example by dielectronic recombination with electrons in a superimposed cold electron beam (Schmidt et al. 1994), or can proceed by straightforward optical observation (Doerfert et al. 1997). Ion storage times for MeV-ion beams are much longer (many seconds, in some cases minutes) than with the aforementioned Kingdon trap, and they can be measured directly and more reliably as well.

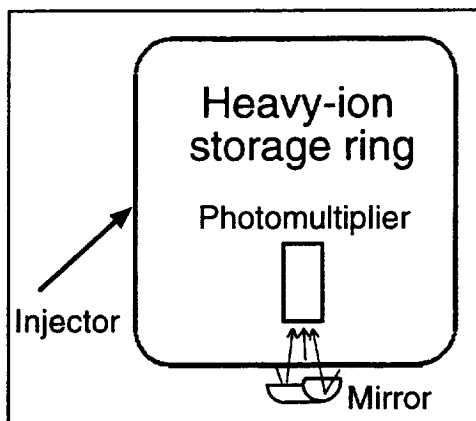


Figure 2. Schematics of atomic lifetime measurements at a heavy-ion storage ring. A single-charge state, single-isotope ion beam is injected into the storage ring and stacked for about 30 turns. Then injection ends, and the optical emission from the coasting ion beam is monitored for up to a few seconds.

At present, this type of heavy-ion storage ring experiment seems to be the technique of lowest systematic error, and it is also capable of high statistical precision in the lifetime range 0.5 to 500 ms. This lifetime range covers both, ground-state intercombination transitions in several light ions (Doerfert et al. 1997; Träbert et al. 1998, 1999b, 1999c) and forbidden transitions in quite a number of ions of astrophysical interest (Eidelsberg et al. 1981; Lynch et al. 1991; Träbert et al. 1998, 2000a, 2000b; Calamai et al. 2000). The experimental lifetime results obtained so far on intercombination and on M1/E2 transitions lie within the range of scatter of the theoretical predictions, but carry much smaller uncertainties, often with a precision of 1% and better. Such a precision is testing theory in some cases, but not in all. For example, the $2s^2 \ ^1S_0 - 2s2p \ ^1P_1^o$ resonance transition in Be-like ions can be calculated by elaborate algorithms to a precision of better than 0.1%, which for nanosecond-lifetimes (and shorter) cannot be reached by experiment yet. The same calculations yield the intercombination transition rate with a precision of no better than about 1%, but the heavy-ion storage ring measurements can do much better than that for the millisecond lifetimes involved here (Jönsson et al. 1998). For “forbidden” transition rates, that is for M1 and E2 transitions, the calculations for a long time have been claimed to be “easy” and reliable even in the absence of tests. However, the usual theoretical uncertainty estimates were in the 10 to 20% range. Now storage ring measurements yield lifetime results that are more precise by an order of magnitude and confirm only some, but not all of the calculations. Apparently, conceptual simplicity does not necessarily translate into calculational reliability. However, the blame for scattered predictions does not rest on theory alone, as some earlier RF ion trap measurements later turned out to be rather misleading. As stated by Alan Hibbert (Belfast) years ago, “the incidental agreement of experimental and theoretical data is no proof that either of them is correct”. A certain competition of experimenters and theoretician seems to be beneficial for both.

Most of the systems studied so far at the TSR storage ring at MPI Heidelberg have transitions that lie in the near ultraviolet, which is a selection governed by the constraints of the initial detector arrangement. Detectors for the VUV and EUV are being contemplated, but would have to be mounted inside the storage ring vacuum vessel. Encouragement of the local scientists by the astrophysical data users might help these technical developments to proceed faster.

5. EBIT

A particularly versatile ion trap is the electron-beam ion trap (EBIT) (see also Peter Beiersdorfer’s contribution to this conference), which confines ions - like a Penning trap - mostly by a combination of a strong magnetic field with electrically charged drift tubes. The essential addition to the basic Penning

trap is a high-density electron beam that runs along the axis of the trap and produces ions of any charge state from the ambient gas (under true UHV conditions) or from an injected low-charge ion cloud. This electron beam also compensates the space charge of the ion cloud, thus keeping the ions in place for further ionizing collisions. The stepwise ionization is only limited by the electron beam energy in comparison to the increasing ionization potentials of the ions that are successively produced. Again, any charge state of any element is accessible. As the ions have rather low kinetic energies, high-resolution spectroscopy is feasible. For lifetime measurements, the electron beam is suddenly switched off (thus removing the dominant collision partners while the ions remain trapped in the Penning trap), and the light intensity of a given line is followed as a function of time.

Lifetime measurements in the X-ray range (using the Livermore EBIT) have reached a precision of better than 0.5% (Crespo López-Urrutia et al. 1998; Träbert, et al. 1999a), and in the visible of better than 2% (Träbert et al. 2000c; 2000d). The systematic errors seem to be under better control in these experiments than in the competing ECRIS/Kingdon trap experiments discussed above. How do we know that? Well, the Kingdon trap lifetime results on M1 transitions in various Ar ions (in the near-UV/visible range) as well as some of the early EBIT lifetime data (at NIST and LLNL) fell short of theoretical predictions by about 10 to 15%. This might have been interpreted either as toothing problems of new experimental techniques or as a possible problem with theory. Meanwhile, however, there are heavy-ion storage ring results on similar atomic systems, and they are not in disagreement with theory. Also, improved data collection techniques at the Livermore EBIT have resulted in lifetime data (Träbert et al. 2000c, 2000d) that turned out to be close to theory and to carry little intrinsic uncertainty. The combination of these experimental findings gives mutual assertion and increased confidence in the capability of EBIT.

6. Conclusion

The major experimental techniques for time-resolved measurements of possible interest in the context of the expanding field of X-ray astrophysics can contribute very different data and supporting information. The elemental purity and, to a lesser extent, the control over charge-states of the fast-ion beam techniques are major assets as they help with the identification of unknown lines. Beam-foil spectroscopy is most easily employed, but does not reach some of the very-long lived levels that can be exploited for the study of low-density astronomical objects. Here ion traps of various designs come into play. A more extensive review of the recent achievements with lifetime measurements using such ion traps of all sizes is being presented elsewhere (Träbert 2000).

For the vast majority of all atomic levels, there will never be enough time and money to do appropriate experimental studies, and therefore theory is needed for the mass production of transition rate data for modeling and similar efforts. Theory may be better than foreseeable experiments could do on many of the electric-dipole (E1) allowed transitions, but that is no general guarantee of reliability, and it does not automatically extend to intercombination or E1-forbidden transitions either. Clearly, theory is not being corroborated by measurement in all cases. Theory appears to be reliable (at the few-percent level of uncertainty) for simple cases like the M1 transition in the ground state of B-like ions, and perhaps only slightly less so for the similar case of F-like ions. With more electrons in the open valence shell, the typical scatter of the theoretical predictions of M1/E2 transition rates in lowly-charged ions of second- and third-row elements rises to about 20% (and sometimes a factor of two or three). 10 to 20% is also the uncertainty estimate given with some such calculations. Here the new experimental data discussed above yield an improvement by an order of magnitude that helps shift the astrophysical error budget away from atomic parameters.

Developments are under way to extend the time-resolved EBIT measurements to the XUV spectral range of present interest. If enough encouragement from prospective users can be mustered, similar extensions of the working ranges of present heavy-ion storage ring experiments seem likely. These developments would bear on EUV coronal transitions, some of which have predicted lifetimes that exceed the practical limit (30 ns) of the beam-foil technique, but might be observable in the low-density environments of storage rings or EBIT. Thus they would not only help with the identification of X-ray features in the spectra obtained by the new or coming space crafts dedicated for X-ray work, but also

with the analysis of forbidden transitions in the VUV detection ranges of the SUMER instrument on the SOHO space craft, and on the FUSE mission.

Acknowledgments. Travel support by Dynamitron Tandem Laboratorium Bochum and financial support by F.N.R.S. (Belgium) are greatly appreciated.

References

- Armour, I.A., Fawcett, B.C., Silver, J.D., and Träbert, E. 1980, *J. Phys. B* 13, 2701.
- Bashkin, S. and Meinel, A.B. 1964, *ApJ* 139, 413.
- Calamai, A.G., Gwinner, G., Tordoier, X., Träbert, E., and Wolf, A. 2000, *Phys. Rev. A* (submitted).
- Church, D.A. 1993, *Phys. Rep.* 228, 254.
- Church, D.A., Moehs, D.P., and Idrees Bhatti, M. 1999, *Int. J. Mass Spectrom.* 192, 149.
- Crespo López-Urrutia, J.R., Beiersdorfer, P., Savin, D.W., and Widmann, K. 1998, *Phys. Rev. A* 57, 238.
- Doerfert, J., Träbert, E., Wolf, A., Schwalm, D., and Uwira, O. 1997, *Phys. Rev. Lett.* 78, 4355.
- Eidelsberg, M., Crifo-Magnant, F., and Zeippen, C.J. 1981, *ApJS* 43, 455.
- Engström, L. 1993, *Physica Scripta T* 47, 49.
- Engström, L. and Bengtsson, P. 1991, *Physica Scripta* 43, 480.
- Ghosh, P.K. 1995, "Ion Traps", Oxford: Oxford University Press.
- Hutton, R., Martinson, I., Nyström, B., Ando, K., Awaya, Y., Bengtsson, P., Kambara, T., Kanai, Y., Kojima, T.M., Nakai, Y., Ishii, K., and Jäger, M. 1997, *Physica Scripta* 55, 431.
- Jönsson, P., Froese Fischer, C., and Träbert, E. 1998, *J. Phys. B: At. Mol. Opt. Phys.* 31, 3497.
- Jupén, C., Isler, R.C., and Träbert, E. 1993, *MNRAS* 264, 627.
- Jupén, C., Litzén, U., and Träbert, E. 1996, *Physica Scripta* 53, 139.
- Lapierre, A. and Knystautas, E.J. 1999, *J. Phys. B* 32, 4977.
- Lynch, J.P. and Kafatos, M. 1991, *Astrophys. J. Suppl.* 76, 1169.
- Mannervik, S., Short, R.T., Sonnek, D., Träbert, E., Müller, G., Lodwig, V., Heckmann, P.H., Blanke, J.H., and Brand, K. 1989, *Phys. Rev. A* 39, 3964.
- Moehs, D.P. and Church, D.A. 1998, *Phys. Rev. A* 58, 1111.
- 1999a, *Phys. Rev. A* 59, 1884.
- 1999b, *ApJ* 516, L111.
- Moehs, D.P., Church, D.A., and Phaneuf, R.A. 1998, *Rev. Sci. Instrum.* 69, 1991.
- Möller, G., Träbert, E., and Heckmann, P.H. 1998, *Z. Physik D* 9, 5.
- Müller, H.R., Heckmann, P.H., and Träbert, E. 1982, *Z. Physik A* 308, 283.
- Müller, A. and Wolf, A. 1997, in "Accelerator-based Atomic Physics - Techniques and Applications", edited by S.M. Shafroth, J.C. Austin, Washington: Am. Inst. Phys.
- Neill, P., Träbert, E., Beiersdorfer, P., Brown, G.V., Harris, C., Savin, D.W., Smith, A.J., and Utter, S.B. 2000, *Physica Scripta* 61, (in press).
- Pinnington, E.H., Guo, B., Ji, Q., Berends, R.W., Ansbacher, W. and Biémont, E. 1992, *J. Phys. B* 25, L475.
- Pinnington, E.H., Ji, Q., Guo, B., Berends, R.W., van Hunen, J., and Biémont, E. 1993, *Can. J. Phys.* 71, 470.
- Schmidt, H.T., Forck, P., Grieser, M., Habs, D., Kenntner, J., Miersch, G., Repnow, R., Schramm, U., Schüssler, T., Schwalm, D., and Wolf, A. 1994, *Phys. Rev. Lett.* 72, 1616.
- Smith, S.J., Chutjian, A. and Greenwood, J.B. 1999, *Phys. Rev. A* 60, 3569.
- Träbert, E. 1996, *J. Phys. B: At. Mol. Opt. Phys.* 29, L217.
- 1997, in "Accelerator-based Atomic Physics - Techniques and Applications", edited by S.M. Shafroth and J.C. Austin, Washington: Am. Inst. Phys., p. 567

- 1998, MNRAS 297, 399.
- 2000, Physica Scripta 61 (in press).
- Träbert, E., Armour, I.A., Bashkin, S., Jelley, N.A., O'Brien, R. and Silver, J.D. 1979, J. Phys. B 12, 1665.
- Träbert, E., Beiersdorfer, P., Brown, G.V., Smith, A.J., Gu, M.F., and Savin, D.W. 1999a, Phys. Rev. A 60, 2034.
- Träbert, E., Brandt, M., Doerfert, J., Granzow, J., Heckmann, P.H., Meurisch, J., Martinson, I., Hutton, R. and Myrnäs, R. 1993, Physica Scripta 48, 580.
- Träbert, A.G., Calamai, J.D., Gillaspay, G., Gwinner, X., Tordoir, and A. Wolf 2000a, Phys. Rev. A (submitted).
- Träbert, E., Doerfert, J., Granzow, J., Heckmann, P.H., Jupén, C., Hutton, R., and Takács, E. 1996, 5th Int. Colloquium on Atomic Spectra and Oscillator Strengths for Astrophysics and Laboratory Plasmas (ASOSALP V), Meudon (France), edited by W. L. Tchang-Brillet, J.-F. Wyart and C.J. Zeippen, Meudon
- Träbert, E., Gwinner, G., Wolf, A., Tordoir, X., and Calamai, A.G. 2000b Phys. Lett. A 264, 311.
- Träbert, E., Heckmann, P.H., Hutton, R., and Martinson, I. 1988, J. Opt. Soc. Am. B 5, 2173.
- Träbert, E., Hutton, R., and Martinson, I. 1987, MNRAS 227, 27.
- Träbert, E., Schneider, G., and Heckmann, P.H. 1983, Physica Scripta 27, 407.
- Träbert, E., Utter, S.B., and Beiersdorfer, P. 2000c, Phys. Lett. A (submitted). (work in progress).
- Träbert, E., Utter, S.B., Beiersdorfer, P., Brown, G.V., Harris, C. Neill, P., Savin, D.W., and Smith, A.J. 2000d, ApJ (in press).
- Träbert, E., Wolf, A., Linkemann, J., and Tordoir, X. 1999b, J. Phys. B 32, 537.
- Träbert, E., Wolf, A., Pinnington, E.H., Linkemann, J., Knystautas, E.J., Curtis, A., Bhattacharya, N., and Berry, H.G. 1998a, Can. J. Phys. 76, 899.
- Träbert, E., Wolf, A., Pinnington, E.H., Linkemann, J., Knystautas, E.J., Curtis, A., Bhattacharya, N., and Berry, H.G. 1998b, Phys. Rev. A 58, 4449.
- Träbert, S., Wolf, A., Tordoir, X., Knystautas, E.J., and Gwinner, G. 1999c, J. Phys. B 32, L491.
- Yang, L., Church, D.A., Tu, S., and Jin, J. 1994, Phys. Rev. A 50, 177.

Tokamak Spectroscopy for X-ray Astronomy

Kevin B. Fournier^{*}, M. Finkenthal^{†1}, D. Pacella[‡], M. J. May[†], V. Soukhanovskii[†],
M. Mattioli[‡], M. Leigheb[‡], and J. E. Rice[‡]

^{*}*Lawrence Livermore National Laboratory, P.O. Box 808, L-41, Livermore, CA 94551*

[†]*Plasma Spectroscopy Group, The Johns Hopkins University, Baltimore, MD 21218*

[‡]*Associazione EURATOM-ENEA sulla Fusione, Centro Riccerche Frascati
C.P. 65 - 00044 Frascati, Rome, Italy*

[‡]*Plasma Science and Fusion Center, MIT, Cambridge, MA 02139-4307*

Abstract. This paper presents the measured x-ray and XUV spectra of three astrophysically abundant elements (Fe, Ca and Ne) from three different tokamak plasmas. In every case, each spectrum touches on an issue of atomic physics that is important for simulation codes to be used in the analysis of high spectral resolution data from current and future x-ray telescopes. The utility of the tokamak as a laboratory test bed for astrophysical data is demonstrated. Simple models generated with the HULLAC suite of codes demonstrate how the atomic physics issues studied can affect the interpretation of astrophysical data.

1. Introduction

We are at the beginning of a new age of x-ray astronomy. With the launch of the Chandra X-ray Observatory (CXO) and the X-ray Multi-Mirror Mission (XMM) astrophysicists will be able to study the x-ray universe with unprecedented spectral resolution. Ongoing solar missions such as SOHO and TRACE rely on precise spectroscopy to probe conditions and dynamics in the solar chromosphere. In every case, the study of well resolved high energy emission spectra relies on ionization equilibrium calculations (Arnaud and Raymond 1992), and in the case of collisional plasmas, emission line tabulations (Bickhouse, Raymond, and Smith 1995). There are many issues known to plague existing codes for simulating x-ray emission from astrophysical sources, such as incomplete sets of lines for different ions (Beiersdorfer et al. 1999), and inaccurate atomic data. In order to exploit fully the abundance of x-ray data that will soon be arriving, ionization equilibrium models and emission models need to be well tested and made robust. The solution is to be found in laboratory experiments. Recent programs of observations of astrophysically abundant elements at electron beam ion traps (Bbrown et al. 1998) and tokamaks (Wargelin et al. 1998) are shedding light on the issues of completeness and accuracy in x-ray emission models.

The tokamak is a toroidally symmetric vessel for containing a hot, low density thermonuclear plasma (up to several keV and $10^{12} - 10^{14} \text{ cm}^{-3}$, respectively). The working gas in the vessel is usually a mixture of hydrogen isotopes or helium. The hot plasma is confined by magnetic fields. The principal magnetic field (of the order of tens of kG) is a toroidal field created by external field coils. However, in order to obtain equilibrium and stability it is necessary to have a poloidal magnetic field. In tokamaks this field is produced by currents in the plasma itself. The resulting net magnetic field spirals around the torus. The tokamak can provide an excellent source of emission from astrophysically abundant elements in high temperature plasmas; metallic impurities can be introduced into the plasma mechanically or injected by laser ablation from glass slides, gasses can be puffed through fueling valves on the vessel. The current profile which provides heating and confinement can be well controlled, so the shape and temperature of the plasma can be set by the users' needs. The temperature and density conditions in the plasma are known by independent diagnostics. Electron temperatures are measured by monitoring

¹Racah Institute of Physics, Hebrew University, Jerusalem, Israel

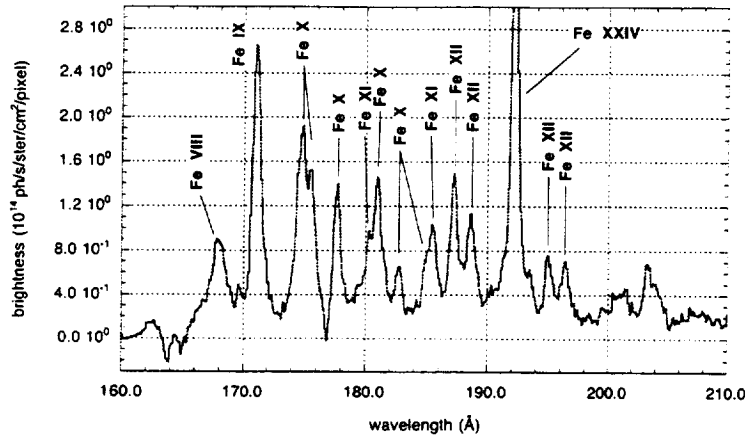


Figure 1. Fe spectrum measured following injection into the Frascati Tokamak Upgrade.

electron cyclotron emission, or by Thomson scattering of laser light. Electron densities are known by interferometry or reflectometry. The fact that the temperature and density conditions are known independently of spectroscopy means that spectroscopic models can be rigorously tested by observations. In what follows, we will discuss high spectral resolution observations of x-ray and soft x-ray emission following the controlled introduction of an impurity into a tokamak plasma (May et al. 2000). These observations are made with x-ray crystal spectrometers (Rice and Marmor 1990; Bartiromo et al. 1995) and a grazing incidence grating spectrometer (Stratton et al. 1984).

Throughout this paper, we will compare our observed tokamak spectra to collisional-radiative (CR) simulations. Our application of CR modeling techniques to tokamak spectra have been discussed elsewhere (Fournier et al. 1996). In brief, we use the HULLAC package of atomic structure codes to generate the data required to calculate CR emissivities for x-ray and XUV transitions. HULLAC provides fully relativistic calculations of energy levels and radiative transition rates as well as semi-relativistic calculations of autoionization rates (Klapisch et al. 1977); it also calculates semi-relativistic collisional excitation rates in the distorted wave approximation (DWA) (Bar-Shalom et al. 1988). These data are used to find the quasi-steady state level populations (and thus line emissivities) for one or more ions of a given element. In what follows, we compare observations of x-ray, soft x-ray and XUV emission from three different astrophysically abundant elements made following injection into tokamak plasmas to CR simulations.

2. M-shell Iron Spectra

Ionization balance models such as that of Arnaud and Raymond (1992) are essential to creating simulations of x-ray and XUV emission from astrophysical objects. As the spectral resolution and collecting area of x-ray telescopes dramatically increases, the interpretation of individual emission lines will strongly test ionization balance models. It is essential that such models be tested under controlled laboratory conditions. Figure 1 shows the spectrum of iron following an injection into the Frascati Tokamak Upgrade (Associazione EURATOM - ENEA, Frascati, Italy). By ramping down the plasma current profile during the later phase of the discharge, we can create a unique plasma configuration that is characterized by a broad, single temperature shelf in the outer part of the plasma. By injecting our samples into this 'ramp-down' state, we can study emission from a single temperature plasma.

The spectrum in Figure 1 shows emission from several M-shell iron ions, K-like FeVIII to P-like FeXII. The strong resonance line of L-shell Li-like FeXXIV is also seen (this is because our spectrometer's line of sight intersects a hotter part of the plasma closer to the core). The temperature profile measured with Thomson scattering as well as charge state distribution measurements indicate that the iron ions are emitting from a 10 cm wide, 80 eV plasma. A simulation using HULLAC CR models and the ionization equilibrium calculations of Arnaud and Raymond (1992) is shown in Figure 2 for $T_e = 84$ eV and $N_e =$

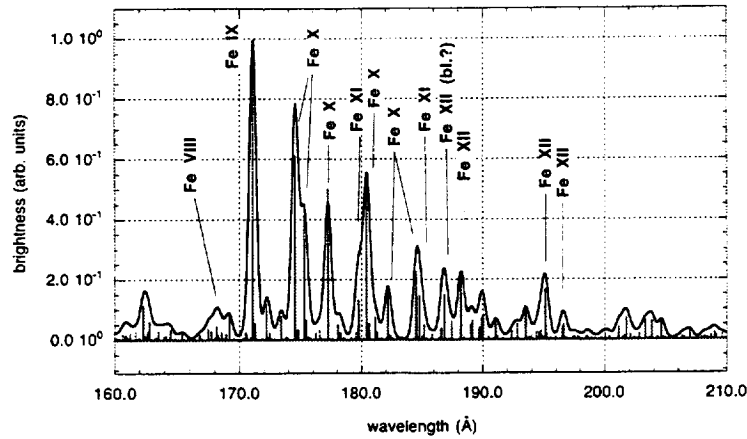


Figure 2. Synthetic Fe spectrum including charge states FeVIII to Fe XIII at $T_e = 84$ eV and $N_e = 6 \times 10^{13} \text{ cm}^{-3}$.

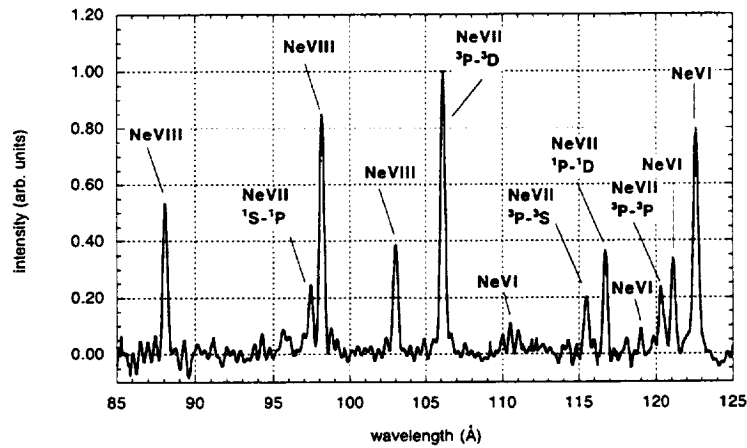


Figure 3. Neon spectrum measured in the Tore Supra Tokamak. The labeled features are $\Delta n=1$ ($n=2-n=3$) transitions.

$6 \times 10^{13} \text{ cm}^{-3}$. Simulations going from 68 to 108 eV ($\log(T_e \text{ K})=5.9$ to 6.1) are found to be extremely temperature sensitive due to the rapidly changing charge state distribution. By performing a spline fit to the curves of Arnaud and Raymond, we find the best match to the experimental spectrum at 84 eV, in good agreement with the Thomson scattering data. Figure 2 has two synthetic spectra at 84 eV, one in which each line has been given a fwhm of 0.65 \AA (comparable to the experimental resolution) and one in which each line is given a fwhm of 1 m\AA . The simulation is similar to the data, the correct relative heights of FeIX (171 \AA) and FeX (174.5 , 175.3 and 177.2 \AA) are recovered (the feature at 174.5 \AA in the simulation is more blended than are the two FeX lines in Figure 1). The FeX and FeXI lines at 177.2 and 180.4 \AA , respectively are also in the correct ratio. The FeXII resonant line at 195.1 \AA is in agreement with Figure 1; however, the lines around 188 \AA may be blended with the FeXVIII resonance line in second order.

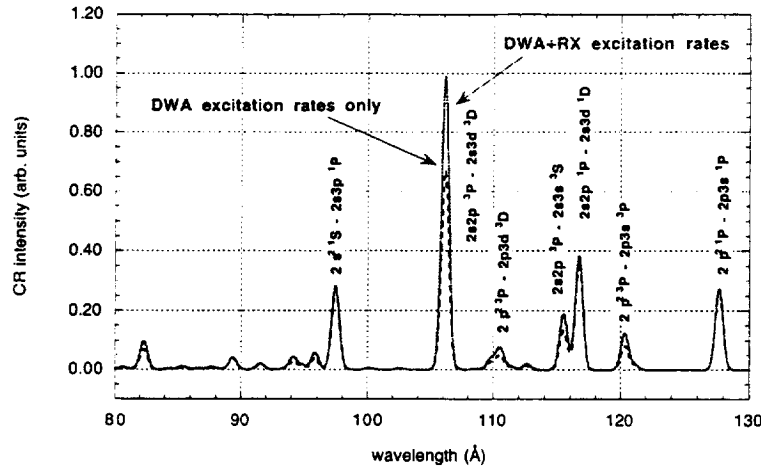


Figure 4. NeVII spectrum computed with and without resonant enhancement of the $2s^2 - 2s2p \ ^3P$ excitations.

3. L-shell Neon Spectra

The soft x-ray emission from highly charged L-shell neon ions has been observed in the Tore Supra Tokamak (Association Euratom - CEA sur la Fusion, Cadarache, France) (Mattioli et al. 1999). These emission lines fall within the range covered by the low-energy transmission grating spectrometer onboard the CXO. A typical neon spectrum following the injection of the gas is shown in Figure 3; lines from Li-like NeVIII, Be-like NeVII and B-like NeVI have been labeled. Simulations for these ions' spectra were run with the HULLAC suite of codes. There are two independent tests of the simulations in these data. First, the simulation for the features from a single charge state is tested against the spectrum of that ion; this tests the quality of the atomic data used in the simulation. Second, the combined spectra of the different ions must match the observed data; this tests the ionization equilibrium models used for the simulation (as was done above for M-shell iron).

In the present work, the simulation for NeVII is used to test collisional excitation rates. The calculation that used DWA collisional excitation rates failed to match the observed line intensities. The discrepancies were systematic, the relative strengths of transitions between singlet levels were consistent with the data, but the relative strengths of all transitions between triplet levels were underestimated. The spectrum of NeVII has been studied in tokamak discharges before (Finkenthal et al. 1987; Hunag et al. 1998). The measured NeVII relative line intensities in this work show excellent agreement with those measured in (Huang et al. 1998). The transitions between singlet levels are fed (primarily) by excitations from the ground level $2s^2 \ ^1S$ or the excited $2s2p \ ^1P$ level, the transitions between triplet levels are fed by excitations from the $2s2p \ ^3P$ levels. The authors in (Finkenthal et al. 1987) conclude that in order to get the populations in the $2l2l'$ levels correct, R-matrix collision strengths must be used. Comparing HULLAC's DWA $\Delta n=0$ excitation rates between the ground level and the $2s2p \ ^3P$ levels with sophisticated R-matrix calculations (Ramsbottom et al. 1995), we find that the $2s^2 - 2s2p \ ^1P$ excitation rate agrees to better than 10%, while the $2s^2 - 2s2p \ ^3P$ DWA excitation rates are underestimated by as much as 60%. By substituting the R-matrix rate coefficients for the $2s^2 - 2s2p \ ^3P$ excitations, the population in the $2s2p \ ^3P$ levels is enhanced by $\approx 50\%$, the increased population is then collisionally transferred to the upper levels of the triplet-triplet transitions in Figure 3. Two simulations for the spectrum of NeVII are shown in Figure 4. The dashed line is the simulation done using only the DWA collisional excitation rates. The solid line in Figure 4 is the NeVII spectrum calculated including resonant enhancement (RX) of the $2s^2 - 2s2p$ excitations. The overall agreement between the data in Figure 3 and the simulation with RX is excellent. This level of agreement is better than that found between the simulations and observations in Huang et al. (1998). This is most likely due to the larger atomic models used in the

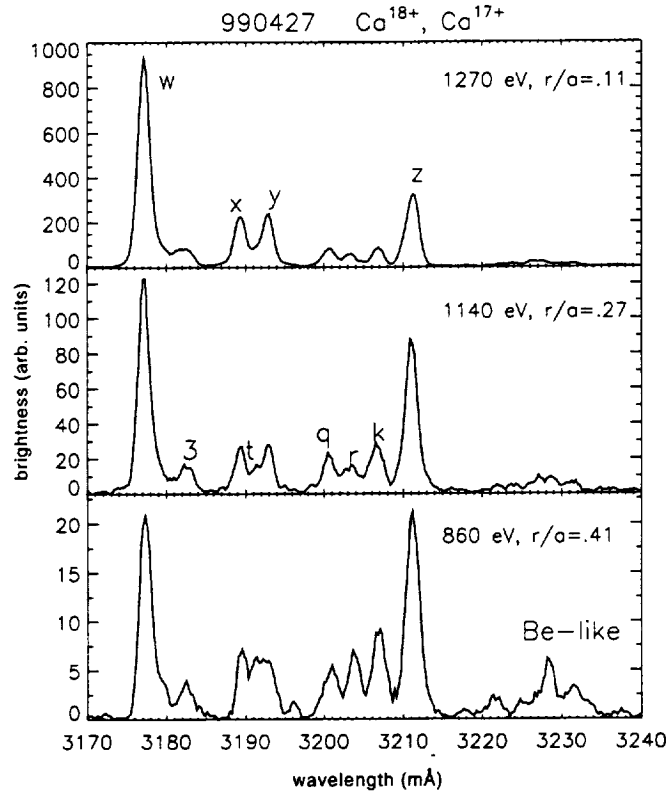


Figure 5. Calcium x-ray spectra measured from three different lines of sight in the Alcator C-Mod tokamak.

present work, which include DWA calculations of the full spectrum of collisional transitions between all $2\ell 3\ell'$ levels.

4. K-shell Calcium Spectra

Figure 5 shows the K-shell x-ray spectrum from calcium injected in the Alcator C-Mod Tokamak (Plasma Science Fusion Center, Massachusetts Institute of Technology). High resolution observations of the K-shell spectra of calcium and iron are important for diagnosing conditions in solar flares (Kato et al. 1998). The figure shows the calcium spectrum from three different lines of sight in the plasma which correspond to three different peak electron temperatures.

The effect on the spectrum of moving out in radius in the plasma (moving to cooler temperatures) is significant. First, the absolute level of the signal drops because the excitation rates for all transitions are falling as the temperature is reduced. Further, the ratio of the He-like resonant line 'w' to the He-like $1s^2 \ ^1S - 1s2s \ ^3S$ 'z' line changes as the spectrum evolves from a collisionally excited ionizing spectrum to one that is recombination dominated. Finally, the emission from inner shell excited Be-like lines is visible in the spectrum observed from the coolest part of the x-ray emitting plasma.

Simple calculations show that a small population of hot electrons in addition to the Maxwellian bulk electron distribution can strongly affect diagnostic ratios. An example of our calculations is shown in Figure 6. For this simulation, we have assumed a bulk electron distribution with a temperature of 1.4 keV and a density of $1.0 \times 10^{13} \text{ cm}^{-3}$ and a population of 20 keV electrons 3% of the bulk. The two simulations have been normalized to the 'w' line. We observe that the presence of the hot electrons enhances the resonance 'w' line, the intercombination 'x' and 'y' and the forbidden 'z' lines differently.

This is due to the different weights of the direct and exchange terms in the collisional excitation rates of these lines. The radial direct and exchange parts of the excitation cross sections have different high energy asymptotes. This different energy dependence results in the 'w' line being more enhanced by the 20 keV electrons than are the 'x', 'y' and 'z' lines.

5. Conclusions

We have presented observations of M-shell Fe XUV spectra, soft x-ray L-shell Ne spectra and K-shell Ca x-ray spectra. In each case, the observed element was injected into a hot, well diagnosed tokamak plasma. In the case of the Fe emission, ionization equilibrium calculations have been benchmarked. In the case of the Ne emission, a case is shown where DWA collision rates needed resonant enhancement. In the case of the Ca emission, the evolution of the K-shell spectrum was seen going from the case of an ionizing to a recombining plasma. Also, the effect on the K-shell models of a small population of hot electrons was demonstrated. This work was performed under the auspices of the U.S. Department of Energy at the Lawrence Livermore National Laboratory under contract No. W-7405-ENG-48.

Acknowledgments. Support for this work was provided by NASA through Chandra award No. EL9-1007A issued by the Chandra X-ray Observatory Center, which is operated by the Smithsonian Astrophysical Observatory.

References

- Arnaud, M. and Raymond, J. 1992, *ApJ* 398, 394.
 Bartiromo, R. et al. 1995, *Nuclear Instruments and Methods in Physics Research B* 95, 537.
 Bar-Shalom, A., Klapisch, M., and Oreg, J. 1988, *Phys. Rev. A* 38, 1773.
 Beiersdorfer, P. et al. 1999, *ApJ* 519, L185.
 Brickhouse, N.S., Raymond, J.C., and Smith, B.W. 1995, *ApJS* 97, 551.
 Brown, G.V., Beiersdorfer, P., Liedhal, D.A., and Widmann, K. 1998, *ApJ* 502, 1015.
 Finkenthal, M. et al. 1987, *ApJ* 313, 920.
 Fournier, K.B. et al. 1996, *Phys. Rev. E* 53, 1084.
 Huang, L.K., Lippmann, S., Stratton, B.C., Moos, H.W., and Finkenthal, M. 1998, *Phys. Rev. A* 37, 3927.

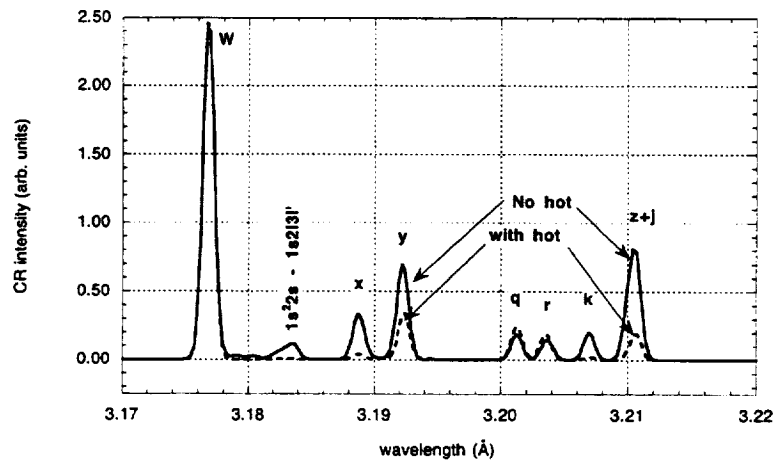


Figure 6. Calcium x-ray spectra with and without a small fraction of hot electrons added to a bulk Maxwellian distribution. The two spectra have been normalized to the intensity of the 'w' line.

- Kato, T., Fujiwara, T., and Hanaoka, Y. 1998, *ApJ* 492, 822.
Klapisch, M., Schwob, J., Fraenkel, B., and Oreg, J. 1977, *J. Opt. Soc. Am.* 67, 148.
Mattioli, M. et al. 1999, *Phys. Rev. E* 60, 4760.
May, M.J. et al. 2000, *Phys. Rev. E* 61, 3042.
Ramsbottom, C. A., Berrington, K.A., and Bell, K.L. 1995, *At. Data Nucl. Data Tables* 61, 105.
Rice, J.E. and Marmor, E.S. 1990, *Rev. Sci. Instrum.* 61, 2753.
Stratton, B.C. et al. 1984, *Nucl. Fusion* 24, 767.
Wargelin, B.J., Beiersdorfer, P., Liedhal, D.A., Kahn, S.M., and von Goeler, S. 1998, *ApJ* 496, 1031.



X-Ray Photoionized Plasmas in the Laboratory

R.F. Heeter¹, J.A. Emig¹, M.E. Foord¹, R.S. Thoe¹, P.T. Springer¹, J. Bailey², M. Cuneo², and C. Deeney²

¹*Lawrence Livermore National Laboratory, PO Box 808, Livermore, CA 94551*

²*Sandia National Laboratories, PO Box 5800, Albuquerque, NM 87185*

Abstract. The advanced spectroscopic capabilities of the new X-ray telescopes Chandra and XMM lead to a need for improved benchmarking of models for the photoionized accretion-disk plasmas which represent over half of known astrophysical X-ray sources. We report the first laboratory experimental results using 120 TW, 180 eV Z-pinch plasmas to drive iron samples into the photoionized equilibrium. The pinch spectrum, temperature, power and uniformity have been characterized in order to qualify it as a photoionization driver. Preliminary time-integrated (8 Å to 18 Å) and time-resolved (12.5 Å to 16 Å) absorption and emission spectra of photoionized L-shell Fe and K-shell Na and F were observed using X-ray crystal spectrometers. Plans for upcoming experiments are also discussed.

1. Introduction

This paper presents the basic approach and first results of laboratory experiments developed to help resolve one of the important physics challenges arising in X-ray astronomy, and outlines the foreseeable progress which is expected in this area in the coming year. A large fraction of astrophysical X-ray sources are accretion-powered objects where an intense core X-ray source illuminates and photoionizes the surrounding gas. The Chandra and XMM observatories are capable of obtaining spectroscopic data with much higher resolution than previously possible in X-ray astronomy. However, the usefulness of excellent spectroscopic data depends greatly upon one's confidence in the basic atomic physics of the models with which the data is interpreted. Users of these data interpretation tools ought to be able to specify a set of plasma conditions, calculate the ionization balance and other properties of such a plasma, and get similar results from multiple codes. We present the results of such a comparison for four major photoionization equilibrium models in Section 2. Confidence in the models can be greatly increased if the model predictions are directly benchmarked against experimental data obtained in well diagnosed laboratory experiments under known plasma conditions; however, until recently the photoionization dominated equilibrium was inaccessible to laboratory experiments. In Sections 3 and 4 we describe how Z-pinch driven intense X-ray sources now enable laboratory astrophysics experiments in the photoionization regime. We report the first results and future plans from such a project in Sections 5 and 6. In future publications we expect to present fully diagnosed experimental photoionization data with which to better benchmark the models and thereby improve the physics foundations for X-ray astronomy.

2. Comparison of Models for Photoionized Plasmas

The photoionization equilibrium in plasma physics arises when the dominant terms in the ionization balance equations are the processes of photoionization (absorbed photon ejects electron from ion) and recombination (electron recombines with ion and emits photon or excites another electron). This situation occurs when the ratio of the X-ray flux to the electron density is sufficiently high that collisional ionization processes are negligible relative to photoionization processes. We are particularly interested in the low density regime where 3-body recombination may also be neglected relative to 2-body recom-

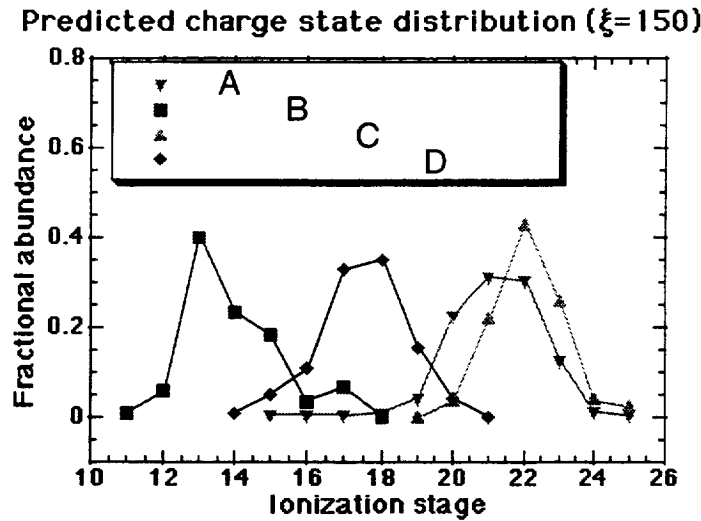


Figure 1. Informal comparison of four photoionization codes at $\xi = 150$ erg cm/s.

bination processes, such that

$$n_i \Gamma_{rad} \int_x^\infty S(E) \sigma_i(E) E^{-1} dE = n_e n_{i+1} \alpha_{i+1}. \quad (1)$$

On the left side, n_i is the density of a given ion species, Γ_{rad} is the total radiation flux, and the integral term uses the spectral shape $S(E)$ and the photoionization cross section $\sigma_i(E)$ to determine the photoionization rate coefficient. On the right side, n_e is the electron density, n_{i+1} is the density of the next ionization stage, and α_{i+1} is the recombination rate coefficient for that stage. One traditionally sets $\xi \equiv \frac{4\pi\Gamma_{rad}}{n_e}$ and it then follows from Equation 1 that the ionization balance $\frac{n_{i+1}}{n_i}$, and indeed much of the physics of these non-LTE photoionized plasmas, is determined solely by fundamental atomic physics data (σ, α) and ξ , the photoionization parameter (Tarter et al. 1969; Tarter and Salpeter 1969).

In order to assess which experiments might best benchmark the models used for photoionized plasmas, we obtained iron ionization balance predictions from four photoionization codes used in the astrophysical community at $\xi \approx 150$ erg cm/s. The results appear in Figure 1, and show disagreement: predictions for the dominant charge state range from Fe XIV to Fe XXIII. These results should be considered preliminary, and consequently the codes are not identified until we can formalize the comparison. However, it appears that users of these data analysis tools should expect considerable disagreement between them (either due to “pilot error” or differences in the physics) and that even simple ionization balance data would be useful in testing the models experimentally. We are actively collaborating with several photoionization modeling groups in this area.

3. Z Pinch X-Ray Sources for Photoionization

The production of strongly X-ray photoionized plasmas in the laboratory has only recently become possible, with the advent of intense Z-pinch X-ray sources. To achieve a given photoionization parameter ξ one needs to maximize the X-ray flux on a given sample, while minimizing the sample density. The first consideration implies placing the sample as close as possible to the strongest possible X-ray source. The second consideration must be balanced against the need to obtain high quality absorption and emission signals, which require maximizing the product of density and scale length. To minimize the density

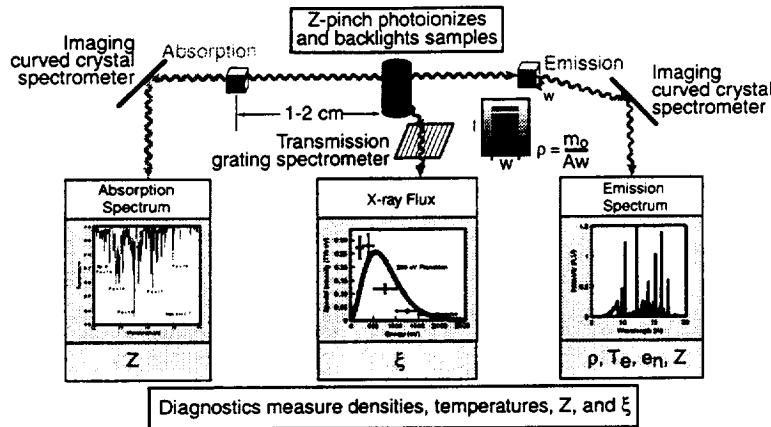


Figure 2. Experimental Concept.

one would like the largest possible sample, but the scale length is constrained by the characteristics of the X-ray source and the need to maintain the entire sample at roughly the same photoionization equilibrium.

The strongest laboratory X-ray source on Earth today is the Z Machine at Sandia National Laboratory, which routinely produces upwards of 100 TW (10^{21} ergs/s) by driving 18 MA of electrical current through cylindrical arrays of 100–400 fine wires. The array as a whole is some 20–70 mm in diameter and 10–20 mm tall to start with, and each wire is on the order of 10 microns in diameter, about a tenth the thickness of a human hair. The Lorentz force acting on the parallel currents causes the wire array to accelerate inwards, reaching velocities on the order of 100 km/s over some 100 ns. The convergence of the array results in stagnation on axis, at which time the kinetic energy of the imploding wires is converted into a 5–10 ns pulse of thermal X-rays with a characteristic temperature of 100–200 eV (1–2 million K) from a region with a typical diameter of 1–2 mm.

It is interesting to compare the X-ray fluxes achieved at Z with astrophysical sources. Foil samples may be placed as close as 15 or 16 mm from the center of the pinch. Working in cylindrical geometry one finds that a 100 TW, 1 cm long pinch produces an X-ray flux at the sample in excess of 3×10^{19} ergs/s/cm², which is comparable to the X-ray flux just 1500 km from a neutron star with a luminosity of 10^{37} ergs/s. The 100 ns run-in time of the pinch provides time for a foil to “blow down” to 10^{-4} or less of solid density, and enables Z to produce photoionization regimes with $\xi \sim 100$ erg cm/s, comparable to conditions found in such accretion powered astrophysical objects as X-ray binaries and active galactic nuclei. Some care must be taken with this comparison because the details of the photoionizing spectrum, plasma composition and plasma density are necessarily different. Nonetheless, the fundamental processes governing the photoionization equilibrium are the same. We therefore anticipate that benchmarking of the photoionization codes with Z-pinch data will enable astronomers to more accurately (or at least more confidently) use these models to interpret X-ray astronomy data.

4. Experimental Objectives and Concept

To properly benchmark the models, one must characterize the flux, spectrum (temperature) and uniformity of the pinch, photoionize a sample into an astrophysically interesting regime, and then measure the absorption and emission of the sample while simultaneously determining the sample density and temperature, preferably in a model independent way. The conceptual layout of such an experiment is shown in Figure 2. In this concept, the pinch is to be characterized using several Sandia diagnostics, which include time gated pinhole cameras, time resolved absolutely calibrated transmission grating spectrometers, calibrated X-ray diodes and bolometers, and a radially and temporally resolved X-ray streak camera. The sample absorption and emission, as well as one band of the pinch spectrum, are to be measured with one or more curved crystal spectrometers, with the Z pinch used as a backlighter for the

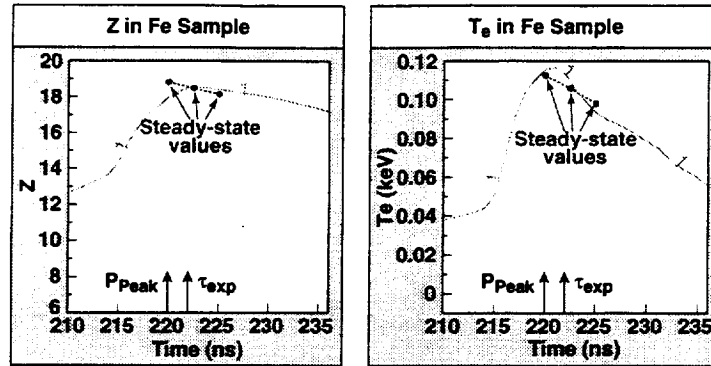


Figure 3. Simulated iron ionization (Z) and electron temperature (T_e) vs. time, with equivalent steady-state values shown.

absorption measurement. The ratio of the absorption spectrum to the pinch spectrum then yields the opacity. The sample temperature is to be extracted from the slope of the recombination continuum as well as line ratios of low- Z tracers in the sample. The sample density is to be obtained by imaging the expansion of the foil with a time gated pinhole camera, using the known initial conditions of the foil.

Although reasonably straightforward in principle, this concept has a number of subtleties which require significant attention to be paid to the experimental design. For instance, in order to compare the time dependent experiment with time independent equilibrium models, the sample must have time to come into equilibrium with the radiation field of the pinch. One must then produce time gated measurements of the sample in the “steady state” regime, before the X-ray pulse from the pinch terminates. One would also like the sample to ionize and expand in a uniform manner, so that all parts of the sample are in the same equilibrium. One also needs the sample to be sufficiently opaque that an absorption spectrum may be obtained, and sufficiently massive that an emission spectrum may be obtained. Given the millimeter scale lengths available in a Z pinch, these considerations all tend towards higher density samples. This conflicts with the desire to minimize the sample density in order to eliminate 3-body processes and maximize the photoionization parameter. One must therefore take care in designing the experiment, to ensure that a balance may be found whereby all these objectives can be achieved simultaneously.

These experimental design issues have been addressed using 1-D and 2-D time dependent radiation hydrodynamics simulations with the LASNEX (Zimmermann and Kruer 1975) code. The resulting sample is a foil composed of 200 Å of iron (the astrophysically interesting component) co-mixed with 300 Å of sodium fluoride (tracers to be used as temperature diagnostics). The foil is hydrodynamically tamped with 1000 Å of Lexan (C,H, and O) placed on either side, forming a sandwich configuration. The foil is 1 mm high and 0.5 mm wide, and placed face-on to the pinch to provide maximum uniformity of illumination. As shown in Figure 3, the run-in phase of the pinch allows the foil to blow down, and the 5–10 ns duration of the X-ray pulse is such that the foil conditions reach equilibrium from 2–4 ns following the peak of the X-ray pulse. Here equilibrium conditions are defined as conditions whose values at a given time match the values expected in steady state for the same X-ray drive at that time. This 2 ns time window poses one of the key challenges for the experiment: it forces the use of time gated rather than time integrated spectrometers to obtain the actual photoionization data, and is comparable to the timing jitter of the best available trigger signals on the machine. At the start of this 2 ns window, we calculate that the iron part of the foil will have expanded (in thickness) from 0.5 to 1200 microns. This maximizes ξ by bringing the foil density down as much as possible, and also allows the expansion of the foil to be imaged edge-on with a time gated pinhole camera. Based on 2-D (R-Z) calculations which account for the actual pinch geometry, we expect an electron density $n_e \sim 10^{19}/\text{cm}^3$ and a mass density $\rho \approx 10^{-4}$ to $10^{-5}\text{g}/\text{cm}^3$, for ξ on the order of 10 to 100 erg cm/s. Under these conditions, preliminary calculations suggest that the charge balance is insensitive to 3-body recombination effects

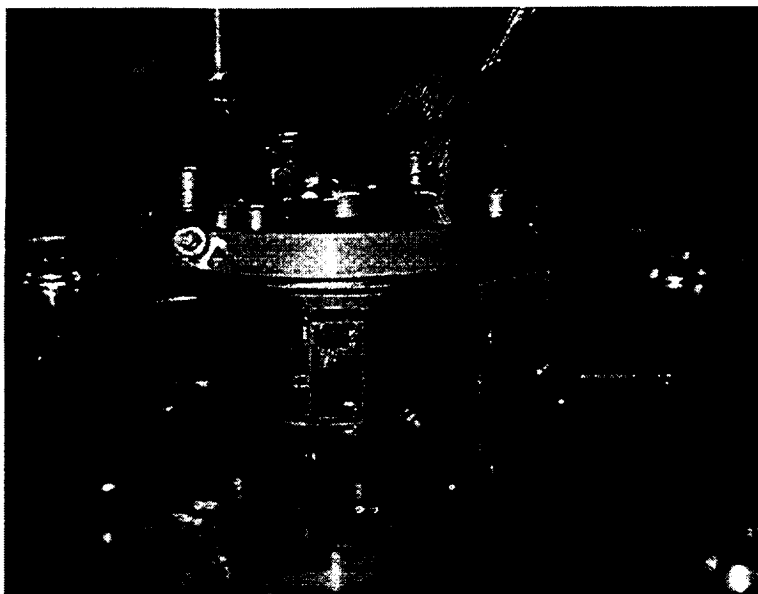


Figure 4. First generation experiment.

and the low-density photoionization equilibrium described in Equation 1 is reached, although further modeling (with experimental data) is required to confirm this.

5. Initial Experiments and Results

Two preliminary photoionization experiments were carried out at Z in September 1999. The principal objectives of these two “shots” were to characterize in detail a particular pinch configuration and to validate the basic experimental design by obtaining as much foil data as possible. We used a 20 mm diameter tungsten wire array with 300 wires, each 10 μm in diameter. Tungsten was chosen because it has a line-free spectrum in the spectral range of interest (750–1300 eV, or roughly 8–16 \AA), and the small (20 mm) many-wire pinch was chosen to provide the maximum X-ray flux onto the sample.

Figure 4 provides a view of the actual “target” (experiment). The wires of the array can be seen diverging out the top of the current return can, which is basically a cylinder with slots cut out to allow instruments to see through to the pinch. Two of the experimental foils can be seen: the first is face-on to the camera in the center of the picture, and the second is seen edge-on off to the right. Various graphite windows were used to limit the fields of view of various instruments. Graphite was chosen so that in the spectral range of interest only the foils and pinch would be visible. For the same reason, all pinch-facing high-Z surfaces were coated first with gold and then with boron. A schematic top view of the experiment is shown in Figure 5, which also details the various diagnostic instruments and their lines of sight.

The experimental results are as follows. In both shots (Z476 and Z477), the pinch produced 120 TW ($\pm 10\%$) of predominantly thermal X-rays with a characteristic temperature of 180 eV (Cuneo 1999, private communication). At the time of interest (2–4 ns after the peak X-ray power), radially resolved streak camera data gives a FWHM of 1.5 mm for the pinch diameter (Lazier 1999, private communication). Pinhole camera images of the X-ray emission above roughly 600 eV show adequate uniformity of the pinch at this time (Breeze 1999, private communication). A time integrated crystal spectrometer with spatial resolution along the pinch axis (vertical) direction obtained a high quality time integrated spectrum. This spectrum is shown in Figure 6, with tentative line identifications using a semi-empirical wavelength scale (Bailey 1999, private communication). The upper trace is a lineout taken through the top part of the foil, where no iron was deposited, and is simply the pinch spectrum with absorption from the Lexan part of the foil. The lower trace is a lineout taken through part of the foil

containing the Fe:NaF mixture, and shows numerous lines from the sodium Lyman and Helium series, fluorine Lyman series, and both neon-like and fluorine-like iron (Fe XVII and Fe XVIII). Of particular interest is the Fe XVII 2p-nd series, with n ranging from 3 to at least 8. The iron spectral lines were identified based on recent data from the EBIT facility at LLNL (Brown et al. 1998; Brown 2000). One reason why the line identifications are only tentative is that the relative line strengths in photoionized plasmas are expected to be considerably different from those in collisional plasmas, which complicates the line identification process, especially when one has only one or two spectra to analyze (Liedahl et al. 1990). The time integrated spectrum in Figure 6 is not ideal to benchmark photoionization models since over much of the integration period the foil was not expected to be in the photoionized regime, but it validates our ability to photoionize Fe into the L shell and produce highly ionized Na and F for spectral diagnostic use.

To obtain time resolved absorption and emission data we fielded a 3-crystal, 2-ns gated Johann curved crystal spectrometer belonging to LLNL. This spectrometer had not previously been used at Z, and a number of difficulties were encountered in this “shakedown” experiment, but we did obtain time gated data from 1-3 ns after the X-ray peak (a respectably close 1 ns from the desired “steady state” window), albeit with higher backgrounds than we would have liked. In these spectra we have tentatively identified lines belonging to Ne-like Fe XVII in absorption, along with the Lyman- α line of Fluorine, plus Fe XVII and Fe XVIII in emission. More importantly, we have identified solutions to the experimental difficulties and gained confidence that we can successfully field this instrument in our second generation experiments, which are scheduled for April or May 2000.

It was hoped that the sample density would be determined by imaging the expansion of the foil with a pinhole camera viewing the foil edge-on through a graphite window. However, we found that the field of view was contaminated by boron blowing back from the wall of the can and by carbon blowing off of the graphite walls, and with only two shots we were unable to properly tune the instrument filtering and gain settings in order to properly resolve the small amount of iron against these background sources. We have, however, identified two techniques to obtain the density measurement in future experiments. The first involves further tuning the pinhole camera, and the second involves placing the foil in a horizontal plane edge-on to the pinch, so that the foil expansion can be imaged spectroscopically in absorption with high signal. Other improvements to the experiments are also being developed.

6. Conclusions and Future Work

Photoionized plasmas are common in astrophysics, and detailed X-ray spectra of such plasmas are now being obtained by new missions such as Chandra and XMM. However, interpretation of these spectra rely on models which are difficult to bring into agreement. We have developed the first capability to produce near-steady-state, uniform photoionized plasmas in the laboratory, using foil samples placed near the Sandia Z Machine. In our first generation experiments the pinch appeared to work well as a photoionization driver, and we produced, as intended, L-shell iron, including a detailed time integrated absorption spectrum with Fe XVII and Fe XVIII, and time resolved absorption and emission spectra showing the same species with lower signal-to-noise. These first generation experiments were not expected to yield all of the data needed to benchmark the photoionization models. Based on these promising initial results, we are implementing various improvements in preparation for an upcoming second generation experiment scheduled for April/May 2000.

Acknowledgments. The authors especially thank T. Dimwoodie at Sandia for timing and data acquisition support. We also thank C. Coverdale, S. Breeze, D. Jobe, S. Lazier, J. McGurn, T. Nash and the Z Machine operations team at Sandia for experimental support, and the LLNL LDRD program for financial support. This work was performed under the auspices of the U.S. Department of Energy by University of California Lawrence Livermore National Laboratory under contract no. W-7405-Eng-48.

References

Brown, G.V. 2000, PhD thesis, Auburn Univ.

- Brown, G.V., Beiersdorfer, P., Liedahl, D.A., Widmann, K. and Kahn, S.M., 1998, *Astrophysical Journal*, 502, 1015
- Liedahl, D.A., Kahn, S.M., Osterheld, A.L. and Goldstein, W.H. 1990, *ApJ* 350, L37
- Tarter, B., Tucker, W. and Salpeter, E.E. 1969, *Astrophysical Journal*, 156, 943
- Tarter, C.B. and Salpeter, E.E. 1969, *Astrophysical Journal*, 156, 953
- Zimmermann, G.B. and Kruer, W.L. 1975, *Comments on Plasma Physics and Controlled Fusion*, vol. 2, 85.

Modeling X-Ray Photoionized Plasmas: Ion Storage Ring Measurements of Low Temperature Dielectronic Recombination Rate Coefficients for L-Shell Iron

D. W. Savin¹, N. R. Badnell², T. Bartsch³, C. Brandau³, M. H. Chen⁴, M. Grieser⁵, G. Gwinner⁵, A. Hoffknecht³, S. M. Kahn¹, J. Linkemann⁵, A. Müller³, R. Repnow⁵, A. A. Saghir⁵, S. Schippers³, M. Schmitt⁵, D. Schwalm⁵, A. Wolf⁵, and P. A. Závodszky⁶

¹Columbia Astrophysics Laboratory, Columbia University, New York, NY 10027, USA

²University of Strathclyde, Glasgow, G4 0NG, United Kingdom

³Institut für Kernphysik, Strahlencentrum der Justus-Liebig-Universität, D-35392 Giessen, Germany

⁴Lawrence Livermore National Laboratory, Livermore, CA 94550, USA

⁵Max-Planck-Institut für Kernphysik, D-69117 Heidelberg, Germany

⁶National Superconducting Cyclotron Laboratory, Michigan State University, East Lansing, MI, 48824 USA

Abstract. Iron L-shell ions (Fe XVII to Fe XXIV) play an important role in determining the line emission and thermal and ionization structures of photoionized gases. Existing uncertainties in the theoretical low temperature dielectronic recombination (DR) rate coefficients for these ions significantly affects our ability to model and interpret observations of photoionized plasmas. To help address this issue, we have initiated a laboratory program to produce reliable low temperature DR rates. Here we present some of our recent results and discuss some of their astrophysical implications.

1. Astrophysical Motivation

The ionization and heating of the media surrounding accretion-powered compact sources, such as active galactic nuclei (AGNs), X-ray binaries (XRBs), and cataclysmic variables, are dominated by photoionization. Theoretical models show that the ionization and thermal structures of these sources are determined by photoionization balanced by radiative recombination (RR) and dielectronic recombination (DR). These models also predict that the electron temperature at which an ion forms (Kallman et al. 1996) is far below the temperature at which the ion would form in coronal equilibrium (Mazzotta et al. 1998). Recent *ASCA* observations of the XRB Cyg X-3 have largely validated the predicted low temperatures (Liedahl and Paerels 1996). Under these conditions, low temperature DR is the dominant recombination channel for many ions.

Iron ions play an important role in determining the line emission and thermal and ionization structures of photoionized plasmas (Kallman et al. 1996; Hess et al. 1997; Savin et al. 1999). Of particular interest is L-shell iron (Fe XVII to Fe XXIV) which affects the range in parameter space over which photoionized gas is predicted to be thermally unstable (Hess et al. 1997; Savin et al. 1999). The need to better understand this instability has been demonstrated by recent *ASCA* observations of Cyg X-3. These observations have detected line emission from ions of neon, magnesium, silicon, and sulfur which are predicted to form in the region of thermal instability (Liedahl and Paerels 1996). With the recent launches of *Chandra* and *XMM*, many more observations are expected of line emission from ions predicted to form in thermally unstable photoionized plasmas.

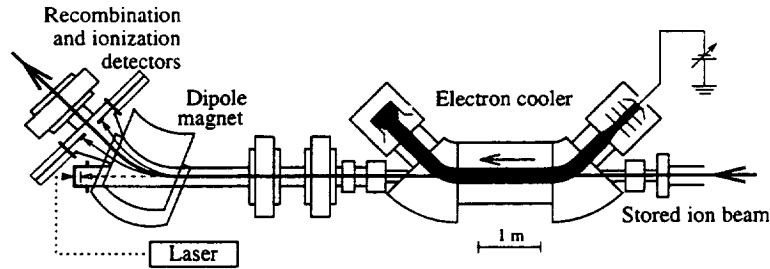


Figure 1. Shown is a partial overview of the TSR experimental arrangement for electron-ion collision measurements. Stored ions enter from the right. The electrons are merged with the ions and travel co-linear with them for ~ 1.5 m after which the electrons are separated from the ions. The ions then travel into a dipole magnet where recombined (ionized) ions are bent less (more) strongly than the primary beam and directed onto a particle counting detector.

2. Experimental Program

“The lack of reliable low temperature DR rates for most third row and higher elements is the dominant uncertainty in the ionization balance in photoionization equilibrium” (Ferland et al. 1998). Low temperature DR rates are theoretically and computationally challenging. There can be up to a factor of 2 spread between different calculated rates (Savin et al. 1999).

To address the needs for modeling X-ray photoionized plasmas, we have initiated a laboratory program to produce reliable low temperature DR rate coefficients for the *L*-shell iron ions. Measurements are carried out using the heavy-ion test storage ring (TSR) (Habs et al. 1989). To date we have carried out measurements of low temperature (*i.e.*, low collision energy) DR onto Fe XVIII (Savin et al. 1999; Savin et al. 1997), Fe XIX (Savin et al. 1999), Fe XX, Fe XXI, and Fe XXII.

DR is a two-step electron-ion recombination process which begins when a free electron collisionally excites an ion, via an $nl_j \rightarrow n'l'_j$ excitation of a bound core electron, and is simultaneously captured. DR is complete when this state emits a photon which reduces the energy of the recombined ion to below its ionization limit. Low energy DR involves a $\Delta n \equiv n' - n = 0$ excitation of the core electron.

Storage rings are uniquely suited for their ability to study low energy DR of highly charged ions (Müller and Wolf 1997). Common laboratory techniques for measuring DR such as electron beam ion traps (Beiersdorfer et al. 1992) and tokamak plasmas (Bitter et al. 1993) can produce the desired ions, but cannot simultaneously reach the required low energies. Crossed electron-ion beam techniques cannot achieve the required low relative velocities (Müller et al. 1987; Savin et al. 1996). Single-pass, merged electron-ion beam techniques can achieve the desired low collision energies (Andersen et al. 1992). However, analysis of such data, particularly for ions with partially-filled shells, is usually complicated by the presence of an unknown quantity of metastable ions in the ion beam. Storage ring measurements overcome this problem by storing the ions long enough for all metastable levels to decay radiatively to the ground state.

Figure 1 shows a schematic of the portion of TSR used to perform DR experiments. Measurements are carried out by merging the ion and electron beams in one of the straight sections of TSR. After demerging, any recombined ions are magnetically separated from the stored ions and directed onto a detector. The relative electron-ion collision energy can be precisely controlled (from 0 eV to ~ 2000 eV) and the recombination signal measured as a function of this energy. The experiments basically follow the procedure described in Kilgus et al. (1992), Lampert et al. (1996). The accuracy of the measured DR resonance strengths is estimated to be better than 20%.

Recombination involves capturing a free electron into a Rydberg level n . Between the cooler and the dipole magnet, some of these captured electrons radiatively decay to lower-lying Rydberg levels. Recombined ions where the captured electron, at the dipole magnet, is in a level $n \gtrsim n_{max}$ are field ionized by the magnet and not detected. For TSR measurements of *L*-shell iron, n_{max} is typically ~ 120 . Theoretical calculations indicate that the contributions to the total *L*-shell iron, low temperature DR

rate coefficient from levels $n > n_{max}$ is $\lesssim 4\%$. DR rate coefficients derived from the experimentally measured DR resonance strengths are estimated to have an accuracy of better than 20%.

Experimental work has demonstrated that DR is sensitive to external electric and magnetic fields (Müller et al. 1987; Savin et al. 1996; Bartsch et al. 1997; Bartsch et al. 1999). However, in TSR the fields are extremely well controlled and we are able to carry out essentially field-free DR measurements. In the interaction region in TSR, external electric fields are insignificant ($E \lesssim 10 \text{ V cm}^{-1}$). The ions also travel parallel to the magnetic field which confines the electrons and hence experience no $\mathbf{v} \times \mathbf{B}$ electric field. In addition, $\Delta n = 0$ DR measurements on lithium-like chlorine have shown that for DR into levels $n \lesssim 80$, field effects are not discernible at electric fields $E \lesssim 15 \text{ V cm}^{-1}$ (Bartsch et al. 1999). Our work here involves DR measurements for ions more highly charged than lithium-like chlorine, and the effect of external fields on the $\Delta n = 0$ DR process is predicted to decrease with increasing charge (Griffin and Pindzola 1987). Also, theoretical calculations indicate that the contributions to the total L -shell iron, low temperature DR rate coefficient from levels $n > 100$ is $\lesssim 10\%$ (Savin et al. 1999). Therefore, we expect external fields to have an insignificant effect on the L -shell iron low temperature DR rates derived from TSR data.

3. Recent Results

In Figure 2 we show preliminary data for $\Delta n = 0$ DR onto nitrogen-like Fe XX and boron-like Fe XXII. These data clearly demonstrate the resonance nature of the DR process. Following the procedures outlined in Savin et al. (1999), Kilgus et al. (1992), Lampert et al. (1996), we can fit the DR resonances to extract the relevant resonance strengths and energies. We then integrate the measured resonances with a Maxwellian electron velocity distribution to yield a total $\Delta n = 0$ DR rate coefficient for plasma modeling (cf., Savin et al. 1999; Savin et al. 1997; Savin 1999).

In Figure 3 we show our experimentally derived rate coefficient for $\Delta n = 0$ DR onto Fe XVIII and Fe XIX (Savin et al. 1999; Savin et al. 1997). We also show various theoretical DR rates published before our measurements were carried out as well as new calculations carried out using our measured Fe XVIII and Fe XIX resonance strength and energy measurements as benchmarks. Lastly, for comparison we have plotted the recommended RR rates.

For Fe XVIII and Fe XIX, the semi-empirical formula of Burgess (1965), the LS -coupling calculations of Roszman (1987a, 1987b), the intermediate coupling calculations of Dasgupta and Whitney (1990, 1994), and the multiconfiguration Dirac-Fock (MCDF) calculations of Chen (1988) all go rapidly to zero below $k_B T_e \sim 20 \text{ eV}$. This is because these calculations were carried out for high temperature plasmas and have not included DR via $2p_{1/2} \rightarrow 2p_{3/2}$ core excitation channels (which is unimportant in high temperature plasmas). We also note here that LS -coupling does not include all possible autoionization channels which can contribute to the DR rate and thus should provide a lower limit to the true DR rate (Griffin et al. 1985; Badnell 1988).

Fe XVIII is predicted to peak in fractional abundance at $k_B T_e \sim 15 \text{ eV}$ in photoionized gas with cosmic abundances (Kallman et al. 1996). As a result, at the relevant temperatures in photoionized gas, the published rates underestimate needed DR rate by a factor of 2 to orders of magnitude.

At temperatures where the $2p_{1/2} \rightarrow 2p_{3/2}$ DR channel is unimportant, our derived rate coefficient is in best agreement with the Burgess formula and the results of Dasgupta & Whitney. As discussed in Savin et al. (1999), this agreement is almost definitely fortuitous. Agreement is poor with the LS -coupling calculations of Roszman which lie above our DR rate. The more sophisticated 1988 MCDF calculations of Chen (1988), which more correctly account for autoionization, are also in poor agreement with the experimental rate. At plasma temperatures $k_B T_e > 100 \text{ eV}$, $\Delta n = 1$ DR begins to dominate the DR process (Chen 1988).

Fe XIX is predicted to peak in fractional abundance at $k_B T_e \sim 70 \text{ eV}$ in photoionized gas with cosmic abundances (Kallman et al. 1996). At this temperature the published calculations all lie above the experimentally derived rate.

For both Fe XVIII and Fe XIX, recent MCDF and multiconfiguration Breit-Pauli (MCBP) are in much better agreement with our experimental results than are previously published rates. The MCBP rates are not shown in Figure 3 but are in good agreement with the MCDF rates. However, we note

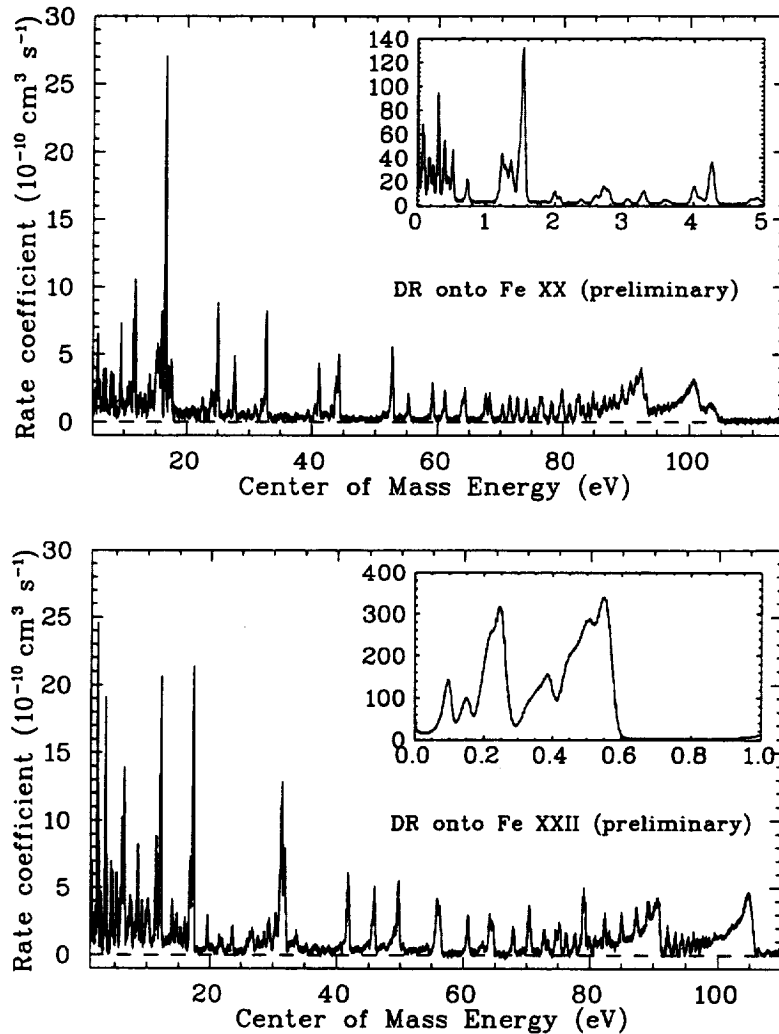


Figure 2. Preliminary data for $\Delta n = 0$ DR onto nitrogen-like Fe XX and boron-like Fe XXII. The measured rate coefficients represent the DR cross sections convolved with the experimental energy spread. The “background” is due primarily to RR with some residual signal due to charge transfer of the ions off rest gas in TSR.

that for Fe XVIII the new theory lies $\sim 35\%$ below the experimental rate at $k_B T_e \sim 10$ eV. And for Fe XIX the new theory lies $\sim 30\%$ above the experimental rate.

It is also worthwhile to point out that the theoretical results for Fe XVIII and Fe XIX from Roszman (1987a) and from Dasgupta and Whitney (1990) are for DR onto the 2P and 3P states, respectively. The results for Fe XVIII from Chen (1988) are for the $^2P_{3/2}$ state, as are our new MCDF and MCBP calculations. For Fe XIX our new calculations are for the 3P_2 state. At low temperatures, DR rate coefficients for different fine-structure states can be very different (Chen 1988) due to differences in resonance energies.

We can draw a number of conclusions from our experimental work to date. First, given the factor of ~ 2 scatter between published $\Delta n = 0$ DR rates, we can infer that a similar uncertainty exists for published low temperature DR rates onto Fe XX through Fe XXIV. It is a goal of our research to produce reliable, experimentally derived DR rates to remove this uncertainty. Second, it is not possible to tell, in the absence of laboratory measurements, whether a theoretical DR rate lies above or below the “true”

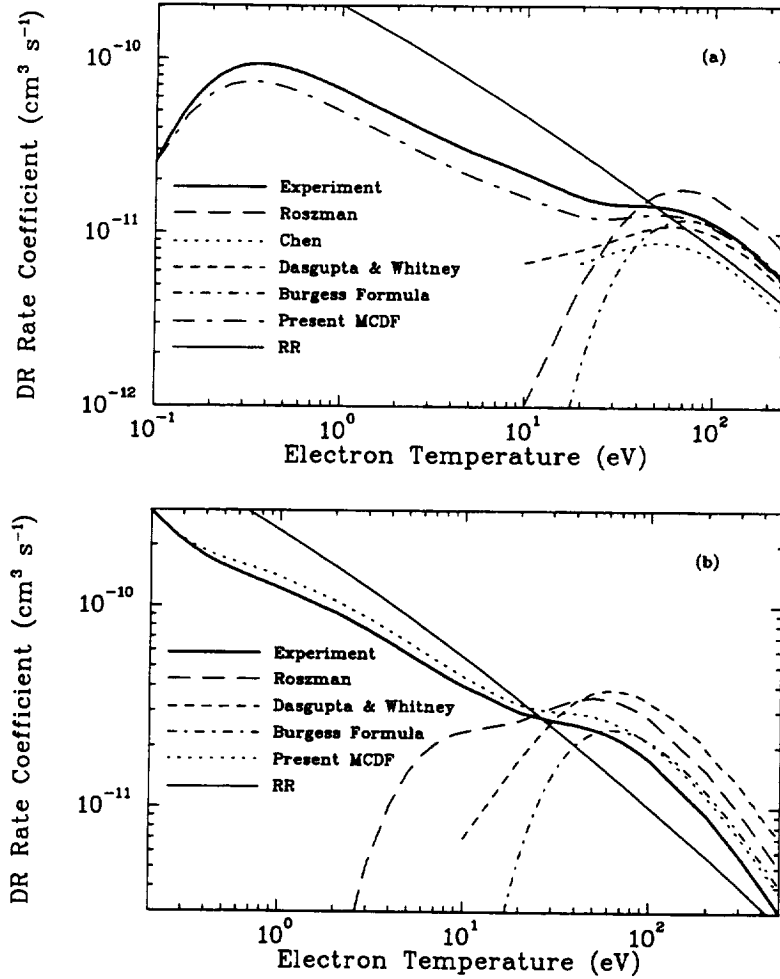


Figure 3. $\Delta n = 0$ DR rates for (a) Fe XVIII to Fe XVII and (b) Fe XIX to Fe XVIII (Savin et al. 1999). The thick solid curve shows the experimentally derived rates. The dotted-long-dashed curve in (a) and the dotted curve in (b) show our new MCDF calculations of Ref. (Savin et al. 1999). Not shown are our new MCBP calculations of Savin et al. (1999) which agree well with the MCDF calculations. The thin solid curve shows the recommended RR rate of Arnaud and Raymond (1992). The other curves show DR rates published before the measurements were carried out. See text for more details.

DR rate, nor by how much. Third, published DR rates do not necessarily provide reliable upper and lower limits to the value of the DR rate. Lastly, measurements of the relevant DR resonance strengths and energies are the only reliable way to verify the accuracy of DR calculations.

4. Astrophysical Implications

There are a number of potential astrophysical implications of our work to date. For example, DR via $2p_{1/2} \rightarrow 2p_{3/2}$ core excitations offers the possibility of new electron temperature and density diagnostics (Savin et al. 1998). Also, the estimated factor of 2 uncertainty in the published $\Delta n = 0$ DR rates for *L*-shell iron can dramatically affect the range in parameter space over which photoionized gas is thermally unstable, making it smaller or larger. However, the uncertainty in these DR rates cannot

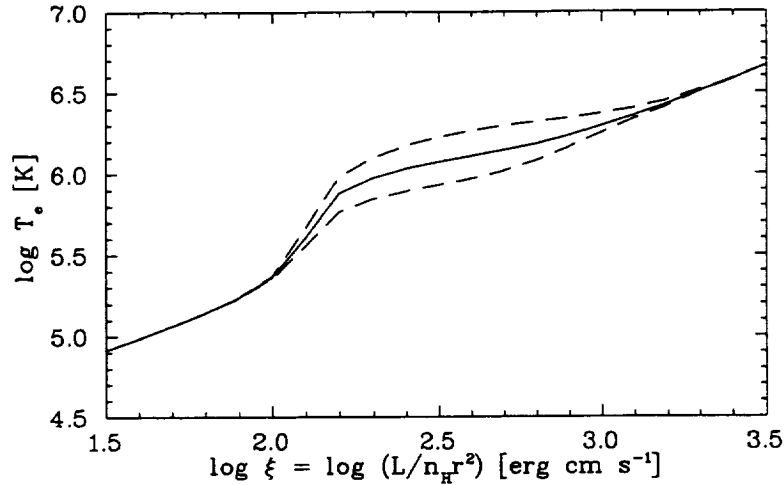


Figure 4. Predicted electron temperature versus ionization parameter ξ for a model AGN ionizing spectrum illuminating a slab of gas with cosmic abundances. The middle curve shows the predicted T_e using our experimentally derived $\Delta n = 0$ DR rates for Fe XVIII and Fe XIX and the unchanged $\Delta n = 0$ DR rates for Fe XX through Fe XXIV. The upper (lower) dashed curve shows our results when the $\Delta n = 0$ DR rates for Fe XX through Fe XXIV are increased (decreased) by a factor of 2.

remove the instability (Savin et al. 1999). Here we will only discuss the implications for line emission from photoionized gas.

We have used XSTAR (version 1.40b; Kallman and Krolik 1997) to investigate the effects on the temperature structure and line emission of photoionized gas due to our estimated factor of 2 uncertainty in the $\Delta n = 0$ DR rates onto Fe XX through Fe XXIV. We have run XSTAR with the relevant $\Delta n = 0$ DR rates unchanged, increased by a factor of two, and decreased by a factor of two. We assume cosmic abundances; and a model AGN ionizing spectrum with a photon number power law of $N \propto E^{-1.8}$ extending from 13.6 eV to 40 keV. Here E is the photon energy. More details are given in Savin et al. (1999).

Figure 4 shows the predicted electron temperature versus ionization parameter $\xi = L/n_H r^2$, where L is the luminosity of the ionizing source, n_H is the hydrogen nucleus density, and r is the distance from the ionizing source. Should a future observation yield a $\log T_e \sim 6.1$ (where T_e is in K), then the uncertainty in the inferred ξ would be a factor of ~ 3.4 . For observations in this range of ξ , this uncertainty will hamper our ability to determine L or n_H to within a factor of ~ 3.4 or r to a factor of ~ 1.8 .

The estimated uncertainty in the DR rates results, for a given value of ξ , is as much as a factor of ~ 1.8 variation between the predicted electron temperatures. The spectroscopic implications of this temperature uncertainty are shown in Figure 5. Here we have used XSTAR to produce synthetic spectra which we have folded through the XMM Reflection Grating Spectrometer (RGS) using XSPEC. The dramatic difference between the two spectra in Figure 5 is due to the different temperatures for the two test cases. The temperature dramatically affects the width of the radiative recombination continua seen in the spectra and in the line-to-continuum ratios.

Acknowledgments. We thank the staff and technicians of the TSR group for support during the beam time. We also thank A. Rasmussen for providing the XMM-RGS response matrix for the synthetic spectra. This work was supported in part by NASA High Energy Astrophysics X-Ray Astronomy Research and Analysis grant NAG5-5123. Travel and living expenses for DWS were supported by NATO Collaborative Research Grant CRG-950911. The experimental work has been supported in part by the German Federal Minister for Education, Science, Research, and Technology (BMBF) under Contract Nos. 06 GI 475, 06 GI 848, and 06 HD 854I. Work performed at Lawrence Livermore National Laboratory was under the auspices of the US Department of Energy (contract number W-7405-ENG-48).

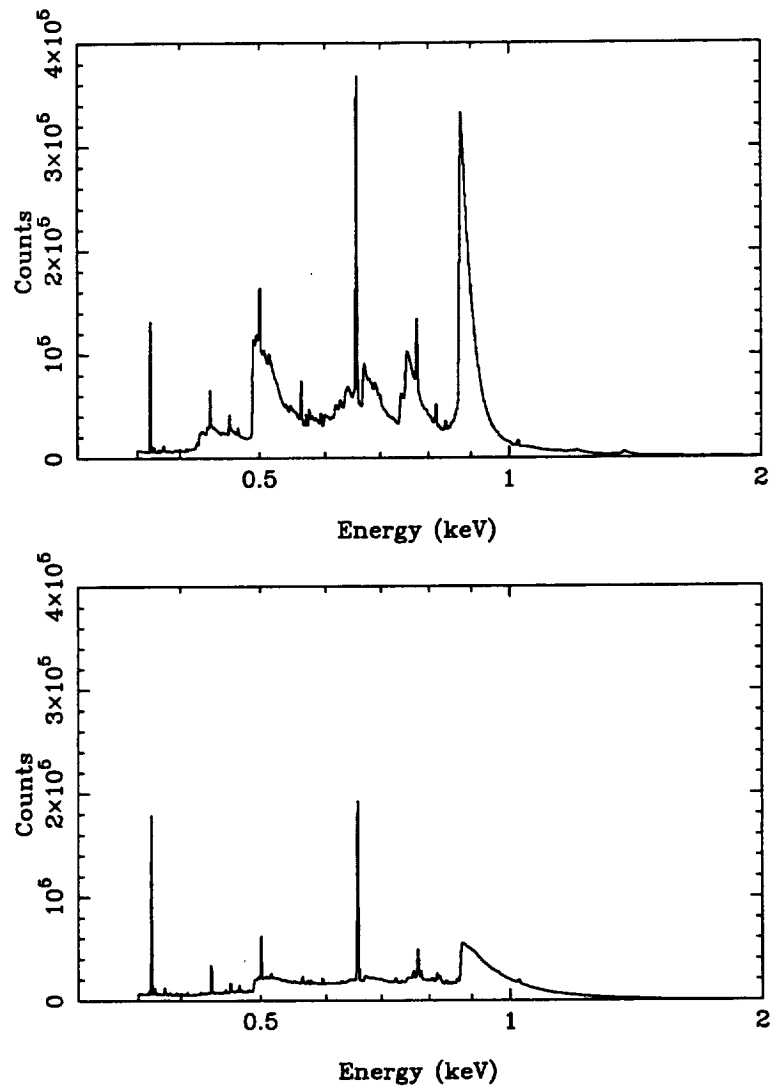


Figure 5. Synthetic spectra using XSTAR for a slab of photoionized gas with cosmic abundances at $\log \xi \sim 2.138$. The spectra have been folded through the *XMM*-RGS response matrix using XSPEC. We use our experimentally derived $\Delta n = 0$ DR rates for Fe XVIII and Fe XIX. The Fe XIX through Fe XXIV $\Delta n = 0$ DR rates have been decreased (increased) by a factor of 2 for the spectrum on the left (right).

References

- Andersen, L. H., Pan, G.-Y., Schmidt, H. T., Pindzola, M. S., and Badnell, N. R. 1992, *Phys. Rev. A* 45, 6332.
- Arnaud, M., and Raymond, J. C. 1992, *Astrophys. J.* 398, 394.
- Badnell, N. R. 1988, *J. Phys. B* 21, 749.
- Bartsch, T., Müller, A., Spies, W., Linkemann, J., Danared, H., DeWitt, D. R., Gao, H., Zong, W., Schuch, R., Wolf, A., Dunn, G. H., Pindzola, M. S., and Griffin, D. C. 1997, *Phys. Rev. Lett.* 79, 2233.

- Bartsch, T., Schippers, S., Müller, A., Brandau, C., Gwinner, G., Saghiri, A. A., Beutelspacher, M., Grieser, M., Schwalm, D., Wolf, A., Danared, H., and Dunn, G. H. 1999, *Phys. Rev. Lett.* 82, 3779.
- Beiersdorfer, P., Phillips, T. W., Wong, K. L., Marrs, R. E., Vogel, D. A. 1992, *Phys. Rev. A* 46, 3812.
- Bitter, M., Hsuan, H., Hill, K. W., and Zarnstorff, M., 1993, *Phys. Scr.* T47, 87.
- Burgess, A. 1965, *Astrophys. J.* 141, 1588.
- Chen, M. H. 1988, *Phys. Rev. A* 38, 2332.
- Dasgupta, A., and Whitney, K. G. 1990, *Phys. Rev. A* 42, 2640.
- Dasgupta, A., and Whitney, K. G. 1994, *At. Data Nucl. Data Tables* 58, 77.
- Ferland, G. J., Korista, K. T., Verner, D. A., Ferguson, J. W., Kingdon, J. B., and Verner, E. M. 1998, *Publ. Astron. Soc. Pacific* 110, 761.
- Griffin, D. C., Pindzola, M. S. 1987, *Phys. Rev. A* 35, 2821.
- Griffin, D. C., Pindzola, M. S., and Bottcher, C. 1985 *Phys. Rev. A* 31, 568.
- Habs, D. et al. 1989, *Nucl. Instrum. Methods* B43, 390.
- Hess, C. J., Kahn, S. M., and Paerels, F. B. S. 1997, *Astrophys. J.* 478, 94.
- Kallman, T. R., Liedahl, D., Osterheld, A., Goldstein, W., and Kahn, S. 1996, *Astrophys. J.* 465, 994.
- Kallman, T. R., and Krolik, J. H. 1997, XSTAR, A Spectral Analysis Tool. The XSTAR code and related documentation is available at ftp://legacy.gsfc.nasa.gov/software/plasma_codes/xstar/.
- Kilgus, G., Habs, D., Schwalm, D., Wolf, A., Badnell, N. R., and Müller, A. 1992, *Phys. Rev. A* 46, 5730.
- Lampert, A., Wolf, A., Habs, D., Kilgus, G., Schwalm, D., Pindzola, M. S., and Badnell, N. S. 1996, *Phys. Rev. A* 53, 1413.
- Liedahl, D. A., and Paerels, F. 1996, *Astrophys. J. Lett.* 468, L33.
- Mazzotta, P., Mazzitelli, G., Colafrancesco, S., and Vittorio, N. 1998, *Astron. Astrophys. Suppl. Ser.* 133, 403.
- Müller, A., Belić, D. S., DePaola, B. D., Djurić, N., Dunn, G. H., Mueller, D. W., and Timmer, C. 1987, *Phys. Rev. A* 36, 599.
- Müller, A., and Wolf, A. 1997, in "Accelerator-Based Atomic Physics Techniques and Applications", ed. S. M. Shafroth, and J. C. Austin (AIP: New York), p. 147.
- Roszman, L. J. 1987a, *Phys. Rev. A* 35, 2138.
- Roszman, L. J. 1987b, *Phys. Rev. A* 35, 3368.
- Savin, D. W. 1999, *Astrophys. J.* 523, 855.
- Savin, D. W., Bartsch, T., Chen, M. H., Kahn, S. M., Liedahl, D. A., Linkemann, J., Müller, A., Schippers, S., Schmitt, M., Schwalm, D., and Wolf, A. 1997, *Astrophys. J. Lett.* 489, L115.
- 1998, in "NIST Special Publication 926, Poster Papers, International Conference on Atomic and Molecular Data and Their Applications (ICAMDATA 97)", ed. W. L. Wiese and P. J. Mohr, Washington, D.C.: U.S. Government Printing Office, p. 96.
- Savin, D. W., Gardner, L. D., Reisenfeld, D. B., Young, A. R., and Kohl, J. L. 1996, *Phys. Rev. A* 53, 280.
- Savin, D. W., Kahn, S. M., Grieser, M., Linkemann, J., Repnow, R., Saghiri, A. A., Schmitt, M., Schwalm, D., Wolf, A., Bartsch, T., Brandau, C., Hoffknecht, A., Müller, A., Schippers, S., Chen, M. H., and Badnell, N. R. 1999, *Astrophys. J. Suppl. Ser.* 123, 687.

The Completeness Criterion in Atomic Modeling

Duane A. Liedahl

Physics Department, Lawrence Livermore National Laboratory
P.O. Box 808, Livermore, CA 94550, duane@virgo.llnl.gov

Abstract. I discuss two variations on the completeness theme in atomic modeling; missing lines as they affect the performance of spectral synthesis codes, and missing configurations as they affect the theoretical emissivities of bright lines, with emphasis on the latter. It is shown that the detrimental effects of working with incomplete atomic models can overshadow those brought about by working with less-than-perfect atomic rates. Atomic models can be brought up to an acceptable level of completeness in a fairly straightforward manner, and on a reasonably short timescale, whereas the long-term goal of comprehensive accuracy is unlikely to be reached on the timescale of the current generation of X-ray observatories. A near-term, albeit imperfect, solution is to hybridize atomic models used to synthesize spectra. A hybrid atomic model is one for which a large-scale atomic model, in which completeness is achieved at the expense of accuracy, is augmented with more accurate atomic quantities as they become available.

1. Missing Lines and Spectral Synthesis Codes

Atomic and spectral databases have a variety of practical uses in X-ray astronomy. For example, since identifying bright lines and evaluating any potential problems associated with line blending are often the first steps in analyzing high-resolution spectra, access to a wavelength-ordered compilation of spectral lines greatly facilitates any first-pass interpretation. But even the nominally simple task of line identification cannot be wholly decoupled from assessments of relative line intensities. Moreover, the goals of X-ray spectroscopists are, fortunately, more ambitious than simple line labeling. In collisionally-ionized plasmas, to which this article is restricted, we are thus brought up against the complexities of calculating collision strengths. In most X-ray spectra, there will be only a handful (say, a few tens or less) of bright lines. Since bright lines are less affected by background contamination and counting statistics than faint lines, they will usually be chosen over faint lines to aid in deriving physical constraints. Therefore, it is only natural that we should first devote our limited resources to improving the subset of the atomic collision database relevant to those bright lines.

The luxury of ignoring the hundreds (if not thousands) of weak lines that accompany the bright lines is one afforded us by the advent of high resolution X-ray spectroscopy. By contrast, with low-to-moderate spectral resolution, such as that available with CCDs, we need the capability to reproduce the entirety of an X-ray spectrum. While it is true that the ensemble of bright lines carries most of the line power in the X-ray band, it is *not* true on a bin-by-bin basis. If weak lines are ignored or otherwise improperly taken into account, *data - model* residuals can frustrate attempts at χ^2 fitting. There is no choice but to treat weak lines. This presents a formidable challenge, entailing the generation and management of a vast quantity of atomic data.

Spectral synthesis codes (SSCs) provide a convenient way to access and process atomic databases. In particular, SSCs allow the efficient generation of theoretical spectra. Various pieces of evidence obtained over the last few years, however, indicate that X-ray SSC databases are, in a practical sense, incomplete, a lesson brought to us by *ASCA* (Brickhouse et al. 2000) and *EUVE* (Schmitt et al. 1996). Note that while the *ASCA* era may be drawing to a close, we will not be leaving the CCD era behind, given the prominent role that the *Chandra* ACIS and *XMM* EPIC instruments are sure to play in X-ray astronomy over the next decade. Thus it remains imperative that the deficiencies identified from earlier studies be fully redressed. It may seem ironic that spectral data in which much of the detail is obscured forces spectral modelers into the most detailed considerations of spectral formation.

The SSC incompleteness problems that have been identified involve the absence of emission lines — the “missing line” problem (Beiersdorfer et al. 1999; Liedahl 1999). In terms of atomic modeling, the missing line problem is equivalent to missing energy levels. Radiative transitions from those levels, were they included, would add a substantial contribution to the total radiative power currently represented in plasma codes. The spectral distribution of the missing flux is non-trivial. In the case of Fe L-shell line emission, it has been found that $n \rightarrow 2$ ($n \geq 6$) emission resolves earlier problems in fitting plasma models to *ASCA* data in the 1.0–1.5 keV range (Liedahl & Brickhouse, in prep; Brickhouse et al. 2000). For the remainder of this article, I want to take the missing line problem as a “given,” and then focus on another (related) problem.

2. Missing Energy Levels and Level Population Kinetics

The missing lines are, individually, more or less unobservable; it is only their aggregate effect that becomes a concern. Of course, were they individually observable they would not have qualified as “missing” for so long. In this section it is shown that even bright-line emissivities can be substantially affected by configurations that are typically left out of calculations. It is often the case that atomic models constructed for the purpose of calculating $n \rightarrow n'$ spectra ignore configurations with electrons in $n + 1$, $n + 2$, etc. For the purposes of this discussion, I will refer to such a model as a *minimal model*. A trivial example of a minimal model would be the 4-level H-like ion, consisting of $1^2S_{1/2}$, $2^2S_{1/2}$, and $2^2P_{1/2,3/2}$, which would allow a simplified calculation of $n = 2 \rightarrow n = 1$ spectra. For some bright lines (say, $u \rightarrow \ell$, with the energy of the upper level u denoted by $E(u)$, etc.), the neglect of higher energy levels causes no problem, if u is populated almost exclusively by electron impact excitation from ground ($ground \rightarrow u \rightarrow \ell$). For others, however, which may depend largely upon indirect population flux paths [$ground \rightarrow k \rightarrow u \rightarrow \ell$, where $E(k) > E(u)$], the calculated line emissivities will vary according to the completeness of the atomic model, and will simply be wrong when using the minimal model. The essential point is, therefore, that *model size alone has a bearing on the outcome of spectral simulations*. Two examples are presented below, Ne-like Fe XVII and Ar-like Fe IX. Admittedly, many of the collisional rate coefficients will not be highly accurate (approximately 2,000,000 electron impact cross-sections were calculated for Fe IX), since no attempt was made to include resonances in the cross-sections. The intention is to compare calculations made with the same set of atomic codes, so as to isolate model size as the only variable. All calculations were performed with the HULLAC (Hebrew University/Lawrence Livermore Atomic Code) atomic physics package (Bar-Shalom et al. 1988; Klapisch et al. 1977). Atomic structure is calculated using a relativistic parametric potential in intermediate coupling. Radiative rates include the multipoles E1, E2, M1, and M2. Collisional rate coefficients are obtained by integrating quasi-relativistic distorted wave cross-sections over a Maxwellian electron distribution. Steady-state level populations relative to ground are determined through inversion of the rate matrix, assuming no coupling to adjacent charge states. Line powers then follow from the level populations and radiative rates.

2.1. Ne-like Fe XVII

With its closed shell ground configuration, Ne-like Fe XVII exists across a broad temperature range, and attains a high ionic fraction near its temperature of peak abundance (Arnaud and Raymond 1992). Its $n = 3 \rightarrow n = 2$ lines fall into the 15–17 Å band, and are often among the brightest seen in solar (McKenzie et al. 1980; Phillips et al. 1982) and stellar (Brinkman et al. 2000; Canizares et al. 2000) X-ray spectra. Models for this ion suffer from a number of problems — lack of resonances in the collisional excitation cross-sections, neglect of dielectronic recombination on level populations, and neglect of inner-shell ionization of Na-like iron in creating Ne-like $2p^53s$, to name a few. In studying the $n = 3 \rightarrow n = 2$ emission spectrum, the minimal model is sometimes still employed. Here I will address only the effects on Fe XVII modeling of using the minimal model.

Three of the bright Fe XVII lines originate in the lowest excited configuration $2s^22p^53s$. The four levels inside this configuration have total angular momenta $J = 2, 1, 0, 1$, in ascending energy order. The electric dipole transitions of the two $J = 1$ levels to the $2s^22p^6$ ($J = 0$) ground level are responsible for bright lines at 16.77 Å and 17.05 Å. The $J = 2$ level, being the first excited level, has nowhere to go but

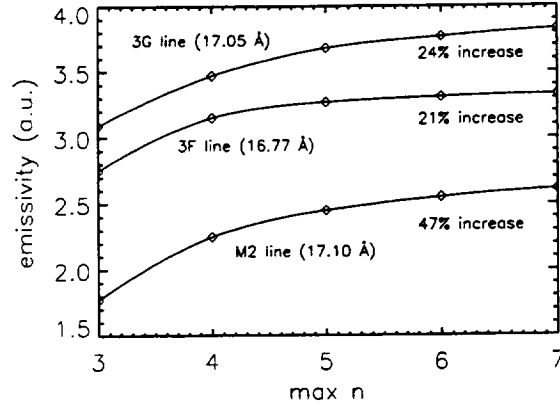


Figure 1. Predicted relative emissivities of three bright Fe XVII (Ne-like) lines for five different models, plotted as continuous curves for clarity. The low-density limit and an electron temperature $kT = 500$ eV are assumed. All three lines (wavelengths and common designations shown) arise from transitions of the type $2s^2 2p^6 - 2s^2 2p^5 3s$. The models are characterized by the value of the highest included shell (x -axis). The percent increases in line power, comparing the $n = 7$ to the $n = 3$ models, are indicated.

to ground, and so decays by a slow M2 transition, producing the bright 17.10 Å line. For convenience, these lines are sometimes designated 3F (16.77 Å), 3G (17.05 Å), and M2 (17.10 Å).

The minimal Ne-like iron model consists of 37 levels distributed among the configurations $2s^2 2p^6$ and $(2s2p)^7 3l$. To illustrate the effect on predicted line powers of varying the model size, four additional HULLAC models were assembled by successively adding shells to the minimal model, up to and including $n = 7$. For each model the temperature is set to $kT = 500$ eV. The results for the line powers of 3F, 3G, and M2 are plotted against the highest included principal quantum number in Figure 1. First, note that the line powers increase most rapidly with model size in going from $n_{\max} = 3$ to $n_{\max} = 4$; addition of “nearby” levels has a more pronounced effect than adding “distant” levels. Second, the curves show signs of converging; adding shells beyond $n = 7$ will have a small effect. In fact, reasonable convergence is obtained for $n_{\max} = 5$. Finally, note that the line powers increase by differing amounts. While the 3F/3G ratio is roughly constant with n_{\max} , the M2/3G (M2/3F) ratio changes from 0.56 (0.64) to 0.68 (0.79) in going from $n_{\max} = 3$ to $n_{\max} = 7$. We remind the reader that the values of these ratios should not be taken too seriously, since, as mentioned earlier, the presence of adjacent charge states has not been taken into account. In other words, the ratios are not strictly independent of temperature. Since Fe XVII is a dominant ion in X-ray spectra, used for determining temperatures, iron abundance, and, in solar coronal studies, the effects of resonant scattering, the errors inherent in the use of the minimal model cannot be dismissed.

2.2. Ar-like Fe IX

Similar to Ne-like iron, Ar-like Fe is the dominant iron ion near its temperature of peak abundance, owing to its closed 3p subshell. In the EUV range the brightest Fe IX lines have upper levels distributed among the twelve excited levels in the first excited configuration $3s^2 3p^5 3d$. Only the three $J = 1$ levels in $3s^2 3p^5 3d$ are connected to the $J = 0$ ground via dipole-allowed transitions — $\lambda\lambda$ 171.1 (from level 13), 217.1 (level 10), and 244.9 (level 3), respectively. By far, the most readily observable Fe IX line is $3p^6 \ ^1S_0 - 3p^5 3d \ ^1P_1$ λ 171.1. Since it is bright, it is the most important proxy for Fe^{8+} , and is used to constrain the emission measure distribution near 10^6 K. Next in importance are the pair of lines just

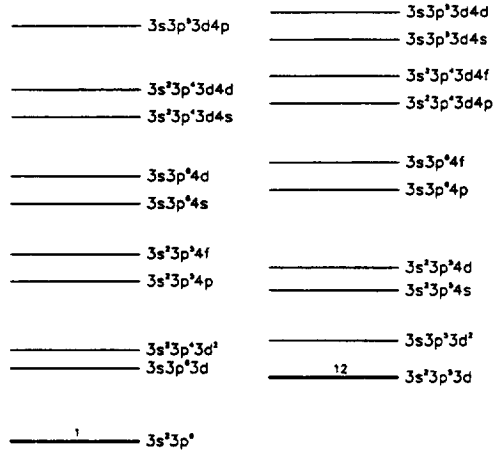


Figure 2. Schematic of 1067-level HULLAC model of Ar-like Fe IX. Even parity configurations are on the left, those of odd parity are on the right. The vertical positioning represents the relative positions (not to scale) of configuration-averaged energies. The ‘1’ and ‘12’ signify the number of fine-structure energy levels corresponding to the $3s^23p^6$ and $3s^23p^53d$ configurations, respectively. Current spectral code predictions are based either upon a 13-level Fe IX model consisting of these two configurations alone (*darkened lines*), or a 17-level model that includes the four levels inside $3s^23p^54s$.

longward of 240 Å; the M2 line from level 4, $3p^6\ ^1S_0 - 3p^53d\ ^3P_2$ λ 241.7; and $3p^6\ ^1S_0 - 3p^53d\ ^3P_1$ λ 244.9. The ratio of these two lines (denoted by 241.7/244.9) serves as a density diagnostic for densities characteristic of stellar coronae (Feldman et al. 1978). In this section, I will emphasize the line powers of these two lines compared to each other and compared to λ 171.1.

Apparent inconsistencies between theoretical predictions and observed Fe IX spectra have been noted in the literature. The ratios 241.7/171.1 and 244.9/171.1 have been reported as being much larger than emission code predictions (Brickhouse et al. 1995; Drake et al. 1995). Also, the ratio 241.7/244.9 appears to imply higher densities than inferred from neighboring ions (Dere et al. 1979; Feldman 1992; Haug 1979). While these two discrepancies are related, and the results shown below are relevant to both problems, only the latter issue will be addressed in detail here. Not surprisingly, in modeling these three lines, the minimal Fe IX model (Fawcett and Mason 1995) is the one most commonly used (e.g., Brickhouse et al. 1995). It consists of the thirteen levels belonging to the ground and first excited configurations.

To determine whether or not the theoretical line powers of the three Fe IX lines mentioned above also depend on model size, we perform an “experiment” similar to that described in the previous section. Using HULLAC, a minimal 13-level model and a larger model (1067 levels) were constructed. The set of configurations included are displayed in Figure 2. The 13-level ion results from stripping the larger model of all energy levels not belonging to $3s^23p^6$ or $3s^23p^53d$. This procedure, as opposed to simply constructing a 13-level model from scratch, removes any differences in calculated rates that might arise from the effects of configuration interaction. Any disagreements in predicted line emissivities between the two models thus reflect differences in the level population kinetics. In terms of accuracy, rate by rate, the distorted wave calculations will not be highly reliable, as they do not treat resonances in the cross-sections, which are important for this ion (P. Storey, priv. comm.). Therefore, to make the experiment meaningful, HULLAC models are compared only to other HULLAC models. This eliminates any ambiguity that might arise from using different atomic datasets. Therefore, the results presented here should be *qualitatively* robust against changes in the set of rate coefficients.

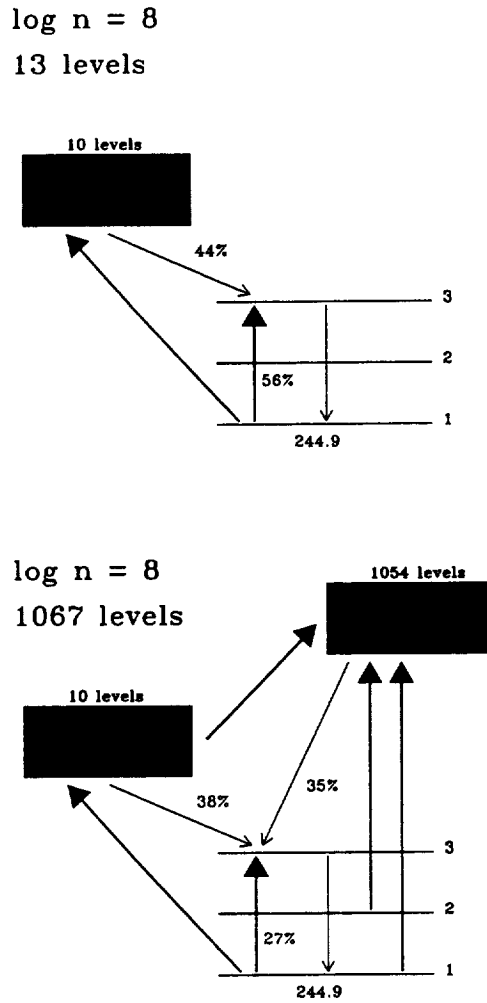


Figure 3. Schematic of level population kinetics leading to emission of $\lambda_{244.9}$ in Ar-like Fe IX, illustrating the dependence on model size (*left panel*: 13 levels; *right panel*: 1067 levels) of the relative weightings of various population flux paths. An electron density of 10^8 cm^{-3} is assumed (cf., Figure 4). Levels 1, 2, and 3 are $3s^2 3p^6 \ ^1S_0$ (ground), $3s^2 3p^5 3d \ ^3P_0$, and $3s^2 3p^5 3d \ ^3P_1$, respectively. The remaining 10 levels of $3s^2 3p^5 3d$ are grouped and symbolized as the box on the left of each diagram. The remaining 1054 levels, spread among the remaining configurations shown in Figure 2, are grouped and represented by the box on the right side of the right panel. Heavy arrows represent collisional transitions, while the lighter arrows represent radiative pathways. Percent values show relative contributions to population influx to level 3 along various pathways.

Probably the most essential improvement in the 1067-level model compared to the 13-level model is the inclusion of the 111 levels inside of the $3s^2 3p^4 3d^2$ configuration, which provide important sinks for $3s^2 3p^5 3d$ levels. Note, however, that the model is still far from complete, as it lacks configurations with principal quantum numbers greater than 4, and does not account for interactions with adjacent charge states. If our intuition derived from studying Fe XVII can be trusted, adding a fifth shell, sixth shell, and so on will become less and less important, and adding the fourth shell, as we have done here, should

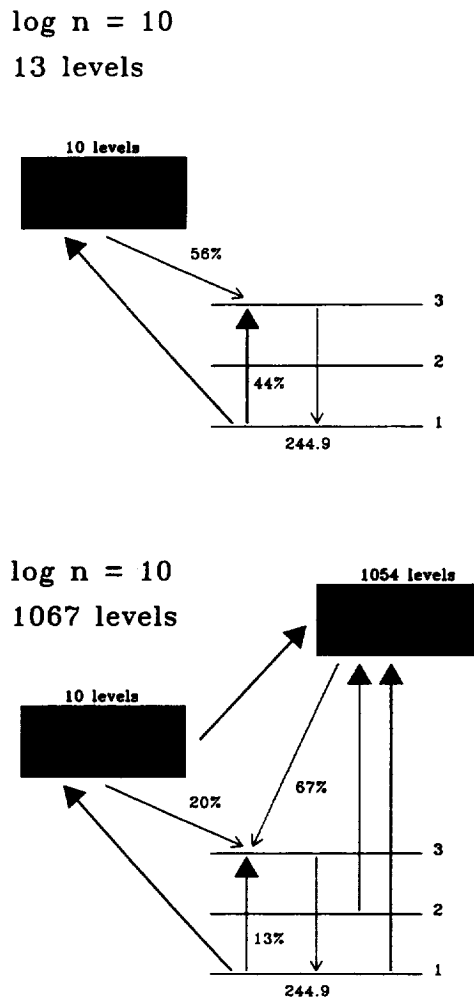


Figure 4. Schematic of level population kinetics in Ar-like Fe IX assuming an electron density of 10^{10} cm^{-3} . See the figure caption to Figure 3 for additional explanation.

go a long way toward accounting for the population kinetics responsible for production of the three lines under consideration.

Tracing population flux paths in Fe IX, even for the 13-level ion, is quite involved. To simplify the description, highly schematized diagrams (Figures 3 and 4) are used. Focusing on 3P_1 (level 3), Figure 3 shows the percent contributions to the population influx at a density of 10^8 cm^{-3} for the two models. Even at this relatively low density, near the lower end of solar coronal densities, the additional configurations can be seen to play an essential role in determining the level 3 population. For example, in the 13-level model, 56% of the influx is attributed to collisional transitions from ground, while in the 1067-level model, this percentage is only 27%. Also note that 3P_0 (level 2), whose radiative decay to ground is strictly forbidden, finds important depopulation channels among $3s^23p^43d^2$. Some of this population flux ends up in level 3, illustrative of the "recirculation" of population that the new configurations allow. Increasing the density to 10^{10} cm^{-3} (see Figure 4) increases the fraction of population influx that

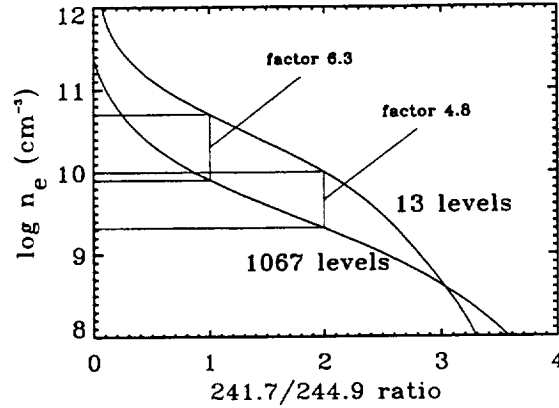


Figure 5. Behavior of the Fe IX 241.7/244.9 emissivity ratios vs. electron density, as determined from two models of the ion which differ in the number of levels included in the rate equations. Coordinate axes are reversed so that, from a hypothetical observed value of the ratio, one reads off the density from the y -axis. Note that use of the smaller model leads to an overestimate of the density for ratios less than 3.0. Two examples are shown: a ratio of 1.0 would imply densities varying by a factor of 6.3, depending on which model is used; a ratio of 2.0 implies densities that vary by a factor of 4.8.

is channeled through the new set of configurations. The contrast of the relative importance of direct excitation from ground is larger than in the lower-density case.

In terms of the brightness of $\lambda 244.9$ relative to $\lambda 171.1$, the net result of adding the new set of configurations is that the ratio $244.9/171.1$ is a factor of 2–3 times higher than predicted using the 13-level model. A similar result is found for $\lambda 241.7$, although its behavior is more complex. In Figure 5, the 241.7/244.9 ratio is plotted against density for the two models. Over the range of density for which this ratio is especially useful, i.e., where both lines are observable and sensitive to density variations, the two models provide substantially discrepant results. For a given observed line ratio the 13-level model leads to an overestimation of the density by factors of a few (see Figure 5). Therefore, use of the larger model partially (if not entirely) alleviates the observed inconsistencies.

A more complete treatment of Fe IX level population kinetics will appear in a future paper (Liedahl, Mewe, & Kaastra, in preparation). Detailed calculations using the R-matrix technique have shown that qualitatively similar corrections to the theoretical line ratios result from the use of more accurate cross-sections (P. Storey, priv. comm.). Studies of the combined effects of better cross-sections and a better treatment of the level population kinetics should prove interesting.

3. Summary of Problems and a Proposed Fix

- *Moderate resolution — weak lines.* Experiences with *ASCA* spectra have shown that the absence of weak lines, even though they may be individually unimportant, compromises our ability to obtain broadband fits to spectroscopic data of low-to-moderate resolution. The spectral distribution of missing lines is poorly known, and has been investigated quantitatively only for a few iron L-shell ions. Broadband fitting places high demands on plasma emission codes, requiring completeness down to the level of statistical or instrumental uncertainties. This problem will resurface in force in the near future, when data from the *Chandra* ACIS and *XMM* EPIC instruments become widely available.

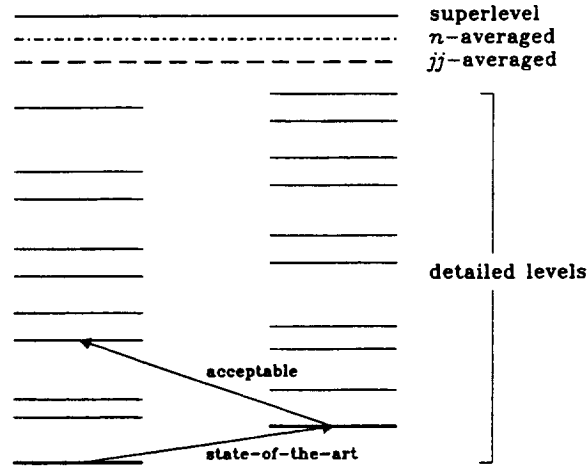


Figure 6. Schematic diagram of a hybrid atomic model, built around the detailed Ar-like Fe IX level structure, represented in Figure 2. Detailed levels are coupled to all other accessible detailed levels by collisional and radiative transitions. A set of jj -averaged ‘levels’ (*dashed line*) consist of artificial levels that lump together detailed levels sharing a relativistic configuration. A set of n -averaged ‘levels’ (*dash-dotted line*) result from lumping levels that share a common set of principal quantum numbers. A ‘superlevel’ represents the remainder of the atomic structure, and is usually included to account for levels characterized by very high principal quantum numbers and their interactions with lower levels, as well as with adjacent charge states. The arrows represent collisional excitation rate coefficients. The enormous number of cross-sections required for a model of this size means that only a subset of the rates can be of ‘state-of-the-art’ quality. For the rest, we can settle for ‘acceptable’ rates, but should not settle for the absence of rates.

- *High resolution — strong lines.* It might seem that, in dealing with high-resolution data, completeness takes a back seat to accuracy, since we can dispense with broadband fits, and concentrate on our favorite handful of lines. There is a different kind of completeness, however, discussed in §2 — the completeness of atomic models. For at least for two important cases, I have shown that the use of incomplete models will lead to significant errors, regardless of the degree of accuracy of the rates contained therein.

To begin to remedy these problems, first, it should be recognized that the benefits of replacing moderate-quality atomic data with high-quality data can be overshadowed by effects arising from model incompleteness. For example, referring back to Figure 4, suppose that the collisional excitation rate coefficient connecting levels 1 and 3 underestimated the actual value by a factor of two. Replacing the old rate coefficient in the 13-level model still neglects the 59% (formerly 67%) fraction of the influx from levels not in the model.

This problem can be addressed through hybridization of atomic models. A hybridization scheme might proceed along the following lines: construct a model that represents shells through, say, $n = 10$, where the atomic structure is broken out into detailed energy levels for the lowest few shells, then, moving to higher shells, averaged down to something manageable, say jj -averaged or n -averaged (see Figure 6). Calculate all appropriate “level”-to-“level” radiative and collisional rates, using a fast distorted wave code for the latter. Some provision needs to be made for coupling to neighboring charge states, of course. With the addition of a superlevel, this constitutes a reasonably complete model (no more missing lines), with reasonably accurate rates. Now, work toward accuracy. As high-quality rates become available, substitute them into the working model, developing priorities based upon a reasonably complete treatment of the population kinetics.

As a final comment, I recommend that future assessments of atomic data quality invoke completeness as an essential criterion of merit.

Acknowledgments. I owe my appreciation to Tim Kallman and Manuel Bautista for their patience and cooperation. Kevin Fournier provided a number of useful comments on an early version of the text. This work was performed under the auspices of the U.S. Department of Energy by the University of California, Lawrence Livermore National Laboratory under Contract No. W-7405-Eng-48.

References

- Arnaud, M. & Raymond, J.C. 1992, *ApJ*, 398, 394.
Bar-Shalom, A., Klapisch, M., & Oreg, J. 1988, *Phys. Rev. A*, 38, 1773.
Beiersdorfer, P., et al. 1999, *ApJ*, 519, L185.
Brickhouse, N., Dupree, A., Edgar, R., Liedahl, D., Drake, S., White, N., & Singh, K. 2000, *ApJ*, 530, 387.
Brickhouse, N.S., Raymond, J.C., & Smith, B.W. 1995, *ApJS*, 97, 551.
Brinkman, A.C., et al. 2000, *ApJ*, 530, L111.
Canizares, C., et al. 2000, *ApJ*, submitted.
Dere, K.P., Mason, H.E., Widing, K.G., & Bhatia, A.K. 1979, *ApJS*, 40, 341.
Drake, J.J., Laming, J.M., & Widing, K.G. 1995, 443, 393.
Fawcett, B.C. & Mason, H.E. 1991, *At. Data Nucl. Data Tables*, 47, 17.
Feldman, U. 1992, *ApJ*, 385, 758.
Feldman, U., Doschek, G.A., & Widing, K.G. 1978, *ApJ*, 219, 304.
Haug, E. 1979, *ApJ*, 228, 903.
Klapisch, M., Schwab, J.L., Fraenkel, B.S., & Oreg, J. 1977, *J. Opt. Soc. Am.*, 67, 148.
Liedahl, D.A., 1999, *Phys. Scr.*, Vol. T83, 110.
McKenzie, D.L., Landecker, P.B., Broussard, R.M., Ruge, H.R., Young, R.M., & Doschek, G.A. 1980, *ApJ*, 241, 409.
Phillips, K.J.H., et al. 1982, *ApJ*, 256, 774.
Schmitt, J.H.M.M., Drake, J.J., & Stern, R.A. 1996, *ApJ*, 465, L51.

Coronal plasmas modeling and the MEKAL code

Jelle S. Kaastra and Rolf Mewe

SRON Laboratory for Space Research, Sorbonnelaan 2, 3584 CA Utrecht,
The Netherlands

Abstract.

An overview is given of the current status of the spectral code development that takes place at SRON Utrecht.

1. A Short History

Starting in the early seventies (Mewe 1972) Rolf Mewe and his colleagues of the Space Research Laboratory in Utrecht started developing a spectral code for the X-ray emission of optically thin plasmas. A milestone was reached in 1985 and 1986, when two papers describing the line emission (Mewe et al. 1985) and continuum emission (Mewe et al. 1986) were published. This spectral code, often abbreviated as the Mewe-Gronenschild code, together with the Raymond & Smith code (1977) served for many years as the basis for many X-ray spectroscopic papers.

At the beginning of the eighties the code was extended with non-equilibrium ionization balance calculations (Gronenschild & Mewe 1982), and motivated by the work on supernova remnants done in Leiden by Fred Jansen and Jelle Kaastra vastly improved. The need for a faster code in order to be able to do spectral fitting to these non-equilibrium spectra of supernova remnants motivated us to improve the performance of the code. Then in 1992 an update of in particular the continuum calculation appeared, and this updated and faster computer code was implemented at HEASARC in the XSPEC package, at which time it was baptized as *meka* code, after the two main authors of this version, Mewe and Kaastra.

Around the same time we started the SPEX project, with the intention to improve, update and extend also the line emission part of the code. In addition we intended to make it more useful by having spectral simulation and fitting options attached to it, as well as more illustrative graphical and tabular output from the program, which helps to understand the physics of the sources being studied. Also different extensions like hydrodynamical models for supernova remnants, and differential emission measure analysis techniques were foreseen.

In 1994 the first version of SPEX became public, with the re-written *meka* code as working horse in the core of the software package. A year before the ASCA satellite had been launched, and in one of the first X-ray spectra of a cluster of galaxies, the Centaurus clusters, the observed spectrum did not match neither the predicted *meka* calculations nor the results of other codes like the Raymond & Smith code (Fabian et al 1994). In particular the ratio of the Fe-L blend from principal quantum level $n = 4$ to $n = 2$ as compared to the blend from principal quantum level $n = 3$ to $n = 2$ did not match the observations. Around the same time, Duane Liedahl was able to produce better results for the Fe-L complex using the HULLAC atomic code, and by joining forces an update of the *meka* code, now named *mekal*, after the three authors, was released (Mewe, Kaastra & Liedahl 1995). This code was both included in the SPEX package as well as a model in the XSPEC package. Apart from the update and extension of the iron L complex, it also contained an improvement of the 300–2000 Å band, triggered by the EUVE spectra of stellar coronae, an update for the Fe VIII to Fe XVI ions, plus the addition of DR satellites for Mg XI. Also the ionization balance for iron was updated using the results of Arnaud & Raymond (1992).

The need for higher accuracy triggered us to try to update the code in a systematic way, working along isoelectronic sequences. The most recent developments in this work are described in the next sections.

2. Wavelength update

The grating spectrometers aboard of Chandra and XMM have a spectral resolution of 0.01–0.05 Å. However, for strong lines the line centroid can be determined much more accurately than the spectral resolution, if systematic wavelength errors can be taken out. Any uncertainties or rounding-off errors in the wavelengths of these lines as used in the spectral code will therefore lead to a significant mismatch of the predicted spectrum as compared to the observed spectrum. Only for the Sun X-ray spectra with such a high spectral resolution have been obtained with good statistics. Therefore using high-resolution solar flare X-ray spectra obtained with the Bragg Flat Crystal Spectrometer (FCS) on SMM, the lines of the *mekal* code in the 5–20 Å band were benchmarked (Phillips et al. 1999). Laboratory measurements of the wavelengths of these lines were also used to confirm the SMM values as well as published identifications from the HULLAC atomic code. The adjustments needed were up to 0.035 Å for line wavelengths above 13 Å but much less at shorter wavelengths. Although these corrections are small in an absolute sense, they are well detectable with Chandra and XMM. The wavelength corrections have been implemented now in the SPEX code.

3. Update of the atomic parameters

The update of our spectral code has two major branches: the ionization balance and the line/continuum formation. Recently, an update of the recombination rates for all ions from H–Ni has been given (Mazzotta et al 1998). Current work by us and Mazzotta on a similar update of the ionization rates is in progress.

In our update of the energy levels and oscillator strengths, we have now finished our systematic survey from the H-sequence up to the Al-sequence. These data are taken from the literature or lacking data, from the Cowan code.

Collision strength (both for proton and electron excitation) are collected from different sources and are fitted up to the Co-sequence. A considerable fraction of the collision strengths found in the literature is based upon the work of Zhang & Sampson and co-workers. The other part of our collision data originates from HULLAC calculations. Both the calculated data and the data gathered from literature are then fitted by a simple formula:

$$\Omega(U) = \sum_{i=0}^6 \frac{c_i}{(U+s)^i} + c_7 \ln U + \sum_i a_i \delta(U - U_i), \quad (1)$$

where $U \equiv E/E_{\text{ex}}$ with E the energy of the incoming electron and E_{ex} the excitation energy of the transition. The constants $c_0 \dots c_7$ and s are free parameters, but are forced to be zero for some transitions, e.g., spin-forbidden transitions have $c_0 = c_1 = c_7 \equiv 0$. Further, if resonances are available these can be approximated by the terms with a_i and U_i : for most applications we do not need to know the detailed resonance structure, but only its integral over some broad electron distribution. To that purpose, nearby resonances can be lumped together, and only their total strength a_i and average energy $U_i E_{\text{ex}}$ needs to be given. In practice, no case required more than effectively four resonance terms.

The advantage of Equation (1) is that it can be integrated analytically for a Maxwellian energy distribution, as well as for a power law distribution. For other distributions, the integration can be done numerically. Some other schemes have been proposed where either the scaled collision strength is calculated using splines or a (spline) approximation is made to the Maxwellian-averaged collision strength. Although this is quite useful for thermal electron distributions, it causes difficulties when other electron distributions are considered, since then one needs to go back to the original collision strengths.

The fitting of the data in the literature or from HULLAC calculations to Equation (1) is done to either the original collision strengths, the Maxwellian averaged rates or both, depending upon what is provided in the original publication or data set. Examples of these fits can be found in Mewe (1999).

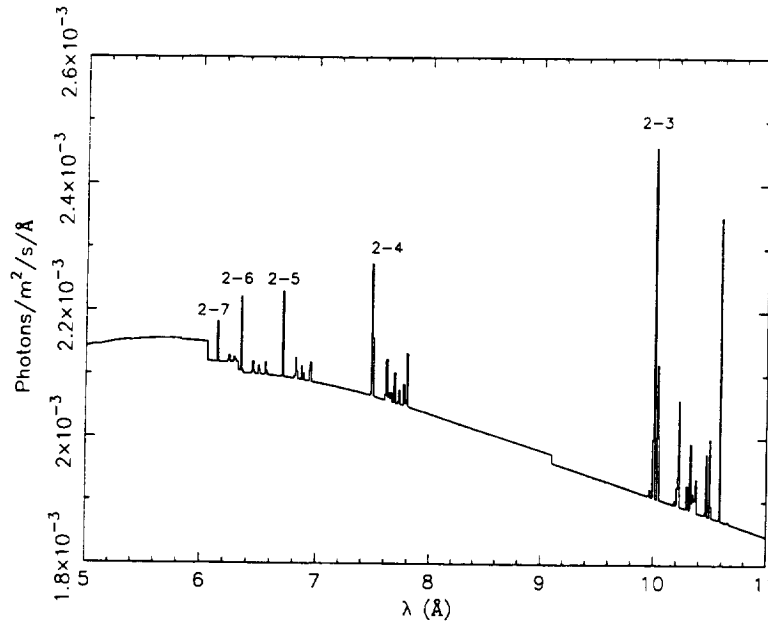


Figure 1. Newly calculated X-ray spectrum of Fe XXV for a temperature of 3 keV.

4. Preliminary results

Although much of the work on validation and implementation of these updated atomic parameters is still in progress, we report here some particular results.

Even for an isoelectronic sequence that is considered to be quite simple, our new results show significant differences with the old *mekal* calculations. For example, in the hydrogenic isoelectronic sequence, the newly calculated Lyman α line power differs in most cases no more than 10 % from the older calculations. But for the higher transitions, like Lyman β , Lyman γ or $H\alpha$ the differences can be larger than 50 %. An illustration can be found in Kaastra (1998).

Here we show some results for He-like ions. Figure 1 shows our new calculations for Fe XXV. We took a temperature of 3 keV. The spectrum shown consists of the complete continuum of all elements, but for the line emission we have selected only the Fe XXV lines. Only the (dominant) excitation contributions to the line formation have been taken into account. The collision rates are based upon Sampson et al. (1983) and Zhang & Sampson (1987). The plot shows the complete spectrum in the Fe-L band, including all transitions up to $n = 7$. In this wavelength range, the old *mekal* code only had 3 lines, and 9 lines in total for all wavelengths. Our present model has 494 lines.

5. Response matrices

One of the powerful features of SPEX is that it is also possible to do spectral simulation and fitting with the same package that calculates the atomic and hydrodynamical models. In general, spectral fitting is done by calculating a model spectrum on a discrete energy grid, folding this through the instrument response by multiplying the model spectrum by the response matrix, and optimizing the parameters of the model spectrum until agreement with the observed spectrum has been reached. This procedure works well with low- to medium resolution spectra, but yields difficulties when high-resolution spectra are analysed. The reason is that in high-resolution spectra the number of model bins becomes very large, in particular for line spectra, since the model spectrum needs to be sampled on a much finer grid than the observed spectrum (in particular for strong lines). Now most grating spectrometers have a rather narrow linespread function, but in addition there is a weaker but broad instrumental scattering

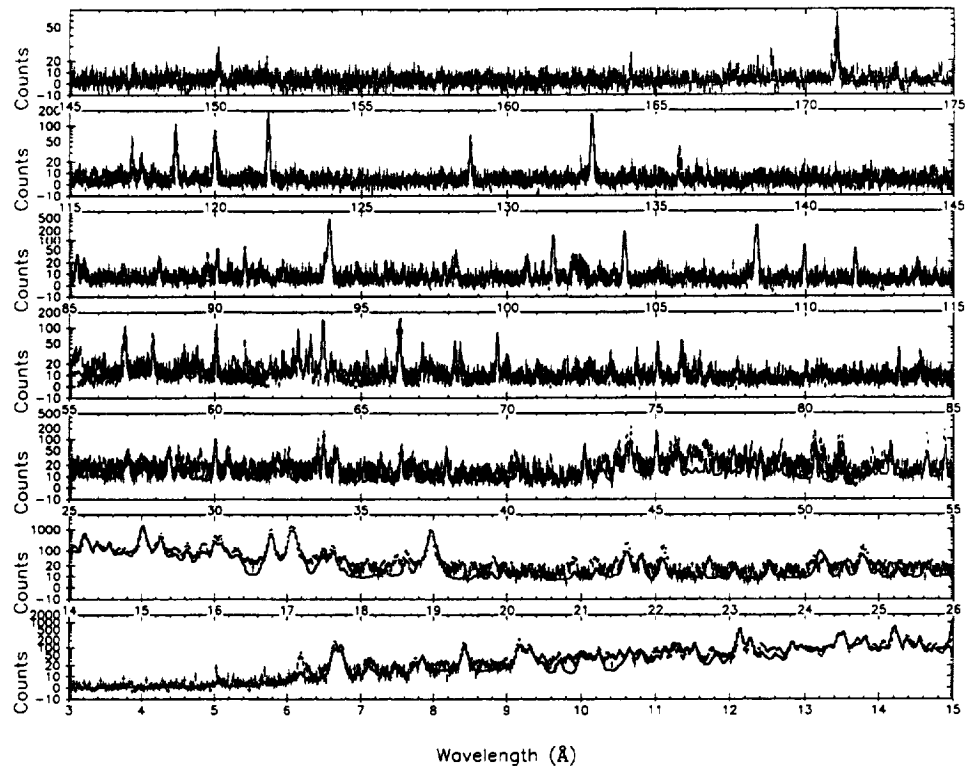


Figure 2. Chandra LETGS spectrum of Capella - both positive and negative spectral orders are plotted as crosses, the best fit model (see text) as solid lines.

component below the main peak. This scattering component in combination with the large number of model bins causes the response matrix to be untractably large.

There is a way out, however, if the following two steps are taken. First, in the classical treatment of response folding, the model spectrum is evaluated by defining an energy grid, and calculating the total number of photons in each individual bin of the grid. Thereby all information on the energy distribution of the photons within the bin is lost, and hence the effective energy resolution of the model is determined by the bin width of the grid. For strong lines, however, the average energy of the photons can be determined much more accurately than the bin width, it is essentially given by the rms width of the line spread function, divided by the square root of the number of photons. The natural way out of the binning problem is to take wider bins, for which not only the total number of photons is calculated, but also the average energy of all photons within the bins. Taking both these numbers consistently into account in the convolution with the response matrix yields accurate results, with a significant reduction in computation time and energy grid size. The second important step is to split up the response matrix in as many components as are required for the line-spread function (lsf). For example, with the RGS spectrometer of XMM the lsf consists of a narrow core and a broad scattering wing. The model spectrum can be convolved with both components separately, and the predicted spectra should be combined at that stage. The reason is that the core of the lsf is narrow and needs a high-resolution energy grid for optimal accuracy, but since it is narrow and has no extended wings the corresponding response matrix is rather sparse. On the other hand, the scattering wings are broad and therefore do not need to be sampled on a very high-resolution grid; a coarser grid is sufficient, and in this way the corresponding response matrix also becomes manageable.

All this has been implemented now in the SPEX package, and in the next section we give an example of its use.

6. The Capella spectrum

We have applied our methods to the Chandra LETGS spectrum of Capella. We binned both the data and model energy grid optimally. The model energy grid had 40000 bins. The observed spectrum had 10252 bins, the final response matrix contained 11 spectral orders, splitted into a narrow and broad response component, the total number of non-zero response elements was 7335000. Without the tricks and methods of the previous section, the size of the matrix would have been an order of magnitude larger. We fitted the spectrum using the *mekal* model with three isothermal components (0.04, 0.2 and 0.53 keV) and solar abundances. This fit is only illustrative, however. A preliminary analysis shows that the abundances deviate somewhat from the solar values, and agree more or less with what Brickhouse et al (2000) derived based upon the EUVE/ASCA data. It should have also been taken into account that the wavelength and efficiency calibration of the LETGS are not yet completely available, and this may also contribute partly to the large reduced χ^2 of the fit (about 4). We hope to improve this later by using the proper calibration as soon as it is available. Also, it should be noted that the fitting was done using the old *mekal* code; we expect that when our updated SPEX code is finished we will also obtain a better agreement.

Acknowledgments. The Laboratory for Space Research Utrecht is supported financially by NWO, the Netherlands Organization for Scientific Research.

References

- Arnaud, M., Raymond, J., 1992, ApJ 398, 394
Brickhouse, N.S., Dupree, A.K., Edgar, R.J., et al., 2000, ApJ 530, 387
Burgess, A., Tully, J.A., 1992, A&A 254, 436
Fabian, A.C., Arnaud, K.A., Bautz, M.W., Tawara, Y., 1994, ApJ 436, L87
Gronenschild, E.H.B.M., Mewe, R., 1982, A&A Supp 48, 305
Kaastra, J.S., 1998, in: The hot universe, IAU Symp. 188, p. 43, eds. K. Koyama et al., Kluwer
Mazzotta, P., Mazzitelli, G., Colafrancesco, S., Vittorio, N., 1998, A&A Supp. 133, 403
Mewe, R., 1972, Solar Phys. 22, 459
Mewe, R., Gronenschild, E.H.B.M., van den Oord, G.H.J., 1985, A&A Supp 62, 197
Mewe, R., Lemen, J.R., van den Oord, G.H.J., 1985, A&A Supp 65, 511
Mewe, R., Kaastra, J.S., Liedahl, D.A., 1995, Legacy 6, 16
Mewe, R., 1999, in: X-ray spectroscopy in astrophysics, p. 109, eds. van Paradijs, J. & Bleeker, J.A.M., Springer.
Phillips, K.J.H., Mewe, R., Harra-Murnion, L.K., et al., 1999, A&A Supp. 138, 381
Raymond, J.C., Smith, B.W., 1977, ApJ Supp. Ser. 35, 419
Sampson, D.H., Goett, S.J., Clark, R.E.H., 1983, ADNDT 29, 467
Zhang, H., Sampson, D.H., 1987, ApJ Supp. Ser. 63, 487

Atomic Databases

Claudio Mendoza

Centro de Física, Instituto Venezolano de Investigaciones Científicas (IVIC)
PO Box 21827, Caracas 1020A, Venezuela
E-mail: claudio@taquion.ivic.ve

Abstract. We describe some of the highlights in the development of atomic databases in the past five years and the ingredients that must be taken into account in order to ensure a successful venture. Also, important issues that have to be addressed in this growing field are briefly discussed.

1. Introduction

Atomic and molecular data are required in a variety of fields ranging from the traditional astronomy, atmospheric and fusion research to fast growing technologies such as lasers, lighting, low-temperature plasmas, plasma assisted etching and radiotherapy. In this context, there are some research groups, both theoretical and experimental, scattered round the world that attend to most of this data demand, but the implementation of atomic databases has grown independently out of sheer necessity. In some cases the latter has been associated with the data production process or with data centers involved in data collection and evaluation; but sometimes it has been the result of individual initiatives that have been quite successful. In any case, the development and maintenance of atomic databases call for a number of skills and an entrepreneurial spirit that are not usually associated with most physics researchers.

In the present report we present some of the highlights in this area in the past five years and discuss what we think are some of the main issues that have to be addressed.

2. Highlights

A summary of the highlights of the field of atomic databases in the last five years must start with the tremendous boost caused by the World Wide Web (WWW). The WWW is certainly leading to a paradigm change in the way scientific information and data are exchanged. Perhaps we are not yet fully aware of the extent of these changes as we just seem to be adjusting to the onset of a major information technology revolution. It is worth pointing out that atomic physics has had a portal (<http://plasma-gate.weizmann.ac.il/API.html>) since November 1994 which, in true web fashion, was the result of an individual initiative, namely by Yuri Ralchenko of the Weizmann Institute in Israel. This portal currently provides up-to-date information about conferences, databases, software, a who's who, jobs, links, resources, atomic servers by country, and includes an electronic preprint archive. Regarding atomic databases, it lists all active sites and classify them by type: numerical and bibliographic databases, data collections and data productions. Although the portal shows a table of data types, it does not display the sites where they are to be found which is useful for first-timers. A review of atomic data and databases on the Internet up to 1996 (<http://plasma-gate.weizmann.ac.il/~fnralch/app.dvi>) can be downloaded from its homepage. There are other portals of more specialized nature linking atomic databases such as *Databases of Atomic & Molecular Data for Astronomy* (<http://cfa-www.harvard.edu/amdata/ampdata/amdata.html>) at the Harvard-Smithsonian Center for Astrophysics.

Another important advance in the field has been the launching of the biennial International Conference on Atomic and Molecular Data and their Applications (ICAMDATA; <http://physics.nist.gov/Divisions/Div842/Icamdata/Homepage/icamdata.html>) that took place at NIST in September 1997, to be followed by a meeting at Keble College, Oxford, in March 2000. This series of conferences is addressing the main issues in the implementation and applications of atomic and molecular databases. It

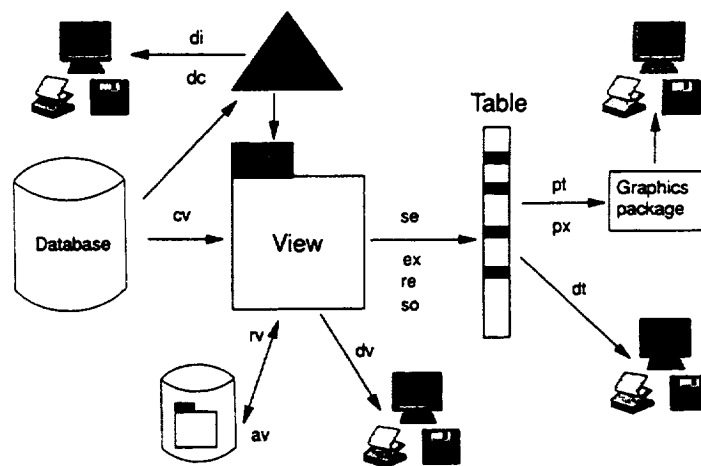


Figure 1. TOPbase database structure

aims at bringing together data producers and users, database developers, data center managers, administrators, and perhaps for the first time, prospective clients from industry (e.g. lighting, semiconductors). One of the key aspects discussed at the first meeting was the general lack of funding for data activities in government agencies. The conference proceedings include a comprehensive review on atomic collision databases and data services by Schultz (1998).

A further aspect that is bound to shape the evolution of atomic databases in the near future is a change in emphasis in high performance computing from number crunching to data intensive applications. This is due to the massive flood of experimental data that is swamping fields such as high energy physics and astronomy and to the huge commercial possibilities of bioinformatics. This situation is rapidly transforming the field of scientific databases from informal inhouse ventures to a new, fast growing, computer engineering discipline. As recently pointed out by Sincell (1999), the data volume and complexity are leading to a double paradigm shift in data storage and dissemination. On the one hand, the heavy data usage is suggesting new subtle ways of data organization and presorting, and on the other, it could transform the existing client-server network architecture to a hierarchical computer grid. In conclusion, it is envisioned that "data mining" will become a new and promising research mode in the near future.

3. Database Developments

When we were involved in the development of TOPbase (Cunto and Mendoza 1992; Cunto et al. 1993), the Opacity Project (The Opacity Project Team 1995) atomic database, a model was proposed for a database structure (see Figure 1). Data stored in secondary memory (disk) are retrieved as a result of a user query by at most two disk accesses through a properly structured set of indexes which can also be used as a table content. The retrieved data give rise to a subdatabase (a *view*) in main memory. The view can be displayed on the monitor, printed or stored as a disk file. Each view is identified by means of a *descriptor* that lists the search parameters that define it. Data in a view can be further massaged in main memory through the *table* structure to satisfy the user ultimate output requirements. The final table can then be displayed, printed, stored in a disk file or graphically processed.

This scheme was devised before the client-server architecture of the web became established and its transcription is not always smooth (refer to the TOPbase web version (<http://heasarc.gsfc.nasa.gov/topbase>)). For instance, the index structure can be smartly exploited to allow, in addition to the query search mode, to a browsing search mode through hyperlinks; the *view descriptor* can be exported to a second web page to become an interactive *view manager*; graphic processing can be carried out efficiently

at the client end through a Java applet. However, data massaging in main memory is very difficult to implement as the browser sockets are disconnected after every page access thus limiting interaction. This means that the user must specify precisely before each query the input and output requirements.

With this model in mind, we proceed to make quick comments on the current atomic database initiatives. The web site containing the *Atomic Spectral Line Database* (<http://cfa-www.harvard.edu/amdata/ampdata/kurucz23/sekur.html>) by Kurucz is a good example of a database that allows the user to specify detailed input/output requirements. The *Atomic and Molecular Database* (<http://amdata.nifs.ac.jp/>) at the National Institute of Fusion Science, Japan, makes extensive use of plots to display data, although it does not as yet allow interactive graphic processing at the client end. An interesting page is that of *Atomic Data for Astrophysics* (<http://www.pa.uky.edu/~verner/atom.html>) where a comprehensive database has been built up entirely from hyperlinks from different data reservoirs. Although the popular *CHIANTI* database (<http://wwwsolar.nrl.navy.mil/chianti.html>) cannot be accessed directly on the web, as its software and data must be both downloaded and installed locally, its success is perhaps due to the environment that it provides for data processing.

4. What makes a successful atomic database?

To answer this important question, we refer to our personal experience with the publication in 1983 of what has become a very successful paper (Mendoza 1983), containing tables of energy levels and radiative and collisional rates for nebula modeling. The actual success of this rudimentary database is not linked to its completeness (it was not extensive), accuracy (it listed the best numbers at the time) or regular updating. The tables have not been updated since the original publication, and in fact, independent attempts to do so have not managed to displace it which, after 17 years, is still regularly cited as an atomic data source of choice. After some consideration of this question, we have arrived at the following conclusions:

1. The development of an atomic database must address the needs of prospective users;
2. The availability of the database has to be timely;
3. The data have to become standard reference.

Item (1) suggests that database functionality must follow closely the way users go about in their work, the data must be labeled and in units and structures familiar to them; therefore development must involve user participation. Point (2) regarding timing is key, and can be illustrated with a frequent situation in astronomy. Usually atomic database developments are demanded when a new detector becomes operational not taking into account that the time spent in computing the data and organizing the database may be as long as that taken to design and construct the detector, and is usually underfunded. As a consequence, users tend to gather, as needed, the best they can find and not bother when the more accurate values appear as the data search stage has already been completed. Relating item (3), it is often found that users prefer to share a common set of data that facilitates model comparison and the tracking of discrepancies; the emphasis is then correctly on the physics rather than on the data.

5. Current issues

As coordinator of an on-line atomic database service for almost ten years, we have found that there is a definite world-wide demand for accurate atomic data, but at the same time little scope for commercial ventures. This means that most projects will start as inhouse initiatives and financing would have to rely on the traditional funding agencies. Moreover, in spite of the present trends to promote liaisons with industry, and we would expect data activities to be one of them, there are at present scarce incentives for the latter thus limiting progress.

In 1996 copyright legislation to protect databases was introduced by the European Union, and a similar Antipiracy Act is being discussed in the USA. There has been an intensive debate (see, for instance, Gardner and Rosenbaum 1998; Maurer and Scotchmer 1999; Liedes 1997) on its actual benefits

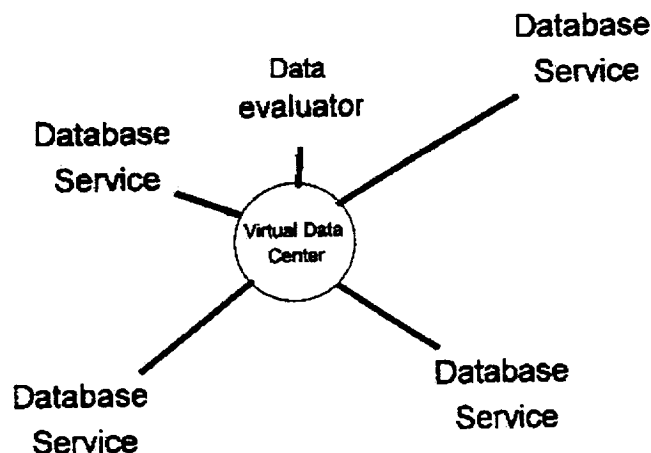


Figure 2. Proposed virtual data center

to the scientific community that has always relied on the open access of data. Proponents of the bill are the American Intellectual Property Law Association, the Information Industry Association and the American Association of Publishers. Critics include the AAAS, the National Academy of Sciences, the Association of Research Librarians, the Digital Future Coalition and the Electronic Freedom Foundation. We are of the opinion that the the Antipiracy Act would harm science by generally restricting data access and by discouraging the implementation of nonprofit databases such as the ones of our concern here.

We have found that there are definite advantages offering database services through a data center although the concept of the latter is rapidly evolving with the growth of the Internet. In Figure 2 we propose the structure of a "virtual data center" which is now envisioned, instead of a data gatherer, as a contractor of distributed database services developed and maintained by data producers. This proposal is in tune with the new web paradigm that information is to be accessed where it is produced. Data evaluation is then integrated as an on-going parallel process rather than a requisite for publication thus speeding up significantly the process of data dissemination. The best example of this concept is the A+M/PMI Data Centre Network (<http://www-amdis.iaea.org/dcn.htm>) that federates 15 national data centers for fusion applications coordinated by the International Atomic Energy Agency (IAEA).

Data centers must play a leading role in the specification of standards and guidelines on IT matters; for instance, the IAEA has established ALADDIN (A Labelled Atomic Data Interface) for the exchange and management of data. However, ALADDIN is implemented in the old fashion way by means of a set of routines rather than actual data structure specifications. Following the distributed model of Figure 2, what is required is the implementation of inter-service data loans or, further, seamless navigation across the databases such that a researcher seeking data in one system can automatically link to the others to complete the process. However, establishing standards can be slow and expensive. Thus, proposals have been mainly concerned with standardizing interfaces (e.g. ALADDIN) rather than the internal functions of the databases (Williams 1997; Pennisi 1999).

The issues concerning accuracy rankings, evaluation and recommendation are among the most difficult to solve. Regarding the accuracy of radiative data, say, an assignment must be given for each transition rather than a transition array, let alone an ion. For instance, in Figure 3 we show the $2s2p^2 - 2s^22p$ transition array in boron-like ions. The accuracy of the A -values for the ${}^2L_J - {}^2P_J^o$, allowed transitions and the forbidden transition within the ${}^2P_J^o$ ground term is much higher than that for the sensitive ${}^4P_J - {}^2P_J^o$, intercombination transition. For the case of the low members of the sequence, e.g. C II and N III, the latter shows both theoretically and experimentally a very broad scatter that

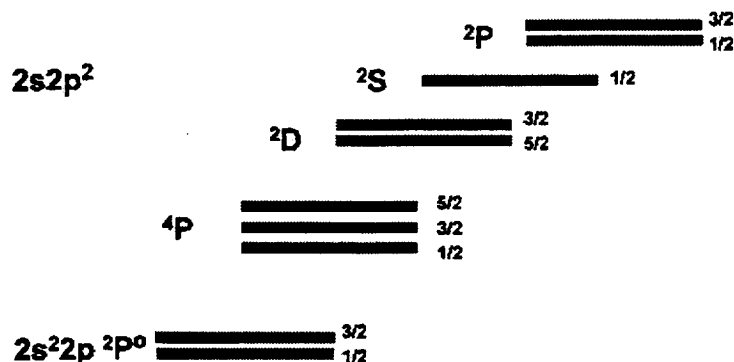


Figure 3. Level structure of the ground and first excited configurations of boron-like ions.

has only been recently sorted out by an experimental benchmark (Träbert et al. 1999, and references therein). This frequent situation makes data evaluation and recommendation a very slow process as every transition must be examined individually.

Finally, it must be stressed that data should always be documented by formal publication and the reference source listed in all database projects.

References

- Cunto W, Mendoza C, 1992, *Rev. Mexicana Astron. Astrofis.* 23, 107
 Cunto W, Mendoza C, Ochsenbein F, Zeippen CJ, 1993, *Astron. Astrophys.* 275, L5
 Gardner W, Rosenbaum J, 1998, *Science* 281, 786
 Liedes J, 1997, *Science* 276, 223
 Maurer SM, Scotchmer S, 1999, *Science* 284, 1129
 Mendoza C, 1983, in *Planetary Nebulae*, Flower DR (ed), Reidel, Dordrecht, 143
 Pennisi E, 1999, *Science* 286, 449
 Schultz DR, 1998, in *Atomic and Molecular Data and Their Applications*, Mohr PJ, Wiese WL (eds), AIP Conference Proceedings 434, American Institute of Physics, Woodbury, New York, p 119
 Sincell M, 1999, *Science* 286, 1840.
 The Opacity Project Team, 1995, *The Opacity Project*, Vol. 1, Institute of Physics Publications, Bristol
 Träbert E, Gwinner G, Knystautas EJ, Tordoir X, Wolf A, 1999, *J. Phys. B* 32, L1
 Williams N, 1997, *Science* 275, 301

REPORT DOCUMENTATION PAGE

Form Approved
OMB No. 0704-0188

Public reporting burden for this collection of information is estimated to average 1 hour per response, including the time for reviewing instructions, searching existing data sources, gathering and maintaining the data needed, and completing and reviewing the collection of information. Send comments regarding this burden estimate or any other aspect of this collection of information, including suggestions for reducing this burden, to Washington Headquarters Services, Directorate for Information Operations and Reports, 1215 Jefferson Davis Highway, Suite 1204, Arlington, VA 22202-4302, and to the Office of Management and Budget, Paperwork Reduction Project (0704-0188), Washington, DC 20503.

1. AGENCY USE ONLY (Leave blank)		2. REPORT DATE October 2000	3. REPORT TYPE AND DATES COVERED Conference Publication	
4. TITLE AND SUBTITLE Atomic Data Needs for X-ray Astronomy: Proceedings			5. FUNDING NUMBERS Code 662	
6. AUTHOR(S) M.A. Bautista, T.R. Kallman, and A.K. Pradhan, Editors				
7. PERFORMING ORGANIZATION NAME(S) AND ADDRESS (ES) Laboratory for High Energy Astrophysics Goddard Space Flight Center Greenbelt, Maryland 20771			8. PERFORMING ORGANIZATION REPORT NUMBER 2000-04370-0	
9. SPONSORING / MONITORING AGENCY NAME(S) AND ADDRESS (ES) National Aeronautics and Space Administration Washington, DC 20546-0001			10. SPONSORING / MONITORING AGENCY REPORT NUMBER CP-2000-209968	
11. SUPPLEMENTARY NOTES A. Pradhan: The Ohio State University, Columbus, Ohio				
12a. DISTRIBUTION / AVAILABILITY STATEMENT Unclassified--Unlimited Subject Category: gg Report available from the NASA Center for AeroSpace Information, 7121 Standard Drive, Hanover, MD 21076-1320. (301) 621-0390.			12b. DISTRIBUTION CODE	
13. ABSTRACT (Maximum 200 words) This publication contains written versions of most of the invited talks presented at the workshop on "Atomic Data Needs for X-ray Astronomy," which was held at NASA's Goddard Space Flight Center on December 16-17, 1999. The workshop was divided into five major areas: Observational Spectroscopy, Theoretical Calculations of Atomic Data, Laboratory Measurements of Atomic Parameters, Spectra Modeling, and Atomic Databases. These proceedings are expected to be of interest to producers and users of atomic data. Moreover, the contributions presented here have been written in a way that can be used by a general audience of scientists and graduate students in X-ray astronomy, modelling, and in computational and experimental atomic physics.				
14. SUBJECT TERMS Observational Spectroscopy, Theoretical Calculations of Atomic Data, Laboratory Measurements of Atomic Parameters, Spectra Modeling, and Atomic Databases			15. NUMBER OF PAGES 171	
			16. PRICE CODE	
17. SECURITY CLASSIFICATION OF REPORT Unclassified	18. SECURITY CLASSIFICATION OF THIS PAGE Unclassified	19. SECURITY CLASSIFICATION OF ABSTRACT Unclassified	20. LIMITATION OF ABSTRACT UL	



